Flexural Behavior of Partially Pretensioned Continuous Concrete Beams

Dr. Nazar Kamil Oukaili
Professor
College of Engineering, University of Baghdad
dr_nazar12000@yahoo.com

Qusai Khudhur Hameed
Ph.D. Student
College of Engineering, University of Baghdad
qusai.gasani@gmail.com

ABSTRACT

This paper describes flexural behavior of two spans continuous rectangular concrete beams reinforced with mild steel and partially prestressing strands, to evaluate using different prestressing level and prestressing area in continuous prestressed beams at serviceability and ultimate stages. Six continuous concrete beams with 4550 mm length reinforced with mild steel reinforcement and partially prestressed with two prestressing levels of ($0.7f_{py}$ or $0.55f_{py}$) of and different amount of 12.7 mm diameter seven wire steel strand were used. Test results showed that the partially prestressed reinforced beams with higher prestressing level exhibited the narrowest crack width, smallest deflection and strain in both steel and concrete at ultimate service load, the deflection decreased by (3.60% & 32.49%) and the crack width decreased by (20.0%) and (75.0%) when increasing the prestressing level from ($0.55f_{py}$) to ($0.7f_{py}$) for beams reinforced with one and two strands respectively. Deflection of beams with two strands decreased by (44.81% & 22.2%) compared with beams of one strand at prestressing level of ($0.7 f_{py}$) and ($0.55 f_{py}$), respectively. At ultimate load, using ACI-Code recommended moment redistribution led to more agreement between theoretical and experimental loads for both ordinary reinforced and partially prestressed beams.

Key words: continuous beams; prestressed concrete; deformation; cracking; redistribution

تصرف الأنثناء للعتبات الخرسانية المستمرة والمسبقة الشد

د. نزار كامل العقيلي
أستاذ
كلية الهندسة-جامعة بغداد

قصي خضر حميد
طالب دكتوراه
كلية الهندسة-جامعة بغداد

الخلاصة

يصف هذا البحث التصرف الانحنائي للعتبات الخرسانية المستمرة بفضائين والمسلحة جزئيا بحديد الاجهاد المسبق والحديد الاعتيادي لتقييم استخدام اجهادات وكميات حديد شد مسبق مختلفة على تصرف العتبات الخرسانية في المراحل التشغيلية والقصوى. تم استخدام ستة عتبات خرسانية مستمرة بطول (4550 ملم) مسلحة بحديد التسليح الاعتيادي وحديد التسليح المسبق الاجهاد ذو قطر 12.7ملم وبمستويين من الشد المسبق (55% و 70%) من اجهاد الخضوع وبعدد مختلف. أظهرت نتائج الفحص بأن العتبات المسلحة جزئيا مع مستوى اجهاد مسبق أعلى كان لها اقل عرض للشقوق واقل هطول وانفعال لكل من حديد التسليح والخرسانة في المرحلة التشغيلية القصوى. زيادة مستوى الاجهاد المسبق قلل منانخفض مقدار الهطول بنسبة (3.6% و 32.49%) وقلل عرض الشق بمقدار (20% و 75%) عند زيادة مقدار الشد من (55%) الى (70%) من اجهاد الخضوع للعتبات المسلحة بظفيرة او ظفيرتين من حديد مسبق الاجهاد على التوالي. استخدام ظفيرتين من الحديد المسبق الاجهاد ادى الى تقليل الهطول بمقدار (44.81% و 22.2%) عند مستويات شد (70% و 55%) على التوالي. النتائج النظرية للحمل الاقصى ابدت توافق اكثر مع النتائج العملية عند استخدام نسب اعادة توزيع العزم الموصى بها من قبل ACI-Codeللعتبات المسلحة اعتياديا والمسلحة جزئيا بحديد الشد المسبق.

الكلمات الرئيسية: العتبات المستمرة، الخرسانة المسبقة الاجهاد، التشوه، التشقق، اعادة التوزيع

1. INTRODUCTION

The use of continuous concrete beams over the interior supports leads to increase the flexural rigidity through providing an alternated load path among the beam, this alternate load path lead to reduce the moments and stresses at midspans results in shallower beams that are stiffer compared with simply supported beams of equal span and with leaser deflection, **Amlan K.**, and **Devdas M.**, **2011**. With low tensile capacity of concrete, flexural concrete members would be cracked at early loading stages with higher deflection. In order to limit tensile stress, cracks and deflection under service load; partial prestressed reinforcement which consists of mild steel and prestressing steel is used in concrete beams, **Nawy**, **2010**. Using such composite reinforcement technique has valuable gains throughout controlling the extent and width of cracks of concrete members which will lead to reduce the deflection of the members.

2. RESEARCH SIGNIFICANCE

In this paper, cracking, deformation and ultimate capacity of two spans continuous concrete beams reinforced with mild steel only and partially prestressed reinforcement will be investigated. The effect of using different prestressing level and prestressing area in negative moment regions of continuous prestressed beams on the flexural behavior of such beams at serviceability and ultimate stages is studied.

3. TEST PROGRAM

Six (200x310mm) cross section continuous concrete beams having length of (4550mm) were tested under two point's monotonic loading until failure. Two beams reinforced with ordinary steel reinforcement and having ultimate failure capacity corresponding to both beams having one or two strands, respectively. Two beams partially reinforced with one (12.7mm) prestressing steel strand with two prestressing levels and ordinary steel reinforcement and two beams partially reinforced with two (12.7mm) of (1860MPa) ultimate tensile strength prestressing steel strands with two prestressing levels and ordinary steel reinforcement. For shear reinforcement, all beams reinforced with (10mm) stirrups spaced at (100mm) through the entire length of the beams. Table 1 shows the reinforcement details for all beams and **Fig. 1** and **Fig. 2** show the cross section and elevation of all tested beams. The designed cylindrical compressive strength of the continuous beams is (35MPa) at (28) days. Table 2 shows the concrete properties of the continuous beams at the time of test. The development of prestressing stress for each strand in concrete beams is shown in Table 3. Normally reinforced beams were designed according to ACI-318 Code to have equal theoretical ultimate capacity corresponding to partially prestressed beams, while the partially prestressed beams were analyzed using strain compatibility method. Concrete beams test was conducted in the Structural Laboratory of the Civil Engineering Department, at the College of Engineering, University of Al-Mustansiriyah.

4. INSTRUMENTATION

Four dial gauges of (0.01mm) accuracy with (50mm) travel length were used to measure the deflection under point load and at mid-span of each side. Different sizes of pre-wired strain gauges of (120Ω) resistance, made in Japan by TML Company are used in this study. Two (2mm) strain gauges are placed on each strand at middle support. Three (5mm) strain gauges are placed on steel bars at both sides of tension zone under load points and at tension zone at middle support. Four (60mm) strain gauges are placed on concrete surface at compression steel level under point load and at (40mm and 80mm) from the bottom face of the beam at middle support.

Six rows of demec points are placed on concrete surface under point load at the right side of the beam at (50, 100, 150, 200, 250 and 300mm) from the bottom face of concrete beam, as shown in **Fig. 3**. Crack width is measured using special tool made of a set of thin steel plates with specific thickness, concrete surface divided to square cells of (50x50mm) to allow for measuring crack propagation at loading stages. Test setup photo shown in **Fig. 4**. One concentrated load was applied on each of the two spans at distance of (725mm) from the center support.

5. ANALYSIS OF TEST RESULTS

5.1 Load Deflection Relationship

Load deflection (P-Δ) curves of tested beams under left load point are shown in **Fig. 5** to **Fig. 7**. **Fig. 5** shows that the increasing of prestressing level in beam (B2) lead to decrease the deflection by (3.60%) at loading level of ($0.5Pu$) compared with beam (B3), and decreased by (7.31%) compared with beam (B1), at same loading level, the deflection of partially prestressed beam (B3) which has the lowest prestressing level decreases by (3.85%) compared with normally reinforced beam (B1). The used beams numbering is same as what mentioned in the original thesis.

Deflection curves at load point in **Fig. 6** shows that when increasing the prestressing level in the partially prestressed beams having two strands, the deflection of beam (B11) decreases by (32.49%) at loading level of (0.5Pu) compared with partially prestressed beam (B12) and by (46.15%) compared with normally reinforced beam (B10), at the same loading level, the deflection of partially prestressed beam (B12) which has the lowest prestressing level decreases by (20.24%) compared with normally reinforced beam (B10).

Fig. 7 shows the deflection at left load point of partially prestressed beams, the figure shows that increasing the number of strands in partially prestressed beam (B11) lead to decrease the deflection at load point by (44.81%) at load level of (0.5Pu) compared with partially prestressed beam (B2) having one strand with same prestressing level, and for the same reason, the deflection of beam (B12) decreases by (21.20%) compared with partially prestressed beam (B3).

From the last two figures, it can be seen that the (P-Δ) curves of partially prestressed beam (B11) and (B12) reinforced with two strands having two portions only, without yielding and the flat part after yielding, this may be attributed to that the tension steel reinforcement were not yields due to the shear failure type of these beams compared with beams (B2) and (B3). It is agreed that the shear failure causes change in the deflection curve when occurs, for these two beams, the shear starts to participate in the beams deflection at stages earlier than the final stages, this participation were steadily occurred with load increments and did not happen suddenly. Figures show also that beam (B11) has higher deflection than beam (B12) where at the lower loading level the beam (B12) experienced higher deflection after cracking load of (170kN), this may be attributed to the opposite effect of higher prestressing level applied on the compression zone of the section at load point.

5.2 Strain in Steel Reinforcement and Concrete

5.2.1 Strain in steel reinforcement

Tensile strain in mild steel reinforcement at tension zones of left load point and middle support of tested beams are shown in **Fig. 8** and **Fig.9** while the tensile strain increments in seven wire steel strand at tension zone of middle support are shown in **Fig. 10**.

Fig. 8 shows the mild steel strain at left load point taking the influence of increasing number of strand in beams (B11) and (B12) reinforced with two strands compared with beams (B2) and

(B3) reinforced with one strand and having same prestressing level of corresponding to beams (B11) and (B12) respectively, and compared with equivalent normally reinforced beams (B1) and (B10).

It can be seen from this figure that the (P-ε) curves approximately coincide up to the cracking of concrete covers of beams having less reinforcement area. These beams show more noticeable change in the curve slope at cracking and the strain increased in higher rate compared with beams reinforced with higher amount of reinforcement. Beams (B10), (B11) and (B12) show higher beam cracking load compared with beams (B1), (B2) and (B3) at both mid-spans and center support although that beams (B11) and (B12) were expected to have lower cracking load at mid-spans due to the opposite effect of prestressing force, these beams shows also less rate of strain increasing after beam cracking and shows less noticeable change in the curve slope at cracking.

Continuous concrete beams (B10), (B11) and (B12) shows higher ultimate failure load compared with beams (B1) (B2) and (B3) without yielding of flexural steel reinforcement at failure due to the fact that these beams failed in shear.

It can be seen from this figure, that when increasing the amount of reinforcement in normally reinforced beam (B10) the strain decreases by (46.82%) at loading level of ($0.5P_u$), compared with beam (B1).

In partially prestressed beam (B11) reinforced with two strands and having prestressing level of ($0.7f_{py}$), steel strain decreases by (53.36%) at loading level of ($0.5P_u$) compared with beam (B2) reinforced with one strand having same prestressing level.

Steel strain at load point of beam (B12) reinforced with two strands and having prestressing level of ($0.55f_{py}$) decreases by (48.22%) at loading level of ($0.5P_u$) compared with partially prestressed beam (B3) reinforced with one strand having same prestressing level.

When comparing the steel strain at left load point of beam (B11) taking the influence of prestressing level compared with (B12), increasing the prestressing level of (B11) lead to decrease the mild steel strain by (37.19%) at loading level of ($0.5P_u$) compared with beam (B12), while it decreased by (46.61%) compared with normally reinforced beam (B10) having equivalent amount of reinforcement.

Fig. 9 shows the steel strain at center support, the same behavior can be seen compared with load point strain in **Fig. 8** at cracking and ultimate points except that it shows higher strain at entire loading stages compared with load point due to the higher moment applied on the sections at center support, it has to be mentioned that the strain gauge reading of beam (B11) at center support were missed from the figure where the strain gauges failed before the test.

It can be seen from this figure, that when increasing the amount of reinforcement in normally reinforced beam (B10) the strain decreases by (41.8%) at loading level of ($0.5P_u$) compared with beam (B1).

Steel strain at center support of beam (B12) reinforced with two strands and having prestressing level of ($0.55f_{py}$) decreases by (39.2%) at loading level of ($0.5P_u$) compared with partially prestressed beam (B3) reinforced with one strand having same prestressing level.

Steel strain at center support of beam (B12) increases by (40.63%) at loading level of ($0.5P_u$) compared with normally reinforced beam (B10).

Fig. 10 shows the strain increments in center support steel strands of beams (B11) and (B12) having two strands with different prestressing level compared with beams (B2) and (B3) having one strand with same prestressing level corresponding to beams (B11) and (B12), respectively.

The figure shows that the beam cracking load of (B11) and (B12) were much higher than beams (B2) and (B3) and the strain values are much lower at entire loading stages, it can be seen that when concrete cover of beams (B11) and (B12) cracks, at different loading level, strand strain increased rapidly followed by tension stiffening at load of approximately (250kN) lead to significantly decrease the strand strain until failure compared with partially prestressed beam (B2) and (B3) reinforced with one strand. The figure shows also that the strand strain of beams (B11) and (B12) coincide until beam cracking, then after, unexpectedly, the strain curve of beam (B11) becomes more flatter until load of (250kN) lead to have higher strain compared with beam (B12), figure shows also that strand strain were not reached the yielding in both beams.

Fig.10 shows that when using two strand in beam (B11) lead to decreases the strand strain by (41.41%) at loading level of ($0.5P_u$) compared with partially prestressed beam (B2) having same prestressing level and one strand, and the strain in beam (B12) decreased by (56.69%) at loading level of ($0.5P_u$) compared with partially prestressed beam (B3) having same prestressing level and one strand. It can be seen also that the increasing of prestressing level in beam (B11) compared with beam (B12), both beams reinforced with two strands, the strain increases by (11.25%) at loading level of ($0.5P_u$).

It has to be mentioned that **Fig.10** shows only the strain occurred due to external load, when summing these strain increments values with effective pre-strain, can be noted that the strand tensile strain at ultimate failure loads were (99.64%), (107.28%) of beams (B2) and (B3), respectively, while the strands strain at ultimate were (76.29%), and (63.62%) of beams (B11) and (B12), respectively, from strand ultimate tensile strain, this came from the fact that these beams failed in shear.

5.2.2 Strain in concrete

Fig. 11 shows the concrete strain (P-ε) curves at right load point taking the influence of increasing number of strand in beam (B11) reinforced with two strands comparing with beam (B2) reinforced with one strand and having same prestressing level of ($0.7f_{py}$), and beam (B12) reinforced with two strands compared with beam (B3) reinforced with one strand and having same prestressing level of ($0.55f_{py}$),, and compared with equivalent normally reinforced beams (B10) and (B1).

It can be seen from this figure that the (P-ε) curves slopes have noticeable change occurred at beams cover cracking load then the strain increased in higher rate in beams reinforced with less amount of reinforcement. Beams (B10), (B11) and (B12) shows higher beam cracking load compared with beams (B1), (B2) and (B3, respectively.

Continuous concrete beams (B10), (B11) and (B12) shows higher ultimate failure load compared with beams (B1), (B2) and (B3) without yielding of flexural steel reinforcement at failure due to the fact that these beams failed in shear.

It can be seen from this figure, that when increasing the amount of reinforcement in normally reinforced beam (B10) the concrete strain decreases by (15.61%) at loading level of ($0.5P_u$) compared with beam (B1).

In partially prestressed beams (B11) and (B12) reinforced with two strands and having prestressing level of ($0.7f_{py}$) and ($0.55f_{py}$), respectively, concrete strain decreases by (51.82%) and (41.21%) at loading level of ($0.5P_u$) compared with beams (B2) and (B3), respectively, reinforced with one strand having same corresponding prestressing level.

When increasing prestressing level in beam (B11), concrete strain decreased by (23.21%) compared with beam (B12) and the concrete strain decreases by (6.30%) in beam (B2) compared with beam (B3).

When comparing the strain of beams (B11) and (B12) with normally reinforced beam (B10) having equal amount of reinforcement, concrete strain decreases by (35.09%) and (15.47%), respectively, at loading level of ($0.5Pu$).

5.3 Crack Width, Crack Patterns and Ultimate Loads

Load-cracking width development at center support and right span are shown in **Fig. 12** and **Fig. 13**, respectively. Concrete covers cracking load with corresponding maximum crack width at ultimate were presented in Table 4, the cracking pattern were shown in **Fig. 14**.

Fig. 12 shows beams cracking width with load at center support, the figure shows that at loading level of (350kN), when increasing the number of strand in beams (B11) and (B12), the crack width decreased by (100%) and (92.0%) compared with beams (B2) and (B3), respectively, having one strand. While increasing the amount of reinforcement in normally reinforced beam (B10) lead to decreases the crack width at center support by (77.78%) compared with beam (B1).

At same loading level, increasing the prestressing level in beam (B11) leads to decrease the crack width by (75.0%) compared with beams (B12). At lower loading level of (250kN), increasing the prestressing level in (B2) lead to decrease the crack width by (20%) compared with beam (B3).

Fig. 13 shows the crack width at right load point of the same beams, since the beams spans cracked at lower load level compared with center support, hence, the load of (250kN) will be used again in comparison. The figure shows that using of two strands in beam (B11) lead to decrease the left span crack width by (83.34%) at loading level of (250kN) compared with partially prestressed beam (B2), while increasing the prestressing reinforcement in beam (B12) decreases the crack width at load point by (62.5%) at loading level of (250kN) compared with partially prestressed beam (B3), increasing the amount of mild steel reinforcement lead to decreases the crack width by (83.34%) at loading level of (250kN) compared with partially prestressed beam (B1).

Increasing the prestressing level in beam (B11) lead to decrease the crack width by (33.34%) compared with (B12) at load of (250kN).

Fig. 14 shows the crack pattern of beams (B1), (B2), (B3), (B10), (B11) and (B12) at ultimate load, average crack spacing taken at left span for the flexure cracks of beams (B1), (B2) and (B3) were (72mm, 75mm, 85mm), respectively, and at center support were (73mm, 67mm, 65mm), respectively. Beams (B10), (B11) and (B12) were failed in shear before developing the three hinges mechanism at ultimate. Average crack spacing taken at left span for the flexure cracks were (110mm, 105mm and 110mm) for Beams (B10, B11 and B12), respectively. At center support, the crack spacing were (112mm, 105mm and 95mm) for beams (B10, B11 and B12), respectively.

Normally reinforced beam were designed according to ACI-318 code using ultimate design method while the partially prestressed beams reinforced beams were designed according to strain compatibility method. Table 5 represent experimental and theoretical failure loads, theoretical failure load calculated using elastic analysis of indeterminate continuous beams after using ACI-Code and strain compatibility method to determine ultimate moment capacities for both normally reinforces and partially prestressed beams, respectively. Final ultimate loads were determined using moment redistribution percentage factor (α) in Eq. (1) and Eq. (3) stated in ACI-Code for both normally reinforced and partially prestressed continuous beams respectively. Table 5 shows that all beams failed at ultimate in load higher than calculated load using elastic analysis only, after applying recommended moment redistribution percentage, calculated loads show more agreement and consistency with experimental failure load for all tested beams.

$$\alpha = 1000 * \varepsilon_t \quad (1)$$

Where:

$$\varepsilon_t = 0.003\left(\frac{d}{c} - 1\right) \tag{2}$$

$$\alpha \le 20\left[1 - \frac{\omega_p + \frac{d}{d_p}(\omega - \omega')}{0.36\beta_1}\right]\% \tag{3}$$

6. CONCLUSIONS

1. Increasing of prestressing level in partially prestressed beams reinforced with one strand leads to decrease the deflection under load point by (3.60%), while the deflection decreased by (7.31%) compared with reference normally reinforced beam. When using two strands the reduction becomes (32.49%) and (46.15%), respectively.
2. Using two strands in partially prestressed beams showed decreases in the deflection at load point by (44.81%) and (22.20%) compared with partially prestressing beams having one strand at prestressing level of (0.7 f_{py}) and (0.55 f_{py}), respectively.
3. Increasing of prestressing level in partially prestressed beams reinforced with two strands leads to decrease mild steel strain by (37.19%), while the deflection decreased by (46.61%).compared with reference normally reinforced beam.
4. Increasing the amount of prestressing reinforcement showed decrease in mild steel strain at load point by (53.36%) and (48.22%) compared with partially prestressing beams having less amount of prestressing reinforcement at prestressing level of (0.7 f_{py}) and (0.55 f_{py}), respectively, while at center support, using two strand leads to decrease the mild steel strain by (39.20%) for at prestressing level of (0.55 f_{py}).
5. Increasing the prestressing level leads to decrease center support steel strand strain by (11.25%) between beams reinforced with two strands, while the steel strand strain decreases by (41.41%) and (56.69%) for both beams compared with partially prestressing beams having one strand at prestressing level of (0.7 f_{py}) and (0.55 f_{py}), respectively.
6. Increasing the prestressing level leads to decrease concrete strain by (6.30%) and (23.21%) for beams reinforced with one and two strands, respectively. Using two strands leads to decrease concrete strain by (51.82%) and (41.21%) compared with partially prestressing beams having one strand at prestressing level of (0.7 f_{py}) and (0.55 f_{py}), respectively.
7. Increasing the prestressing level leads to decrease center support crack width by (20.0%) and (75.0%) for beams reinforced with one and two strands respectively. Using two strands leads to decrease center support crack width by (100.0%) and (92.0%) compared with partially prestressing beams having one strand at prestressing level of (0.7 f_{py}) and (0.55 f_{py}), respectively.
8. At ultimate load, using ACI-Code recommended moment redistribution factor load to more agreement between theoretically calculated and experimental loads for both normally reinforced and partially prestressed beams.
9. Using higher amount of prestressing reinforcement or increasing the prestressing level to control the deflection and crack width and to increase the ultimate load capacity is more effectively cost saving technique than using higher amount of mild steel reinforcement.

7. REFERENCES

- ACI 318, 2014, *Building Code Requirements for Structural Concrete,* American Concrete Institute, Farmington Hills, 503 pp.

- ACI 224R, 2001, *Control of Cracking in Concrete Structures*, American Concrete Institute, Farmington Hills, 46 pp.

- Amlan K and Devdas M., 2011, *Prestressed Concrete Structures*, Indian Institute of technology, Madras, online version.

- Kenneth B., 2003, *Moment Redistribution: Principles and Practice Using ACI 318-02*, PTI Journal, Vol. 1, No.1, pp 3-21.

- Libby, J. R., 1984, *Modem Prestressed Concrete*, Design Principles and Construction Methods, Third Edition, Van Nostrand Reinhold Co. Ltd, New York, 629pp.

- Naaman, A. E., 1977, *Ultimate analysis of prestressed and partially prestressed sections by strain compatibility*, PCI, pp. 32-51.

- Naaman, A. E., *Prestressed Concrete Analysis and Design Fundamentals*, Second Edition, Techno Press, 2004, 1072 pp.

- Nawy, E.G., 2010, *Prestressed Concrete*, Fifth Edition, Pearson Education Inc, 949 pp.

- Precast/Prestressed Concrete Institute (PCI), *Design Handbook* Sixth Edition, Precast/Prestressed Concrete Institute, Chicago, 2010.

8. NOMENCLATURE

c: neutral axis depth
α: allowable percentage of redistribution of support moment calculated by elastic analysis.
$\omega_{p,}$: reinforcement index for prestressed reinforcement.
ω: reinforcement index for tension reinforcement.
ω': reinforcement index for compression reinforcement.
d: effective depths of non-prestressed reinforcement.
d_p: effective depths of prestressed reinforcement.
β_1: equivalent rectangular stress block coefficient.

Table 1. Continuous beams reinforcement details.

<table>
<tr><th rowspan="2">Beam Symbol</th><th colspan="3">Over center support</th><th colspan="2">At mid-span</th></tr>
<tr><th>A_s, mm^2</th><th>A_{ps}, mm^2</th><th>A_s', mm^2</th><th>A_s, mm^2</th><th>A_s', mm^2</th></tr>
<tr><td>B1</td><td>625</td><td>0</td><td rowspan="6">228</td><td rowspan="3">242</td><td rowspan="6">228</td></tr>
<tr><td>B2</td><td rowspan="2">228</td><td rowspan="2">96.6</td></tr>
<tr><td>B3</td></tr>
<tr><td>B10</td><td>938.8</td><td>0</td><td rowspan="3">855.9</td></tr>
<tr><td>B11</td><td rowspan="2">228</td><td rowspan="2">199.2</td></tr>
<tr><td>B12</td></tr>
</table>

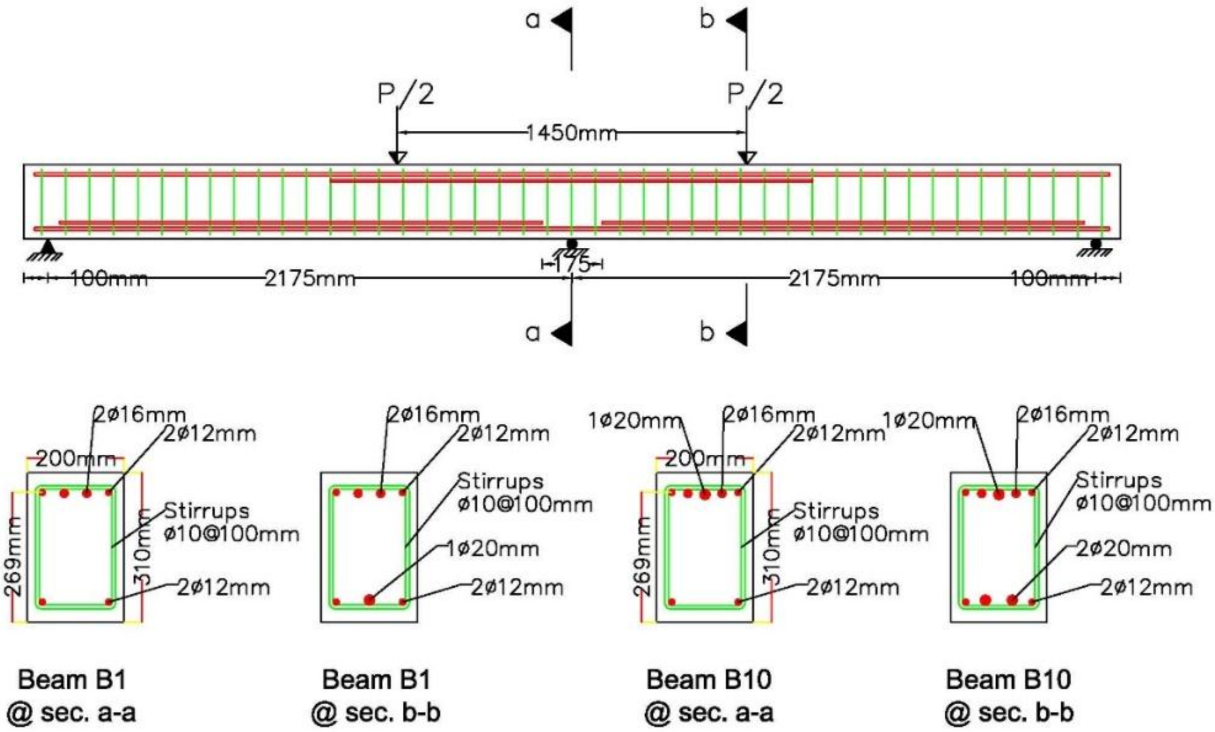

Figure 1. Geometry and reinforcement details of continuous beams (B1 and B10).

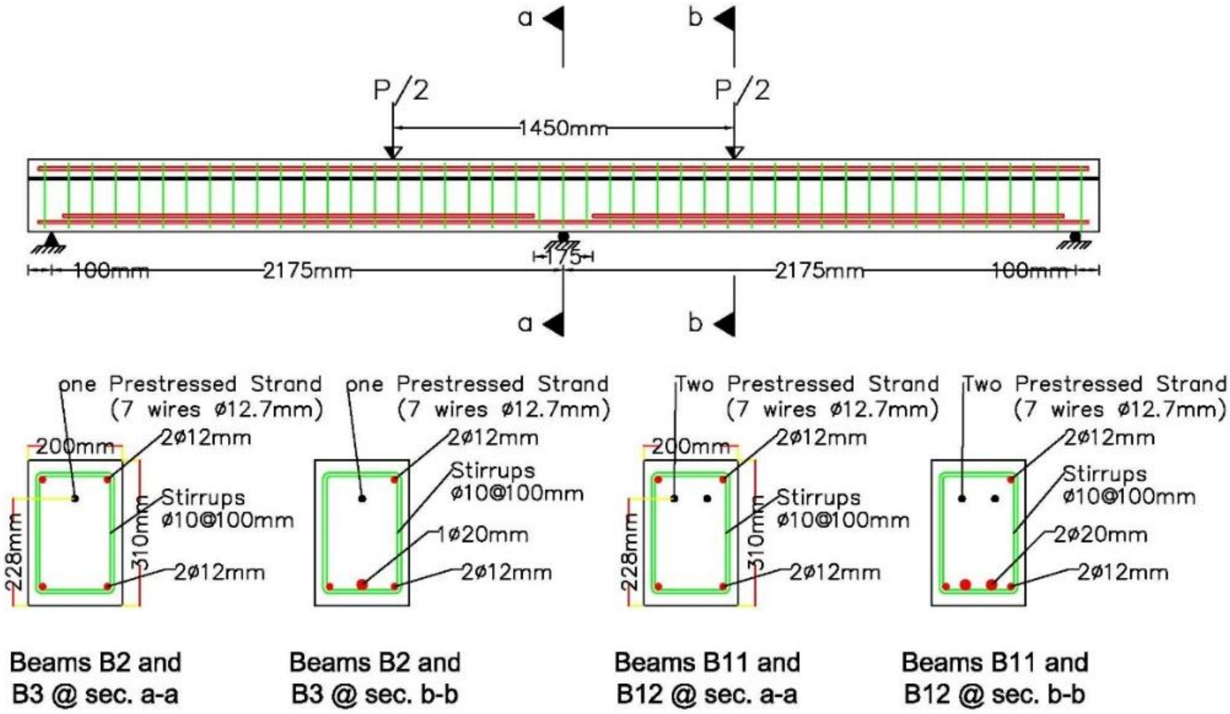

Figure 2. Geometry and reinforcement details of continuous beams (B2, B3, B11 and B12).

Table 2. Concrete properties for tested beams at age of test.

Beam Symbol	**Beam properties**			
	Compressive Strength. f'_c, (MPa)	**Splitting Strength. f_{ct}, (MPa)**	**Modulus of Rupture. f_r, (MPa)**	**Modulus of Elasticity. E_c, (MPa)**
B1	36.8	3.14	4.01	25373
B2	36.1	3.44	4.27	26319
B3	39.2	3.28	4.13	27599
B10	36.8	3.14	4.01	25373
B11	36.1	3.44	4.27	26319
B12	39.2	3.28	4.13	27599

Table 3. Prestress in beams steel strands.

Beam Symbol	Pj Jacking stress, (MPa)	Pi Before release, (MPa)	Pi After release, (MPa)	Pe Effective at time of test, (MPa)
B2	1162.29	1149.05	1121	1009.05
B3	936.05	929.64	909.29	820.88
B11	1175.67	1158.56	1107.37	979.56
B12	907.61	897.79	868.94	780.34

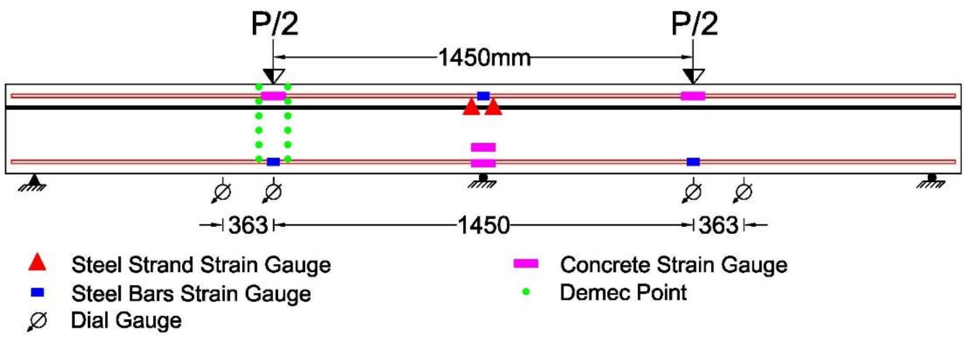

Figure 3. Beams instrumentation and loading details.

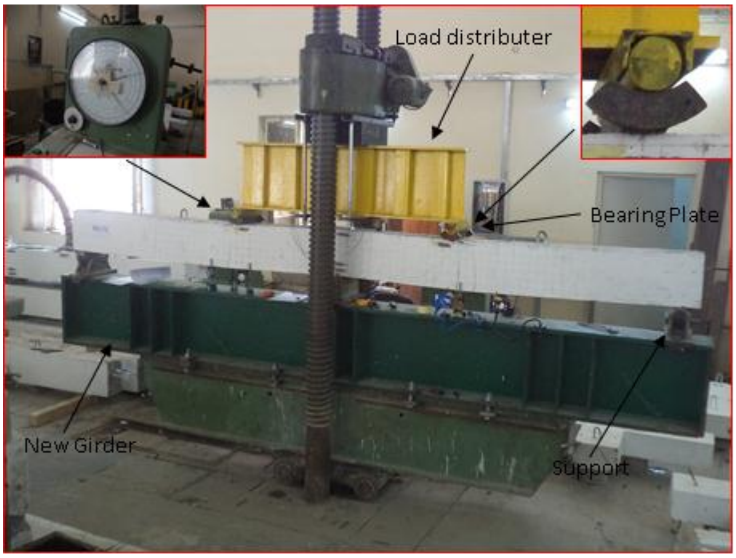

Figure 4. Test setup photo.

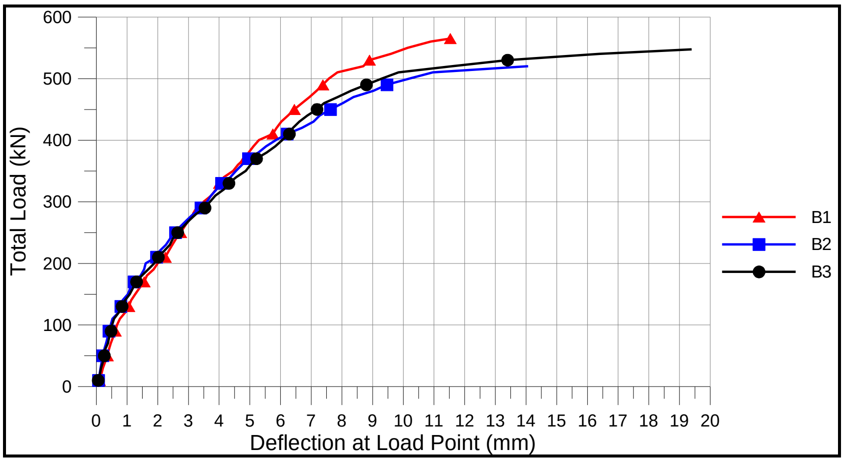

B1: Normally reinforced, **B2:** Partially prestressed with one strand ($0.7f_{py}$), **B3:** Partially prestressed with one strand ($0.55f_{py}$),

Figure 5. Load-deflection curve at load point of beams B1, B2 and B3.

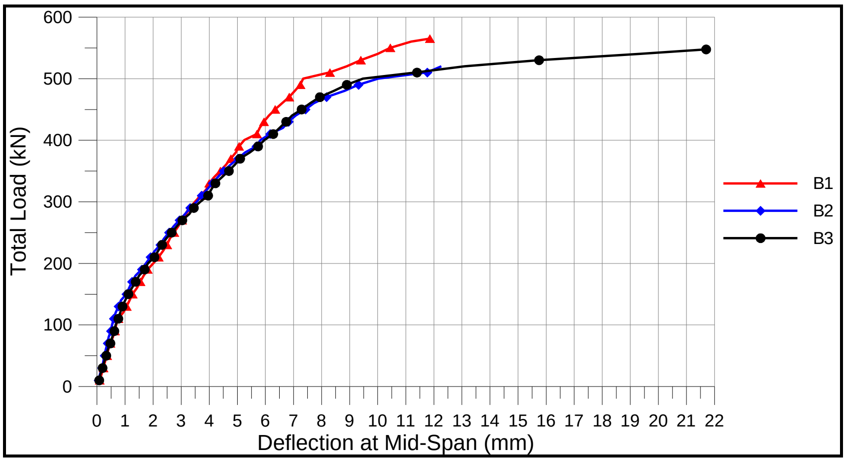

B1: Normally reinforced, **B2:** Partially prestressed with one strand ($0.7f_{py}$), **B3:** Partially prestressed with one strand ($0.55f_{py}$),

Figure 6. Load-deflection curve at mid-span of beams B1, B2 and B3.

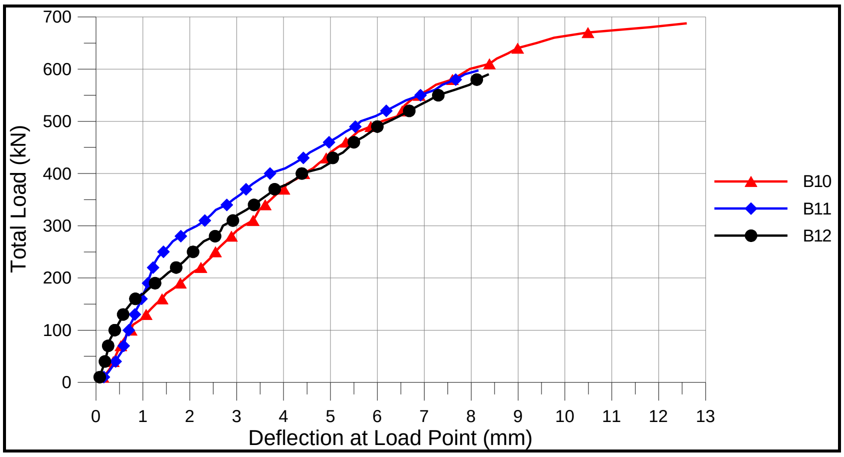

B10: Normally reinforced, **B11:** Partially prestressed with two strands ($0.7f_{py}$), **B12:** Partially prestressed with two strands ($0.55f_{py}$),

Figure 6. Load-deflection curve at load point of beams B10, B11 and B12.

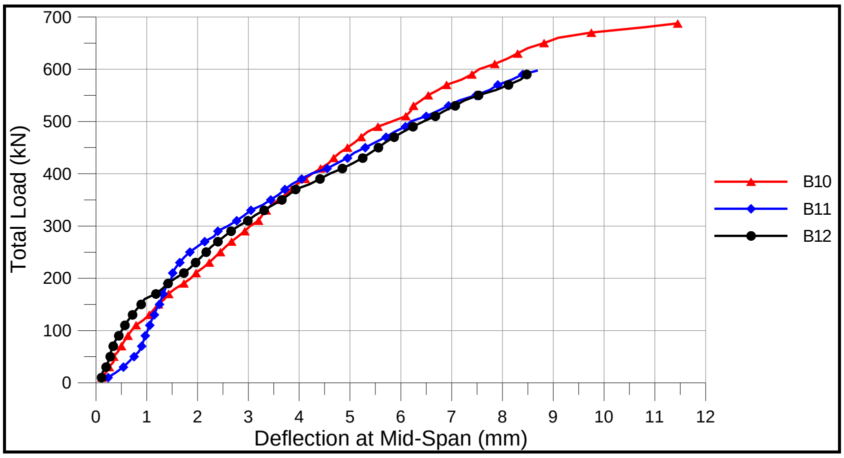

0: Normally reinforced, **B11:** Partially prestressed with two strands ($0.7f_{py}$), **B12:** Partially prestressed with two strands ($0.55f_{py}$),

Figure 6. Load-deflection curve at mid-span of beams B10, B11 and B12.

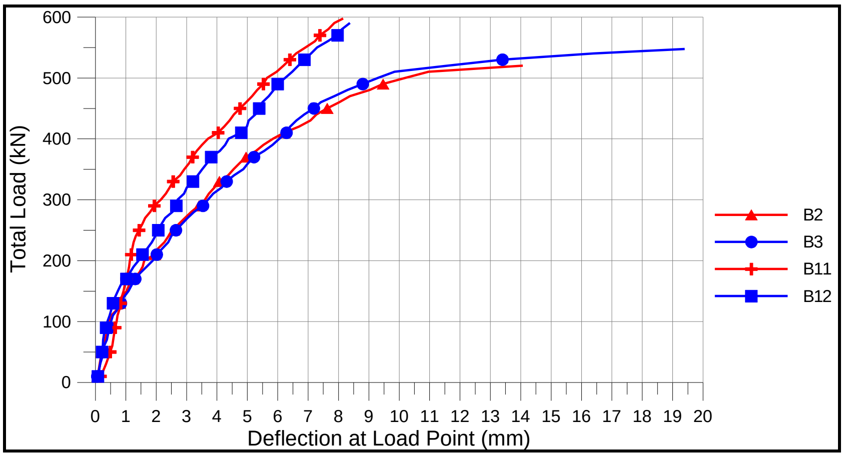

B2: Partially prestressed with one strand (0.7f_{py}), **B3:** Partially prestressed with one strand (0.55f_{py}), **B11:** Partially prestressed with two strands (0.7f_{py}), **B12:** Partially prestressed with two strands (0.55f_{py})

Figure 7. Load-deflection curve at Load point of beams B2, B3, B11 and B12.

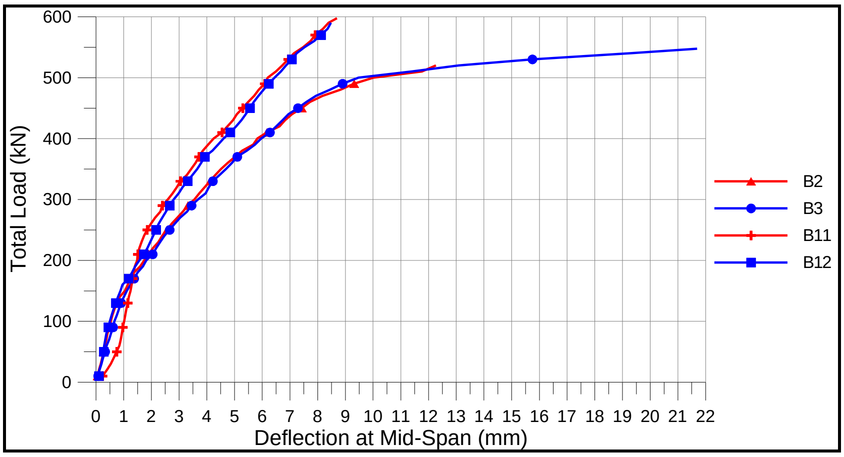

B2: Partially prestressed with one strand (0.7f_{py}), **B3:** Partially prestressed with one strand (0.55f_{py}), **B11:** Partially prestressed with two strands (0.7f_{py}), **B12:** Partially prestressed with two strands (0.55f_{py})

Figure 7. Load-deflection curve at mid-span of beams B2, B3, B11 and B12.

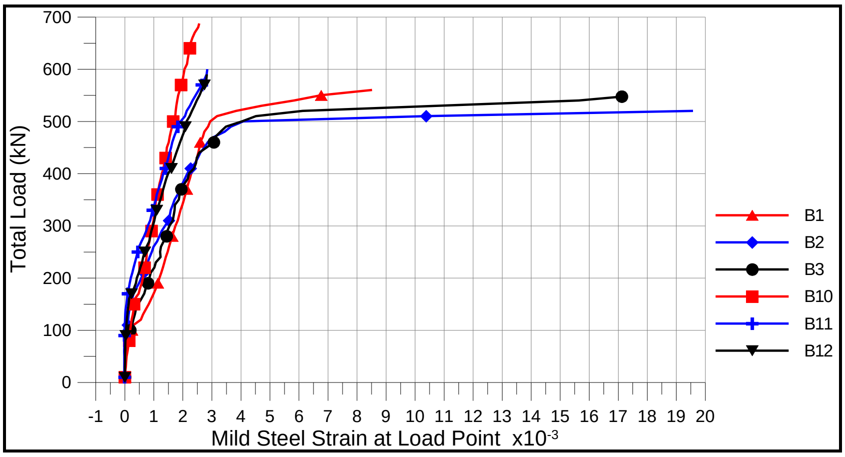

B1: Normally reinforced, **B2:** Partially prestressed with one strand (0.7f_{py}), **B3:** Partially prestressed with one strand (0.55f_{py}), **B10:** Normally reinforced, **B11:** Partially prestressed with two strands (0.7f_{py}), **B12:** Partially prestressed with two strands (0.55f_{py})

Figure 8. Load-strain relationship of mild steel at load point of beams B1, B2, B3, B10, B11 and B12.

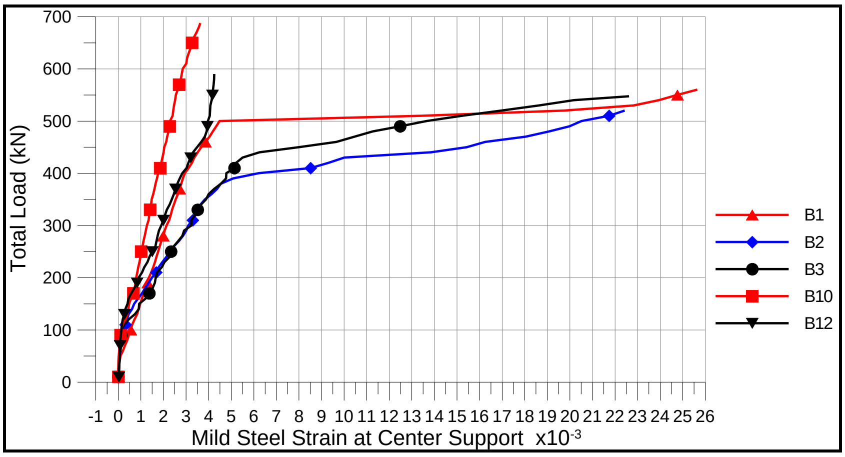

B1: Normally reinforced, **B2:** Partially prestressed with one strand (0.7f_{py}), **B3:** Partially prestressed with one strand (0.55f_{py}), **B10:** Normally reinforced, **B12:** Partially prestressed with two strands (0.55f_{py})

Figure 9. Load-strain relationship of mild steel at middle support of beams B1, B2, B3, B10 and B12.

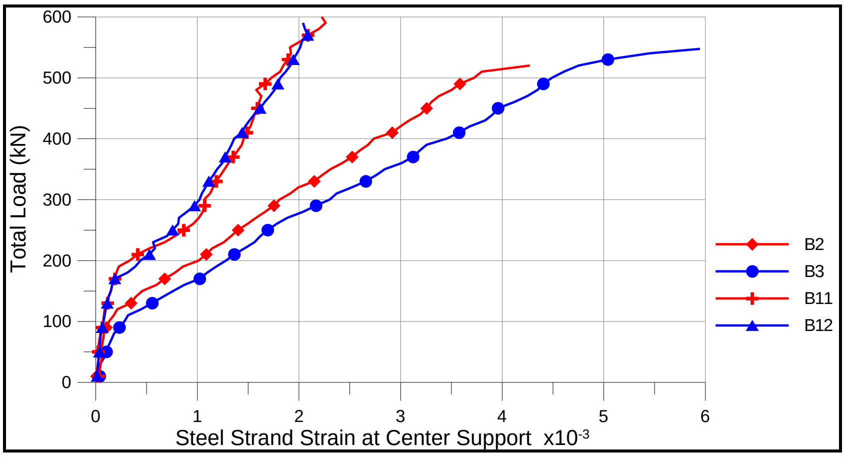

B2: Partially prestressed with one strand (0.7f_{py}), **B3:** Partially prestressed with one strand (0.55f_{py}), **B11:** Partially prestressed with two strands (0.7f_{py}), **B12:** Partially prestressed with two strands (0.55f_{py})

Figure 10. Load-strain relationship of steel strand at middle support of beams B2, B3, B11 and B12.

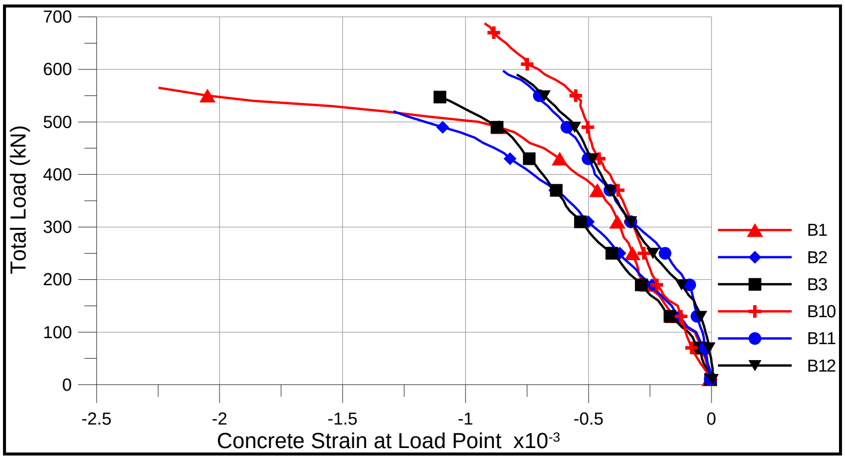

B1: Normally reinforced, **B2:** Partially prestressed with one strand (0.7f_{py}), **B3:** Partially prestressed with one strand (0.55f_{py}), **B10:** Normally reinforced, **B12:** Partially prestressed with two strands (0.55f_{py})

Figure 11. Load-strain relationship of concrete at load point of beams B1, B2, B3, B10, B11 and B12.

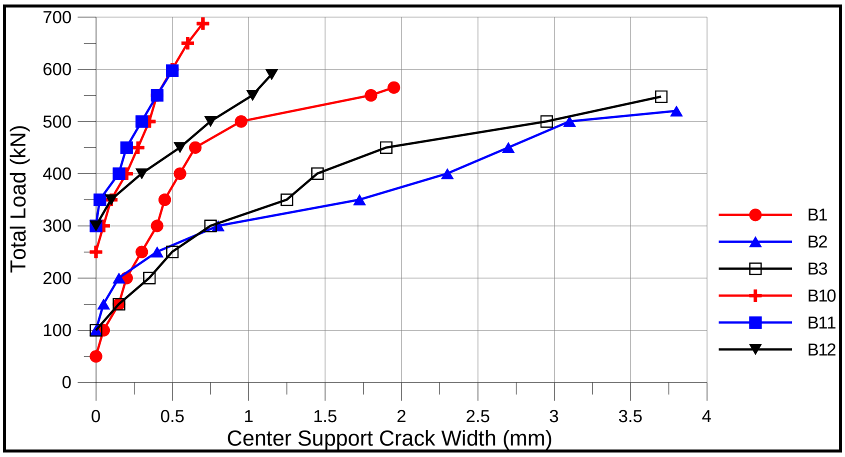

B1: Normally reinforced, **B2:** Partially prestressed with one strand ($0.7f_{py}$), **B3:** Partially prestressed with one strand ($0.55f_{py}$), **B10:** Normally reinforced, **B11:** Partially prestressed with two strands ($0.7f_{py}$), **B12:** Partially prestressed with two strands ($0.55f_{py}$)

Figure 12. Cracking width at center support of beams B1, B2, B3, B10, B11 and B12.

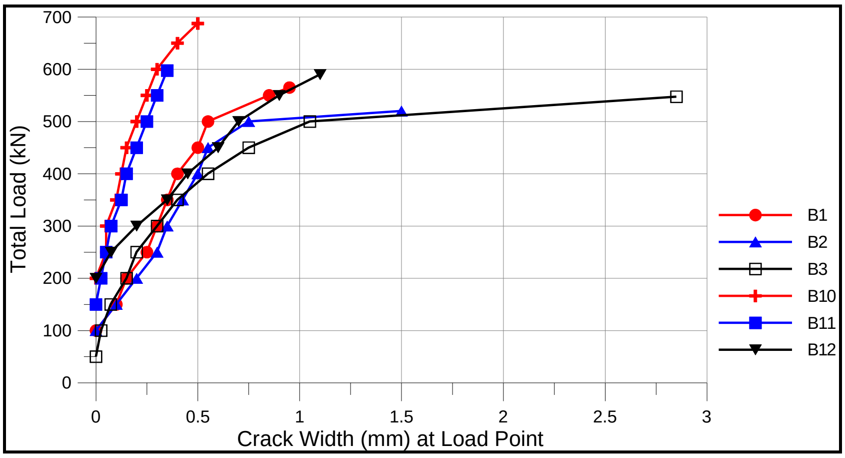

B1: Normally reinforced, **B2:** Partially prestressed with one strand ($0.7f_{py}$), **B3:** Partially prestressed with one strand ($0.55f_{py}$), **B10:** Normally reinforced, **B11:** Partially prestressed with two strands ($0.7f_{py}$), **B12:** Partially prestressed with two strands ($0.55f_{py}$)

Figure 13. Cracking width under load point at right span of beams B1, B2, B3, B10, B11 and B12.

Table 4. Cracking load and maximum crack width at ultimate load.

Beam set	Beam Cracking Load (kN)			Beam Cracking Load/ultimate load % (Pcr/Pu)			Ultimate load, (kN)	Maximum crack width at ultimate (mm)		
	Left Span	Center Support	Right Span	Left Span	Center Support	Right Span		Left Span	Center Support	Right Span
B1	112	58	107	19.82	10.26	18.93	565.0	1.05	1.95	0.95
B2	105	116	102	20.19	22.3	19.61	520.0	1.55	3.8	1.5
B3	94.5	104	107	17.26	18.99	19.54	547.5	3.95	3.7	2.85
B10	170	120	160	24.72	17.45	23.27	687.5	0.5	0.7	0.55
B11	148	196	142	24.76	32.8	23.76	597.5	0.35	0.5	0.45
B12	162	170	162	27.45	28.81	27.45	590.0	1.1	1.65	1.05

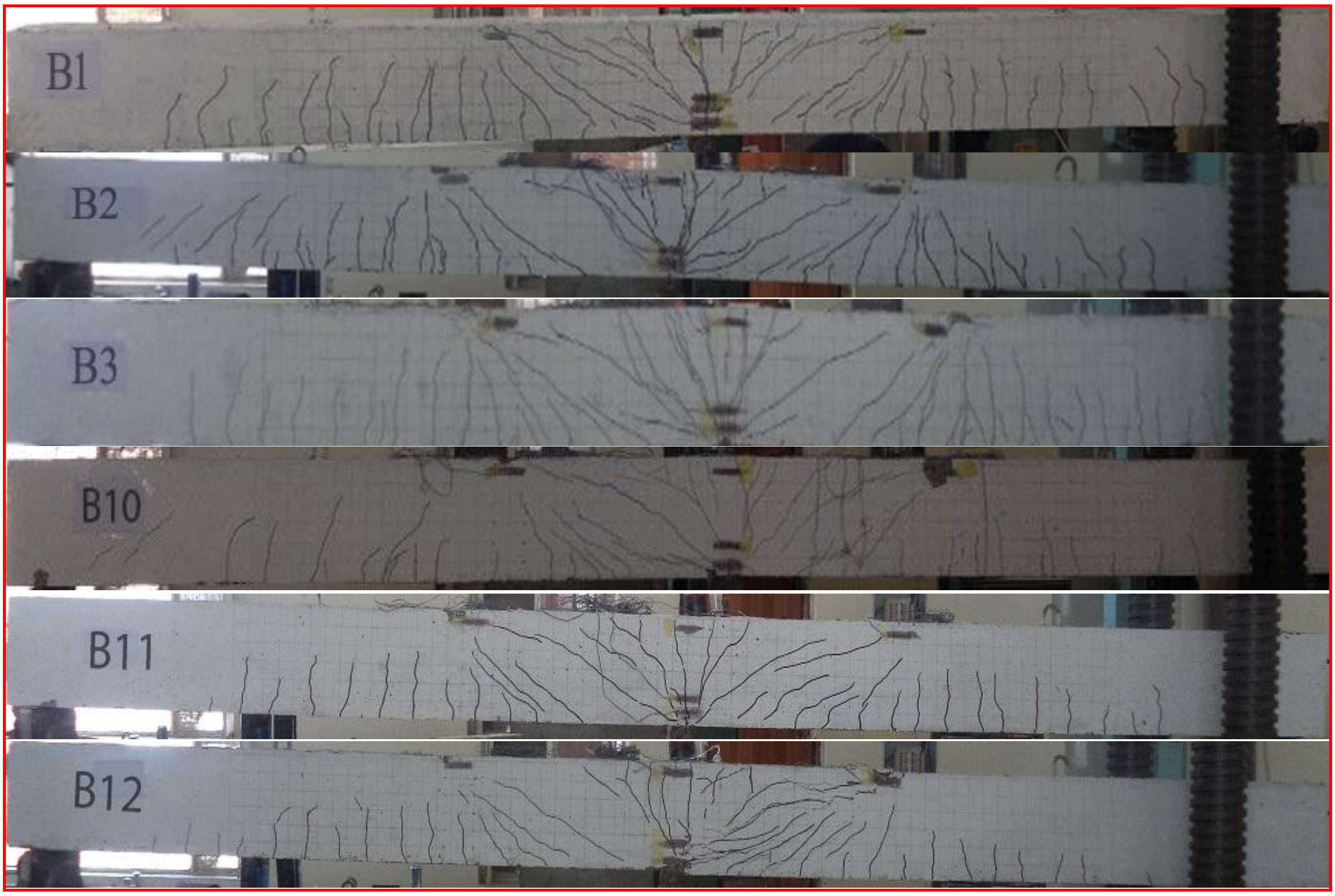

Figure 14. Crack Pattern at ultimate load of tested beams.

Table 5. Experimental and theoretical load capacities for tested beams.

Beam Set	**Experimental Ultimate Load, P_u, Exp.,** (kN)	**Theoretical Ultimate Load, P_{u1}, Cal., using elastic analysis,** (kN)	**(P_u, Exp/ P_u1, Cal.)**, (%)	**Theoretical Ultimate Load, P_{u2}, Cal., using elastic analysis in addition to moment redistribution**, (kN)	**(P_u, Exp/ P_{u2}, Cal.)**, (%)
B1	565	513.782	109.97	587.64	96.15
B2	520	402.264	129.27	475.49	109.36
B3	547.5	405.348	135.07	481.89	113.61
B10	687.5	676.419	101.64	676.419	101.64
B11	597.5	537.964	111.07	605.32	98.71
B12	590	543.685	108.52	618.63	95.37

Contributory Factors Related to Permanent Deformation of Hot Asphalt Mixtures

Dr. Alaa Husein Abd
Asst. Professor
College of Engineering – University of Nahrain
e-mail: Alaah29@yahoo.com

Zahra Ibrahim Qassim
Engineer
College of Engineering – University of Baghdad
e-mail: Eng.zehoor@yahoo.com

ABSTRACT

Permanent deformation (Rutting) of asphalt pavements which appears in many roads in Iraq, have caused a major impact on pavement performance by reducing the useful service life of pavement and creating services hazards for highway users. The main objective of this research is investigating the effect of some contributory factors related to permanent deformation of asphalt concrete mixture. To meet the objectives of this research, available local materials are used including asphalt binder, aggregates, mineral filler and modified asphalt binder. The Superpave mix design system was adopted with varying volumetric compositions. The Superpave Gyratory Compactor was used to compact 24 asphalt concrete cylindrical specimens. To collect the required data and investigate the development of permanent deformation in asphalt concrete under repeated loadings, Wheel-Tracking apparatus has been used in a factorial testing program during which 44 slab samples; with dimensions of 400×300×50 mm; were tested to simulate actual pavement. Based on wheel-tracking test results, it has been concluded that increasing the compaction temperature from 110 to 150ºC caused a decreasing in permanent deformation by 20.5 and 15.6 percent for coarse and fine gradation control asphalt mixtures respectively. While the permanent deformation decreased about 21.3 percent when the compaction temperature is increased from 110 to 150ºC for coarse gradation asphalt mixtures modified with styrene butadiene styrene SBS with 3 percent by asphalt binder weight.

Keywords: modified asphalt, asphalt concrete; Superpave; rutting performance; and wheel tracking test.

العوامل المساهمة والمتعلقة بالتشوه الدائمي للخلطات الاسفلتية الحـــارة

د.علاء حسين عبد
استاذ مساعد
كلية الهندسة- جامعة النهرين

زهراء ابراهيم قاسم
مهندس
كلية الهندسة– جامعة بغداد

الخلاصـــة

ان التشوهات الدائمية (التخدد) في التبليط الاسفلتي تظهر في العديد من طرق العراق ، وتسبب تأثيرا رئيسياً على أداء التبليط وذلك عن طريق تقليل العمر الخدمي للتبليط وجعل استخدام هذه الطرق محفوفة بالمخاطر . ان الهدف الرئيسي من البحث الحالية هو تقييم تاثير بعض العوامل المتعلقة بالتشوهات الدائمية للخلطة الاسفلتية الكونكريتية. لتحقيق الهدف في هذا البحث فقد تم استخدام المواد المتوفرة من الإسفلت والحصى والمواد المالئة والمضافات التي تشمل الاسفلت المحسن .كما أُعتمدت طريقة التبليط عالي الاداء في التصميم وحساب مختلف الخصائص الحجمية واستخدم جهـازالرص الدوراني في رص 24 عينة اسطوانية من الخرسانة الاسفلتية. من اجل توفير البيانات المطلوبة والتحري عن التشوهات الدائمية في الخرسانة الاسفلتية ، تم استخدام جهاز العجلة المسارية لتسليط الاحمال المتكررة ، تم اعداد 44 بلاطة من الخرسانة الأسفلتية تم فحصها لتمثيل واقع التبليط. اعتمادا على نتائج الفحص تبين بان زيادة درجة حرارة الحدل من 110 م الى 150 °م قلل من التشوهات الدائمية بمقدار 20.5 و 15.6كنسبة مئوية للركام الخشن والناعم للخلطات الاسفلتية التقليدية. بينما قلت التشوهات الدائمية بمقدار 21.3بالمئة عند زيادة درجة حرارة الحدل من 110 م الى 150 م للركام الخشن والناعم للخلطات الاسفلتية المحسنة بمادة الستايرين بيوتادين ستايرينSBS المضافة كنسبة 3 بالمئة من وزن الاسفلت الرابط.

1. INTRODUCTION

Permanent deformation (rutting) of asphalt pavements has a major impact on pavement performance. Rutting reduces the useful service life of the pavement. By affecting vehicle handling characteristics, it creates serious hazards for highway users; two major elements contribute to asphalt pavement deterioration, the gradual effects of weathering and the action of vehicle traffic, **Huang, 1993** and **Pavement Design Manual**, **2015**.

Early detection and repair of pavement defects is the most important preventive maintenance procedure. There are five areas of distress for which guidance is needed: fatigue cracking, (wheel path) rutting, thermal cracking, friction, and moisture damage, all of these distresses can result in loss of performance, but rutting or permanent deformation is one of distress that is most likely to cause a sudden failure as a result of unsatisfactory hot mix asphalt or asphalt mixture, other distresses are typically long term failures that show up after a few years of traffic, **Ishai**, and **Craus, 1996**.

Recently, Superpave has been reported as an improved system for performance based design, analysis of asphalt concrete mixes and asphalt pavement performance prediction. It is a structured approach consisting of selection of materials, selection of design aggregate structure, asphalt binder content, and evaluation of moisture susceptibility, **Khan,** and **Kamal, 2012**.

In Iraq, the severity of rutting has been increased in asphalt pavements possibility due to the increase in truck axle loads, tire pressure, and high pavement temperature in summer, as shown in **Fig. 1**.

2. RESEARCH OBJECTIVE

The main objectives of the research is to study the main factors affecting rutting in asphalt concrete mixture in Iraq such as; mix properties, types of filler, loading and temperature conditions by using Superpave mix design system and study the effect of additive on the improvement of asphalt concrete mixes against the permanent deformation .

3. LABORATORY TESTING

3.1 Material

To meet the objectives of this research, available local materials were used including asphalt binder, aggregates and mineral filler. Asphalt binders (40-50 or PG 64-16) was obtained from Al-Daurah refinery in Baghdad and the aggregate from Al-Nibaie quarry in north of Baghdad whereas the mineral filler was brought from lime factory in Karbala Portland cement is from Kubbesa factory which was obtained from market. The aggregates are sieved and recombined in the proper proportions to meet the wearing course gradation as required by **SCRB specifications, 2003**. A 19 mm aggregate maximum size gradation is used in this research. The fractions of aggregate are separated into 9 sizes, as retained on each of the following sieves, 3/4", 1/2", 3/8", No.4, No.8, No.16, No.30, No.50, and No. 200) using dry sieve analysis. Mineral filler (Limestone, Portland cement) has been added according to the desired gradations requirements. The gradation curve for the aggregate is shown in **Fig. 2**; four lines are presented: the upper , the lower curves of the Iraqi specifications of SCRB in addition to the controls points of Superpave system, **Table 1** shows the physical prosperities of asphalt binder .

In this research the Superpave mix design system was adopted with varying volumetric composition. The Superpave Gyratory Compactor was used at the NCCLR to prepare 24 asphalt concrete cylindrical specimens for carrying out volumetric design according to Superpave system, **AASHTO Designation: T 312-2010**. The optimum asphalt content for the selected asphalt binder and selected aggregate gradation was 4.6 percent for conventional coarse asphalt mixtures, while it is about 4.9 percent for SBS modified asphalt mixtures.

3.2 Sample Preparation

The roller compacter apparatus can compact asphalt slabs to a target density using loads per unit roll width about 5-10 ton, which are consistented to those of pavements rollers used in the highway construction. The roller compactor provides a pneumatically powered means of compacting slabs of asphaltic material in the laboratory under conditions, which simulate in-situ compaction.

In this research, compacted asphaltic slabs for rutting testing are prepared at air voids equal to (4%) using Roller Compactor Device at NCCLR according to (EN12697-Part 33:2003) and Superpave system, **AASHTO Designation: T 312-2010**. The dimensions of the compacted slabs used in this work are of (400 mm by 300 mm by 50±6 mm) as proposed by **EN 12697-Part 22:2003.**

Proportion of aggregate and asphalt binder are used for mixing, curing, and compacting. The aggregate retained on the 3/4" sieve is discarded. Mineral filler (Limestone) and cement have been added according to the desired gradations requirements. The aggregate is combined into batch of (13400 gm for slab specimen) on the mixing bowl and heated to the mixing temperatures prior to mixing with asphalt binder which heated to the mixing temperatures corresponding to each binder, as shown in **Fig. 3**.

For the modified binder preparation, the asphalt cement for convention mixture is heated in the factory oven to the temperature of mixing prior to adding the specific 3 percent amount of SBS additive, this percent is chosen according to previous researches prepared by the Ministry of Industry and Minerals, it is preheated in an external oven until liquid at 180 ºC, the desired weight of additive which is determined by multiplying it's percent by the required weight of asphalt content was added gradually and mixed until getting homogenous binder.

The aggregate and asphalt are mixed in mixing bowel on hot plate for three minutes until asphalt had sufficiently coated the surface of the aggregates or until a homogeneous mixture is achieved, as shown in **Fig. 4** . The asphalt-aggregate mixture is then short term oven aged for 2hrs at 135°C for the determination of the maximum specific gravity and 4hrs at the same temperature for compaction in according with **Asphalt institute, 1996**. This aging represents the aging that occurs in the field between mixing and placement and allows for absorption of the asphalt binder into the aggregate pores. The mix is stirred every 30 minutes during the short-term aging process to ensure uniform aging throughout the mix.

Compaction is then performed using the Roller Compactor in accordance with EN 12697-33, the mold and the plates are heated in the oven at the specified compaction temperature to ensure that the mix temperature is not reduced. The load is from 7-10 KN which applied on the specimens to achieve proper compaction and sufficient air voids, as shown in **Fig. 5** and **Fig. 6.**

3.3 Wheel-Tracking Testing

The Pavement Wheel Tracker is a device for testing the wear ability of asphalt mixes by simulating roadway conditions, the test is performed according to **EN 12697-22, 2003** and **AASHTO Designation: T 340, 2010**. The test provides information about the rate of permanent deformation from a moving, concentrated load. It uses a Linear Value Displacement Transducer (LVDT's) to measure the deformation of the specimen. The loaded wheel applies about 700 N (158 pounds) of load at contact points and passes repetitively over the sample for up to 10,000 cycles. Test results are compiled in a Microsoft Access database application which provides several means of reporting results.

Wheel-tracking machine ; as shown in **Fig. 7;** is constructed so as to enable the test specimen in its cradle to be moved backwards and forwards under the loaded wheel in a fixed horizontal plane. The center-line of the tire track is (5 mm) from the theoretical center of the specimen. The center of the contact area of the tyre describes a simple harmonic motion with respect to the center of the top surface of the test specimen with a total distance of travel of (230±10) mm and a constant loading frequency of (26.5±1.0) load cycles per 60 seconds for the test device in approximately 10,000 load cycles or 20 mm maximum allowed deformation is reached.

The experiment design for the permanent deformation testing is a full factorial with; two asphalt contents, three compaction temperatures, two asphalt types: original and modified with SBS and two types of gradations, resulting in a nominal total of 24 slab tests.

The compacted specimens, which are 30 cm in width, 40 cm in length and 5 cm in height, are cooled to room temperature for a period of 24 hours in accordance with (EN-12697-22). The specimens are placed in mold and then placed in on the carriage table of WTD for testing. The specimens in the mold are labeled with information mix type.

The holder of the displacement transducer is disengage and reference plate is adjust in order the transducer probe is compressed approximately 70% of its total travel. This allowed having sufficient travel available to measure the track formation on the sample. Starting the software, supplied with the machine, and entering the required test information into the computer. The testing device automatically stops the test when the device applies the number of desired passes or when reaching the maximum allowable rut depth, as shown in **Fig. 8.**

If the maximum allowed deformation is reached before 10,000 passes, the wheel is lifted off the failed sample. Test results are compiled in a Microsoft Access database application which provides several means of reporting results.

Finally at the end of the test the arm will return automatically to its upper position while the display will show the results of the test which can be saved in the archives and/or transmitted to an external computer.

4. RESULTS AND ANALYSIS

Permanent deformation and vertical permanent strain (εp) were measured at testing temperature of 40°C, and frequency level 53 passes per minute, and two selected compaction temperatures of 110^{o}C and 150^{o}C and two asphalt contents are used and two types of gradation with two types of filler are used , SBS polymer was used as modifier to asphalt binder .

4.1 Effect of Compaction Temperature

This research investigates the influence of compaction temperature on coarse and fine asphalt mixes for modified and unmodified binders.

For this, Superpave mix designs for two compaction temperatures of 110 °C and 150 °C and two asphalt binders (control, 3% styrene butadiene styrene (SBS) modified) were carried out. A total of 24 specimens were manufactured with a short-term aged for 2 h at the mixture compaction temperatures prior to test.

Fig. 9 shows effect of compaction temperature on Permanent deformation (i.e. rut depth, RD). It can be seen that permanent deformation decreased when compaction temperature change from 110 to 150 ºC as shown in **Table 2**. It can be related to shear susceptibility of mixtures and it's sensitive to temperature changes. The rut depth (RD) decreased about 20.5 and 15.6 percent when the compaction temperature is increases from 110 to 150 ºC for coarse and fine gradation control asphalt mixtures respectively as shown in **Fig. 9**. While the rut depth (RD) decreases about 21.3 percent when the compaction temperature is increases from 110 to 150 ºC for coarse gradation SBS modified asphalt mixtures as shown in **Fig. 10**.

The results from this study showed that the compaction temperatures significantly affected the volumetric properties of the SBS modified mixes. The mixtures containing SBS-modified binders, the rut depth decreased by 21.3 percent and the air–void contents significantly decreased with an increase in compaction temperature because the binder in modified asphalt mixtures is stiffer than in conventional mixtures; therefore, there is a need for a higher compaction temperature

4.2 Effect of Asphalt Content

Based on the data shown in **Fig. 11** to **13**, it appears that the examined asphalt content has influence on the plastic response of the material. The plastic strain is increased with the increases in asphalt content from optimum AC to opt. +0.5 percent asphalt content for conventional and modified asphaltic mixtures. For (RD) value, it can be found that it increases about 10.6 percent when asphalt content increases from 4.6 to 5.1 percent for conventional coarse asphalt mixture, while it increased about 8 percent when asphalt content from 4.9 to 5.4 percent for SBS modified asphalt mixture, as shown in **Table 3.**

It can be concluded for Superpave mixtures, the total asphalt content plays an important significant role in controlling overall rutting resistance of the conventional and modified asphaltic mixtures, i.e. rutting performance is highly influenced by total asphalt content , voids in mineral aggregate (VMA), voids filled with asphalt , (VFA), and dust-to-binder ratio.

4.3 Effect of Aggregate Gradation

Aggregate presents major portion of asphalt concrete. It was found that researchers have come to different conclusions with regard to the effect of aggregate gradation on resistance to rutting of asphalt mixtures.

Two gradations of aggregate that are typically used to produce hot mix asphalt in Iraq were used in this research. They are: coarse and fine gradation, one of them passing below the restricted zone (on the Superpave gradation chart) and the other above the restricted zone. **Fig.14** shows the results showed effect of aggregate gradation of mixture on permanent deformation, it concluded that rutting resistance of asphalt paving mixes is affected by the mix gradation of aggregate. Coarser gradation had higher resistance to rutting from fine gradation of aggregate by 65.6 percent.

4.4 Effect of Type of Filler

The resistance of asphalt mixture to permanent deformation is related to the stiffness of asphalt binder, mixture volumetric, and the bonding interaction between asphalt binders and aggregate. Mineral filler is usually added into asphaltic mixture to stiffen asphalt binder and improve asphaltic mixture density and strength. These fillers are typically fine powders with particle sizes in the range of 0–100 μm, two types of filler were used in this research, there are: limestone and cement.

However, the properties of mineral fillers of the compacted mixtures can influence on the permanent strain for conventional and modified mixtures as depicted in **Fig. 15**. The percentage of change in in Permanent Deformation is presented in **Table 4.** It can be observed that the rut depth (RD) decreases about 23.5 and 30.6 percent when the cement filler is used in asphaltic mixtures instead of limestone filler for coarse and fine gradation mixtures respectively. The effect of type of filler on the mixture rutting potential was more significant for the fine mixture than the coarse mixture.

4.5 Effect of SBS Polymer additive

During the preparation of the samples it was noted that the mixes with the polymer-modified binder were more difficult to mix and compact. Any cooling of the mix greatly increases the viscosity of the asphalt and the stiffness of the mix.

In this research, the addition of additive (SBS) polymer tends to improve the mix properties. In Superpave mix design, the results showed that rutting performance of the asphaltic samples has improved for the polymer modified cases.

The percentage of change in permanent deformation with Polymers Content is presented in **Table 5.** It can be observed that the permanent displacement (RD) decrease about 37.22 and 29.5 percent when SBS polymer is used for coarse and fine gradation mixtures respectively, as shown in **Fig. 16**.

Based on the above evaluation, the use of asphalt modified by SBS polymers gives the coarse wearing course better rutting resistance than the fine gradation of the same asphalt performance grade.

At the testing temperature of 40 ̊C±5, the asphaltic mixtures appeared to maintain stiffness levels. However, it should be noted that when SBS polymer modifier is used, the HMA become stiffer at the high testing temperature. It can be concluded that SBS polymer-modified binder made the polymer modified mixtures stiffer than control mixes with unmodified asphalt binder at high temperature.

5. CONCLUSIONS

Considering all results of laboratory tests and analysis, the following conclusions are presented:

1- Wheel-track permanent deformation results for asphaltic wearing course mixes indicate that increasing of compaction temperature from 110 to 150 ºC will decrease the permanent deformation by 20.5 and 15.6 percent for coarse and fine gradation control asphalt mixtures respectively. While the rut depth (RD) decreases about 21.3 percent when the compaction temperature is increased from 110 to 150 ºC for coarse gradation SBS modified asphalt mixtures.

2- The permanent deformation is increased with the increases in asphalt content from optimum AC to opt. + 0.5 percent asphalt content for conventional and modified asphaltic mixtures. For (RD) value, it can be found that it increases about 10.6 percent when asphalt content increases from 4.6 to 5.1 percent for conventional coarse asphalt mixture , while it increased about 8 percent when asphalt content from 4.9 to 5.4 percent for SBS modified asphalt mixture

3- Wheel-track permanent deformation results showed effect of aggregate gradation of mixture on permanent deformation, it concluded that rutting resistance of asphalt paving mixes is affected by the mix gradation of aggregate. Coarser gradation had higher resistance to rutting from fine gradation of aggregate by 65.6 percent for conventional asphalt mixtures.

4- The permanent deformation decreases about 23.5 and 30.6 percent when the cement filler is used in asphaltic mixtures instead of limestone filler for coarse and fine gradation mixtures respectively. The effect of type of filler on the mixture rutting potential was more significant for the fine mixture than the coarse mixture.

5- The permanent displacement (RD) decrease about 37.22 and 29.5 percent when SBS polymer is used for coarse and fine gradation mixtures respectively. Based on the results, the use of asphalt modified by SBS polymers gives the coarse wearing course better rutting resistance than the fine gradation of the same asphalt performance grade.

6. REFERENCES

- AASHTO Guide for Design of Pavement Structures, 2010, *The American Association of State Highway and Transportation Officials*, Washington, D. C., USA.

- ASTM, 2009, *Road and Paving Materals*, Annual Book of ASTM Standards, Volume 04.03, American Society for Testing and Materials," West Conshohocken, USA.

- European Standards EN 12697, 2005, *Bituminous mixtures Test methods for hot mix asphalt*, published under the authority of European Committee for Standardization and Technical Committee CEN/TC 227 "Road materials", August.

- Huang, Y., 1993, *Pavement Analysis and Design*, Prentice Hall, Englewood Cliffs, New Jersey, USA.
- Ishai, Ilan and J. Craus, 1996 , *Effects of Some Aggregate and Filler Characteristics on Behavior and Durability of Asphalt Paving Mixtures*, Transportation Research Record 1530, National Research Council, Washington, D.C., pp. 75-86.

- Kamran M. Khan, Mumtaz A. Kamal, 2012, *Rutting Based Evaluation of Asphalt Mixes*, Pak. J. Engg. & Appl. Sci. Vol. 11, (p.60- 65)

- Pavement Design Manual, 2015, Colorado Department of Transportation , USA.

- SCRB/R9, 2003, *General Specification for Roads and Bridges*, Section R/9, Hot-Mix Asphalt Concrete Pavement, Revised Edition. State Corporation of Roads and Bridges, Ministry of Housing and Construction, Republic of Iraq.

NOMENCLATURES

Term	Meaning
NCCLR	National Center for Construction Laboratories and Researches
NCHRP	Cooperative Highway Research Program
SBS	Styrene-Butadiene-Styrene
Superpave	Superior Performing Asphalt Pavement

Figure 1. A Plate shows Rutting Occurring in Pavements.

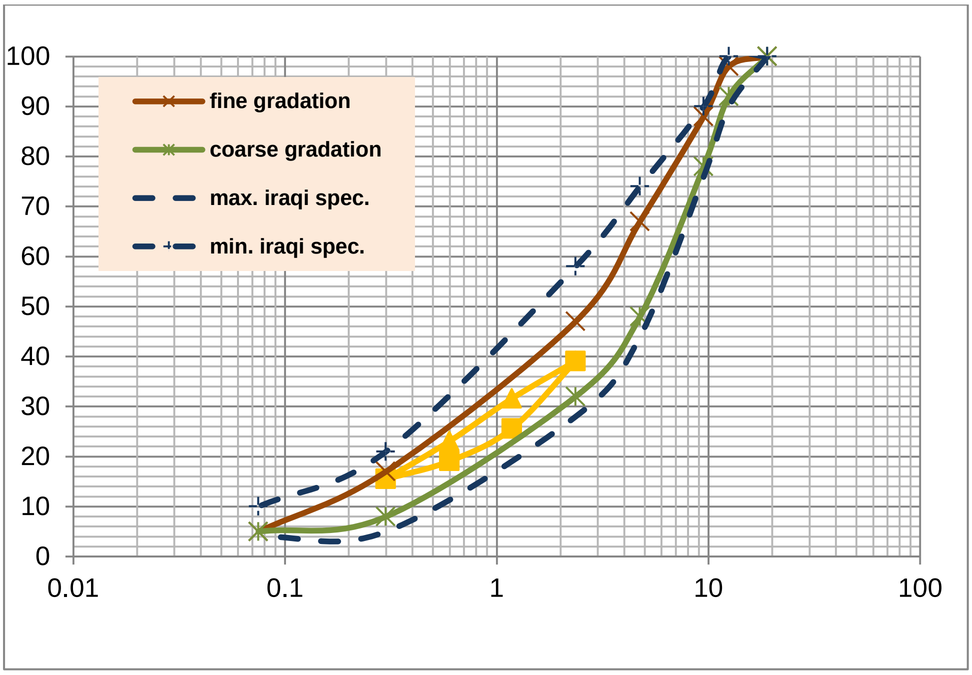

Figure 2. Selected Gradation for Aggregated Used.

Figure 3 . Preparation of Asphalt mixture.

Figure 4. Mixing of Asphalt Mixtures.

Figure 5. Asphaltic Slab before testing.

Figure 6. Wheel-Track device.

Figure 7. Slab under compaction effort.

Figure 8. Slab under loaded Wheel during testing.

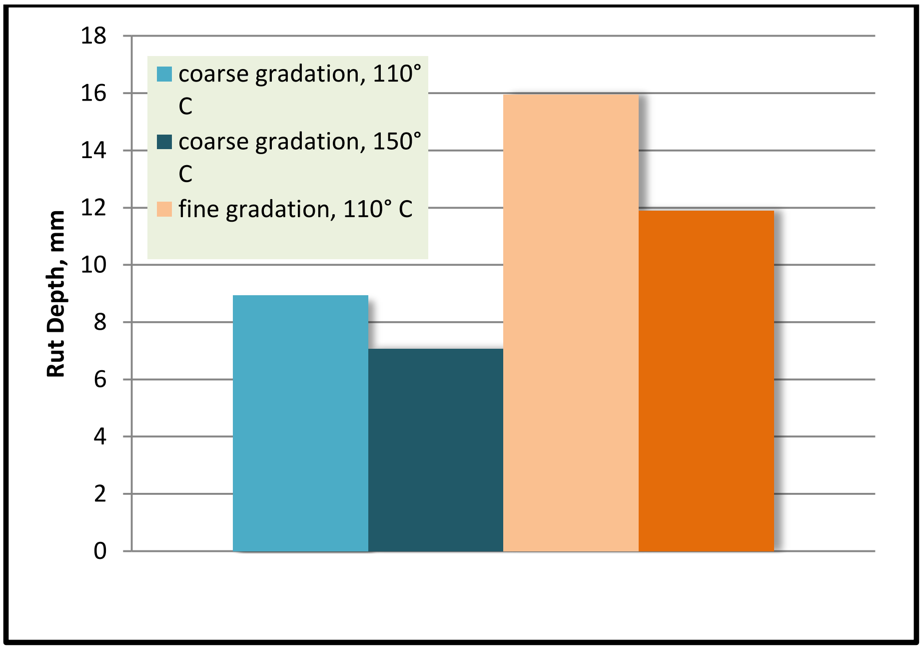

Figure 9. Effect of Compaction Temperature of control mixtures on Permanent Deformation.

Figure 10. Effect of Compaction Temperature on Permanent Deformation of Modified mixtures.

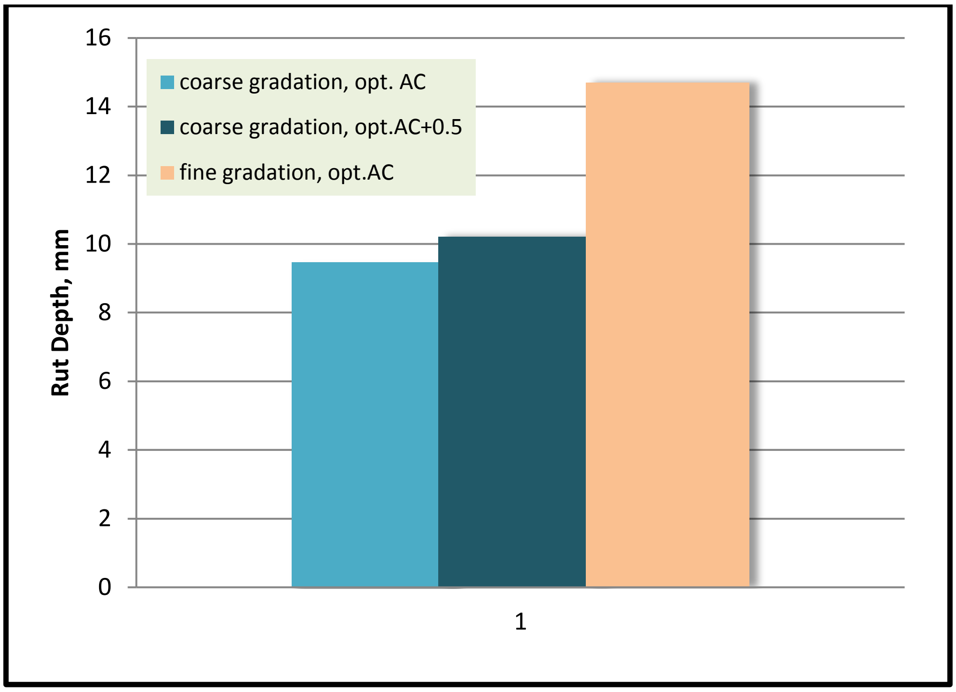

Figure 11. Effect of Asphalt content of conventional mixture on Permanent Deformation.

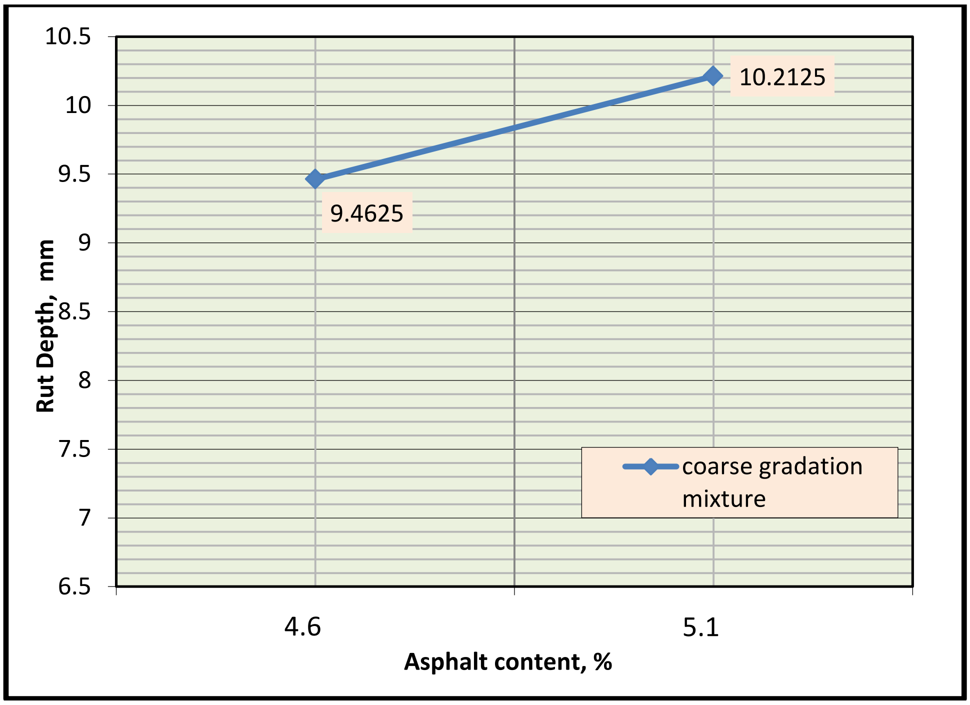

Figure 12. Change in Permanent Deformation with Asphalt content.

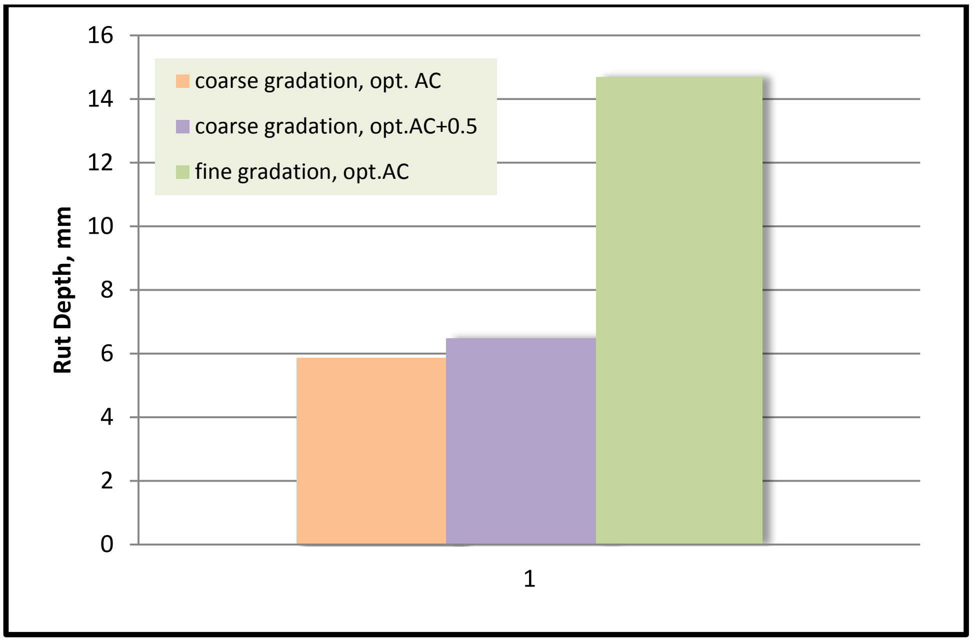

Figure 13. Effect of Asphalt content of modified mixture on Permanent Deformation.

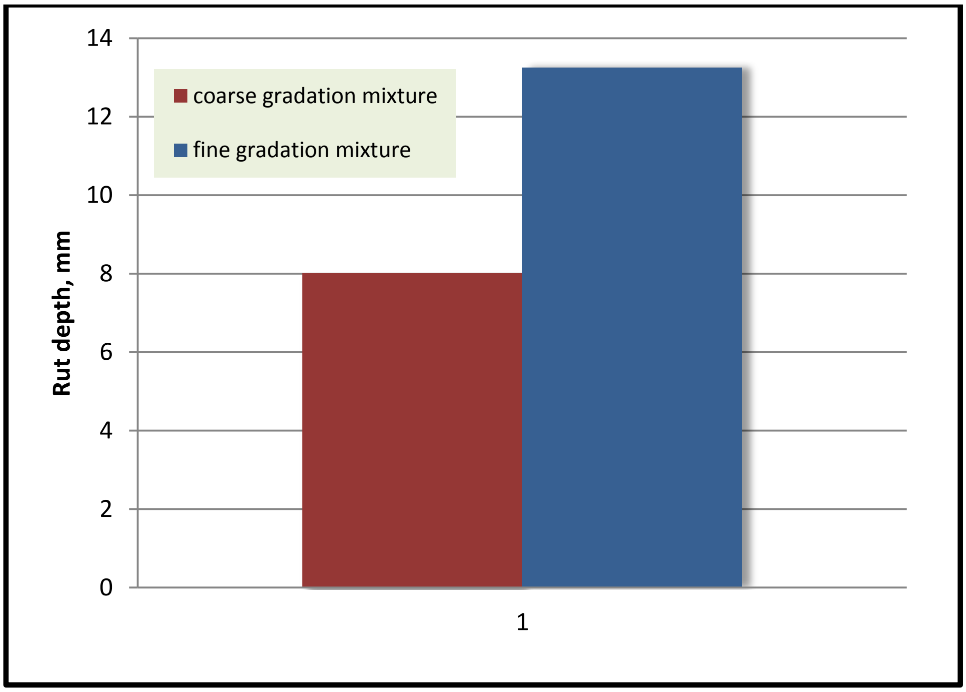

Figure 14. Effect of Aggregate Gradation of mixture on Permanent Deformation.

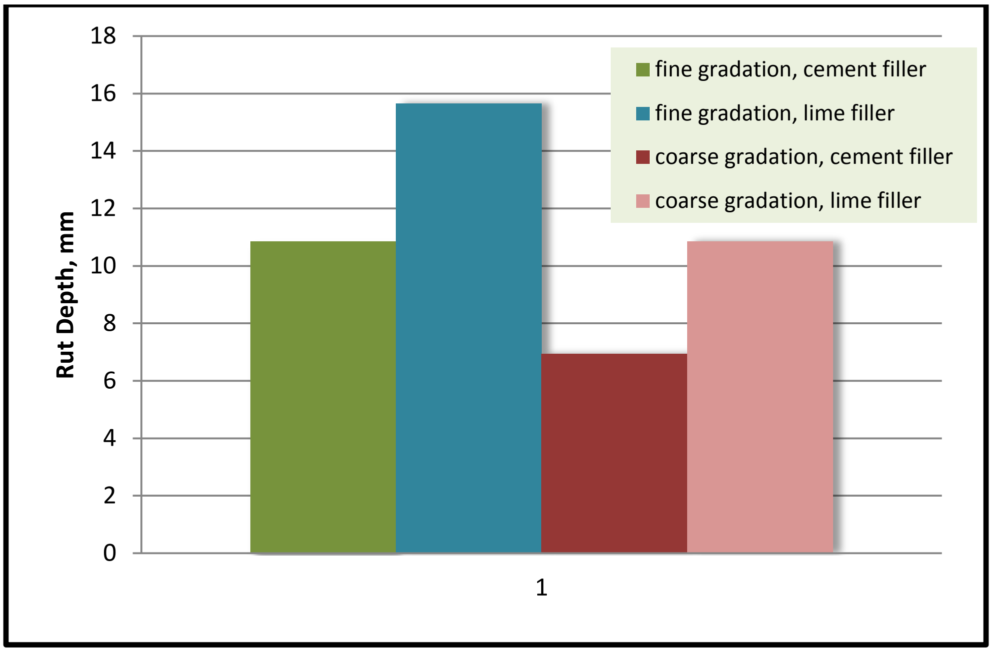

Figure 15. Effect of Type of Filler in mixture on Permanent Deformation.

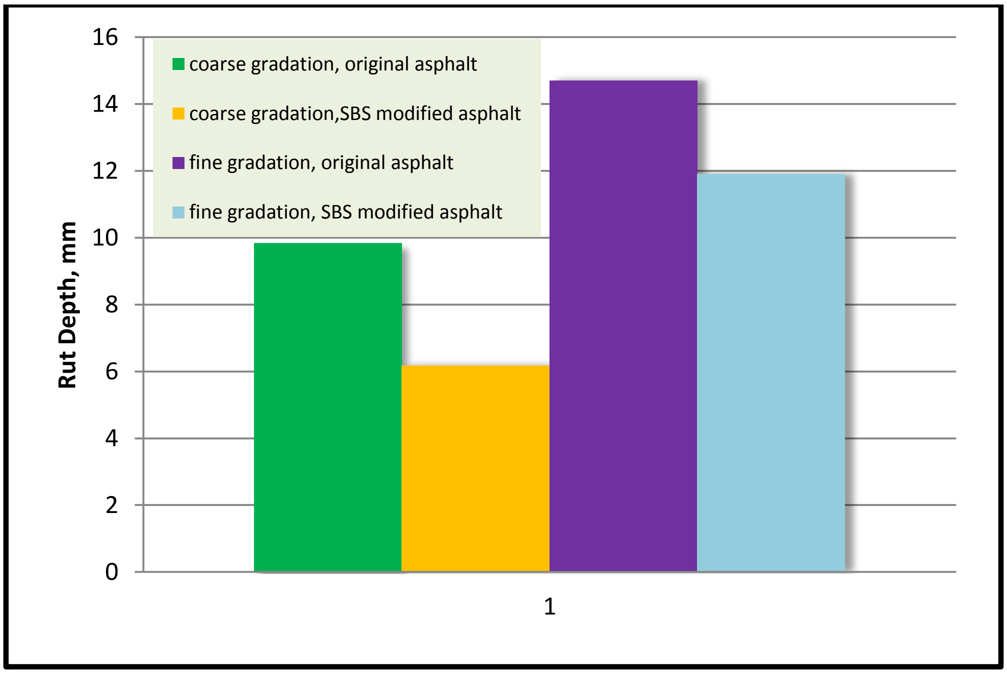

Figure 16. Effect of SBS Polymer on Permanent Deformation of mixtures.

Table 1. Properties of Asphalt Cement, according to ASTM Requirement and Iraqi Specifications.

Test	Test Conditions	ASTM Designation	Units	Penetration grade 40-50	
				Test results	SCRB specification
Penetration	100 gm, 25°C, 5 sec., (0.1mm)	D-5	1/10 mm	45	40-50
Rotational Viscometer,	135 °C	D-4402	Pas.sec.	0.52	……
	165 °C			0.13	
Ductility	25°C, 5 cm/min	D-113	cm	>100	>100
Flash Point	……	D-92	°C	289	Min.232
Specific Gravity	25°C	D-70	……	1.043	……
Softening Point	(4±1) °C/min.	D-36	°C	49	……
Residue from thin film oven test, D-1754					
%Retained penetration, of original	(25 °C , 100 gm , 5 sec)	D-5	1/10 mm	67.4	>55%
Mass loss	163 °C, 50gm, 5 hr	D-1754	%	0.38	< 0.75
Ductility of Residue	25 °C , 5 cm/min	D-113	cm	>100	> 25

Table 2. Percentage of Change in Permanent Deformation with Compaction Temperature.

Rut Depth , mm	Effect of Temperature, 110° to 150 °C (%)	
	Coarse gradation	Fine gradation
Control asphalt Mixtures	-20.5	-15.6
Modified asphalt Mixtures	-21.3	-

Table 3. Percentage of Change in Permanent Deformation with Original Asphalt Content.

Variable	Effect of Asphalt Content	
	4.6 % to 5.1 %	4.9 % to 5.4 %
	Original Asphalt Content	Modified Asphalt Content
Rut Depth , mm	10.6	8.0

Table 4. The Change in Permanent Deformation with Type of Filler.

Rut Depth , mm	Effect of Type of Filler , %
	From (lime) to (cement)
Coarse gradation	-23.5
Fine gradation	-30.6

Table 5. Percentage of Change in Permanent Deformation with Polymers Content.

Variable	Effect of Polymer (SBS) Content (%)	
	Coarse gradation	Fine gradation
Rut Depth , mm	-37.22	-29.5

Non-Isothermal Crystallization Kinetics Model of PBT/ MWCNTs Nanocomposites

Saad Raheem Sultan
Lecturer
Chemical Engineering Department,
University of Technology
Saadraheem76@gmail.com

Amer Aziz Abdul-rahman
Lecturer
Chemical Engineering Department,
University of Technology
ameraa1972@yahoo.com

Ayad Dari Jaafar
Asst. Lect.
Chemical Engineering Department,
University of Technology
ayad.dari@yahoo.com

ABSTRACT

The non-isothermal crystallization kinetics and crystalline properties of nanocomposites poly butyleneterephthalate, [PBT] /multiwalled-carbon nanotubes (MWCNTs) were tested by differential scanning calorimetry (DSC). PBT/(MWCNTs) nanocomposite was prepared by ultrasonicated of MWCNTs (0.5, 1, 2, 4 wt %) in dichloromethane (DCM) and after that the powdered PBT polymer was added to the MWCNTs solution. The non-isothermal crystallization results show that increasing the MWCNTs contents, decreased the melting temperature (Tm) of PBT/(MWCNTs) nanocomposite as compared with pure PBT, while resulting in improving the degree of crystallinity. These results indicated that a little amount of MWCNTs can be evident strong nucleating agent in PBT nanocomposites. Avrami kinetics model results given a good agreement with the frequent investigation. The Kissinger method shows the MWCNTs had a well nucleation effect on the crystallization of PBT, and the enhancement activation energy (Ea) with increased the MWCNTs in PBT/ (MWCNTs) nanocomposite.

Keywords: crystallization, kinetics, poly (butyleneterephthalate), carbon nanotubes, nanocomposites

نمذجة حركية تبلور البولي بيوتلين تيرفيثالات المدعم بأنابيب النانو كاربون المتعدد الجدران

م.د. سعد رحيم سلطان، م.د. عامر عزيز عبدالرحمن و م.م. أياد داري جعفر
قسم الهندسة الكيمياوية – الجامعة التكنولوجية

الخلاصة

تمت دراسة حركية وخواص التبلور لمركب البولي بيوتلين تيرفيثالات المدعم بالانابيب النانوية الكاربونية المتعددة الجدران باستخدام الماسح التفاضلي الكروموتوغرافي. تم تحضير المركب بنسب وزنية مختلفة من الانابيب النانوية الكاربونية. اثبتت نتائج حركية التبلور ان زيادة نسبة الانابيب النانوية الكاربونية تنقص من درجة حرارة الانصهار بالمقارنة مع البولي بيوتلين تيرفيثالات النقي بالاظافة الى تحسين درجة التبلور.هذة النتائج تبين التداخل الواضح للآنابيب النانوية الكاربونية في البوليمر. نموذج Avrami اعطاء نتائج جيدة ومطابقة مع البيانات العملية، كذلك نموذج Kissinger لحساب طاقة التنشيط اثبت ان زيادة نسبة الانابيب النانوية الكاربونية تزيد من طاقة التنشيط لحركية التبلور.

الكلمات الرئيسية : تبلور ،حركية، بولي بيوتلين تيرفيثالات. انابيب النانو كاربون ، مركبات نانوية

1. INTRODUCTION

Poly butyleneterephthalate is a traditional semi crystalline polymer and used in various engineering and electrical applications such as an insulator and housings, because of high rate of crystallization, hardness, thermal stability, and extremely good flow properties, **Mai, et al.,2006, Usuki, et al., 2005**.
Many researchers have been devoted toward the performance of crystallization and mechanical properties of PBT such as injection molding, **Xiao, et al., 2007, Kim, et al., 2006**, with different nanoparticles including carbon nanotube (CNT), **Kim, et al., 2009, Rejisha, et al., 2017**, organic clay **Saeed,** and **Khan, 2015, Chang, et al., 2005,** etc. The importance of the use of carbon nanotubes (CNT) in new types of nano scale polymer appeared where it adds enhancements for exceptional properties with high balanced amounts and little volume.
Carbon nanotubes (CNT) have been discovery by **Iijima, 1991**. Three types of nanotubes can be considered of minor importance which are: 1- single-walled carbon nanotubes [SWCNTs], 2- multi-walled carbon nanotubes [MWCNTs] and 3- double-walled carbon nanotubes [DWCNTs]. A multiwall carbon nanotubes (MWCNTs) are made up of various layers of carbon tubes having a common axis, with diameters from (10 – 50) nm and length above than 10 mm.
A well dispersed and entrenched were observed by functionalized carbon nanotubes (FCNT) inside PBT polymer by solution casting technique, which consequently led to make efficient properties of the nanocomposite such as the mechanical and thermal ones when compared with a neat PBT, **Saeed and Khan, 2014**.
Rejisha, et al., 2014. evaluated the action of (MWCNT) on the properties of poly butyleneterephthalate(PBT)/polycarbonate (PC) blends. The authors showed that small amount of MWCNT shows better rise in the properties of the blends of PBT/PC nanocomposite when compared to nanoclays or inorganic fillers.
Recently, solution casting technique was used to get (kaolin clay/PBT) composites films by **Saeed, and Khan, 2015**.The product showed that the supplements of clay polymer matrix were significantly better on the module and tensile strength of [PBT] polymer matrix, and when combination of clay into matrix, the dimensions of sphere ulites of PBT were reduced.

In the present work, the effect of MWCNTs on the crystalline properties of PBT was investigated. In addition, the non-isothermal crystallization kinetics behaviors of PBT/ (MWCNTs) nanocomposite were carried out using differential scanning calorimetry (DSC).

2. EXPERMENTS

2.1 Materials

The PBT was purchased from (Shenzhan Plastic Company China). The Multi walled carbon nanotubes (MWCNTs) (purity >95 %) was supplied from Shenzhen Company. The solvent dichloromethane (DCM) was obtained by Merc Company.

2.2 Sample Preparation

The different weight percentage of MWCNTs solution (0.5 - 4 wt %) was prepared by adding MWCNTs to dichloromethane and ultrasonicated with ultrasonic cleaning bath for 90 min at ambient temperature. After that the PBT polymer was added to prepare MWCNTs solution. Finally, the produced PBT/(MWCNTs) nanocomposite was stirred at 1500 rpm for 30 min.

2.3. Differential Scanning Calorimetry (DSC)

Differential Scanning Calorimetry (DSC) is a primary technique for measuring the PBT/ (MWCNTs) nanocomposite crystallinity and melting points. The DSC test is proceeding under the gas flow rate of nitrogen with a heating rate about 20 ^{o}C/min using SETARAM, 131 EVO, France instrument as shown in **Fig. 1**. Through the test, the variance for heat flow between the sample and reference is registered by a computer. Depending on the DSC operating conditions, the test is held for about 1 hour. When making changes in phase are detected, where the exothermic changes such as crystallization, cross-linking and oxidation represented the upward peak while the endothermic changes such as glass temperature (T_g) and melting temperature (T_m) represented the downward peak on the DSC diagram.

3 REUSELTS AND DISCUSSION

3.1 Non-Isothermal Crystallization Method

Non-isothermal crystallization kinetics as well as crystalline behavior of PBT/MWCNTs nano composite were scrupulous by utilized (DSC) test at a given heating and cooling rates. From (DSC) tests, the parameters for the melting enthalpy (ΔH_m), peak for the crystallization temperature (T_p) and for the melting temperature (T_m) can be obtained.
The crystallinity percentage (X_c) can be calculated from:

$$X_c = \frac{\Delta H_m}{\Delta H^o} \times 100 \tag{1}$$

The theoretical value for the heat of fusion for 100 % crystal PBT ($\Delta H°$=140 J/g) was acquired and listed in **Table 1**, **Sabu T. and Visakh P. 2011**.

The DSC curves for virgin PBT as well as PBT/MWCNTs nanocomposites are illustrated in **Fig. 2 (a and b)**. It is obvious that the peak crystallization temperature (Tp) of virgin PBT at 190 °C, while the Tp for PBT/MWCNTs nanocomposite has moved to a high temperature (200–203 °C). These results indicate that the MWCNTs represent professional nucleating agent for the PBT nanocomposite crystallization rate as compared with the virgin PBT polymer.

Fig. 2-b depicts the second scan DSC for the virgin PBT as well as PBT/MWCNTs nano composites samples. It was found that increasing the MWCNTs contents resulted in melting

temperature (Tm) decrease as compared with pure PBT. **Table 1** shows the result in enhancement the degree of crystallinity (Xc). In context, it has been revealed that 1 wt% MWCNTs gives an 11 % higher crystallinity of PBT/MWCNTs nanocomposite than its pure PBT, these resulted specified the appearance of nucleation PBT crystallization in the nanocomposite, this is due to the interaction between surface treated MWCNTs nanoparticles and the PBT segments. **Saligheh,** and **Forouharshad, 2011**.

In addition, when the stacking of nanotubes is little, the portability of the PBT macromolecular chains can be improved in this way, the crystallization rate and level of crystallinity of the PBT samples expanded, when the substance of nanotubes expanded, the fillers began to hinder the activation of the PBT macromolecular chains and keep macromolecular sections from acquiring request arrangement of crystal lattices cross sections. Hence, the fuse of a little amount of MWCNTs could adequately upgrade the crystallization of the PBT nanocomposite through heterogeneous nucleation, **Saligheh,** and **Forouharshad, 2013**.

3.2 Crystallization Kinetics Model

The crystallization kinetics analyzing for the polymer materials can be demonstrated by Avrami model. Relative crystallinity (X_t) can be connected with crystallization time (t) by the suggested model, **Fanfoni, M. and Tomellini M., 1998**:

$$1 - X_t = \exp(-Kt^n) \tag{2}$$

Or,

$$\ln(-\ln(1 - X_t)) = (n \ln t) + (\ln K) \tag{3}$$

Where dH/dt is enthalpy rate and equation (4) can be used to calculate X_t:

$$X(t) = \int_0^t \left(\frac{dH}{dt}\right) dt \Big/ \int_0^\infty \left(\frac{dH}{dt}\right) dt \tag{4}$$

Accordingly, figure (3) shows the relation of relative crystallinity with crystallization time of pure PBT as well as PBT/MWCNTs nanocomposites. It seems that the PBT/MWCNTs nanocomposites require less crystallization time to approach the same relative crystallinity at different rates of cooling as compared with pure PBT.

Fig.4 shows the relation of ln (-ln(1-Xt)) with ln(t) of the pure PBT as well as PBT/MWCNTs nanocomposites according to equation (3) will give the slope (n), the Avrami index, and the intercept, ln(K). Table (2) shows the kinetic parameters for the samples of the nano composites. The parameter of Avrami index (n) describes the growing mechanism and geometry of crystallization, and the parameter ln(K) describes the growth rate under the non-isothermal crystallization process.

From **Table 2**, it can be seen that the Avrami index (n) values for pure PBT are larger than that of PBT nanocomposites. Similar values were also reported by some researchers for PBT within the range of (3.0 − 4.0). Apparently, the (n) value decreases with the MWCNTs content which shows that MWCNTs nanoparticles gives a good nucleating agents for PBT, **Hu,et al., 2008.**

3.3 Activation Energy For PBT/MWCNT Nanocomposites

The thermal dynamic examination will provide the data of polymer intraparticles. Kissinger strategy may be the ultimate regularly utilized, through the activation energy of non-isothermal crystallization that can be effectively gained**, Kim, 2011**.

The equation below shows the fundamental form of Kissinger equation, where (β) the cooling rate, (T_p) the peak temperature, (Ea) the activation energy and (R) the gas constant. **Zhiying et al., 2014.**

$$\ln\left(\frac{\beta}{T_p^2}\right) = \text{const.} - \frac{Ea}{RT_p} \qquad (5)$$

Fig. 5 shows the test of Eq. (5) by plotting $\ln(\beta/T_p^2)$ with ($1/T_p$). From the straight line and taking the slope, Kissinger activation energy (Ea) for PBT-MWCNTs nanocomposites can be determined. The Ea values for PBT-MWCNTs nanocomposites at different MWCNT nano particles are shown in **Fig. 6**. It is clearly noticed the Ea values of all composites samples are higher than the pure PBT. It has been revealed that 4 wt% MWCNTs gives an 10 % higher Ea of PBT/MWCNTs nanocomposite than its pure PBT. This is a good signale that MWCNTs nanoparticles own well nucleation results on the crystallization of PBT/MWCNTs Nanocomposites, **Kim, et al., 2005**.

4 CONCLUSIONS

PBT/(MWCNTs) nanocomposite has been successfully synthesized by ultrasonicated of MWCNTs (0.5, 1, 2, 4 wt%) solution in PBT polymer. (DSC) analysis were utilized to investigate the kinetics for PBT/ (MWCNTs) nanocomposite as non-isothermal crystallization. A little amount of MWCNTs can evidently be a strong nucleating agent in PBT nanocomposites. On other hand, Avrami kinetics model results had given a good agreement with the frequent investigation and the existence of MWCNTs in PBT/(MWCNTs) nanocomposite gives an 10 % higher increases of the activation energy (Ea).

REFERENCES

- Chang, Y W, Kim, S S, & Kyung, Y B, 2005, *Poly (butyleneterephthalate)–clay nanocomposites prepared by melt intercalation: morphology and thermo mechanical properties,* Polymer International, 54(2), 348-353.
- Fanfoni, M. and Tomellini M., 1998. *The Johnson-Mehl- Avrami-Kohnogorov model: A brief review.* Volume 20, Issue 7, pp 1171–1182. doi:10.1007/BF03185527.

- Forouharshad, M S., Arasteh R F., 2010. *Manufacture and characterization of poly (butylenesterephthalate) nanofibers by electro spinning*, J MacromolSci Part B: Phys 49(4):833–842.
- Hu G., Feng X., Zhang S., *Yang M.,* 2008, *Crystallization behavior of poly(ethylene terephthalate)/multiwalled carbon nanotubes composites*, J. Appl. Polym. Sci. 108, 4080–4089.
- Iijima, S., 1991, *Helical Microtubles of Graphitic Carbon*, Nature, 354, 56-58.
- Joseph, H., Koo, 2006,*Polymer Nanocomposites Processing, Characterization, and Applications*, McGraw-Hil.
- Kaganj, AB, Rashidi A., Arasteh R., 2009, *Crystallization behavior and morphological characteristics of poly(propylene)/multi-walled carbon nanotube nanocomposites*, J ExpNanosci 4(1):21–34.
- Kim, J. Y.; Kang, S. W. & Kim, S. H. ,2006, *Thermo tropic Liquid Crystal Polymer Reinforced Poly (butylenesterephthalate) Composites to Improve Heat distortion Temperature and Mechanical Properties*, Fibers & Polymers, 7, 358-366.
- Kim, J. Y., 2009, *The Effect of Carbon Nanotube on the Physical Properties of Poly(butyleneterephthalate) Nanocomposite by Simple Melt Blending*, J. Appl. Polym. Sci., 112, 2589-2600.
- Kim, J. Y. , 2011, *Advances in Nanocomposites Synthesis, Characterization and Industrial Applications*. Dr. Boreddy Reddy (Ed.), ISBN: 978-953-307-165-7.
- Kim, J. Y.; Kang, S. W.; Kim, S. H.; Kim, B. C. & Lee, J. G. ,2005, *Deformation Behavior and Nucleation Activity of a Thermo tropic Liquid-crystalline Polymer in Poly (butylenesterephthalate)-Based Composites. Macromol*. Res., 13, 19-29.
- Mai,Y.and Zhong-Zhen Y.,2006, *Polymernanocomposites*, Boca Raton Boston New York Washington, DC.
- Rejisha, C. P., S. Soundararajan, N. S., and Palanivelu K., 2014, *Effect of MWCNT on Thermal, Mechanical, and Morphological Properties of Poly butyleneterephthalate/Polycarbonate Blends. Hindawi Publishing Corporation*, Journal of Polymers, Volume 2014, Article ID 157137, 7.
- Sabu T. and Visakh P. 2011. *Handbook of Engineering and Speciality Thermoplastics: Vol. 3. Polyethers ad polyesters*. John Wiley & Sons.
- Saeed, Kh. and KhanI., 2014, *Preparation and properties of single-walled carbon nanotubes/poly (butyleneterephthalate) nanocomposites*. Iranian Polymer Journal, Volume 23, Issue 1, pp 53-58.
- Saeed,Kh. and KhanI., 2015, *Characterization of clay filled poly (butylenes- terephthalate) nanocomposites prepared by solution blending.Polímeros* ,vol.25 no.6 São Carlos.
- Saligheh, O. A., Forouharshad M F., 2011, *Poly(Butylene Terephthalate)/single wall carbon nanotubes composite nanofibers by electro spinning*. J MacromolSci Part B: Phys 50(6):1031–1041.
- Saligheh, O. A., Forouharshad M. F., R. Araste, R. Eslami-Farsani, R. Khajavi& B. Yadollah Roudbari, 2013, *The effect of multi-walled carbon nanotubes on morphology, crystallinity*

and mechanical properties of PBT/MWCNT composite nanofibers, J Polym Res 20:65 DOI 10.1007/s10965-012-0065-5.

- Usuki, A.,Hasegawa N. Kato, M.,2005,*Inorganic Polymeric Nanocomposites and Membranes*. AdvPolymSci 179: 135–195, DOI 10.1007/b104481. Springer-Verlag Berlin Heidelberg.
- Xiao, J. F., Hu, Y. A., Lu, H. D., Cai, Y. B., Chen, Z. Y. J., & Fan, W. ,2007, *Effect of order of mixing on morphology and thermal properties of the compatibilized PBT and ABS alloys/OMT nanocomposites*,J. Appl. Polym. Sci., 104(4), 2130-2139.
- Yang,W. ,Han Z.,Benhong Y., Hongdian L., Lei S. and Yuan H., 2014, *Facile preparation of modified carbon nanotube-reinforced PBT nanocomposites with enhanced thermal, flame retardancy, and mechanical properties,* Polymer Composites DOI: 10.1002/pc.23354.
- Zhiying Z., Jia C., Haijing L. and Changfa X. 2014. *Applicability of Kissinger model in nonisothermal crystallization assessed using a computer simulation method*. Journal of Thermal Analysis and Calorimetry, Volume 117, Issue 2, pp 783-787.

NOMENCLATURE

Ea = activation energy, kJ/mol.
K =crystallization rate constant, min $^{-1}$.
n =avrami index, dimensionless.
R =gas constant, J /mol. K.
t =crystallization time, min.
Tg =glass Temperature, ^{o}C.
Tm, =melting Temperature, ^{o}C.
Tp =peck Crystallization Temperature, ^{o}C.
Xc =crystallization percentage, dimensionless.
Xt =relative crystallization, dimensionless.
β =cooling rate, ^{o}C/min.
ΔH_m =melting enthalpy, J/g.
ΔH^o =heat of fusion for 100% crystal of PBT, J/g.

Table 1. Data of PBT and PBT/MWCNTs Nanocomposite for Nonisothermal crystallization.

Cooling rate (^{o}C/min)	5	10	20	40	At 10 ^{o}C/min		
Sample	T_p(^{o}C)				T_m, (^{o}C)	ΔH_m (J/g)	X_c (%)
Neat PBT	190.00	183.50	175.72	165.80	224.6	50.13	35.81
PBT/(0.5 wt%)MWCNTs	197.02	190.30	182.51	172.02	224	53.01	37.86
PBT/(1 wt%)MWCNTs	199.10	192.41	184.80	174.54	223.6	55.67	39.76
PBT/(2 wt%)MWCNTs	202.00	195.20	187.72	177.18	223.8	55.55	39.68
PBT/(4 wt%)MWCNTs	205.05	198.37	190.63	180.51	223.5	54.83	39.16

Table 2. Parameters come by Avrami kinetics model.

Test Samples	n	$K \times 10^2$
Neat PBT	3.0303	0.726854
PBT/ (0.5 wt. %) MWCNTs	2.7504	0.941266
PBT/ (1 wt. %) MWCNTs	2.3065	5.269683
PBT/ (2 wt.%) MWCNTs	1.7968	16.05741
PBT/ (4 wt. %) MWCNTs	1.5786	30.09233

Figure 1. DSC SETARAM, 131 EVO instrument.

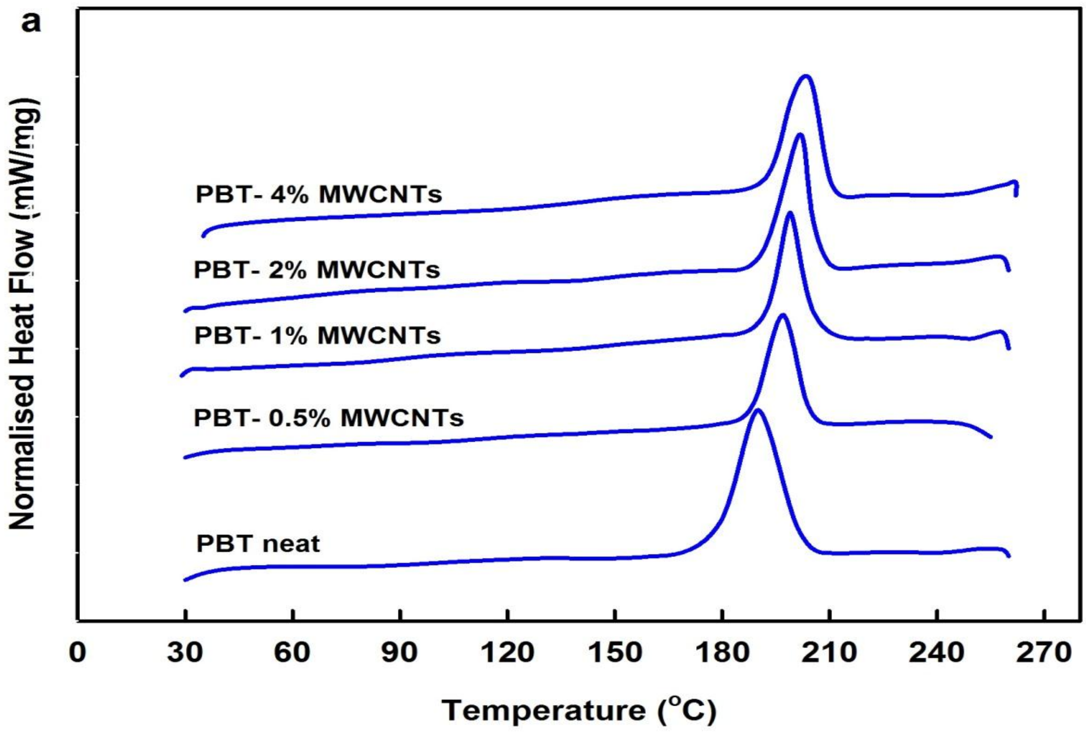

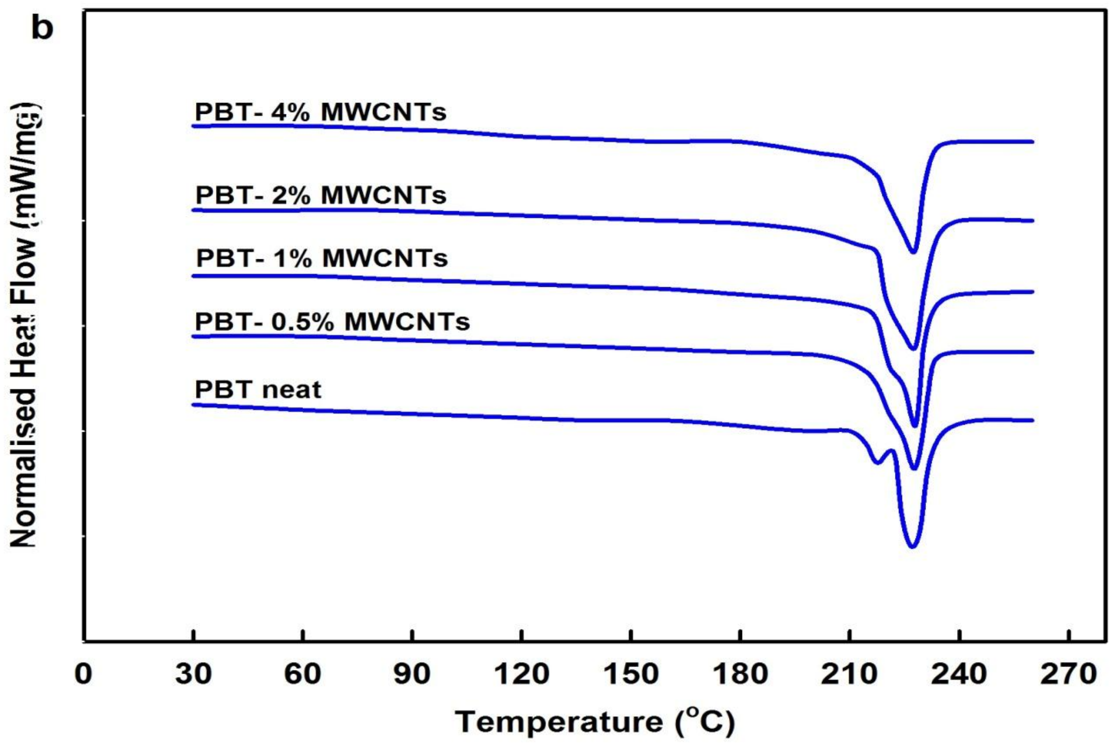

Figure 2. (DSC) trace for electrospun PBT/MWCNTs nanocomposite. (a) Non-isothermal crystallization for nanocomposite, (b) 2ndscans of nanocomposite.

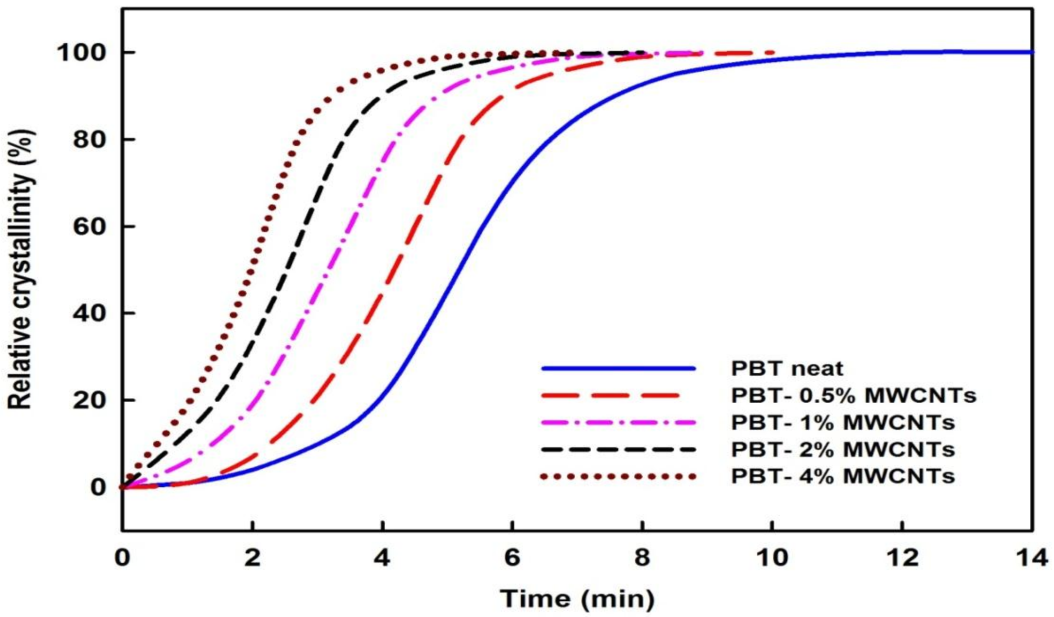

Figure 3. Divergence of relative crystallinity together with crystallization time. (Pure PBT as well as PBT/MWCNTs nanocomposites.)

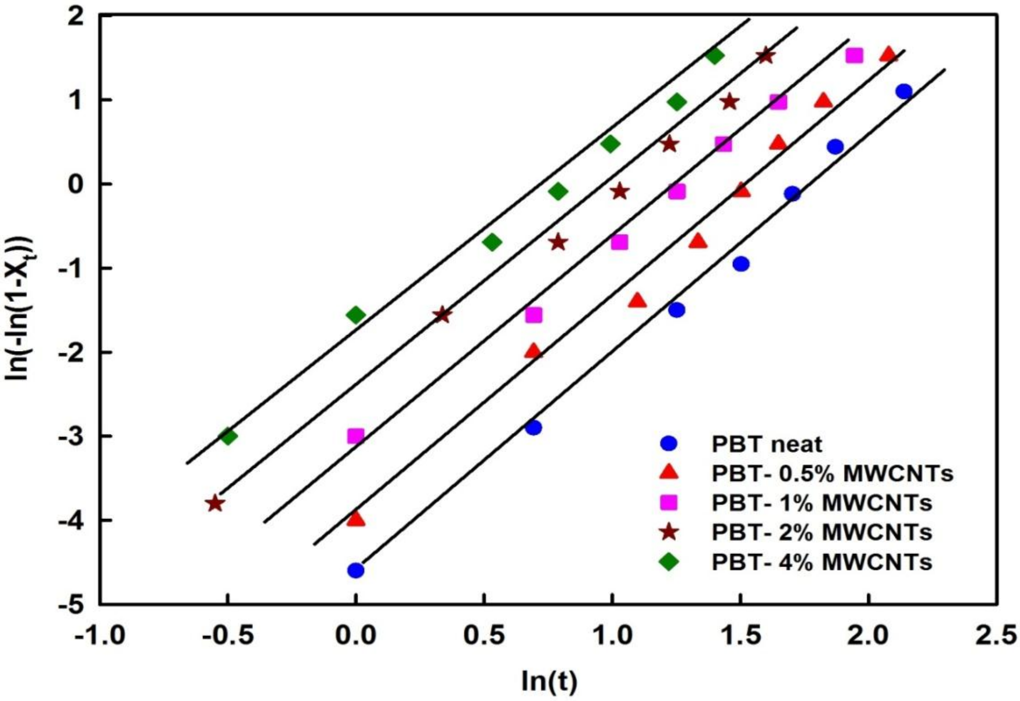

Figure 4. Plots of ln (-ln (1-X_t)) vs. ln (t). (Pure PBT as well as PBT/MWCNTs nanocomposites.)

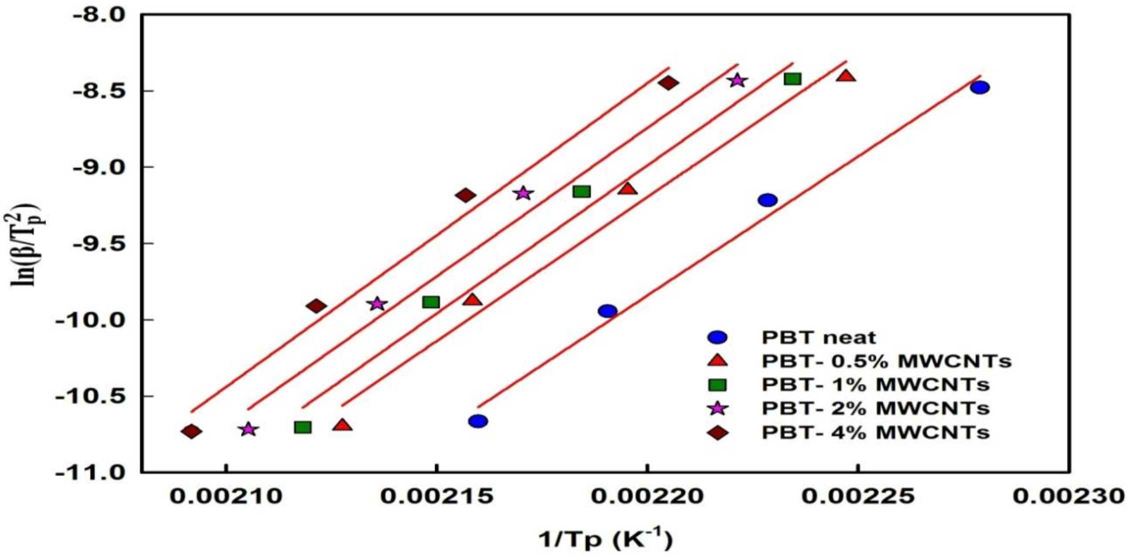

Figure 5. Influence of $\ln(\beta/T_p^2)$ on ($1/T_p$). (Pure PBT as well as PBT/MWCNTs nanocomposites.)

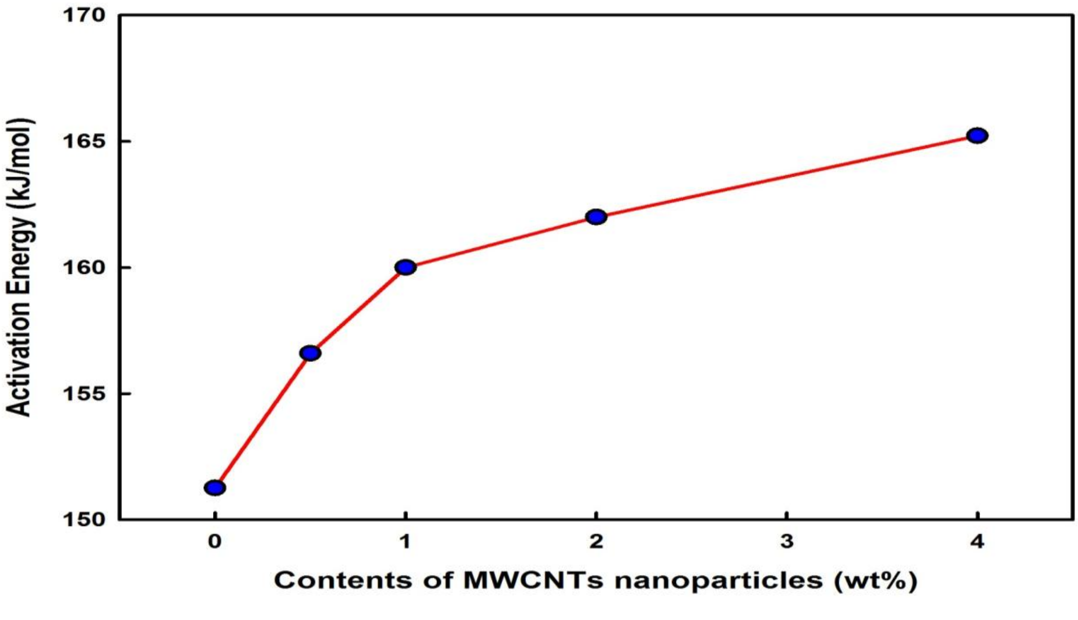

Figure 6. The Ea values for PBT/MWCNTs nanocomposites at different MWCNT nano particles.

Removal of Lead (II) from Aqueous Solution Using Chitosan Impregnated Granular Activated Carbon

Ali Mousa Ridha
Engineering Technical College– Baghdad, Middle Technical University
Email: alimreng1966@yahoo.com

ABSTRACT

The use of biopolymer material Chitosan impregnated granular activated carbon CHGAC as adsorbent in the removal of lead ions pb^{2+} from aqueous solution was studied using batch adsorption mode. The prepared CHGAC was characterized by Scanning Electronic Microscopy (SEM) and atomic-absorption spectrophotometer. The adsorption of lead ions onto Chitosan-impregnated granular activated carbon was examined as a function of adsorbent weight, pH and contact time in Batch system. Langmuir and Freundlich models were employed to analyze the resulting experimental data demonstrated that better fitted by Langmuir isotherm model than Freundlich model, with good correlation coefficient. The maximum adsorption capacity calculated from the pseudo second order model in conformity to the experimental values. This means that the adsorption performance of lead ions onto CHGAC follows a pseudo second order model, which illustrates that the adsorption of Pb^{2+} onto CHGAC was controlled by chemisorption. The granular activated carbon GAC impregnated by Chitosan was effectively applied as adsorbent for the elimination of lead ions from aqueous solution.

Keywords: adsorption, heavy metal ions, chitosan, granular activated carbon.

ازالة ايون الرصاص من المحلول المائي باستخدام الجيتاسون المحمل على الكاربون المنشط الحبيبي

علي موسى رضا
مدرس
الكلية التقنية الهندسية-بغداد، الجامعة التقنية الوسطى

الخلاصة

في هذا البحث تم استخدام مادة البوليمر الحيوي الشيتوزان المحمل على الكاربون المنشط الحبيبي CHGAC كمادة مازة في إزالة أيونات الرصاص Pb^{2+} من محلول مائي باستخدام الامتزاز نمط الدفعات (Batch adsorption mode). يعتبر البوليمر الحيوي من المواد المازة المهمة الواسعة الاستخدام لامكانياته العظيمة في الكثير من التطبيقات. تم دراسة تاثير كل من الاوزان المختلفة من الجيتاسون المحمل على الكاربون، pH الوسط الحامضي، وزمن التماس على عملية الامتزاز ايون الرصاص على الشيتوزان المحمل على الكاربون المنشط الحبيبي CHGAC. تم اجراء تحليل للمادة المازة المحضرة (CHGAC) بواسطة المسح الإلكتروني المجهري (SEM) ومقياس الطيف الضوئي للامتصاص الذري. ان ثوابت موديل لانكماير وفرندلخ المبنية على النتائج التجريبية لعملية الامتزاز لازالة ايون الرصاص وجد منها معامل الارتباط التي اوضحت بان الموديل لانكماير هو الافضل مقارنة مع موديل فرندلخ واكثر ملائمة لوصف امتزاز ايون الرصاص على الجيتاسون المحمل على الكاربون المنشط. تم حساب اعلى قدرة امتزاز من نموذج التفاعل من الدرجة الثانية وفقا للقيم التجريبية. وهذا يعني أن أداء عملية امتزاز أيونات الرصاص على المادة المازة CHGAC يتبع نموذج التفاعل من الدرجة الثانية، كذلك اوضحت أن امتزاز pb^{2+} على جيتاسون المحمل على الكاربون CHGAC هو كيميائيا.

الكلمات الرئيسية: الامتزاز، المعادن الثقيلة، جيتاسون، الكاربون المنشط الحبيبي.

1. INTRODUCTION

Water pollution caused by lead is a universal matter and has received worldwide attention. Lead is very toxic to human beings, animals, plants, and the general environment. Heavy metals such as lead, copper, mercury, and zinc in water that's used for drinking purpose can cause severe health hazards to human being and serious damage to the environment if not treated properly **Kundra, et al., 2012**.

Lead is present in low concentration in wastewater and is difficult to remove from water. Pollutants in industrial wastewater are almost invariably so toxic that the wastewater has to be treated before its reuse or disposal in water bodies **Singh,** and **Kaushal, 2013**. It was found that one-third of the total water pollution comes in the form of effluent discharge, solid wastes and other hazardous wastes **Lokhande, et al. 2011**. Wastewater is contaminated with lead from many industries such as battery manufacturing processes, metal-plating facilities, mining operations, paints, pigments, and other industries **Bernard, et al. 2013**.

Treatment processes for metal contaminated waste streams include chemical precipitation, ion exchange, membrane separations (ultra filtration, reverse osmosis, electrodialysis) and adsorption. Natural materials or low cost material from industrial or agricultural operations may have a potential as inexpensive sorbents for heavy metal removal where, the cost is an important parameter for the comparison of sorbent materials. Adsorption is considered the simplest and most cost-effective technique **Vereš,** and **Orolínová, 2009** . These low-cost adsorbents include cheap zeolites, clay, coal fly ash, sewage sludge, agriculture waste, tea waste, rice husk, coconut husk, name leaves, and biomass **Thomas,** and **Crittenden, 1998; Kumar, et al., 2013; Abdelhamid et al. 2012; Parmar,** and **Thakur, 2013**.

The maximum lead limit for industrial wastewater discharged is 0.1 ppm maximum concentration according to Iraqi regulation 2001 for the preservation of water sources, 2001.

Biopolymers are high potential adsorbents due to their biodegradability, non-toxicity, efficiency. These are cheap and thus are competitive with ion-exchange resins and activated carbon. They contain chemically active functional groups that serve as efficient sites to bind metal ions. Notably, Chitosan has the highest adsorption capacity among the biopolymers. It is a deacetylated derivative of chitin, the second most abundant organic compound in nature next to cellulose, and is extracted from the shells of crustaceans. It has several desirable characteristics such as biocompatibility, biodegradability, renewability, bioactivity, and non-toxicity **Juang, et al., 1997; Varma** and **Kennedy 2004; Zhoua,** and **Yangb, 2007**. For over a decade, Chitosan has received considerable attention as an adsorbent for transition metal ions and organic species **Annadurai, et al., 2008**. It chelates larger amounts of metal than chitin due to its excellent binding capacity, mostly attributed to the free amino groups exposed after chitin deacetylation. Moreover, Chitosan is soft and has a tendency to agglomerate or form gel. It is partially soluble in dilute mineral acids such as nitric acid (HNO_3), hydrochloric acid (HCl), and phosphoric acid (H_2PO_4) **Gyliene,** and **Visniakova, 2008; Nomanbhay, and Palanisamy, 2005** , and also soluble in dilute organic acids such as acetic acid (HAc), formic acid, etc. **(Chen, et al., 2008)**. In recent year, numerous studies of metal ion adsorption by Chitosan have been performed such as the removal of copper **Sağ,** and **Aktay, 2002**, chromium **Boddu, et al., 2003**, cadmium **Evans, et al., 2002**, iron **Wan, et al., 2005**, nickel, and lead ions from aqueous solution **Paulino, et al., 2007**.

The objective of this work is to use chitosan impregnated onto granular activated carbon as low cost adsorbent materials for the removal of lead from aqueous solution. Equilibrium is studying and carrying out for batch adsorption lead onto the chitosan impregnated granular activated carbon. The effect of batch adsorption parameters such as the mass of adsorbent, pH, and contact time had been investigated and the adsorption isotherms experiments have been interpreted by Langmuir and Freundlich isotherms.

2. MATERIALS AND METHOD

2.1 Materials

2.1.1 Adsorbent

Chitosan (moderate molecular weight, by Sigma–Aldrich Company) is used as received without any treatment. The granular activated carbon GAC (Filtrasorb 400, Calgon, Pittsburg, PA) was dried in the oven at 100 ^{o}C and 24 h to elimenate any moisture existing and then kept in an air tied bottle until use. The physical properties of GAC were examined at laboratory of Cincinnati University, USA and presented in Table 1.

2.1.2 Adsorbate

Anhydrous lead nitrate salt $pb(NO_3)_2$ was used as pb^{2+} metal ions. Analytical-grade of lead nitrate salt (99% purity, and molecule weight 331.2 g/mol). 1000 mg/l standard stock solution of lead ions pb^{2+} was obtained by dissolving lead nitrate salt $pb(NO_3)_2$ in deionized water. The chemicals used in this research are annular grade produced by Sigma–Aldrich company.

2.2 Preparation of Chitosan impregnated over granular activated carbon

Impregnation of chitosan over granular activated carbon CHGAC was done using the methods of **(Wan, et al., 2004)** with only slight modifications. “Standard stock solution of the chitosan was prepared as 10 g/L in 1% (v/v) of acetic acid solution. The granular activated carbon GAC was soaked in the chitosan solution for 24 h at room temperature. After filtration and washing with distilled water to remove excess chemicals and reach neutral pH, the adsorbent was immersed in sodium hydroxide 0.1M solution in order to obtain the adsorbed Chitosan. Finally, the prepared adsorbent was dried in oven at 80 ^{o}C for 6 h and kept in a desiccator until experimental use”.

2.3 Batch Adsorption Experiments

The removal of pb^{2+} from aqueous solution onto CHGAC was achieved in a batch adsorption system. The effect of operating variables on the adsorption process has been studied by:

2.3.1 Effect of Adsorbent weight

The removal of pb^{2+} from aqueous solution onto CHGAC was performed in a batch adsorption system. To evaluate the best dosage of the CHGAC for removal of pb^{2+} ions, the different dosages (5, 15, 25, 50, 75,100, 200, 300, 400 mg) of CHGAC were placed to 50 mL of lead ions solution pb^{2+}. The initial concentration of pb^{2+} solution was maintained at 100 mg/L. All experiments were carried out at 25^{o}C, pH 7, and 100 mg/L initial concentration of pb^{2+} ion solution. The desired pH was kept using 1 M HCl and 1 M NaOH. The CHGAC solution was added in bottles and then shaken for 10 days in a rotary shaker. The agitation speed was fixed at 140 rpm. The samples were then separated after shaking by filtration employing filter paper. The pb^{3+} ion concentrations of supernatant were measured by using the atomic-absorption spectrophotometer.

2.3.2 Effect of pH

The effect of pH on the removal process of lead ions pb^{2+} from aqueous solution onto biopolymer adsorbent was studied in batch adsorption system. The experiments were conducted to evaluate the best pH of metal ions solution, the best amount of adsorbent was placed in 50 ml of metal ions pb^{2+} solution at initial concentration of 100 ppm and desired pH value. The pH of the initial metal ions Pb^{2+} concentration was varied at 2, 4, 6, 8, and 10. The contents in the bottles were shaken in the rotary shaker at 150 rpm and 25^{o}C. Then the samples were filtered and the lead ions pb^{2+} solution concentration of the filtrate was analyzed by the atomic-absorption spectrophotometer.

2.3.3 Effect of time

The effect of contact time for the removal of Pb^{2+} onto biopolymer composite was investigated for varied time range 2h to 10 days. The best amount of adsorbent was added to the bottles containing 50ml of lead ions solution at initial concentration of 100 ppm. The contents in the bottles were mixed in the rotary shaker at 150 rpm and 25^{o}C. The bottles were then pulled out of the shaker at predetermined time intervals. Then the samples filtered and the lead ions solution concentration of the filtrate was analyzed by the atomic-absorption spectrophotometer.

2.4 Adsorption isotherm models

An adsorption isotherm is a curve relating the equilibrium concentration of an adsorbent onto the surface of solid substance, qe, to the concentration of the adsorbent in the liquid phase, C_e, with which it is in contact. The analysis of the equilibrium adsorption isotherms data is very important to study the adsorption capacity and equilibrium coefficient for **Sulaymon, et al., 2012**. The applicability of relationship between the experimental adsorption capacities and the metal ions concentrations (adsorption isotherm) have been widely used by the Langmuir and Freundlich models **Kaushal, and Upadhyay, 2014.** The amount of adsorption at equilibrium, qe(mg/g), is given by Eq. (1): **Grassi, et al., 2012**.

$$qe = \frac{(Co - Ce)V}{m} \tag{1}$$

Where C_o and C_e (mg/L) are the initial and equilibrium concentration of the solute, respectively, V is the volume of the liquid (L), and m is the mass of solid substance (g). Sorption efficiency can be described by an adsorption isotherm according to the general Eq. (2) **Oliveria, et al., 2005**.

$$Sorption\ efficiency = \frac{C_o - C_e}{Co} \times 100\% \tag{2}$$

There are several models for predicting the equilibrium distribution.

2.4.1 Langmuir isotherm model

The Langmuir sorption isotherm (Langmuir, 1916) model maybe the well known and most widely used in sorption isotherm. This model is used to illustrate quantitatively the formation of a monolayer adsorbate (metal ions) on the outer surface of the adsorbent solid substance), and after that no further adsorption takes place. Thereby, the Langmuir is valid for representing the equilibrium distribution of adsorbate (metal ions) between the solid surface and bulk solution

Dada, et al., 2012. It has provided significant agreement with a wide range of experimental data. The Langmuir isotherm equation is shown in Eq. (3)**Abdul Latif, et al., 2013 .**

$$q_e = \frac{q_m k_L C_e}{1 + k_L C_e} \tag{3}$$

Then Eq. (3) can be rearrangement in linear form: **Saibaba,** and **King, 2013**.

$$\frac{1}{q_e} = \frac{1}{q_m} + \frac{1}{q_m k_L}\frac{1}{C_e} \tag{4}$$

Where C_e is the equilibrium concentration of metal ions (adsorbate) in the bulk solution (mg/l), q_e is the equilibrium adsorption capacity (mg/g), k_L (L/g) is Langmuir parameters and q_m (mg/g) the maximum adsorption capacity.

2.4.2 Freundlich isotherm model

The Freundlich equation isotherm (Freundlich, 1906) is an adsorption isotherm, which is a relation of the solute concentration on the surface of an adsorbent (solid substance), to the solute concentration in the liquid with which it is in contact.

Freundlich adsorption isotherm is applicable for heterogeneous systems and involves formation of multilayers. Freundlich adsorption isotherm can be provided from the following formulas **Ho, 2003**:

$$q_e = k_f C_e^{1/n}. \tag{5}$$

The logarithmic form of the equation gives:

$$log\, q_e = log\, k_f + \frac{1}{n} log\, c_e, \tag{6}$$

where n and K_f are Freundlich constants. They provided from the intercept and slope of a linear plot of log $q_e$verses log C_e **Saibaba,** and **King, 2013**.

2.5 Kinetic of Adsorption

The kinetic of adsorption of metal ions Pb^{2+} on polymer composite has been evaluated. The experimental data were examined by pseudo-first-order kinetics, pseudo-second-order kinetics of adsorption process.

2.5.1 Pseudo first-order kinetics

The pseudo-first-order kinetics model also known as the Lagergren kinetic equation is widely used to understand the kinetic behavior of the system **Ho, 2003**. It is given by the Eq. (7)

$$log\,(q_e - q_t) = log\, q_e - \frac{k_1}{2.303}\, t, \tag{7}$$

Where q_e and q_t are the adsorption capacity of metal ions pb^{2+} at equilibrium and at time(mg.g^{-1}), k_1 is reaction rate constant of the pseudo first order (min^{-1}).

2.5.2 Pseudo second-order kinetics

The pseudo-second-order kinetics model is represented by the Eq. (8)

$$\frac{t}{q_e} = \frac{1}{k_2 . q_e^2} + \frac{t}{q_e}, \tag{8}$$

Where k_2 is the reaction rate constant of the pseudo-second-order model.

3. RESULTS AND DISCUSSION

3.1 Scanning Electronic Microscopy

The scanning electronic microscopy (SEM) images of the surface morphology of activated carbon, chitosan, and chitosan-impregnated activated carbon are presented in Figure 1. It is clear that the surface of GAC before the impregnation of chitosan is irregular with coarse particles with different particle sizes and rough surface (**Fig. 1a**). The chitosan surface has regular shape with smooth structure and larger particle sizes than CHGAC as shown in (**Fig. 1b**).The morphology of CH-GAC obtained by SEM in **(Fig. 1c**) has irregular surface with many pores on the surface. These results might explain the enhancing of adsorption capacity of CHGAC for lead ions. This phenomenon could have been due to the reduction of the pores. Consequently, the reduction of the particles size increases the adsorption capacity of lead ions onto adsorbent GAC. The above results are confirmed by **Maghsoodloo, et al., 2011**.

3.2 Adsorption Equilibrium

3.2.1 Effect of adsorbent weight

The effect of different chitosan impregnated GAC adsorbent dosage 5, 10, 20, 30, 40, 50, 60, 80,100 mg on the percentage of adsorption efficiency is presented in **Fig. 2**. This figure illustrates that the increase of adsorbent amount will increase the percentage of adsorption efficiency. It has been observed that the adsorption rate increased quickly in the beginning adsorption period at adsorbent dosages from 5 to 50 mg. This behavior could be explained by large surface area of composite adsorbent as well as large number of sites for the adsorption of lead ions. In addition, it can be found that the observed constancy in the percentage of lead adsorption efficiency at upward of 50 mg. This behavior may be due to very weak interaction between the adsorbent and adsorbate. In solution, the concentration appears to obtain a steady state with adsorbed species and so regardless the amount of adsorbent present, there will be a residual concentration of ions in solution. Adsorption of metal ions on these types' materials is generally attributed to weak interaction between the adsorbents and absorbents. In conclusion, according to the reasons mentioned, the 50 mg is selected as an optimum amount of chitosan impregnated GAC.

3.2.2 Effect of pH

The pH is one of the most important operational parameters of adsorption of heavy metals. The effect of different pH 2, 4, 6, 8, and 10 on the lead adsorption at chitosan impregnated GAC (adsorbent) are shown in **Fig. 3**. The experiments of batch adsorption were conducted with the metal solution of 50mL in volume and 50 mg/L initial concentration, 10 days agitation time at 150rpm, and optimum dosage of 50 mg for composite adsorbent. **Fig. 3** shows that the rate of lead adsorption is mainly controlled by the pH of lead ion solution, the percentage of lead adsorption efficiency started to increase with the increase in pH from 2-5.5. Therefore, the percentage of lead adsorption efficiency increased from 18.8 % to 99.4%, for composite adsorbent. Whereas, the percentage of adsorption efficiency gradually decreased with increase pH from 5.5-10. At pH higher than 5.5 the lead ions is precipitated due to the formation of hydroxide and removal process due to lead ions adsorption was very low. In contrast, at pH less than 5.5, the concentration of protons was high and lead ions binding sites became positively charged repelling the lead. Consequently, the optimum pH value for synthetic solution of lead ion can be obtained at (5.5).

3.2.3 Effect of time

The effect of contact time on the lead adsorption onto composite adsorbent is presented in **Fig. 4**. The optimum weight of CHGAC adsorbent was added to the bottles containing metal ion solutions pb^{2+} of optimum pH. The bottles were mixed in a rotary shaker at different time-periods varying between 3 and 30 hours at 140 rpm and 25^{o}C. The lead solution was then filtered by filter paper. The remaining of pb^{2+} ion concentrations in the filtrate was determined by using the atomic-absorption spectrophotometer. It can be seen that the adsorption efficiency of lead onto composite adsorbent increased with an increase in contact time. Thus, the adsorption rate was very high at the beginning of adsorption period. Lead adsorption efficiency of 99 % was obtained within first 2 hours using composite adsorbent. This behavior could be explained by the availability of large number of vacant sites for lead adsorption, which is well agreed with **Wan, et al., 2011**. Therefore, the optimum contact time for lead ions removal was selected at 6 hr.

3.3 Adsorption Isotherms models

The adsorption isotherms curves from experimental data are evaluated by plotting the mass of the metal ions adsorbed per unit mass of adsorbent (q_e) and the equilibrium concentration of the adsorbate (C_e). The experimental data for the lead adsorption onto the CHGAC adsorbent was examined over an initial concentration range from 20 mg/l to 200 mg/l. **Fig. 5** describes the adsorption isotherm curves for Pb ions onto Chitosan-impregnated activated carbon. The efficiency of the lead ions adsorbed was obtained using Eq. (2).

The isotherm adsorption models were applied to the experimental data for Pb adsorption onto chitosan-impregnated activated carbon to understand the potential adsorption mechanism. These models comprised Langmiur isotherm theoretical model and Freundlich isotherm theoretical model. **Fig. 5** demonstrates the experimental data and the isothermal models data obtained from Langmiur and Freundlich isotherm. The correlation coefficients and constants for Langmiur and Freundlich isotherm models are presented in Table 2. The resulting data in **Fig. 5** showing that the adsorption capacity of Pb metal ions onto chitosan impregnated activated carbon increases with increasing the solution concentration. This could be explained according to the amino functional group in chitosan composition where the suitable chemical attracting such as electrostatic binding can take place between adsorbent and adsorbate.

All the adsorption sites on the adsorbent surface were relatively free of lead metal ions (vacant). After that lead metal molecules were reached to the adsorbent surfaces may attach instantly to the protonated functional groups of the chitosan ($-NH_3$). The values of the correlation coefficient R^2 from Table 2 demonstrate that Langmuir isotherm better fit to the experimental adsorption data than Freundlich adsorption isotherm.

3.4 Kinetics of Lead Adsorption

The experimental data were analyzed by pseudo first order kinetics Eq. (7) and the pseudo second order kinetics Eq. (8) to describe the mechanism of adsorption reaction.

3.4.1 Pseudo first order model

The value of rate constant k_1 and qe are obtained from the slope and intercept of plots of log (qe-qt) against time respectively as shown in **Fig. 6**. The calculated values of qe as listed in Table 3 are much lower than the experimental values. The values of correlation coefficients R^2 of pseudo first order model are lower than pseudo second order model indicating that the Pb adsorption does not obey pseudo first order kinetic.

3.4.2 Pseudo second order model

The value of rate constant k_2 and qe can be evaluated from the slope and the interception of plot of (t/qt) against time respectively as shown in **Fig. 7.** The values of the rate constants, maximum adsorption capacity, and the correlation coefficients are presented in the Table 3. The pseudo second order models depend on the assumption that the rate-controlling step may be chemisorption, which involves valence forces by sharing or electron exchange between the adsorbent and the adsorbate. The maximum adsorption capacity calculated from the pseudo second order model is in accordance with the exponential values. This implies that the adsorption obeys a pseudo second order model. The plot of (t/qt) versus t directly increases with linear slope showing that chemisorption is the main rate-controlling step of the adsorption process.

The granular activated carbon impregnated by chitosan was effectively used as an adsorbent for the elimination of lead ions from aqueous solution. The experimental data have been analyzed by Langmuir isotherm model is more acceptable than using Freundlich model. Where, the parameters of these models with correlation coefficients were calculated. The results of adsorption data exhibited a better fit to Langmuir isotherm model. The adsorption performance of lead ions onto CHGAC followed a pseudo second order kinetic model, which described that the adsorption of Pb^{2+} onto CHGAC was controlled by chemisorption. The maximum adsorption capacities calculated from the pseudo second order model are in accordance with the exponential values.

REFERENCES

- Abdelhamid B., Ourari A., and Ouali M. S., 2012. copper (II) ions removal from aqueous solution using bentonite treated with ammonium chloride. *American Journal of Physical Chemistry*, 1, pp.1–10.
- AbdulLatif M.H., Noor T.H. Al and Sadiq K.A., 2013. Adsorption Study of Symmetrical Schiff Base Ligand 4, 4-[hydrazine-1, 2-diylidenebis (methan-1-yl-1-ylidene) bis (2-methoxyphenol)] on Granulated Initiated Calcined Iraqi Montmorillonite via Columnar Method. *Advances in Physics Theories and Applications*, 24, pp.38–51.
- Annadurai G., Ling L. Y. and Lee J.F., 2008. Adsorption of reactive dye from an aqueous solution by chitosan: Isotherm, kinetic and thermodynamic analysis. *Journal of Hazardous Materials*, 152, pp.337–346.
- Bernard E., Jimoh A. and Odigure J., 2013. Heavy metals removal from industrial wastewater by activated carbon prepared from coconut shell. *Research Journal of Chemical Sciences …*, 3(8), pp.3–9. Available at: http://www.isca.in/rjcs/Archives/vol3/i8/1.ISCA-RJCS-2013-087.pdf [Accessed August 25, 2015].
- Boddu V. M., Abburi K., Talbott J. L., and Smith E.D., 2003. Removal of hexavalent chromium from wastewater using a new composite chitosan biosorbent. *Environmental Science & Technology*, 37, pp.4449–4456.
- Chen Arh-hwang , Sheng-chang Liu, Chia-yuan Chen and Chia-yun Chen, 2008. Comparative adsorption of Cu (II), Zn (II), and Pb (II) ions in aqueous solution on the crosslinked chitosan with epichlorohydrin. *Journal of hazardous materials*, 154(1-3), pp.184–191.

- Dada A.O, Olalekan A.P , Olatunya A.M. and DADA O, 2012. Langmuir, Freundlich, Temkin and Dubinin--Radushkevich isotherms studies of equilibrium sorption of Zn^2 unto phosphoric acid modified rice husk. *Journal of Applied Chemistry*, 3(1), pp.38–45.
- Evans J. R., Davids W. G., MacRae J. D. and Amirbahman, A., 2002. Kinetics of cadmium uptake by chitosan-based crab shells. *Water research*, 36, pp.3219–3226.
- Grassi M., Kaykioglu G., Belgiorno V. and Lofrano G., 2012. Removal of emerging contaminants from water and wastewater by adsorption process. In *Emerging compounds removal from wastewater*. Springer, pp. 15–37.
- Gyliene O., & Visniakova S., 2008. Heavy metal removal from solutions using natural and synthetic sorbents. *Environmental Research Engineering and Management*, 43, pp.28–34.
- Ho, Y.-S., 2003. Removal of copper ions from aqueous solution by tree fern. *Water research*, 37(10), pp.2323–2330.
- Juang R. S., Tseng R. L., and Wu F.C.L., 1997. Adsorption behavior of reactive dyes from aqueous solutions on chitosan. *Journal of Chemical Technology & Biotechnology*, 70, pp.391–399.
- Kaushal R.K. and Upadhyay K., 2014. Treatability Study of Low Cost Adsorbents for Heavy Metal Removal from Electro Plating Industrial Effluent : A Review. *International Journal of ChemTech Research*, 6(2), pp.1446–1452.

- Kumar S., Panda A. K., and Singh R. K., 2013. No TitlePreparation and Characterization of Acids and Alkali Treated Kaolin Clay. *Bulletin of Chemical Reaction Engineering & Catalysis*, 8(1), pp.61–69.
- Kundra R., Sachdeva R., Attar S. and Parande M., 2012. Studies on the removal of heavy metal ions from industrial waste water by using titanium electrodes. *J. Curr. Chem. Pharm. Sc*, 2(1), pp.1–11.
- Lokhande R.S., Singare P.U. and Pimple D.S., 2011. Toxicity Study of Heavy Metals Pollutants in Waste Water Effluent Samples Collected from Taloja Industrial Estate of Mumbai, India. *Resources and Environment*, 1(1), pp.13–19.
- Maghsoodloo Sh., Noroozi B., Haghi A.K. , Sorial G.A. , 2011. Consequence of chitosan treating on the adsorption of humic acid by granular activated carbon. *Journal of Hazardous Materials*, 191(1-3), pp.380–387. Available at: http://dx.doi.org/10.1016/j.jhazmat.2011.04.096.
- Nomanbhay S. and Palanisamy K., 2005. Removal of heavy metal from industrial wastewater using chitosan coated oil palm shell charcoal. *Electronic Journal of Biotechnology*, 8(1), pp.43–53.
- Oliveria E. A. and Montanher S.F., Andrader A.D. and Nobrega J.A, 2005. Equilibrium studies for the sorption of chromiumand nickel from aqueous solution using rice bran. , 40, pp.38–45.
- Parmar M. and Thakur L.S., 2013. Health Hazards And Their Removal Techniques By Low Cost Adsorbents: A Short Overview. *International Journal Of Plant, Animal And Environmental Sciences*, 3(3), pp.143–157.
- Paulino A. T., Guilherme M. R., Reis A. V., Tambourgi E. B., Nozaki, J. and Muniz E.C., 2007. Capacity of adsorption of Pb2+ and Ni2+ from aqueous solutions by chitosan produced from silkworm chrysalides in different degrees of deacetylation. *Journal of hazardous materials*, 147, pp.139–147.
- Sağ Y. and Aktay, Y., 2002. Kinetic studies on sorption of Cr(VI) and Cu(II) ions by chitin, chitosan and Rhizopus arrhizus. *Biochemical Engineering Journal*, 12(1), pp.143–153.
- Saibaba Narayana K V and King P., 2013. Equilibrium and thamodynamic studies for dye removal using biosorption. Impact: *International Journal of Research in Engineering & Technology (IMPACT:IJRET)*, 1(3), pp.17–24. Available at: http://www.impactjournals.us/journals.php?id=77&jtype=2&page=3.
- Singh U. and Kaushal R.K., 2013. Treatment of Waste Water With Low Cost Adsorbent – A Review. *International Journal of Technical & Non Technical Research*, 4, pp.33–41.
- Sulaymon A. H., Mohammed T. J., and Al-Najar J., 2012. Equilibrium and kinetics Studies of Adsorption of Heavy Metals ontoActivated Carbon. *Canadian Journal on Chemical Engineering & Technology*, 3(4), pp.86–92.
- Thomas W.J. and Crittenden B., 1998. *Adsorption Technology and Design*, Available at: http://books.google.com/books?id=tXOqBBn8m-sC&pgis=1.
- Varma A. J., Deshpande S. V., and Kennedy J.F., 2004. Metal complexation by chitosan and its derivatives: A review. *Carbohydrate Polymers*, 55, pp.77–93.
- Vereš J. and Orolínová Z., 2009. Study of the treated and magnetically modified bentonite as possible sorbents of heavy metals. *Acta Montanistica Slovaca*, 14(2), pp.152–155.

- Wan Ngah W. S., Ab Ghani S. and Kamari A., 2005. Adsorption behaviour of Fe(II) and Fe(III) ions in aqueous solution on chitosan and cross-linked chitosan beads. *Bioresource Technology*, 96, pp.443–450.
- Wan M. W., Petrisor I. G., Lai H. T., Kim D. and Yen T.F., 2004. Copper adsorption through chitosan immobilized on sand to demonstrate the feasibility for in situ decontamination. *Carbohydrate Polymers*, 55, pp.249–254.
- Wan M. W., Kan C. C., Rogel B. D. and Dali M. L., 2010. Adsorption of copper (II) and lead (II) ions from aqueous solution on chitosan-coated sand. *Carbohydrate Polymers*, 80, pp. 891–899
- Ying Shan Zhou, Dong Zhi Yang, and Jun Nie, 2007. Preparation and characterization of crosslinked chitosan-based nanofibers. *Chinese Chemical Letters*, 18, pp.118–120.

Table 1. The Physical Properties of Granular Activated Carbon (Sigma–Aldrich Company).

Product name	Granular Activated Carbon, GAC
Composition	Carbon C
BET Surface area m^2/g	819.2815
Average pore diameter (4V/A):	49.890 Å
BJH adsorption cumulative volume of pores between 17.000 Å and 3000.000 Å diameter	0.307097 cm^3/g
T-Plot Micropore volume	0.315204 cm^3/g

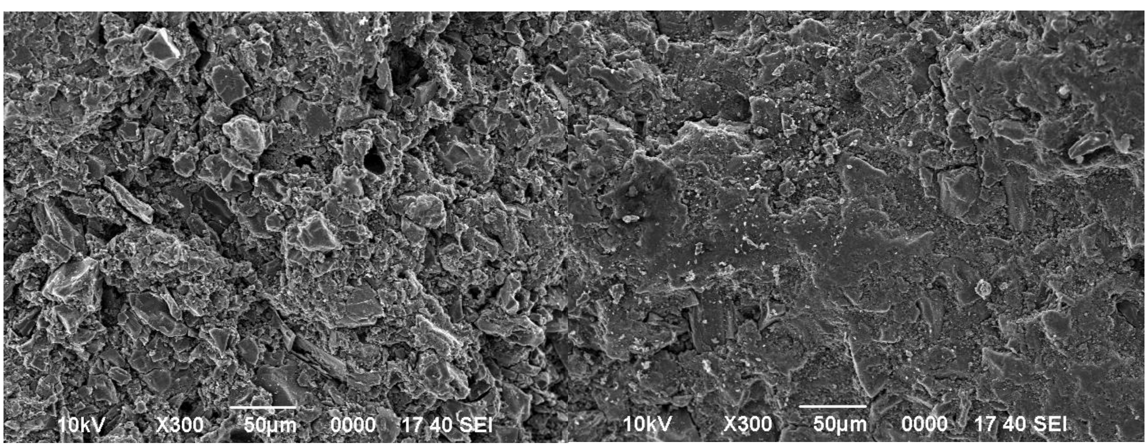

(a) (b)

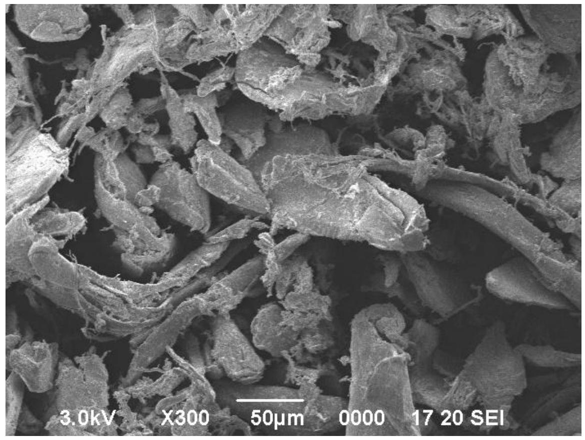

(c)

Figure 1. SEM images of (a) Chitosan (b) Granular Activated Carbon GAC and(c) Chitosan impregnated granular activated carbon CHGAC.

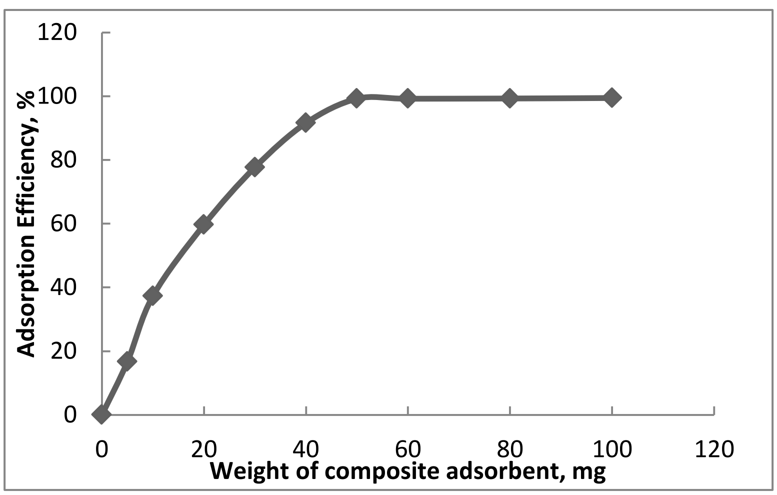

Figure 2. Effect of amount of chitosan impregnated GAC on the adsorption of lead ions (pb^{+2}).

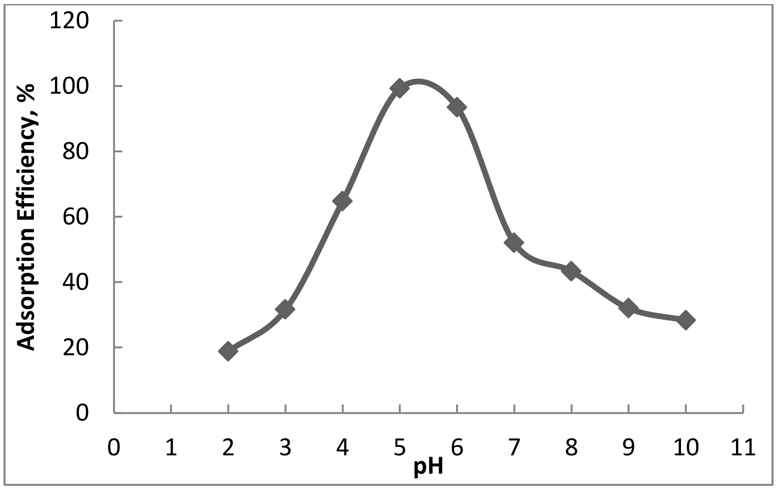

Figure 3. Effect of pH on the removal efficiency of Pb^{+2} onto CHGAC.

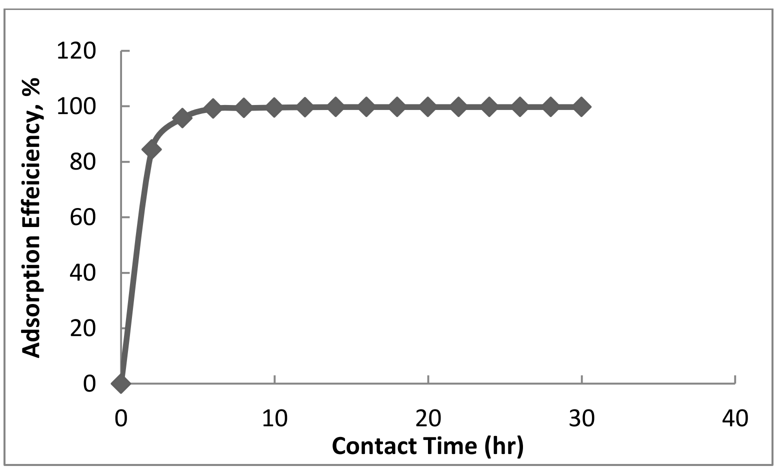

Figure 4. Effect of time on the removal efficiency of Pb^{2+} onto CHGAC.

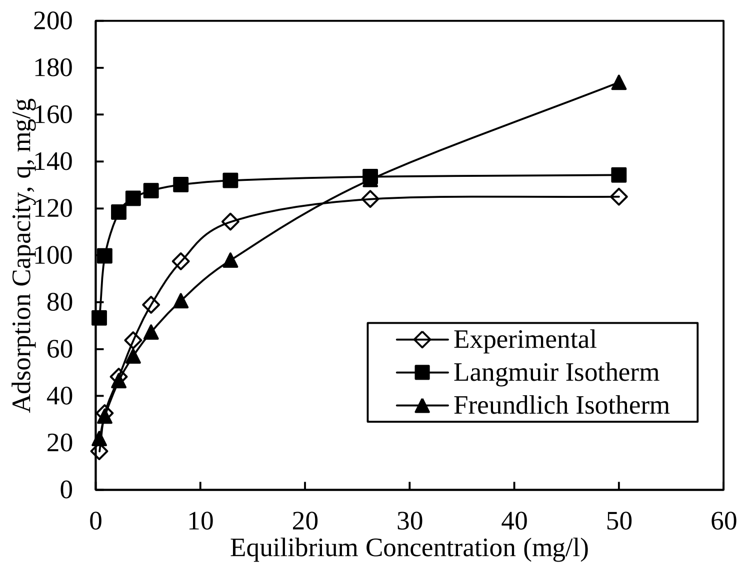

Figure 5. Adsorption isotherm of experimental, Langmuir, and Freundlich of CHGAC 20^{o}C.

Table 2. Langmuir isotherm and Freundlich isotherm constants of CHGAC.

Langmuir Constants			Freundlich Constants		
q_m	k_L	R^2	1/n	k_f	R^2
135.1351	3.155405	0.9981	0.4232	33.18945	0.9232

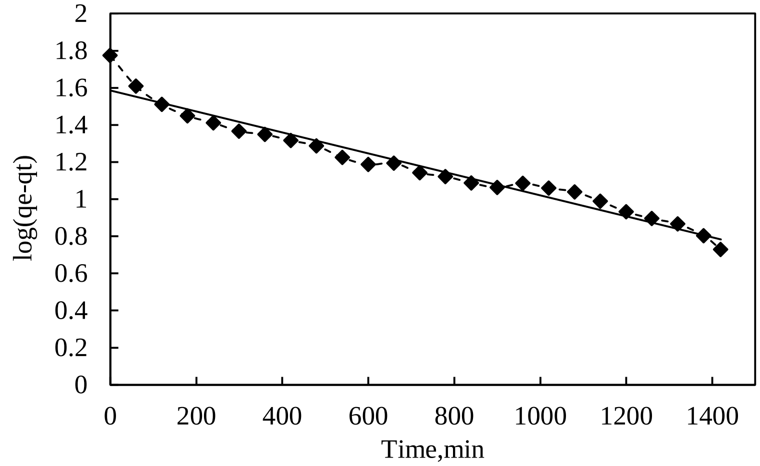

Figure 6. Pseudo first order kinetic for Pb adsorption onto chitason impregnated GAC at room temperature.

Table 3. Kinetics models parameters for Pb adsorption onto Chitason impregnated GAC.

Pseudo first order			Pseudo second order			qe, exp
k_1	qe, cal	R^2	k_2	qe, cal	R^2	
-0.00139	38.4858	0.9545	0.00011	56.8182	0.9891	59.3533

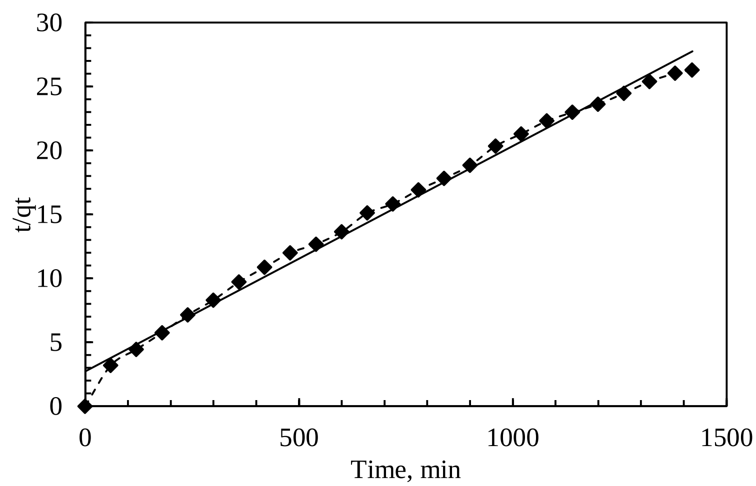

Figure 7. Pseudo second order kinetic for Pb adsorption onto chitason impregnated GAC at room temperature.

Design and Implementation of Enhanced Smart Energy Metering System

Dr. Oday A.L.A Ridha
Assistant professor
College of Engineering -Baghdad University
Email: oday_ridha@yahoo.com

Dhurgham M. Jasim
College of Engineering -Baghdad University
Email: dhurgham.zwaid@yahoo.com

ABSTRACT

In this work, the design and implementation of a smart energy metering system has been developed. This system consists of two parts: billing center and a set of distributed smart energy meters. The function of smart energy meter is measuring and calculating the cost of consumed energy according to a multi-tariff scheme. This can be effectively solving the problem of stressing the electrical grid and rising consumer awareness. Moreover, smart energy meter decreases technical losses by improving power factor. The function of the billing center is to issue a consumer bill and contributes in locating the irregularities on the electrical grid (non-technical losses). Moreover, it sends the switch off command in case of the consumer bill is not paid. For implementation of smart energy meter, the microcontroller (PIC 18F45K22) is used. For communication between billing center and smart energy meters, ZigBee technology is adopted. The necessary program for smart energy meter is written in MicroC PRO, while the program for billing center is written in visual C#.

Key words: smart energy meter, billing center, ZigBee, power factor correction

تصميم وتنفيذ منظومة مقاييس طاقة ذكية مطورة

أ. م. د. عدي عبد اللطيف عبد الرضا
قسم الهندسة الالكترونية والاتصالات
كلية الهندسة/ جامعة بغداد

ضرغام محمد جاسم
قسم الهندسة الالكترونية والاتصالات
كلية الهندسة/جامعة بغداد

الخلاصة

في هذا العمل تم تصميم وتنفيذ منظومة مقياس طاقة ذكية تتكون من مركز جباية و مجموعة من المقاييس الذكية للطاقة الموزعة. وظيفة مقياس الطاقة الذكي هي قياس وحساب كمية الطاقة المستهلكة و تكلفتها وفق نظام التعرفة المتعددة. وهذا يساهم بشكل فعال في تقليل الاجهاد على الشبكة الكهربائية وزيادة وعي المستهلك. اضافة الى ذلك يساهم مقياس الطاقة الذكي في تقليل الخسائر التقنية من خلال تحسين عامل القدرة. وظيفة مركز الجباية هي اصدار فاتورة المستهلك والمساهمة في الكشف وتحديد مكان وجود المخالفات على الشبكة الكهربائية (الخسائر غير التقنية). كما يقوم ايضا على ارسال الايعازات الخاصة بقطع او توصيل القدرة الى المستهلك وذلك اعتمادا على دفع الفاتورة. استخدم المسيطر الدقيق (PIC18F45K22) في تنفيذ مقياس الطاقة الذكي. كما واعتمدت تقنية ال ZigBee كوسيلة اتصال بين مركز الجباية ومقاييس الطاقة الذكية. تمت كتابة البرنامج للمسيطر الدقيق داخل المقياس الذكي بواسطة لغة (MikroC Pro) بينما البرنامج الخاصة بمركز الجباية فتمت كتابتها بواسطة لغة (Visual C#).

1. INTRODUCTION

Smart grid combines renewable energy with information technology to provide a quality power for consumers. The existence of two-way flow energy and information between consumer and provider enables a variety of advanced utility applications; such as energy management services, advanced metering and reporting, power quality management, and many other functions, **RAHMAN, and MTO, 2011**. Smart grid helps in decreasing the transmission and distribution losses and improves power quality by managing the power consumption of the consumer. Smart energy meter is considered essential component to smart grid that reduces technical and Nontechnical losses, **Pedro, 2009**. It performs real time calculations of consumed energy and its price according to a multi-tariff scheme to mitigate the problem of peak demand.

The problem of peak demand can be mitigated by increasing the number of power plants but the disadvantage of this approach is not only the high cost but also increasing CO_2 emission. Onother approach to mitigate peak demand problem is applying a multi tariff in smart energy meter for calculating the consumed energy, imposition punitive tariff at peak demand time pushes the consumer for switching off unnecessary appliance at peak demand time, **Depuru, et al, 2011**. There are two main methods for achieving multi tariff scheme, the first method is done by receiving notification signal from billing center each time zone as in **Anjana, and Prasanna, 2014**, but this way is inefficient when the number of consumers' nodes is increased to a more realistic number. In this case, the network will suffer from high collisions and may break down. Onother approach for achieving multi tariff scheme is done by smart energy meter using real time clock (RTC) module, RTC module is used to keep track of time, support multi-tariff scheme and it can be used to provide historical peak demand, in addition a RTC module is used to determine the day of sending data to the billing center, a table of tariffs are stored in the smart energy meter that can be updated by billing center via ZigBee. This method is more expensive compared with the first method but it is efficient.

On other side, the network load is inductive, i.e., load contains inductive component such as air conditioner, refrigerator, induction motor and etc. which causes poor power factor where up to 0.7 in summer in Iraq. Smart energy meter improves power quality by achieving residential power factor correction (PFC). Residential PFC is becoming more popular in some regions of the world. In 2001, a distributer of electrical energy in Peru performed a project to improve power factor for a limited region including 26,000 households. It was found that improving power factor from 0.84 to 0.93 led to saving of around 19, 300 MWh per year that means a cost saving of close to 900,000$. The advantages of residential PFC go far beyond the energy savings; because PFC reduces the current of loading that leads to reduce losses in transmission line (I^2R) and increases the grid capacity, **Alexandre, 2007**. The proposed smart energy meter achieved power factor correction based on developed algorithm and capacitors bank in order to compensate reactive power, thus bringing power factor near to 0.95.

2. RELATED WORKS

With the development of electronic chips and programming languages, smart energy meters evolved gradually with more hardware and software capabilities. So many researches have been conducted to develop a general purpose of smart energy meter in both hardware and software.

Smart energy meter was designed and develop to measure energy consumption by consumer and send it to the service provider. Both ZigBee and GSM technologies are used to perform Bi-directional communication between service provider and consumer. ZigBee technology is used to transmit information from meter to the base station where the bill is calculated. GSM network is installed at base station for messaging all consumers and service provider employees, **Vivek, and Ranthkenthiwar, 2014**. Advanced metering infrastructure based on power line carrier (PLC) is proposed to automatically collect information from different kinds of meters. Energy consumption, water and gas can be measured by the meters and then data is sent to the gateway through PLC. A gateway reads different data and communicates with data acquisition center (DAC) through GSM. The gateway consists of two parts Neuron Core and Transceiver. Transceiver is used to transfer data on the PLC while Neuron Core represents the processing unit, **Popa, 2011**. Smart energy meter is designed and implemented to vehicle-to-grid. This energy meter is interface between electric vehicles and smart grid. It is able to measure bi-directional consumed energy, voltage and current. This energy meter also achieves bi-direction measurement when the difference in phase angle between voltage and current determines the direction of energy consumption, **Libiao, et al, 2011**. A remote meter-reading system is designed to get data from the sensors and meters and control on the appliance in residence area. The structure of this system consists of sensors, measure meters, intelligent terminal, management center and wireless communication network. Bluetooth technology is used to send and receive data and control signal between intelligent terminal and meters, while GSM network is used to communicate between intelligent terminal and management center, **Liting, et al, 2006.**

Automatic meter reading system based on GSM technology is implemented enables the consumer to check the status of electricity from anywhere. It also enables utility to cut off and reconnect the meter connection by SMS, **Zahid Iqbal, 2014**. Wireless sensor and actuator network are implemented for monitoring the energy consumption of appliances in the home. The structure of the network consists of energy measurement nodes and central server, the central server displays the reading from measurement nodes via user interface in real time and enables user to remotely power on or power off individual device. This system presents a practical way to control the energy consumption in home, **Edwin, et al, 2013**. The prepaid electricity meter is designed to be able to conduct money transactions remotely in order to enable the consumer to recharge his account from home, besides; the proposed meter helps utility companies to eliminate electricity theft, **Sai, et al, 2014**. A power factor corrector is designed and implemented using PIC microcontroller, it can improve power quality by compensating excessive reactive components. The system includes sensing and measuring power factor value of the load. A proper algorithm is used to determine and trigger sufficient capacitors to improve power factor, **Nader, 2007**.

In this paper, the proposed system provide a low cost smart energy meter, monitoring and improving power quality by developing a proper algorithm, achieving multi tariff with proper solution by using a dedicated IC (DS1307), bi-directional communication is achieved to ensure sending and receiving data and commands between smart energy meter and billing center by using ZigBee technology.

3. PROPOSED SMART METERING SYSTEM

The proposed system consists of two parts, smart energy meter for the consumer and the billing center for the service provider.

3.1. Smart Energy Meter

Smart energy meter provides the real time measurement and calculation of amount and cost of consumed energy and displays related information for consumer. When the inductive load undermines power quality as result of poor power factor, the smart energy meter can improve power quality by switching on the capacitors bank for continuously keeping the power factor of the load near unity. Moreover, the smart energy meter can be used to detect the irregularities on the electrical grid. Smart energy meter is composed of the analog unit, controller unit (PIC microcontroller), real time clock and calendar (RTCC), liquid crystal display, wireless communication module and capacitors bank. The hardware architecture of the proposed smart energy meter is shown in the **Fig.1**.

3.1.1 Analog unit

Smart energy meter interfaces to the relatively high voltage while the acceptable input voltage of PIC microcontroller is 5V, so the analog unit scales and converts the voltage and current to voltages which are sufficiently small and cannot cause damage to delicate electronics. The voltage of power line is usually 220 Vrms (-312 to 312 Vp-p), therefore it is scaled by the voltage divider to a level and dynamic range is compatible with the analog to digital (ADC) of PIC microcontroller, a low power consumption resistors are used to divide measured voltage. The values of current are sensed by using current sensor IC (ACS712). ACS712 current sensor is a precise, low offset, linear hall sensor circuit. Current sensor IC converts applying AC current flowing through two of its pins into proportional voltage using integrated Hall IC.

3.1.2 Controller unit

The values sensed by the voltage and current sensors are provided to the analog channel of the PIC microcontroller. The processing unit calculations of PIC microcontroller rescales all the measurements by sensors to get the original value and performs all the power parameters calculations. All the calculated values are displayed on display unit as shown in **Fig.2**. The controller unit selected for smart energy meter design is the PIC18F45K22 microcontroller from Microchip, due to it's multiple on-chip resources, low cost and suitable processing accuracy that can reduce and simplify the design appropriately. PIC18F45K22 microcontroller has 10 bit ADC with a multiple of channels. The multiplexer provides the capability of connecting multi-analog signals to a single ADC. It has a multiple of timers that are used to provide interrupt to notify the CPU every time interval. Regular interrupt is important to execute a certain instructions at a certain time. This technique enables to create multitasking easily which executes multiple application programs. The built-in serial port of the microcontroller represents smart energy meter communication port. This is used with aid of ZigBee module to send and receive data.

3.1.3 Real time clock and calendar (RTCC)

The proposed smart energy meter contains a tiny real time clock and calendar module (RTCC) to keep track of time, support multi-tariff scheme and it can be used to provide historical Peak demand, in addition a tiny RTCC module is used to determine the day of sending data to the billing center. A tiny RTCC module is based on the chip DS1307 which supports the I2C protocol. This tiny RTCC module provides seconds, minutes, hours, day, month, and year information. The end of the month date is automatically adjusted for months with fewer than 31 days, including corrections for leap year. The clock operates in either the 24-hour or 12-hour format with AM/PM indicator. A Tiny RTCC module contains Lithium cell battery (CR1225) to save time and 56-Byte Nonvolatile (NV) RAM for data storage. A tiny RTCC module uses the I2C bus to communicate with PIC microcontroller.

3.1.4 Power quality and size of capacitors bank.

Usually the network load is inductive, i.e., load contains inductive component. PFC removes inductive component by adding (equal in magnitude) capacitive component through connecting a capacitor. Due to the load of the home is varied, fixed capacitors is inappropriate to improve the power factor and may led to overcompensation, so automatic switching of capacitors is a good method of obtaining the full electrical benefits from a capacitor installation. In order to calculate the amount of required capacitor compensation for improving power factor, an effective algorithm for switching sufficient capacitors bank has been developed (in PIC microcontroller).

In this work, PFC is performed in smart energy meter by using capacitors bank. The capacitor banks consist of eight capacitors of different values, the values of these capacitors are chosen in such away like the weight of binary digits representing a decimal number. These values are 128, 64, 32, 16, 8, 4, 2 and 1 μFas shown in **Fig.3**. The value of chosen capacitors provide a high value of micro farad reach to 255 μF, so the number of capacitors can be reduced according to the expected loads in each and individual home.

4. BILLING CENTER

The main function of the billing center as the name implies is to bill consumers according to the amount of consumed energy. It receives a consumption data from the smart energy meter which represent the amount and the cost of the consumed energy to issue a consumer bill and the other measurements to give a good estimate of the grid status. Moreover, the billing center can send the commands of switching on or off the electrical power. It sends the switch off command when the bills are not paid, and it sends the switch on command when the bills are paid.

Detection and localization of a faulty meter, irregularities on the electrical grid, and leakages can be determined at billing center by using a master meter with each group of home meters. A difference between the power reading of the master meter of the group and the summation power of individual home meters within the same group means either one or more meters are faulty, or there is an irregularity, or a leakage in the electrical grids.

The billing center is implemented by using personal computer (PC), communication transceiver (ZigBee module) and the interfacing circuit which is used to establish the proper connection between the communication transceiver and the personal computer as shown in **Fig.4**. The transceiver used in the billing center is the same as in the smart energy meter. The difference in the two ZigBee modules is in the addresses in the network and some of setting which makes the billing center represents a coordinate, while smart energy meter represent node. The data from the meters is received through ZigBee module then sends it to PC.

5. SOFTWARE DESIGN OF THE PROPOSED SYSTEM

The software used in the proposed metering system consists of two parts; first part is executed in smart energy meter whereas the second part is executed in the billing center.

5.1 Software of the Smart Energy Meter

The software of smart energy meter is responsible for initializing and managing the operation and interaction among hardware modules of the smart energy meter. The software operations of the smart energy meter are illustrated in the flowchart of the main program shown in **Fig.5** and the flowchart of interrupt service routine shown in **Fig.6**. Interrupt service routine (ISR) occur once every 2 msec in order to sample voltage and current at regular time. ISR ensures that the sampling rate (Fs) to be 500 Hz which provides 10 samples per cycle. ISR is also responsible for the flags condition. Flags conditions are required for executing the operations in the main program as shown in **Fig.6**. First, for sampling rate (Fs) and N samples of the power line source, the RMS voltage can be calculated by using Eq. (1).

$$V_{rms} = \sqrt{\frac{\sum_{i=0}^{N-1} v_i^2}{N}} \qquad (1)$$

Where N is the number of samples, v_i is the sampled voltage.

As mentioned early the voltage of power line is scaled to level that is compatible with delicate electronics, so the measured value must be rescaled to the engineering value (actual voltage) in the processing unit calculations. To do so, the sampled voltage in Eq. (1) multiplies by voltage proportionality constant for the circuit design (K) as shown in Eq. (2).

$$V_{rms} = \sqrt{\frac{\sum_{i=0}^{N-1} (K\, v_i)^2}{N}} \qquad (2)$$

The time taken to calculate the RMS voltage can be reduced by modifying Eq. (2) to Eq. (3):

$$V_{rms} = T * \sqrt{\sum_{i=0}^{N-1} v_i^2} \quad (3)$$

Where $T = \frac{k}{\sqrt{N}}$

The divisions and multiplications are reduced to one operation in Eq. (3) for each RMS voltage calculation. In this Eq. (3), T can be calculated offline.

The same above procedure is used for RMS current and energy calculations using Eq. (4) and Eq. (5), respectively.

$$I_{rms} = \sqrt{\frac{\sum_{i=0}^{N-1} i_i^2}{N}} \quad (4)$$

$$E = \frac{1}{fs} \sum_{i=0}^{N-1} v_i * i_i \,, \quad (5)$$

where fs is sampling frequency and i_i is i[th] sampled of the current.

The second part of the program represents subroutine for displaying where the parameters on the screen are updated every 1 sec.

The third part of program is responsible for measuring and correcting power factor of the load where the smart energy meter enters this subroutine every 3 seconds. The flowchart shown in **Fig.7** illustrates the operations of power factor correction.

The power factor (PF) of the load can be calculated by dividing the active power (P) by apparent power (S), when the PF of the load is equal to 0.9 or more, no need to add capacitors to the load, if the PF of the load is less than 0.9, the processing unit of PIC microcontroller calculates the desired capacitances to improve the power factor of the load.

The reactive power utilized in the load ($varL$) is calculated as:

$$var_L = \sqrt[2]{S^2 - P^2} \quad (6)$$

In order to improve PF to 0.95, new reactive power is calculated as:

$$var_a = P * \tan \hat{\Theta} \tag{7}$$

$\hat{\Theta}$: The phase angle between voltage and current that is chosen 18° for obtaining PF=0.95.

Now, the reactive power is required to compensate(var_c):

$$var_c = var_L - var_a \tag{8}$$

The required capacitors to improve power factor to be 0.95 is

$$C = \frac{var_c}{2\,\pi * f * (V_{rms})^2} \tag{9}$$

After calculating the required capacitances, the control unit sends control signal to the relay unit to connect the required capacitors.

The last part of the program is responsible for sending data to the billing center which is executed every month. The accumulated amount of consumed energy and the cost are delivered to the billing center.

During its operation, the smart energy meter checks whether there is a command message from the billing center that requests switching on or off the building as shown in flow chart of interrupt service routine in **Fig.6**.

In order to perform the functions of the smart energy meter, the control unit is programmed with MikroC PRO programming language.

5.2 Software of the Billing Center

The flowchart in **Fig.8** shows the methodology of performing billing center functions.

1. First the billing center enters the initialization routine, in which:

   - The transceiver communication module parameters are initialized.
   - Communication network is established.
   - Smart energy meters are joined to the network.

2. Second, after receiving the data, the billing center creates a table that stores the data and indicates the current status of the each consumer.

3. Third, the billing center sends command signal to the smart energy meter to reset energy counter.

4. Forth, the billing center checks the budget and the bill of the consumer, where it has ability to send a command to the smart energy meter for switching the power on or off at any time.

Any failure in communication between the billing center and the smart energy meter is unacknowledged and retransmitted. The programming language Visual C# is used to create a GUI for the billing center to facilitate the operation of the billing and controlling the status of the consumer, **Fig.9** shows the GUI for billing center. The table in the bottom left of the figure is related to the multi-tariff and the time zones, where the rectangles labeled "Currently" indicate the current time zone and tariff. The text boxes "Time zone" indicate the duration of the time zone, where all the four time zones, in this work, has the same period (6 hours). The text boxes "Price" indicate the price of consumed energy in the corresponding time zone. It must be mention that the price must be proportional to the energy demand.

6. MEASUREMENT ERRORS

Reducing the error to the minimum possible level in any measurement system is extremely important. Instrumental error is a common source of the measurement errors that are inherent in manufacture of an instrument. It arises due to the operation principle of instrument such that arises in the analog to digital convertor (ADC), **Morris, 2001**. The accuracy of ADC has an effect on overall measurement system performance and efficiency. Systematic errors arise in ADC due to the sampling operation, **STMicroelectronics, 2003**, the effect of sampling error (e_s) in power measurement is inversely proportional to the sampling frequency, sampling errors can be calculated as shown in the equation below, **Gerard, 1984**:

$$e_s = \frac{V_p\, I_p}{2N} \cdot \frac{\sin N\gamma}{\sin \gamma} \cos(N-1)\ \gamma \qquad (10)$$

Where $\gamma = \frac{2\pi f}{f_s}$,f_s: sampling frequency, f: power line frequency, γ:samples interval in radian, N : number of samples.

Quantization errors affect measurement accuracy in sampled-data-acquisition systems. Mean square value of error quantization is

$$e_{eq} == \frac{\Delta^2}{12} \qquad (11)$$

Where $\Delta = \frac{2V_p}{2^n}$, V_p is amplitude value of signal, n is number of bit, It is also known as successive approximation register.

And

$$e_{eq} = \frac{V_p^2}{3 * 2^{2n}} \qquad (12)$$

It is clear from the Eq. (12) that the error caused by quantization is reduced when the resolution of ADC (n) increases, **Istevan, 1985**. In this research the proposed smart energy meter: *fs* =500 Hz, N= 25, n = 10 bit. The accuracy is proportional to the number of taken energy samples per period, where a number of eight samples per period (*fs* =400) of the power line give a percentage of error of less than 1%. The total errors due to the sampling process and quantization can be calculated by adding the two errors together.

Limiting error is considered another type of measurement error that arises in electrical circuit due to the tolerance in the circuit components such as resistors, capacitors, etc. This error can be reduced by choosing components with low tolerance. For precise measurement systems, the error in passive components is compensated using calibration. Calibration here means applying a signal with a known value then adjusts the meter (resistors or parameters) until getting compatibility between the signal value and the meter's reading. This calibration may implemented by the hardware or software, **Microchip, 2005**.

The temperature coefficient of circuit components must be taken into account in the design and implementation of the smart energy meter, especially in the case of device works in extremely hot conditions, as in Iraq.

7. IMPLEMENTATION AND TESTING

Fig.10 shows the Proteus simulation of smart energy meter. Voltage and current sensor of smart energy meter are connected to the resistor and inductor load which are connected in series to measure all power parameters, and then trying to correct power factor by using capacitors bank.

The smart energy meter is tested in real scenarios by using real loads as shown in **Fig.11**, where the smart energy meter is connected to some of household appliance to test different cases of the loads, the accuracy of the smart energy meter readings were compared with the professional power clamp meter as shown in **Table 1**. The measurement values by analog unit are given to the PIC microcontroller, and then displaying on LCD screen. The readings that are displayed on LCD are compared with that are received in billing center. The connecting and disconnecting of smart energy meter to the wireless network is also checked.

8. CONCLUSIONS

The characteristics of the metering system are investigated and there are several facts that had become clear when testing overall implemented system. These facts are: firstly, implementation of smart metering system can be constructed in Iraq by using available local market components. Secondly, smart metering system can play an important role in increasing the consumers' awareness through displaying instantaneous power consumption and its cost. Moreover, the system can effectively improve power factor of electrical grid. Increasing consumers' awareness and improving power factor can effectively reduce wasted energy and consequently ensure reliable power supply. Thirdly, ability of real time calculating of the consumed energy and its cost enables implementing a multi tariff scheme. This scheme cannot be achieved in a traditional meter. Finally, the smart metering system can be effectively detect and locate irregularities on the electrical grid and a malfunction smart energy meter(s).

9. REFERENCES

- Anjana Shree M, Prasanna Vadana D, *2014, Smart Meter for Power Factor Enhancement in Real Time*. International Conference on Embedded Systems, IEEE, Vol.3, No.14.
- Alexandre José, 2007,*Homecap: Residential Power Factor Correction*, TDK EPCOS Worldwide Company, Peru, Application Note.
- Cao Liting, Tian Jingwen, And Zhang Dahang, 2006. *Networked Remote Meter-Reading System Based On Wireless Communication Technology*, International Conference on Information Acquisition, Shandong, China, IEEE, No. 6, pp. 172-176, August .
- Edwin Chobot, Daniel Newby, Renee Chandler, 2013. *Design And Implementation Of A Wireless Sensor And Actuator Network For Energy Measurement And Control At Home*.International Journal of Embedded Systems and Applications, Vol. 3, No. 1, pp. 1-15, March .
- Gerard N. Stenbakken, 1984. *Wideband Sampling Wattmeter*, IEEE, Vol. 103, No. 10, pp. 2919-2926, October .
- H. M. Zahid Iqbal, M. Waseem, 2014. *Automatic Energy Meter Reading using Smart Energy*, Conference paper, IEEE, Vol. 1, No. 11.
- Istevan Kollar, 1985.*Programming Error introduced by digital power/energy measurement*. International Journal of Technical University of Budapest, pp. 1-7.
- Libiao Qiao, Xiaojun Liu, 2011. *Design and Implementation of the Smart Meter in Vehicle-to-Grid*, ,International Conference on electric utility and power technology, IEEE, Vol. 2, No. 11, pp. 618-621, August .
- MD M RAHMAN, and AMANULLAH MTO, 2011. *Technologies Required for Efficient Operation of a Smart Meter Network*, Conference on industrial electronics and application, IEEE Vol.3, No.8, PP.125-130.
- Microcontroller Division Applications, 2003. U*NDERSTANDING AND MINIMISING ADC CONVERSION ERRORS*, STMicroelectronics Technology Inc., U.S.A., Application Note.
- Pedro Antmann, 2009. R*educing Technical And Non-Technical Losses In The Power Sector*, The Energy Unit Of The World Bank, Background Paper.
- Popa Mircea, 2011.*Smart Meters Reading Through Power Line Communications*, Journal Of Next Generation Information Technology, Vol. 2, No. 3, pp. 92-100, August.
- Reddy, Sreenadh,Soma Shekara Depuru, Lingfeng Wang, And Nikhil Gudi, 2011.*Smart Meters For Power Grid – Challenges,Issues, Advantages And Status*, ELSEVIER, No. 11, pp. 1-7.

- R. Barsoum Nader, 2007.*Programming of PIC Micro-Controller for Power Factor Correction,* In International Conference on Modeling & Simulation, Malaysia.
- Sai Kiran Ellenki 1 , Srikanth Reddy G 2014 . *An Advanced Smart Energy Metering System for Developing countries , International Journal Of Scientific Research And Education*, Vol. 2, No. 1, pp. 242-258.
- S., Morris Alan, 2001. *Measurement and Instrumentation Principles*, Third Edition Ed.: ELSEVIER.
- Sandip chattopadhyay, 2005. *Designing Energy Meters with the PIC16F873A*, Microchip Technology Inc., U.S.A., Application Note.
- Vivek A. Dongre And Prof. A P. Rathkanthiwar., 2014. *Zigbee And Gsm Based Wireless Meter With Tamper Detection And Control System*, International Journal of engineering research and application, International Conference on Industrial Automation and Computing (ICIAC-12-13th) pp. 37-48, April.

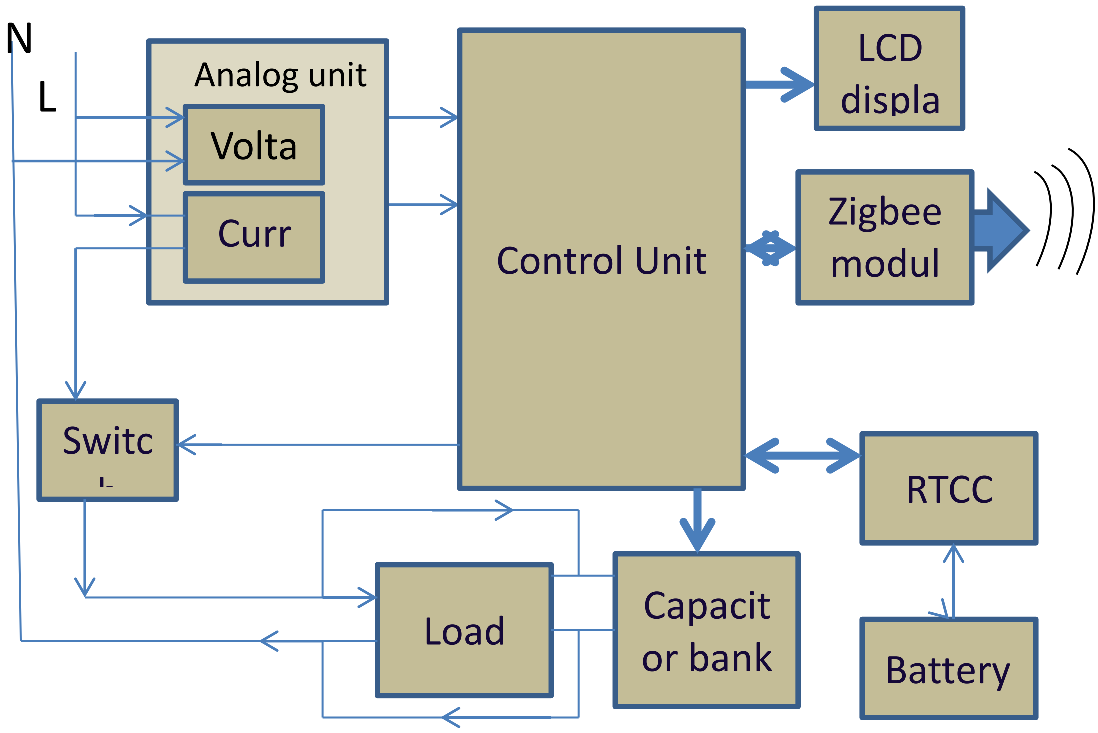

Figure 1. Block diagram of smart energy meter.

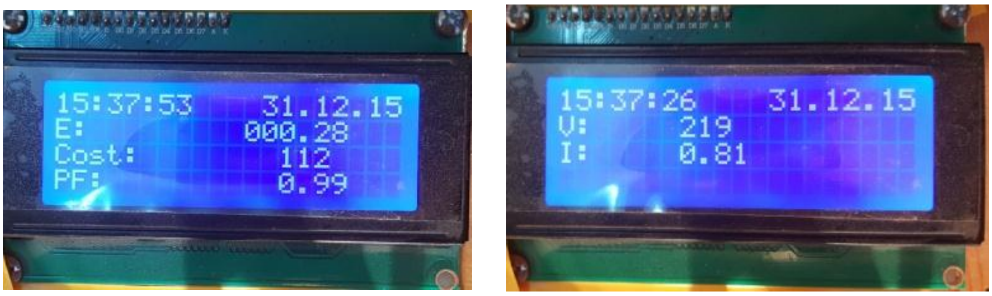

Figure 2. Two page of smart energy meter's LCD screen.

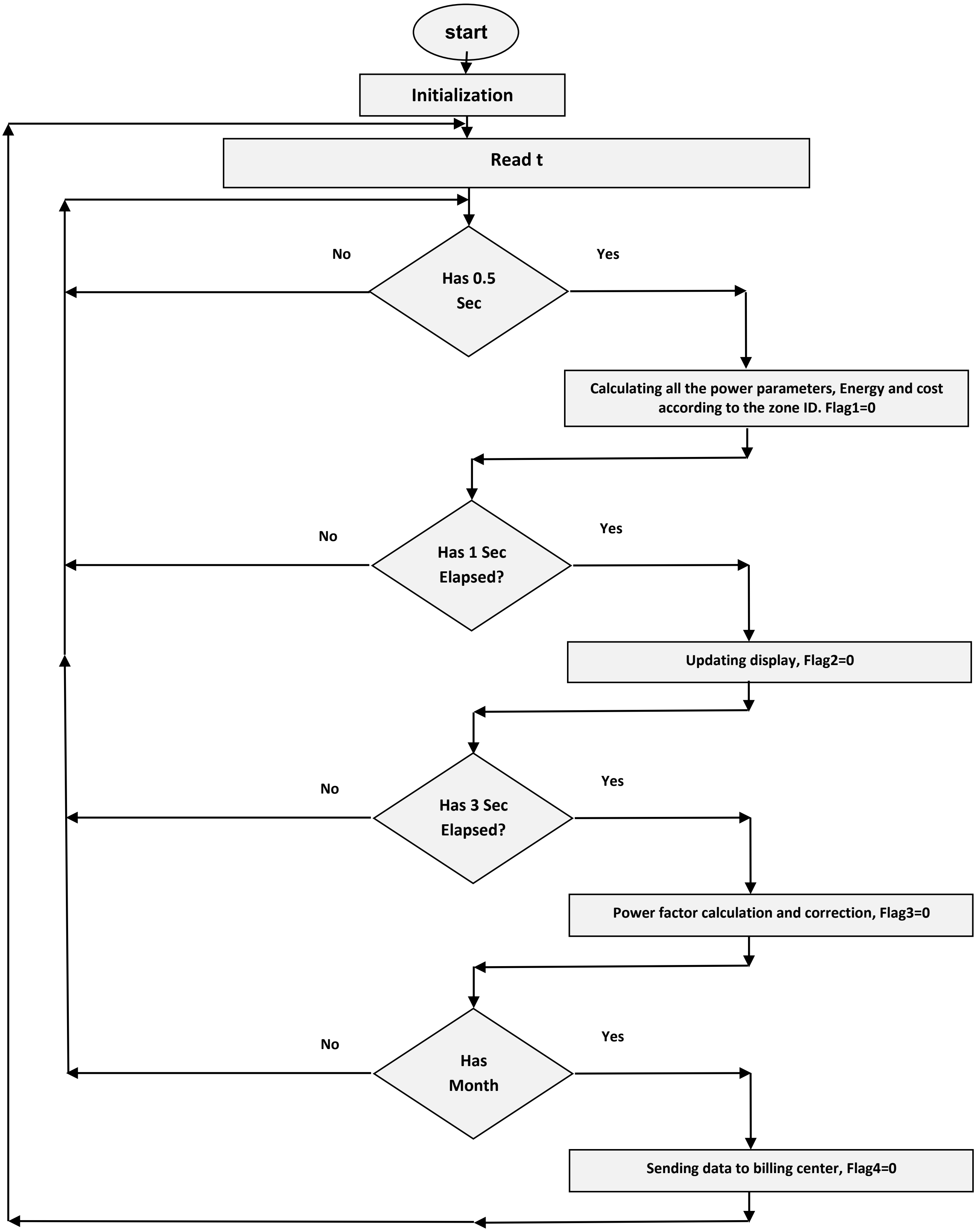

Figure 3. Flowchart of main program of smart energy meter.

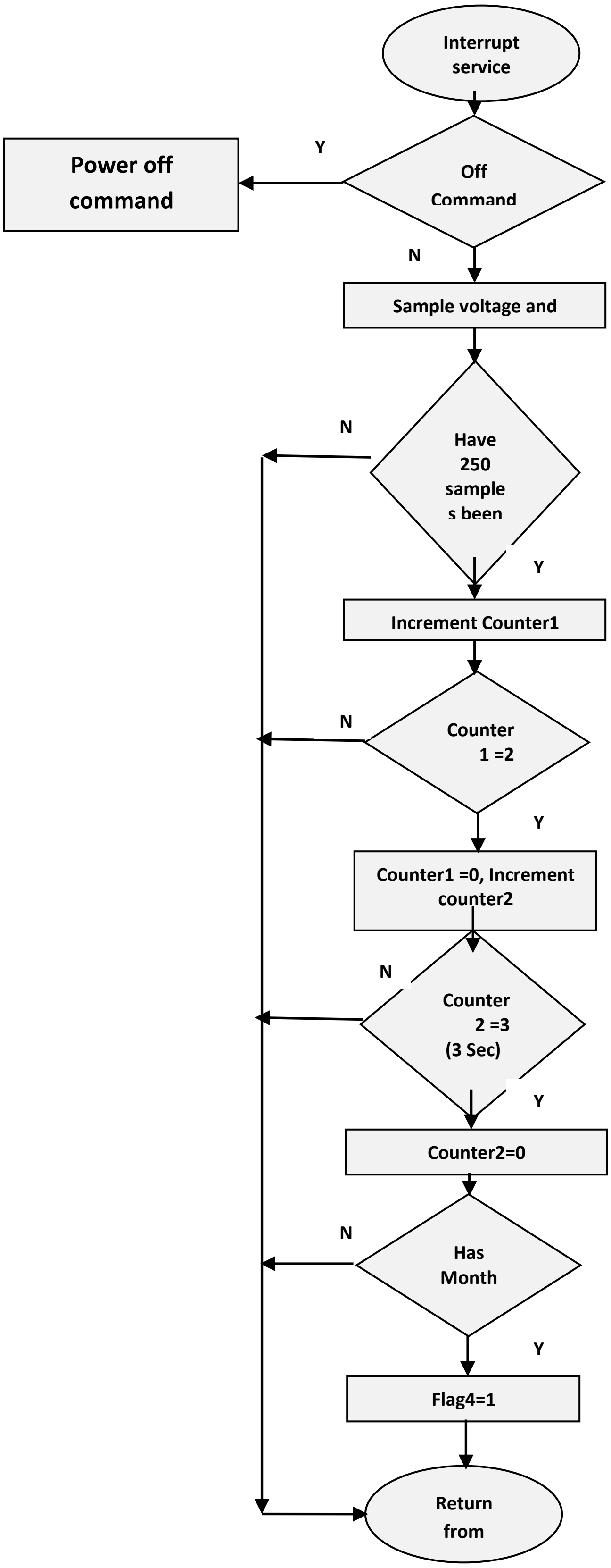

Figure 4. Flowchart of interrupt service routine.

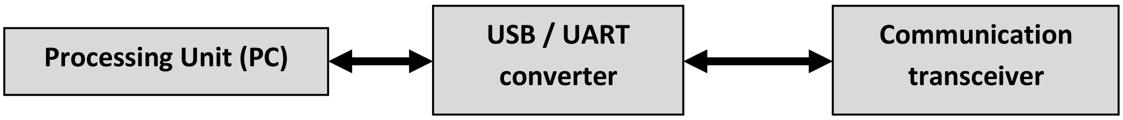

Figure 5. Block diagram of the billing center.

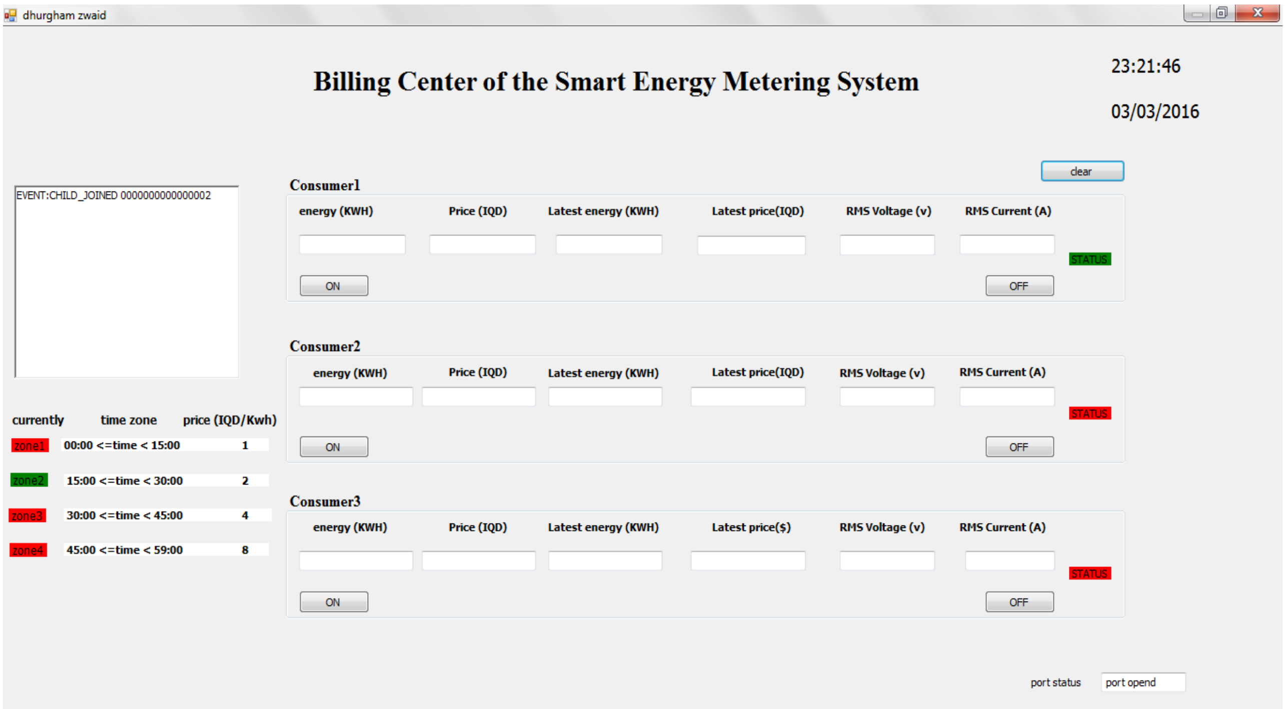

Figure 6. The GUI of the billing center.

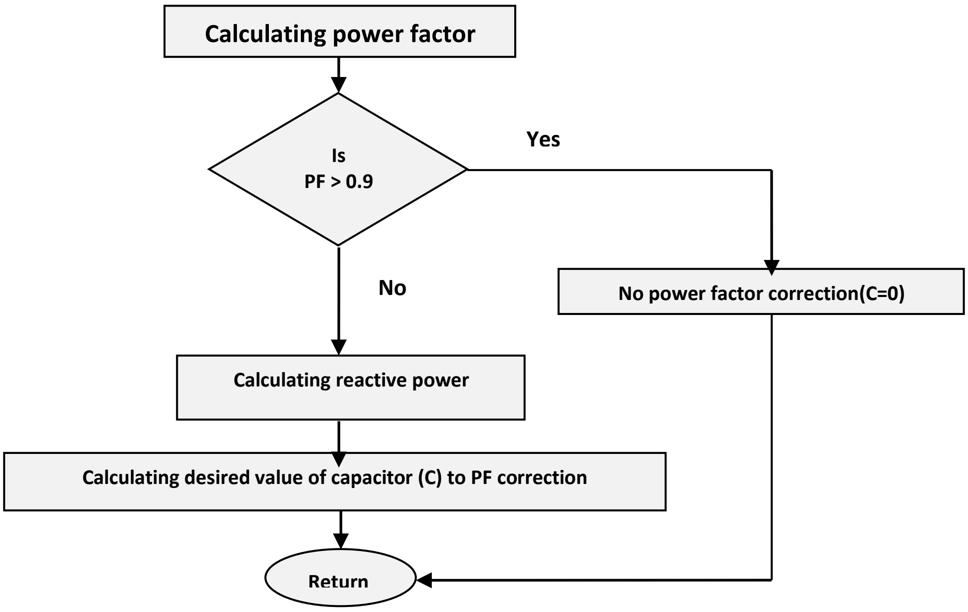

Figure 7. Flowchart of power factor correction.

Table 1. Smart energy meter readings comparing with professional power meter.

Type of load	Current (A)			active power (W)			Apparent power (VA)			Power Factor		
	Smart Meter reading	Professional Power meter	error (%)	Smart Meter reading	Professional Power meter	error (%)	Smart Meter reading	Professional Power meter	error (%)	Smart Meter reading	Professional Power meter	error (%)
Refrigerator	0.65	0.63	3	127	125	1.6	149	146	2	0.85	0.84	1.1
Water dispenser	0.87	0.9	3.3	116	113	2.6	199	200	0.5	0.59	0.56	5.3
One lamp 195 W	0.83	0.85	2	197	195	1	200	195	2.5	0.98	0.99	1
Two identical lamps 390 W	1.63	1.66	1.8	391	389	0.5	392	389	0.7	0.97	0.99	2

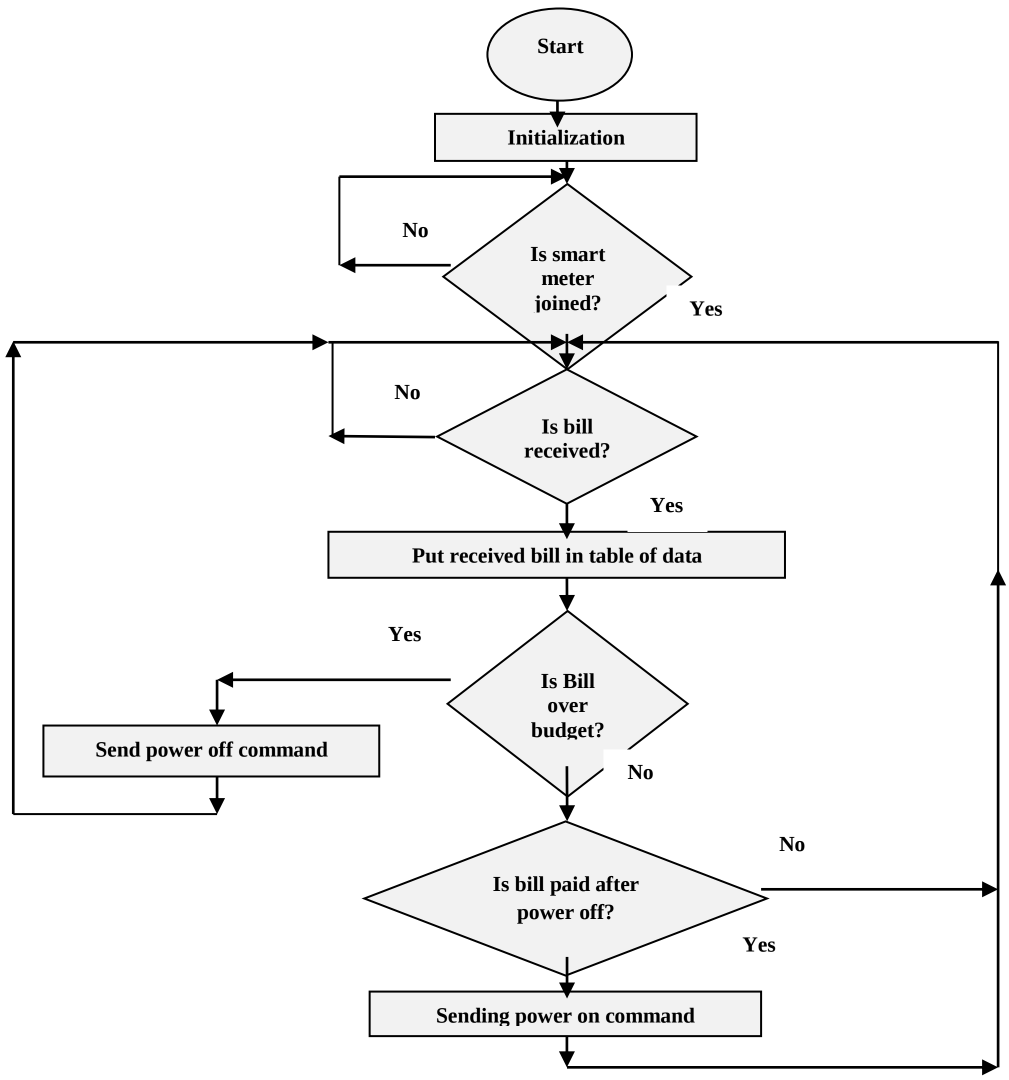

Figure 8. Flowchart of the billing center.

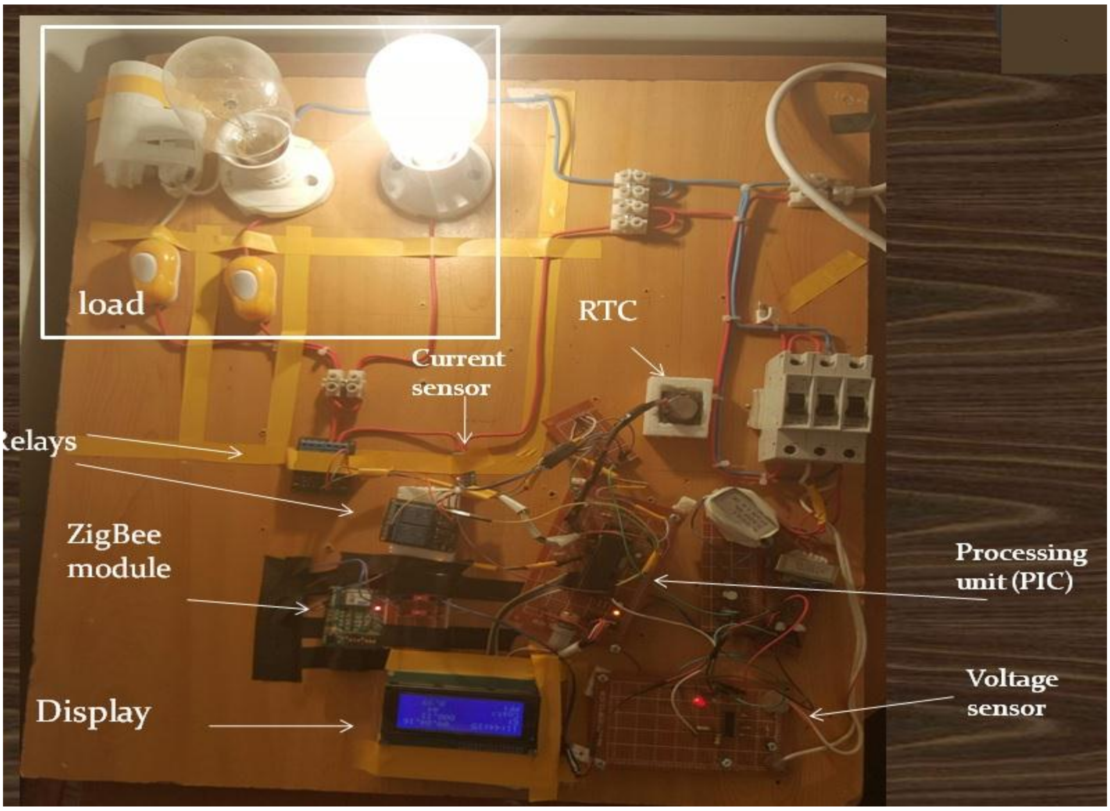

Figure 9. Implemented smart energy meter.

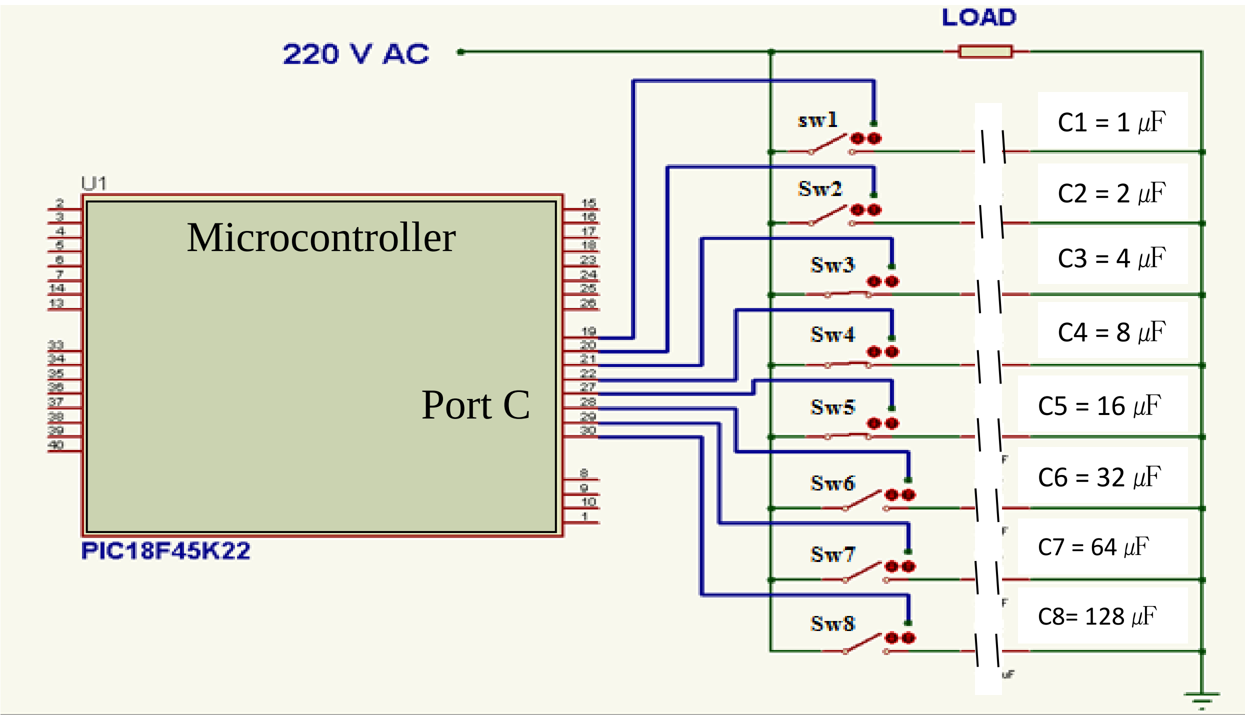

Figure 10. Connection capacitors bank to the controller unit.

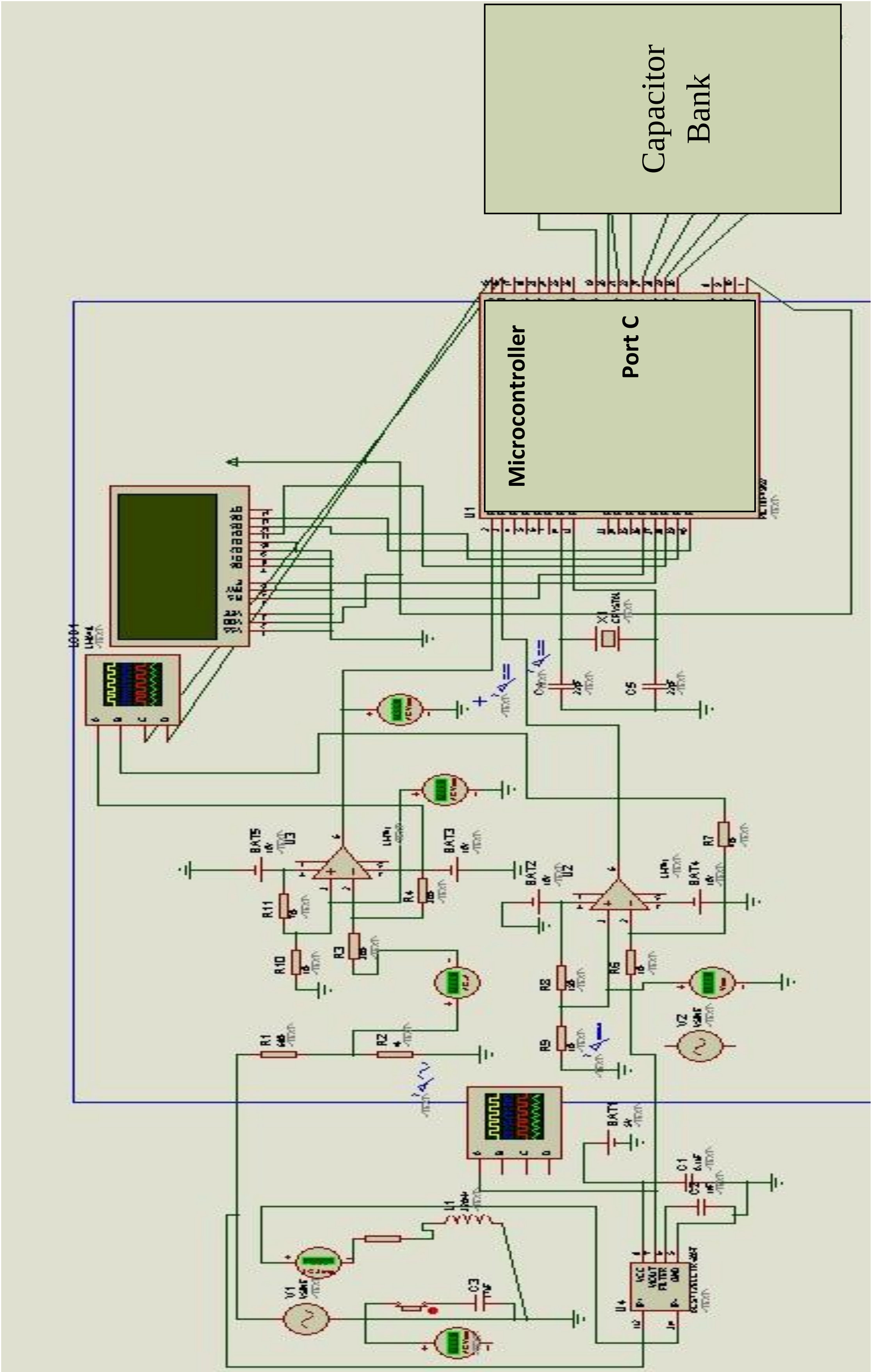

Figure 11. Proteus simulation of smart energy meter.

Composite Techniques Based Color Image Compression

Zainab Ibrahim Abood
Instructor
Engineering College-Baghdad University
Email:zainab2012254@yahoo.com

ABSTRACT

Compression for color image is now necessary for transmission and storage in the data bases since the color gives a pleasing nature and natural for any object, so three composite techniques based color image compression is implemented to achieve image with high compression, no loss in original image, better performance and good image quality. These techniques are composite stationary wavelet technique (S), composite wavelet technique (W) and composite multi-wavelet technique (M). For the high energy sub-band of the 3rd level of each composite transform in each composite technique, the compression parameters are calculated. The best composite transform among the 27 types is the three levels of multi-wavelet transform (MMM) in M technique which has the highest values of energy (En) and compression ratio (CR) and least values of bit per pixel (bpp), time (T) and rate distortion (R(D)). Also the values of the compression parameters of the color image are nearly the same as the average values of the compression parameters of the three bands of the same image.

Key words: image compression, color images, composite techniques, composite transforms, compression parameters.

التقنيات المركبة المستندة على ضغط الصورة الملونة

زينب ابراهيم عبود
مدرس
كلية الهندسة- جامعة بغداد

الخلاصة

ضغط الصورة الملونة حاليا ضروري للنقل والتخزين في قواعد البيانات حيث ان اللون يوحي الى الطبيعة السارة والطبيعية لأي جسم. لذلك ثلاث تقنيات مركبة مستندة على ضغط الصورة الملونة تم تنفيذها للحصول على ضغط أعلى، عدم فقدان معلومات من الصورة الاصلية، أداء أفضل والحصول على الجودة في الصورة. هذه التقنيات هي تقنية المويجات الثابتة المركبة (S)، تقنية المويجات المركبة (W) وتقنية المويجات المتعددة المركبة (M). تم حساب معاملات الضغط للجزء العالي الطاقة للمستوى الثالث لكل تحويل مركب في التقنية المركبة. التحويل المركب الافضل من بين 27 نوع هو المستويات الثلاثة لتحويل المويجات المتعددة (MMM) في تقنية M والتي فيها قيمة الطاقة (En)ونسبة الضغط (CR) أعلى القيم وعدد ال bit per pixel (bpp) والوقت (T) ومعدل التشويه ((R(D)) أقل القيم. كذلك قيم معاملات الضغط للصورة الملونة تقريبا مساوية لمعدل قيم معاملات الضغط للحزم الثلاثة لنفس الصورة.

الكلمات الرئيسية: ضغط الصورة، الصور الملونة، التقنيات المركبة، التحويلات المركبة، معاملات الضغط.

1. INTRODUCTION

In the color image, the spatial component correlation among the three bands red, green, and blue is significant. In order to get a good compression performance, the correlation among the three bands must be reduced by converting the color image into the de-correlated color space, **Miry, 2009**.

For three different kinds of images, standard Lena, satellite urban and satellite rural image, various statistical parameters of the image such as Rate Distortion, Kurtosis, symmetry and Skewness, are derived for Set Partitioning in Hierarchical Trees (SPIHT) compression scheme, they are derived for a fixed level and fixed rate of decomposition for the three kinds of images and they are used for explanation of the Peak Signal to Noise Ratio (PSNR) and Compression Ratio (CR). The results of urban images are the best for SPIHT compression scheme as compared with the satellite rural image, **Nagamani, and Ananth, 2012**. **Abood, 2013** introduced three dimension two level, wavelet transform, multi-wavelet transform and hybrid (wavelet-multi-wavelet) techniques. The parameters root-mean-square difference, energy retained, Peak Signal to Noise Ratio, entropy and compression ratio are measured for each 3-D two-level technique. According to these parameters, a comparison between these techniques is presented and the results illustrated that the three dimension two level hybrid technique is the best for image compression.

Dhumal and Deshmukh presented image compression technique using Singular Value Decomposition (SVD) transform. This (SVD) can transform the matrix into product, which allows anyone to refactor the digital image into three orthogonal matrices. The using of the singular values of the refactoring allows representing any image with a set of decreased values, which can store the original image useful features, take less storage space in the memory, so it is used for image compression, **Dhumal and Deshmukh, 2016**. **Sudhakar, and Sudha, 2011** introduced an efficient color compression technique i.e. higher compression ratio and better quality by using multi-wavelet transform and the embedded coding of the multi-wavelet coefficients through (SPIHT) algorithm.

2. COLOR IMAGE COMPRESSION

Images use either 24-bit or 8-bit color. In the case of 8-bit, the range of the pixel value is 0-255 (i.e. 256 different colors). In the case of 24-bit, each pixel in the image uses 24-bit and each 8-bit in the 24-bit is used to represent three band colors red, green and blue (R, G, B).

For Images compression, the needing for efficient techniques is usually increasing because the images need large size of disk space so it is a big disadvantage during storage and transmission, **Dutta, et al., 2012**.

3. COMPRESSION PARAMETERS

3.1 Bit per Pixel (bpp)

The precision of a sample can be represented by a number of bits in the pixel; the higher precision value is better which represents the picture quality. Here the compression ratio is measured in terms of the bpp, **Dutta, et al., 2012**.

$$bpp = \frac{8 \times compressed\ image\ size}{original\ image\ size} \tag{1}$$

3.2 Computation Time (T)

The computation time is normalized and calculated by:

$$T = \frac{2}{3}\,(1 - 4^{-L})\,N^2 \tag{2}$$

where N ^{2} is the size of the image, and L is the number of the level, **Dia, et al., 2009**.

3.3 Energy (En)

Energy is the sum of squared elements in the image, **Abood, et al., 2013**:

$$En = \sum_i \sum_j x^2\,(i, j) \tag{3}$$

3.4 Compression ratio (CR)

A logical way to measure how good the compression algorithm compresses an image is to look at the compression ratio which is the ratio of the number of bits that required to represent the image before compression to the number of bits that required to represent the image after compression, **Sayood, 2006**, so the ratio between the size before compression and the size after compression, **Shini, et al., 2016**:

$$CR = \frac{size\ befor\ compression}{size\ after\ compression} \tag{4}$$

3.5 Mean Absolute Error (MAE)

If $x(i,j)$ is the original image and $y(i,j)$ is the reconstructed image, then the Mean Absolute Error will be, **Kumar, and Rattan, 2012**:

$$MAE = \frac{1}{N^2}\sum_{I=1}^{N}\sum_{j=1}^{N}\left|(x(i,j) - y(i,j))\right| \tag{5}$$

3.6 Rate Distortion R (D)

Rate is the average number of the bits used in representing each sample value. Distortion is the measure of a difference between original image and compressed image. R (D) function is the lowest rate that while keeping the distortion equal to or less than D, the output can be encoded.

$$R(D) = \frac{1}{2} \times log_{10}\left(\frac{\sigma^2}{MSE}\right) \tag{6}$$

where (σ^2) represents the Variance, **Nagamani, and Ananth, 2012**, and

$$MSE = \frac{1}{N^2}\sum_{I=1}^{N}\sum_{j=1}^{N}(x(i,j) - c(i,j))^2 \tag{7}$$

where $c(i,j)$ represents the compressed image, **Abood, 2013**.

4. TRANSFORMATION

In image compression, it is desirable to select the useful transform that reduces the size of resultant image as compared to the original image, **Kharate, and Patil, 2010**. If the sampled functions have discrete time and frequency then wavelet transform used is so called Discrete Wavelet Transform (DWT). This technique is based on sub-band coding algorithm. Compression is based on the approximation of regular signal components using the filter coefficients and detailed coefficients, **Hamsalakshmi, and Kalaivani, 2016**.

Stationary wavelet transform (SWT) is designed to overcome the lack of the translation-invariance of the DWT. The SWT is a redundant scheme, as its output in each level contains a similar number of samples as in the input, **Saminu, and Özkurt, 2015**.

Algorithms based on the wavelets have been worked well in the image compression. Scalar wavelets don't possess all properties wanted for a better performance in the compression but 'Multi-wavelet' overcomes this problem because it possesses multi-filters, **Radhakrishnan, and Subramaniam, 2008**. Theoretically, Multi-wavelets should work even better because of the extra freedom in the multi-filters' design, **Miry, 2008**.

5. THE PROPOSED ALGORITHM

Fig. 1 shows the block diagram of the overall proposed system, which is illustrated as follows:

1. Input color image, in the other side input the same color image but with isolated bands i.e. taking the red, green and blue bands of the same color image.
2. Convert the color image, red, green and blue bands to gray image.
3. As a preprocessing, convert each gray image to a double-precision and resize them to be of size (1024*1024).
4. Input the processed images to three composite techniques S, W and M as shown in **Fig. 2**.

There are " 3^n " different cases, where " 3 " refers to 3-level composite stationary wavelet transform (s), 3-level composite wavelet transform (w), and 3-level composite multi-wavelet transform (M), while " n " refers to the number of level. The three composite techniques are:

a. Composite technique S, which contain (3^{n-1}) different cases of a 3-level composite transform of s, w and M, i.e. sss, ssw, ssM, sws, sww, swM, sMs, sMw and sMw. For example, in swM, the 1st level is "s", the 2nd level is "w" and the 3rd level is "M". Wavelet transform is applied to the high energy sub-band of "s" and multi-wavelet transform is applied to the high energy sub-band of "w".

b. Composite technique W, which contain (3^{n-1}) different cases of a 3-level composite transform of w, s and M, i.e. www, wws, wwM, wsw, wss, wsM, wMw, wMs and sMM. For example, in wsM, the 1st level is "w", the 2nd level is "s"and the 3rd level is "M". Stationary wavelet transform is applied to the high energy sub-band of "w" and multi-wavelet transform is applied to the high energy sub-band of "s".

c. Composite technique M, which contain (3^{n-1}) different cases of a 3-level composite transform of M, s and w, i.e. MMM, MMs, MMw, MsM, Mss, Msw, MwM, Mws and Mww. For example, in Msw, the 1st level is "M", the 2nd level is "s" and the 3rd level is "w". Stationary wavelet transform is applied to the high energy sub-band of "M" and wavelet transform is applied to the high energy sub-band of "s".

5. For each high energy sub-band of the 3rd level in each composite technique, the compression parameters are calculated according to Eq's.1, 2, 3, 4, 5 and 6.
6. The final decision is taken for the techniques that have best compression.

6. RESULTS AND DISCUSSION

In all tables, the best values are written as red values and the suffix " av " in S_{av}, W_{av} and M_{av} refers to the average of parameters' measurements of the images in the composite S, W and M techniques respectively. Table 1 shows the results of the compression parameters for the color images in the S composite technique, the sMM composite technique has the least values of Bpp, T (in second) and R(D), and has the highest values of En and CR, while ssM has the least value of MAE (3.7004 e-16). **Fig. 3** illustrates the chart of these results.

Table 2 shows the results of the compression parameters for the color images in the W_{av} composite technique, the wMM composite technique has the least values of Bpp, T and R(D) (0.0078, 0.0006, 4.5269) respectively, and has the highest values of En and CR (5.247 and 1024) respectively, while www has the least value of MAE (2.8291 e-16). **Fig. 4** illustrates the chart of these results.

Table 3 shows the results of the compression parameters for the color images in the composite M_{av} technique, the MMM composite technique has the least values of Bpp (0.0020), T (0.0001) and R(D) (2.7253), has the highest values of En (41.6531) and CR (4096), while Mww has the least value of MAE (0.6679e-15). **Fig. 5** illustrates the chart of these results.

Therefore, using multi-wavelet in the image compression improves the image reconstruction, image compression and decrease the computation time, so, for good compression in the color image the composite techniques sMM, wMM and MMM must be used.

Tables 4, 5 and 6 show the results of the compression parameters for the color (red, green and blue bands) images in the S_{av} composite technique, where RS_{av}, GS_{av} and BS_{av} refer to the average of parameters' measurements of the images in the red, green and blow bands of S technique, all bands have the same bpp, T and CR in each composite technique (i.e., in RS_{av}, GS_{av} and BS_{av}, sss has bpp (8), T (0.6562) and CR (1)). The sMM composite technique has the least values of bpp, T and R, and has the highest values of En and CR, while ssM has the least value of MAE (3.7122e-16). **Fig. 6** illustrates the chart of the compression parameters for the color (red-band) images in the S_{av} composite technique.

Tables 7, 8 and 9 show the results of the compression parameters for the color (red, green and blue bands) images in the W_{av} composite technique, all bands have the same bpp, T and CR in each composite technique (i.e., in RW_{av}, GW_{av} and BW_{av}, www has bpp (0.1250), T (0.0102) and CR (64). The wMM composite technique has the least values of bpp, T and R(D), and has the highest values of En and CR, while www has the least value of MAE (2.0579e-16). **Fig's. 7 and 8** illustrate the charts of the compression parameters for the color (red and blue bands) images in the W_{av} composite technique.

Table 10, 11 and 12 show the results of compression parameters for the color (red, green and blue bands) images in the M_{av} composite technique, all bands have the same bpp, T and CR in each composite technique (i.e., in RM_{av}, GM_{av} and BM_{av}, Mww has bpp (0.0313), T (0.0025) and CR=256). The MMM composite technique has the least values of bpp, T and R, and has the highest values of En and CR, while Mww has the least value of MAE (5.764e-16). **Fig's. 9, 10 and 11** illustrate the charts of the compression parameters for the color (red, green and blue bands) images in the M_{av} composite Technique.

Therefore, for good compression in the color image of isolated bands the composite techniques sMM, wMM and MMM must be used, so for either color image or color image of isolated bands the composite techniques sMM, wMM and MMM can be used for good compression.

Fig. 12 shows samples of database images used in this work.

7. CONCLUSIONS

In this study, three composite techniques S, W and M based color image compression is implemented. For color image and color image of isolated bands the best composite technique among the 27 types is the MMM in M technique which has the highest values of En and CR which are 41.6531 and 4096 respectively, and least values of bpp, T and R(D) which are 0.002, 0.0001 and 2.7253 respectively for color image. Also it is concluded that the values of the compression parameters of the color image are nearly the same as the average values of the compression parameters of the three bands of the same image.

This work is useful to achieve image with high compression, no loss in original image, better performance and good image quality. As future works, one can use these composite techniques in speech compression, speech recognition and image recognition to show which technique is the best that gives a high speech compression performance, speech recognition performance and image recognition performance.

8. REFERENCES

- Abood, Z. I., 2013, *Image Compression Using 3-D Two-Level Techniques*, Journal of Engineering, Vol. 19, No. 11, PP. 1407-1424.

- Abood, Z. I., Muhsin, I. J., and Tawfiq, N. J., 2013, *Content-based Image Retrieval (CBIR) using Hybrid Technique*, International Journal of Computer Applications, Vol. 83, No 12, PP. 17-24.

- Dhumal, P., and Deshmukh, S. S., 2016, *Survey on Comparative Analysis of Various Image Compression Algorithms with Singular Value Decomposition*, International Journal of Computer Applications, Vol. 133, No. 6, PP. 18-21.

- Dia, D., Zeghid, M., Saidani, T., Atri, M., Bouallegue, B., Machhout, M., and Tourki, R., 2009, *Multi-level Discrete Wavelet Transform Architecture Design*, Proceedings of the World Congress on Engineering, Vol.1, PP. 1-5.

- Dutta, S., Abhinav, A., Dutta, P., Kumar, P., and Halder, A., 2012, *An Efficient Image Compression Algorithm Based on Histogram Based Block Optimization and Arithmetic Coding*, International Journal of Computer Theory and Engineering, Vol. 4, No. 6, PP. 954-957.

- Hamsalakshmi, C., and Kalaivani, R., 2016, *Analysis of Wavelets Based Compression in 1D Signals, 2D and 3D Images*, International Journal of Engineering Research & Science, Vol. 2, Issue 3, PP. 92-97.

- Kharate, G. K., and Patil V.H., 2010, *Color Image Compression Based On Wavelet Packet Best Tree*, International Journal of Computer Science Issues, Vol. 7, Issue 2, No 3, PP. 31-35.

- Kumar, R., and Rattan M., 2012, *Analysis Of Various Quality Metrics for Medical Image Processing* Research, International Journal of Advanced Research in Computer Science and Software Engineering, Vol. 2, Issue 11, PP. 137-144.

- Miry, A. H., 2008, *Multiwavelet and Estimation by Interpolation Analysis Based Hybrid Color Image Compression*, Al-Khwarizmi Engineering Journal, Vol. 4, No. 3, PP. 138-145.

- Nagamani, K., and Ananth, A. G., 2012, *Evaluation of SPIHT Compression Scheme for Satellite Imageries Based on Statistical Parameters*, International Journal of Soft Computing and Engineering, Vol. 2, Issue 2, PP. 127-130.

- Radhakrishnan, S., and Subramaniam, J., 2008, *Novel Image Compression Using Multi-wavelets with SPECK Algorithm*, International Arab Journal of Information Technology, Vol. 5, No. 1, PP. 45-51.

- Sayood k., 2006, *Introduction to Data Compression*, Book, Third Edition, PP 5.

- Saminu, S., and Özkurt, N., 2015, *Stationary Wavelet Transform and Entropy-Based Features for ECG Beat Classification*, International Journal of Research Studies in Science, Engineering and Technology, Vol. 2, Issue 7, PP 23-32.

- Shini, A. H., Abood, Z. I., and Ismaeel, T. Z., 2016, *Hybrid Techniques based Speech Recognition, International Journal of Computer Applications*, Vol. 139, No. 10, PP. 12-18.
- Sudhakar, R., and Sudha, V. K., 2011, *Color Image Compression Using Multi-wavelets with Modified SPIHT Algorithm*, IEEE, PP. 216-222.

9. NOMENCLATURE

bpp	bit per pixel
c(i, j)	compressed image
CR	compression ratio
DWT	discrete wavelet transform
En	energy
L	number of the level
M	composite multi-wavelet technique
M_{av}	average of parameters measurements of the images in the composite M technique
MMM	three level of multi-wavelet transform
N^2	size of the image
PSNR	peak signal to noise ratio
R(D)	rate distortion
R, G, and B	three band colors red, green and blue
S	composite stationary wavelet technique
S_{av}	average of parameters measurements of the images in the composite S technique
SPIHT	Set Partitioning in Hierarchical Trees

SVD	singular value decomposition
SWT	stationary wavelet transform
T	time in second
σ^2	variance
W	composite wavelet technique
W_{av}	average of parameters measurements of the images in the composite W technique
$x(i, j)$	original image
$y(i, j)$	reconstructed image

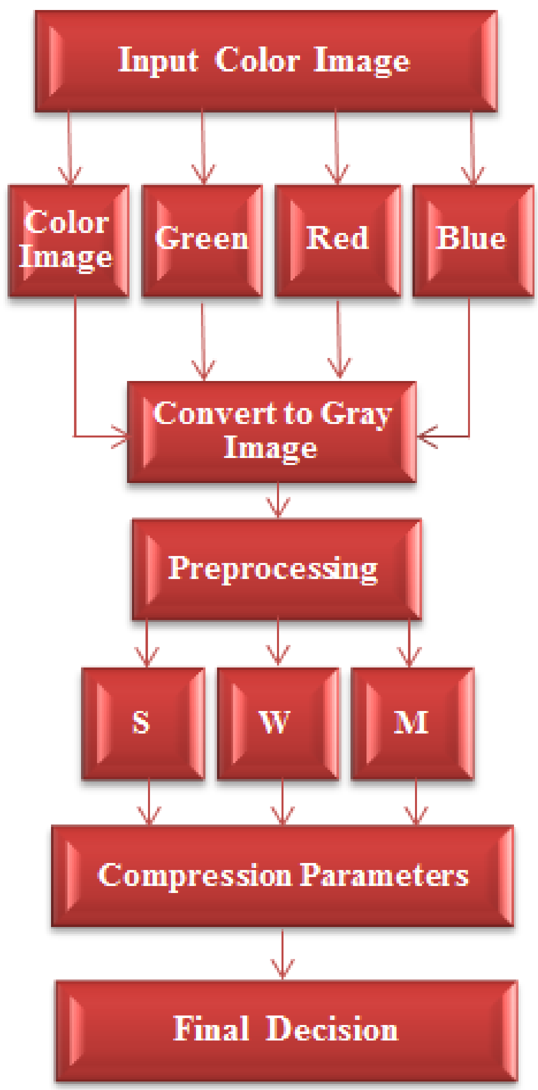

Figure 1. Block diagram the proposed system**.**

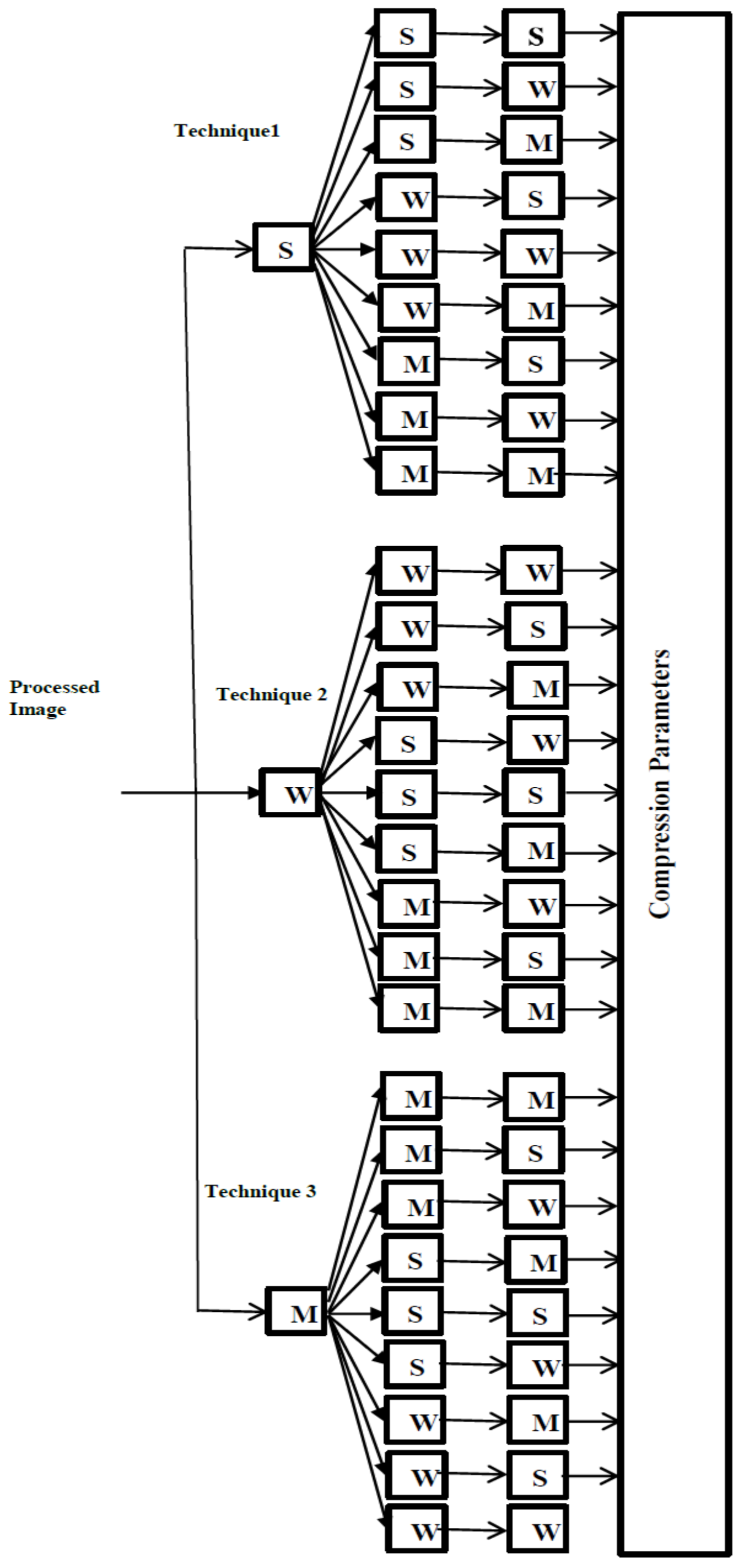

Figure 2. Three composite techniques S, W and M.

Table 1. Compression parameters for color S_{av} technique.

S_{av}	Bpp	T	En	CR	MAE	R(D)
SSS	8.0000	0.6562	0.0104	1	3.6349 e-08	46.9122
SSW	2.0000	0.164	0.0418	4	4.3843 e-16	29.77
SSM	0.5000	0.041	0.1668	16	3.7004 e-16	19.1907
SWS	2.0000	0.164	0.0209	4	7.4415 e-08	29.9228
SWW	0.5000	0.041	0.0418	16	4.4821 e-16	18.74355
SWM	0.1250	0.0102	0.8333	64	3.9505 e-16	11.9701
SMS	0.5000	0.041	0.1668	16	1.5224 e-07	19.4199
SMW	0.1250	0.0102	0.3336	64	8.9287 e-16	12.0112
SMM	0.0313	0.0025	2.6671	256	8.3379 e-16	7.481

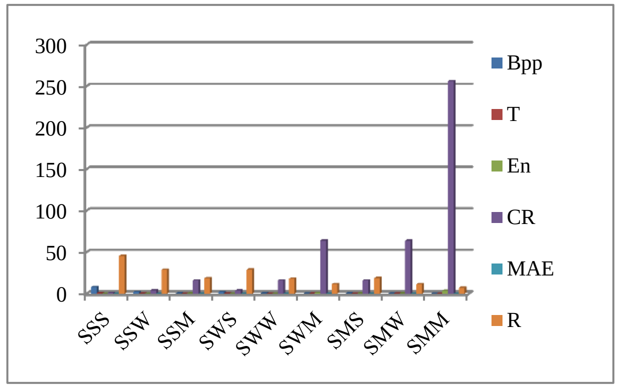

Figure 3. Chart of compression parameters for color S_{av} technique**.**

Table 2. Compression parameters for color W_{av} Technique.

W_{av}	bpp	T	En	CR	MAE	R(D)
WWW	0.1250	0.0102	0.0835	64	2.8291 e-16	11.6792
WWS	0.5000	0.041	0.0417	16	8.0035 e-08	18.9526
WWM	0.0313	0.0025	0.6676	256	4.0864 e-16	7.3689
WSW	0.5000	0.041	0.0417	16	4.453 e-16	18.8101
WSS	2.0000	0.164	0.0209	4	7.2764 e-08	30.0081
WSM	0.1250	0.0102	0.3331	64	4.4041 e-16	11.9957
WMW	0.0313	0.0025	0.6663	256	6.6639 e-16	7.3927
WMS	0.1250	0.0102	0.3329	64	1.5659 e-07	12.2132
WMM	0.0078	0.0006	5.247	1024	8.8067 e-16	4.5269

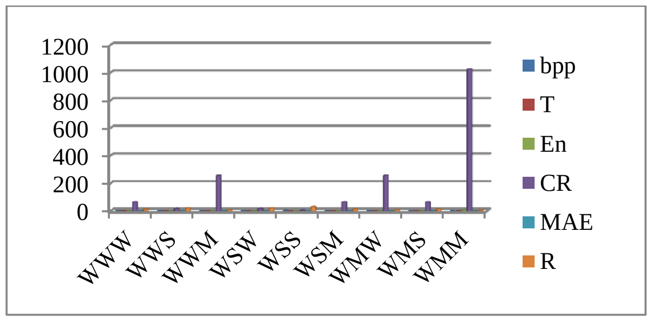

Figure 4. Chart of compression parameters for color W_{av} Technique.

Table 3. Compression parameters for color M_{av} Technique.

M_{av}	bpp	T	En	CR	MAE	R(D)
MMM	0.0020	0.0001	41.6531	4096	1.7564 e-15	2.7253
MMS	0.0313	0.0025	2.6599	256	3.1418 e-07	7.7415
MMW	0.0078	0.0006	5.3211	1024	1.7487e-15	4.5744
MSM	0.0313	0.0025	2.6618	256	0.8773e-15	7.5056
MSS	0.5000	0.041	0.1668	16	1.4258e-07	19.5198
MSW	0.1250	0.0102	0.3336	64	1.038e-15	12.0967
MWM	0.0078	0.0006	5.2578	1024	0.8868e-15	9.0584
MWS	0.1250	0.0102	0.6667	64	1.5535e-07	12.2269
MWW	0.0313	0.0025	1.3342	256	0.6679e-15	7.4038

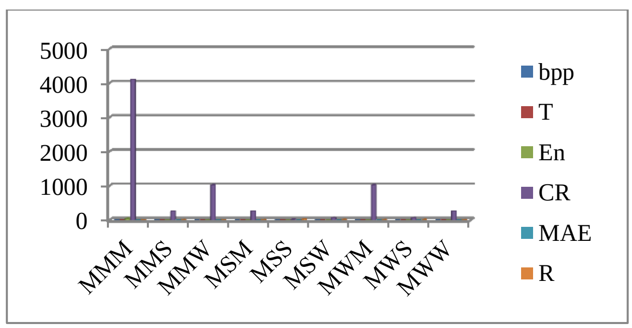

Figure 5. Chart of compression parameters for color M_{av} technique.

Table 4. Compression parameters for color RS_{av} technique.

RS_{av}	Bpp	T	En	CR	MAE	R(D)
SSS	8.0000	0.6562	0.0139	1	2.6766e-08	45.6397
SSW	2.0000	0.164	0.0278	4	4.9682e-16	28.8685
SSM	0.5000	0.041	0.4444	16	3.7122e-16	18.5319
SWS	2.0000	0.164	0.0278	4	1.7694e-07	28.9787
SWW	0.5000	0.041	0.0556	16	5.0499e-16	18.0765
SWM	0.1250	0.164	0.8867	64	4.0739e-16	11.4774
SMS	0.5000	0.041	0.2218	16	1.7711e-07	18.7105
SMW	0.1250	0.164	0.4439	64	10.028e-16	11.5127
SMM	0.0313	0.0025	3.5285	256	8.8049e-16	7.1199

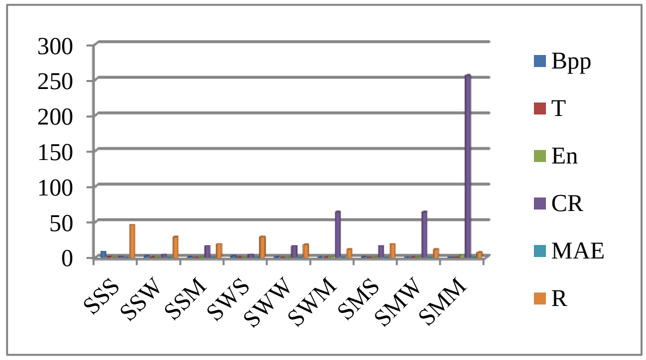

Figure 6. Chart of compression parameters for color RS_{av} technique.

Table 5. Compression parameters for color GS_{av} Technique.

BS_{av}	Bpp	T	En	CR	MAE	R(D)
SSS	8.0000	0.6562	0.0077	1	2.4355 e-08	43.5858
SSW	2.0000	0.164	0.0154	4	4.109 e-16	27.4134
SSM	0.5000	0.041	0.1233	16	3.139 e-16	17.5073
SWS	2.0000	0.164	0.0291	4	7.3346 e-08	27.5322
SWW	0.5000	0.041	0.0308	16	4.182 e-16	17.053
SWM	0.1250	0.164	0.2464	64	3.4341 e-16	10.7557
SMS	0.5000	0.041	0.1232	16	1.4695 e-07	17.6896
SMW	0.1250	0.164	0.2465	64	8.3144 e-16	10.7892
SMM	0.0313	0.0025	1.9658	256	7.3989 e-16	6.6005

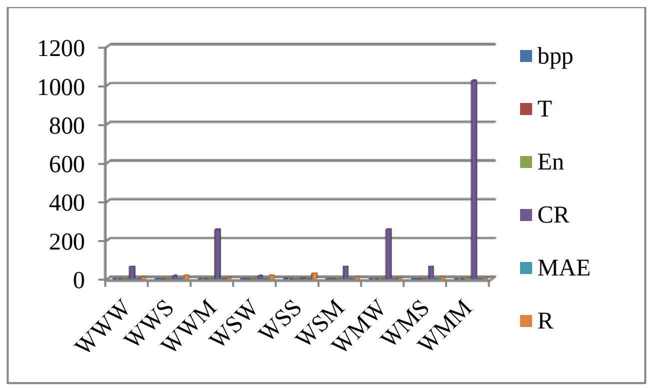

Figure7. Chart of compression parameters for color RW_a Technique.

Table 6. Compression parameters for color BS_{av} Technique.

GS_{av}	Bpp	T	En	CR	MAE	R(D)
SSS	8.0000	0.6562	0.0109	1	3.5877 e-08	46.2749
SSW	2.0000	0.164	0.0219	4	4.6147 e-16	29.3214
SSM	0.5000	0.041	0.1753	16	3.7439 e-16	18.9114
SWS	2.0000	0.164	0.0219	4	8.1965 e-08	29.5521
SWW	0.5000	0.041	0.0439	16	4.7271 e-16	18.4816
SWM	0.1250	0.164	0.3503	64	4.0381 e-16	11.829
SMS	0.5000	0.041	0.1752	16	1.649 e-07	19.2451
SMW	0.1250	0.164	0.3506	64	9.3767 e-16	11.8875
SMM	0.0313	0.0025	2.8057	256	8.4953 e-16	7.4211

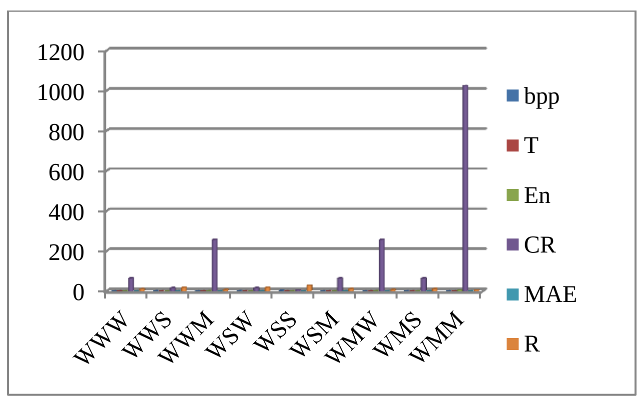

Figure 8. Chart of compression parameters for color BW_{av} technique.

Table 7. Compression parameters for color RW_{av} Technique.

RW_{av}	bpp	T	En	CR	MAE	R(D)
WWW	0.1250	0.0102	0.0978	64	2.0579e-16	11.1799
WWS	0.5000	0.041	0.0489	16	0.8846e-07	18.2415
WWM	0.0313	0.0025	0.7809	256	4.2887e-16	7.0084
WSW	0.5000	0.041	0.0489	16	5.0518e-16	18.127
WSS	2.0000	0.164	0.0244	4	0.8650e-07	29.0439
WSM	0.1250	0.0102	0.3904	64	4.8328e-16	11.4992
WMW	0.0313	0.0025	0.7802	256	5.7518e-16	7.0322
WMS	0.1250	0.0102	0.3898	64	1.6985e-07	11.685
WMM	0.0078	0.0006	6.1716	1024	0.9338e-15	4.2573

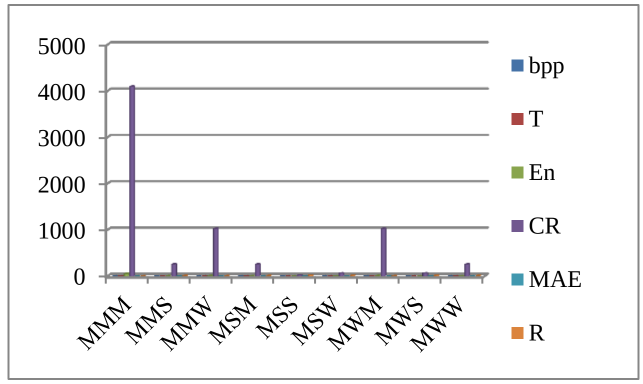

Figure 9. Chart of compression parameters for color RM_{av} Technique.

Table 8. Compression parameters for color GW_{av} Technique.

GW_{av}	bpp	T	En	CR	MAE	R(D)
WWW	0.1250	0.0102	0.0878	64	2.5422e-16	11.5605
WWS	0.5000	0.041	0.0439	16	8.2217 e-07	18.785
WWM	0.0313	0.0025	0.7022	256	4.1294 e-16	7.3111
WSW	0.5000	0.041	0.0439	16	4.6988 e-16	18.5797
WSS	2.0000	0.164	0.0219	4	7.9106 e-08	29.68
WSM	0.1250	0.0102	0.35	64	4.5054 e-16	11.8659
WMW	0.0313	0.0025	0.7	256	6.4163 e-16	7.7097
WMS	0.1250	0.0102	0.3498	64	1.5866 e-07	12.1462
WMM	0.0078	0.0006	5.507	1024	0.8968 e-15	4.5079

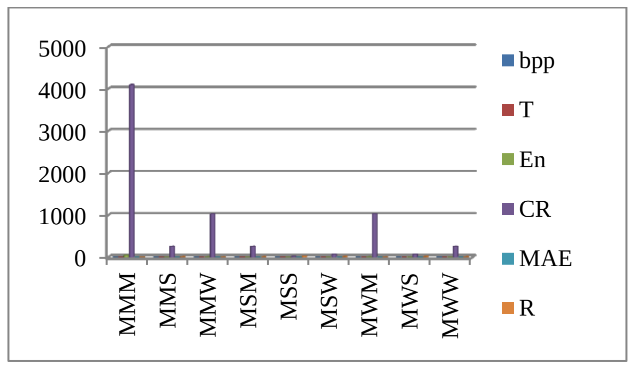

Figure 10. Chart of compression parameters for color GM_{av} technique.

Table 9. Compression parameters for color BW_{av} technique.

BW_{av}	bpp	T	En	CR	MAE	R(D)
WWW	0.1250	0.0102	0.0617	64	1.8531e-16	10.4572
WWS	0.5000	0.041	0.0308	16	7.353e-08	17.2218
WWM	0.0313	0.0025	0.4921	256	3.6406e-16	6.4897
WSW	0.5000	0.041	0.0308	16	4.1816e-16	17.1035
WSS	2.0000	0.164	0.0154	4	7.1514e-08	27.5995
WSM	0.1250	0.0102	0.2462	64	3.9946e-16	10.7752
WMW	0.0313	0.0025	0.492	256	5.1346e-16	6.5223
WMS	0.1250	0.0102	0.2458	64	1.418e-07	10.9722
WMM	0.0078	0.0006	3.8843	1024	7.9147e-16	3.9053

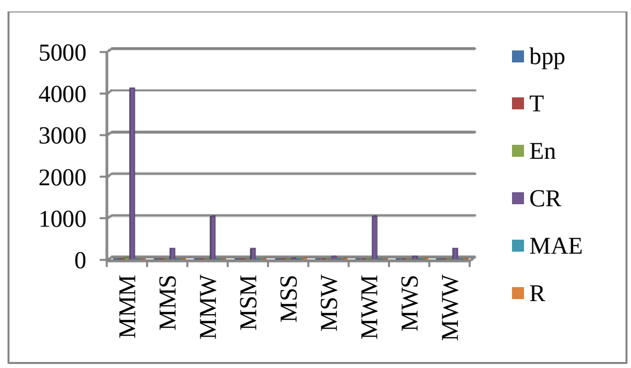

Figure11. Chart of compression parameters for BM_{av} technique.

Table 10. Compression parameters for color RM_{av} Technique.

RM_{av}	bpp	T	En	CR	MAE	R(D)
MMM	0.0020	0.0001	49.232	4096	1.9066e-15	2.5415
MMS	0.0313	0.0025	3.3834	256	3.3501e-07	7.3524
MMW	0.0078	0.0006	5.5971	1024	1.8049e-15	4.3016
MSM	0.0313	0.0025	2.797	256	2.8862e-15	7.1432
MSS	0.5000	0.041	0.1753	16	1.6591e-07	18.796
MSW	0.1250	0.0102	0.3506	64	4.0467e-15	11.5836
MWM	0.0078	0.0006	5.5188	1024	3.7747e-15	4.263
MWS	0.1250	0.0102	0.4252	64	1.7024e-07	11.7003
MWW	0.0313	0.0025	0.851	256	5.764e-16	7.0426

Table 11. Compression parameters for color GM_{av} Technique.

GMav	bpp	T	En	CR	MAE	R(D)
MMM	0.0020	0.0001	43.4204	4096	1.777e-15	2.7268
MMS	0.0313	0.0025	2.7974	256	3.212e-07	7.7344
MMW	0.0078	0.0006	5.5971	1024	1.7535e-15	4.5676
MSM	0.0313	0.0025	2.7970	256	0.8972e-15	7.4546
MSS	0.5000	0.041	0.1753	16	1.5205e-07	19.481
MSW	0.1250	0.0102	0.3506	64	0.9269e-15	11.9998
MWM	0.0078	0.0006	5.5188	1024	0.91e-15	4.5107
MWS	0.1250	0.0102	0.3503	64	1.5999e-07	12.1656
MWW	0.0313	0.0025	0.7011	256	6.4602e-16	7.3571

Table 12. Compression parameters for color BM_{av} Technique.

BM_{av}	bpp	T	En	CR	MAE	R(D)
MMM	0.0020	0.0001	30.9214	4096	1.6232e-15	2.2653
MMS	0.0313	0.0025	1.9564	256	2.854e-07	6.8441
MMW	0.0078	0.0006	3.9098	1024	1.5335e-15	3.9478
MSM	0.0313	0.0025	1.9632	256	7.8752e-16	6.6249
MSS	0.5000	0.041	0.1232	16	1.3692e-07	17.7745
MSW	0.1250	0.0102	0.2464	64	8.2669e-16	10.8593
MWM	0.0078	0.0006	3.8829	1024	8.0253e-16	3.9059
MWS	0.1250	0.0102	0.2459	64	1.4112e-7	10.9813
MWW	0.0313	0.0025	0.4923	256	5.1873e-16	6.5283

Figure 12. Samples of database images.

Effects of Magnetized Water on the Accumulated Depth of Infiltration

Dr. Riyadh Zuhair Al Zubaidy
Professor
College of Engineering-University of Baghdad
E-mail:azzubaidi@hotmail.com

Jinan Namaa Hamza
Assistant Professor
College of Engineering-University of Baghdad
E-mail:janan_namaa@yahoo.com

Amna Sahib Hindal
College of Engineering-University of Baghdad
E-mail:ammona999@yahoo.com

ABSTRACT

This study was carried out to investigate the effects of magnetized water on accumulated infiltration depth. A test rig was designed and constructed for this purpose was installed at the water tests laboratory of the Department of Water Resources Engineering at the University of Baghdad. The investigation was carried out by using two types of soil, different flow velocities throughout magnetizing device and different configuration of magnets over and under the water passage of the magnetizing device. The soils that were used in the experiments are clayey and sandy soils. Six different flow velocities throughout magnetizing device ranged between 0.29 to 1.19 cm/s and ten configurations of arranging the magnets over and under the water passage of the magnetizing device were used. The magnates are sintered neodymium-iron-boron type.

Tests results obtained with magnetized water were compared with those of untreated water. Results showed that magnetizing water increases the accumulated infiltration depth for the two types of soil. The highest increase in the accumulated infiltration depth is achieved under low flow velocity throughout the magnetizing device and with ten magnets. This highest increase for the clayey and sandy soils was 98.2% and 34.2%, respectively.

Key words: magnetized water, infiltration, magnetizing device, water-soil relationship, magnate.

تأثير الماء الممغنط على عمق الارتشاح المتراكم للترب

د. رياض زهير الزبيدي
استاذ
كلية الهندسه-جامعة بغداد

جنان نعمه حمزه
استاذ مساعد
كلية الهندسه-جامعة بغداد

امنه صاحب هندال
كلية الهندسه-جامعة بغداد

الخلاصة

اجريت هذه الدراسة لتحري تاثير الماء الممغنط على عمق الغيض التراكمي في الترب. تم تصميم وبناء منظومة لهذا الغرض وتم نصبها في مختبر المياه التابع لقسم هندسة الموارد المائية في جامعة بغداد.اجري التحري باستخدام نوعين من الترب وسرع جريان مختلفة للماء خلال جهاز المغنطة وبترتيب مختلف للمغانيط فوق وتحت مجرى الماء في جهاز المغنطة. الترب المستخدمة في التجارب كانت تربة طينية والاخرى رملية. تراوحت قيم سرع الجريان الست بين 0.29 و 1.19سم/ثا واستخدمت عشرة من اشكال الترتيب للمغانيط في جهاز المغنطة. كانت المغانيط من نوع نيوديميوم حديد- بورون.

تمت مقارنة النتائج المستحصلة من التجارب باستخدام الماء الممغنط مع تلك المستحصلة باستخدام ماء غير معالج. بينت النتائج بان تعرض الماء للمغناطيس يؤدي الى زيادة في عمق الغيض المتراكم في الترب. تكون الزيادة في عمق الغيض التراكمي عند اقصى قيمة له عند السرعة الواطئة للجريان وعند استخدام العشرة مغانيط. بلغت نسبة هذه الزيادة 98.2% بالنسبة للتربة الطينية و 34.2% بالنسبة للتربة الرملية.

الكلمات الرئيسية: الماء الممغنط، الغيض، جهاز مغنطة، علاقة الماء-تربة، مغناطيس.

1. INTRODUCTION

Many studies and researches throughout the world over the few past decades have reported significant evidences that some properties of water can be changed as it passes through a magnetic field. A study carried out by **Al-Talib** and **Al-Sinjary, 2009** on the effect of magnetic treatment of water on uniformity of sprinkle irrigation showed an increase in irrigation uniformity when using magnetized water. **Abbas, 2009,** investigated the effect of magnetic treatment of salty and fresh irrigation water on infiltration depth and hydraulic conductivity in gypsiferous and calcareous soils. He showed that in gypsiferous soil, magnetizing salty irrigation water increases the value of saturated hydraulic conductivity, while, the magnetizing of fresh irrigation water decreases the value of saturated hydraulic conductivity. In calcareous soils, magnetizing of salty irrigation water decreases the value of saturated hydraulic conductivity, while magnetizing of fresh irrigation water increases the value of saturated hydraulic conductivity. In her study on the effect of magnetizing saline water on hydraulic characteristics for different textured soil, **Al-Kaysi, 2009**, concluded that saturated hydraulic conductivity for all used soil textures decreased when using magnetized water as compared with non-magnetized water. The electrical conductivity of magnetized water affected the saturated hydraulic conductivity, and the lowest value was when distilled water is used. The non-magnetized water was more efficient than the magnetized water to leach salt from soil for all used soil textures. **Kadhem, 2010**, carried out a study to realize the effect of magnetized water on soil reclamation and salt leaching. The main conclusion of his study was that a considerable amount of water can be saved when using magnetized water to leach salts and the magnetized water has a tendency that exceeds the tendency of non-magnetized water in reclamation of soils. The effect of magnetic treatment of irrigation water on soil chemical properties with trickle irrigation was studied by **Mostafazadeh-Fard, et al., 2012**. Their main conclusion was that the soil moisture content with magnetized water was higher than when using non-magnetized water and the magnetic treatment of irrigation water caused high leaching of soil salts. The concentration of anions in the soil such as sulfate, chloride, and bicarbonate and cations such as magnesium, sodium, and calcium at soil depths of 0–60cm when using magnetized water were lower than those when using non-magnetized water. **Mohamed, 2013**, conducted a study to investigate the effects of magnetic treatment of low quality water on some soil properties and plant growth. He concluded that utilization of magnetized water technology considered a promising technique to improve the yield of tomato. After plant harvest, the use of magnetized irrigation water increased soil electrical conductivity and available phosphorus and reduced soil reaction pH. **Al-Talib, et al., 2013**, studied the effect of magnetic treatment of irrigation water on the infiltration rate of soil. They concluded that an obvious increase in water infiltration rate is achieved when using magnetized water, this, in turn, reduces the irrigation time that needed to add the required total irrigation water depth. Magnetized water can increase the discharge and give the same amount of non-magnetized water but with less operational time with the same amount of the constant irrigation depth and, thus, serves to provide the operational capacity of the system that is powered by electricity or liquid fuel by using high irrigation rate of magnetized water without occurrence of surface runoff, which raises the efficiency of water use .

The above mentioned evidences based on experimental tests are some of many other studies that prove that by passing water through field of a permanent magnet or electromagnet can change its physical properties. This change in the physical properties of water can improve the use of water in different areas and have promising potentials especially in the field of irrigation and drainage. These improvements in this field include increasing crops growth and yield, improving quality of irrigation water, increasing efficiency of salt leaching from soils, enhancing the soil, water, and plant relationships, and reducing blockage of emitters used in trickle irrigation. Moreover, obtaining improvements in water properties by field of magnets is so simple, of low cost, safe, and have no harmful effects. However, the effects of magnetic fields on the properties of water are not well developed and are still a challenging subject. Generally, this study was conducted to investigate the soil and magnetized water relationships, specifically, the accumulated depth of infiltration.

2. DESCRIPTION OF THE EXPERIMENTS

The following subsections present a description of the experiments that were carried out to investigate effects of magnetizing water on the accumulated depth of infiltration.

2.1 Materials Used

The physical characteristics of soils used in the experiments are presented in **Table 1**. Results of the chemical and physical characteristics of the water used in the experiments are presented in **Table 2**. Permanent magnets were used of sintered neodymium-iron-boron, NdFeB; these magnets are of BY0X04-N52 type manufactured by K&J Magnetics Inc. The magnet is 5 cm long, 2.5 cm wide, and 1.25 cm depth. Magnetization direction of these magnets is through its thickness and the highest value of its flux is reached at its surface of 7671 gauss.

2.2 The Test Rig

Test rig was designed and constructed to investigate the effects of magnetized water on the accumulated depth of infiltration. **Fig.1** shows a schematic diagram of the test rig. The rig consists of a constant head reservoir that maintains water to two identical magnetizing devices. Water following out of each of the magnetizing device is supplied to two cylinders containing soil. All these components are connected by using rubber tubes of 0.5 cm diameter. Flow throughout these tubes is controlled by using valves. **Fig.2** shows the test rig installed in the laboratory. The magnetizing device is a closed water passage made of a Perspex sheet 4 mm thick, 40 cm long, 7 cm wide, and 2.5 cm high. The water passage of the device has an inlet and an outlet controlled by a valve. Magnets are to be installed on the top and bottom sides of the water passage. **Fig.3** shows a close up photo of the magnetizing device. The cylinders containing the soils were made of a Perspex sheet 60 cm long, 10 cm internal diameter, 4 mm thick, and has a water inlet located at 15cm from the top controlled by a valve. A filtration paper and a metal screen were fixed at the bottom end of the cylinders. The filtration paper was used to prevent the soil from washing out. The metal screen is a support to the filtration paper.

2.3 Design of the Test Runs

Three variables were adopted when designing the test runs. The first was the configuration of magnets; ten configurations of arranging the magnets over and under the water passage of the magnetizing device were used. The second, was the flow velocity throughout magnetizing device, these velocities are 1.19, 0.99, 0.79, 0.69, 0.59, and 0.29 cm/sec. Finally, the third variable was the soil type. As was mentioned previously, two types of soil were used that is a clayey and sandy soil. So, the total numbers of experiments with magnetized water were 120 experiments. In addition to the experiments with magnetized water, a set of experiments was carried out without magnetizing the water as control experiments.

2.4 Configuration of Magnets

To investigate the effect of the number of magnets used, ten configurations of the magnets over and under the water passage of the magnetizing device were used as shown in **Fig.4**. Each configuration was designated with a code, that is $M_{x\text{-}y}$. In this code M refers to the word Magnets and x and y refers to the number of magnates used over and under the water passage of the magnetizing device, respectively. So, the code M_{4-4} refers to 4 magnates used over and under the water passage.

2.5 Preparing of Soils Columns

Four cylinders were prepared, two for the clayey and two for the sandy soil. The same method of packing was adopted in all experiments. The soil was added layer by layer to the cylinder by using a lab spatula. Each soil layer is gently compressed by using a special plunger, simultaneously with shaking until the top of the soil column does not sink any further, **Oliviera, et al., 1996**. The method of adding the layers of soil is repeated until the required total depth of the soil inside the cylinders, of 35cm, is reached. Some samples of the compacted soil layers were tested for their density. Bulk density for the pressed clayey soil has an average of 1050 kg/m^3 and that for the sandy soil is 1690 kg/m^3.

2.6 Description of the accumulated infiltration depth Tests

Infiltration tests were carried out by adding water to a depth of 15 cm over the soil surface. The infiltrated depth is measured by a graded ruler fixed on the outer side of the cylinder. The infiltrated depth is recorded at short time increment during the few minutes after adding the water then increased gradually until reaching the final time of the test. Smaller time increments were used during experiments with sandy soil compared to that with clayey soil.

3. RESULTS AND ANALYSES

One hundred and twenty laboratory test runs were conducted to investigate the effects of magnetized water on the accumulated depth of infiltration. **Fig.5** through **Fig.10** shows the variation of accumulated depth of infiltration under all configurations of magnets and different flow velocities throughout the magnetizing device for clayey soil. **Table 3** presents a summary of the effects of magnetizing water in increasing the accumulated depth of infiltration in the clayey soil under the applied velocities and all configurations of magnets used in the experiments. In general, increasing the number of magnets and reducing the flow velocity increases the accumulated depth of infiltration. At the highest applied flow velocity of 1.19 cm/s with M_{1-0} configuration, a 6.3% increase in accumulated depth of infiltration was achieved. For the same flow velocity with M_{5-5} configuration, this increase was 66.7%, which is 60.4% higher than that with M_{1-0} configuration. When reducing the velocity of flow water through the magnetizing device to its applied minimum value of 0.29 cm/s the effects of magnetizing of water are greatly increased. The increase in accumulated infiltration depth is 25% with M_{1-0} configuration and 98.2% with M_{5-5} configuration. This is about 18.7% and 31.5% increase compared to that with maximum applied flow velocity of 1.19 cm/s with one and ten magnets, respectively.

Fig.11 to **Fig.16** shows the variation of the accumulated depth of infiltration in sandy soil under all configurations of magnets and different flow velocity.

As it was noticed in the experiment with clayey soils, accumulated depth of infiltration increased when using magnetized water. This increase depends on the number of magnets and the value of flow velocity. Increasing the number of magnets and reducing the flow velocity increases the accumulated infiltration depth. But this increase in sandy soil is much less than that in clay soil.

The increase of the accumulated depth of infiltration for sandy soil is 2.2% at the highest applied flow velocity of 1.19 cm/s with M_{1-0} configuration, which is less by 4.1% than that with clayey soil. When M_{5-5} configuration is used with the same velocity, the increase is 17.5%, which is 15.3% less than that with M_{1-0} configuration and less by 49.2% than that with clayey soil. The highest increase is 34.2% at the minimum value of applied flow velocity with $M_{5\text{-}5}$ configuration, which is 16.7% higher than that with the maximum applied flow velocity and less by 64% than that with clayey soil. A summary of the percentage of increase in accumulated depth of infiltration in sandy soil is presented in **Table 4**.

4. CONCLOSIONS

This study aimed to evaluate and investigate the effects of magnetized water on the accumulated depth of infiltration in the two types of soil. The results showed that the accumulated infiltration depth of the two soil types increased when magnetized water is used compared to that with non-magnetized water. The maximum percentage of this increase was 98.2% and 34.2% for clayey soil and sandy soil, respectively. This maximum increase was achieved under the condition of minimum applied flow velocity through magnetizing device of 0.29 cm/s and with ten used magnets. The accumulated infiltration depth in clayey soil is affected by the magnetized water by a maximum value of 64% more than that in sandy soil.

5. REFERENCES

- Abbas, M. K., 2009, *Magnetic Effect of Normal and Salty Irrigation Water on Infiltration Depth in Calcareous and Gypsiferous Soils*, Al-Anbar journal of Agricultural Sciences, vol. 7, no. 3, pp 41-66.
- Al-Kaysi, S. K. H., 2009, *Effect of Magnetizing Saline Water on Hydraulic Characteristics for Different Textured Soils*, PH. D. Dissertation, Department of Soil and Water Sciences, College of Agriculture, University of Baghdad. In Arabic.
- AL-Talib, A. A., and AL-Sinjary, Z. A., 2009, *Effect of Magnetizing Water on Uniformity of Sprinkle Irrigation*, Al-Rafidain Engineering journal, vol. 17, no. 1, pp 68-79.
- AL-Talib, A. A., Mahmoud, M. T., and Abdulgani, A. M., 2013, *The Effect of Magnetizing Irrigation Water on the Infiltration Rate in Soil*, Tikrit Journal of Engineering Sciences vol. 20, no. 4, pp 18-23. In Arabic.
- Kadhem, R. J. M., 2010, *The Use of Magnetized Water in Reclamation Soils Affected by Salts*, Euphrates journal of Agriculture Science, vol. 2, no. 2, pp 97-103. In Arabic.
- Mohamed, A. I., 2013, *Effects of Magnetized Low Quality Water on Some Soil Properties and Plant Growth*, International Journal of Research in Chemistry and Environment, vol. 3, no. 2, pp 140-147.
- Mostafazadeh-Fard, B., Khoshravesh, M., Mousavi, S., and Kiani, A., 2012, *Effects of Magnetized Water on Soil Chemical Components Underneath Trickle Irrigation*, journal of Irrigation and Drainage Engineering, vol. 138, no. 12.
- Oliviera, I. B., Demond, A. H., and Salehzadeh, A., 1996, *Packing of Sands for the Production of Homogeneous Porous Media*, Soil Sci. Soc. Amer. Journal, vol. 60, no. 1, pp 49-53.

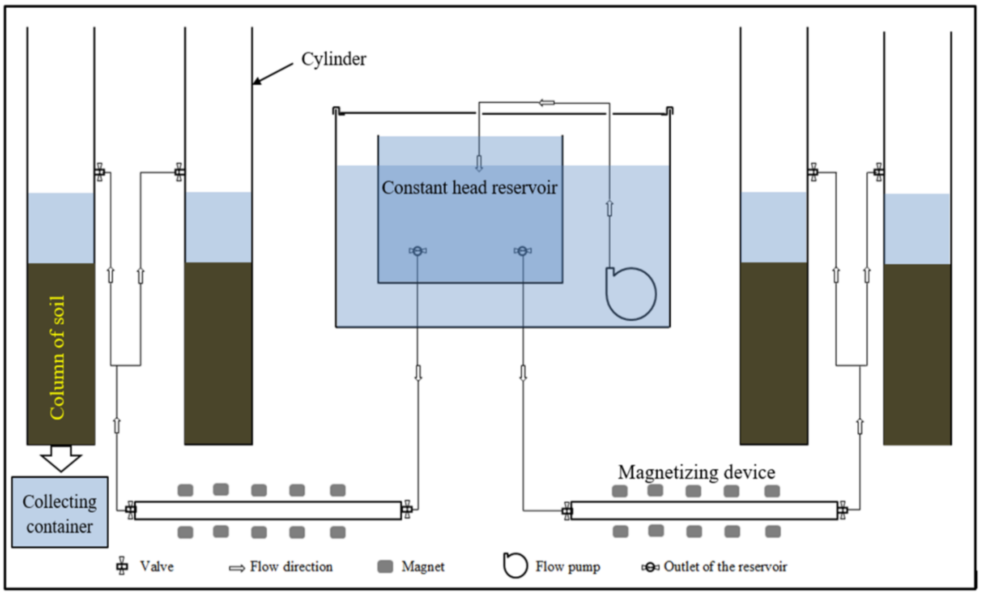

Figure 1. Schematic diagram of the test rig.

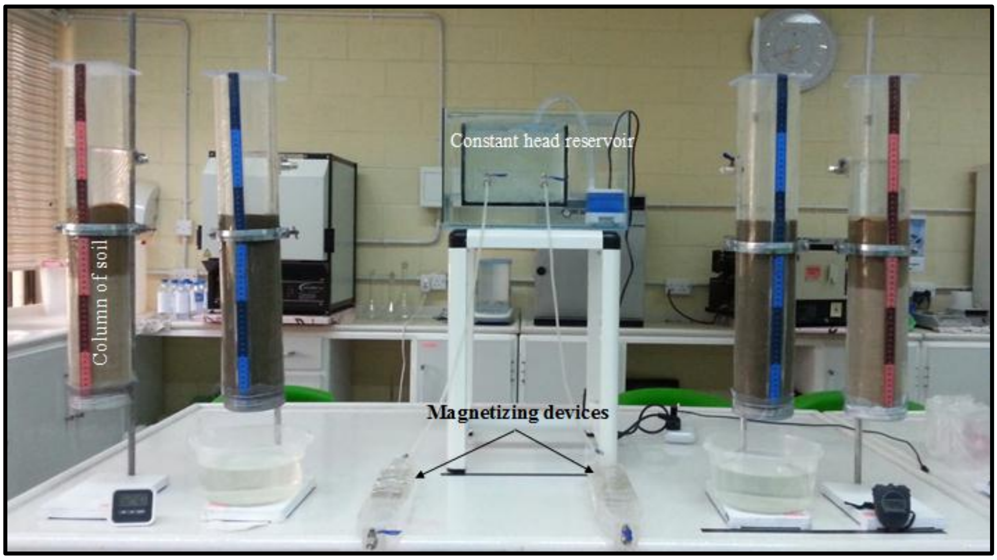

Figure 2. The test rig installed in the laboratory.

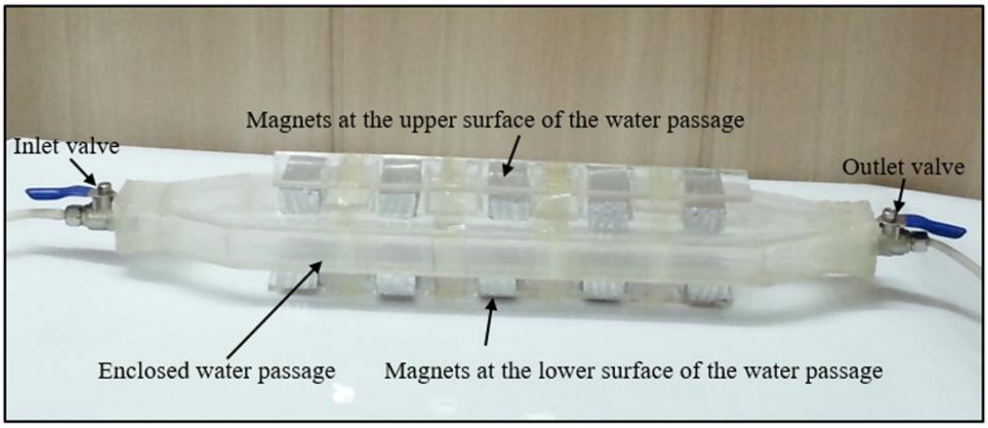

Figure 3. Close up photo of the magnetizing device.

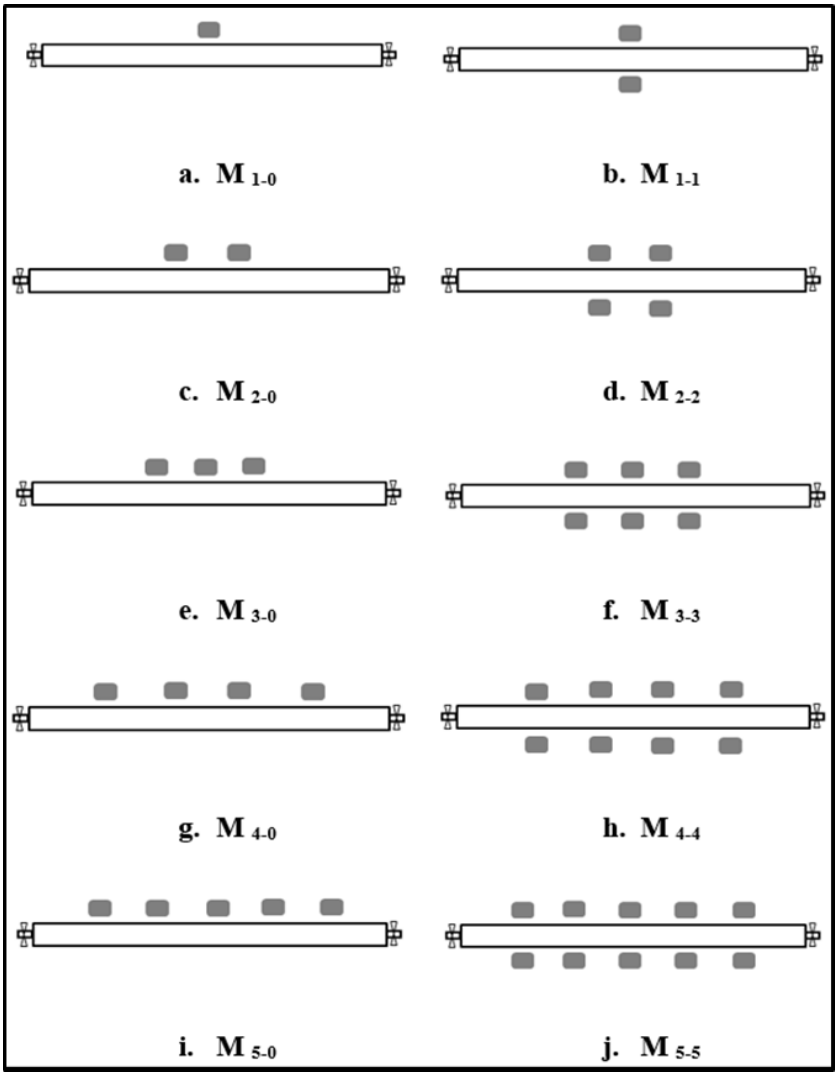

Figure 4. Schematic diagram showing the configurations of magnates.

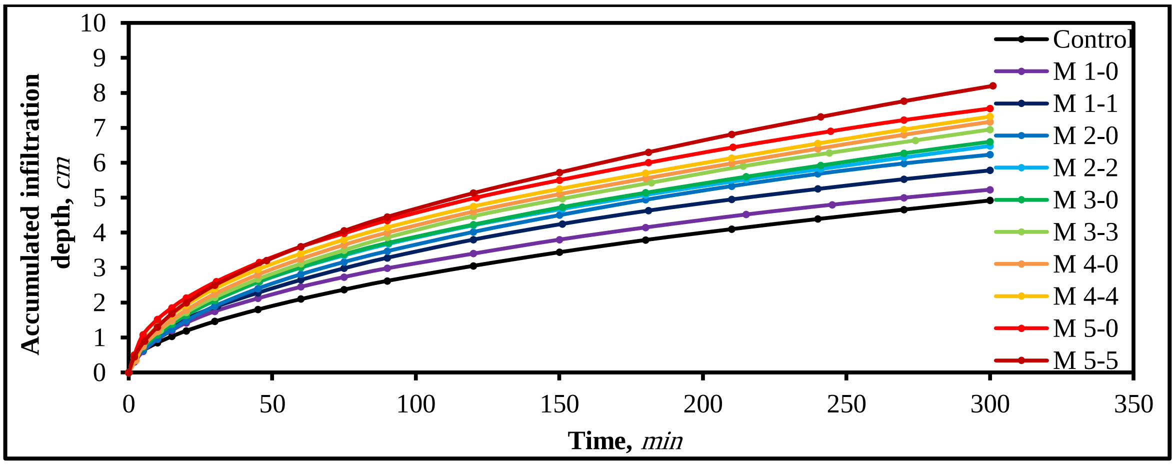

Figure 5. Variation of accumulated infiltration depth with time, for clayey soil,v=1.19*cm/s*.

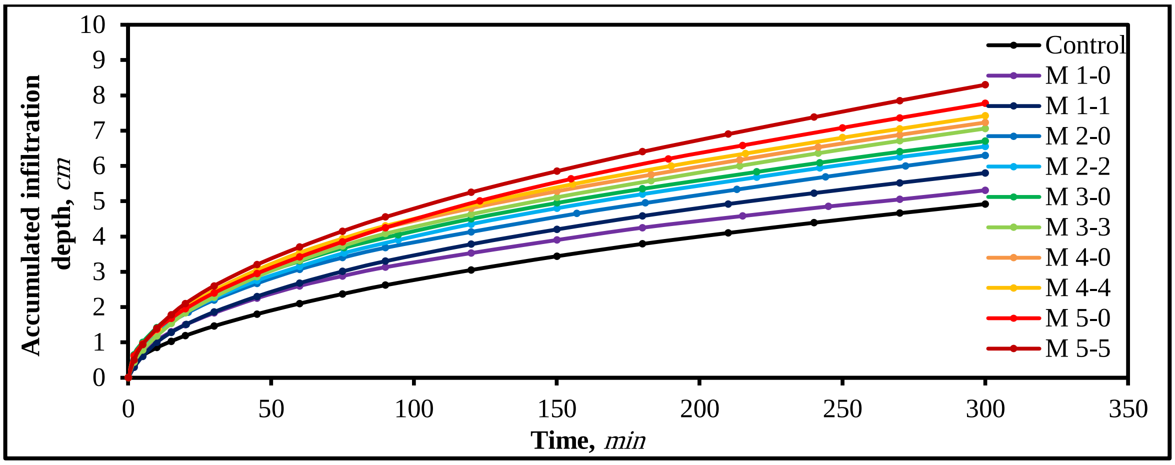

Figure 6. Variation of accumulated infiltration depth with time for clayey soil, *v*=0.99*cm/s*.

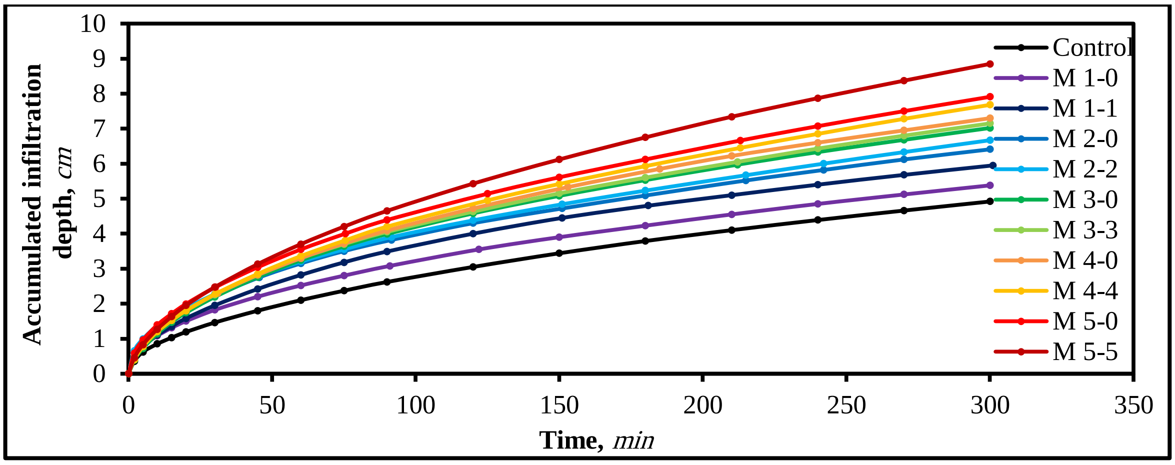

Figure 7. Variation of accumulated infiltration depth with time for clayey soil, *v*=0.79*cm/s*.

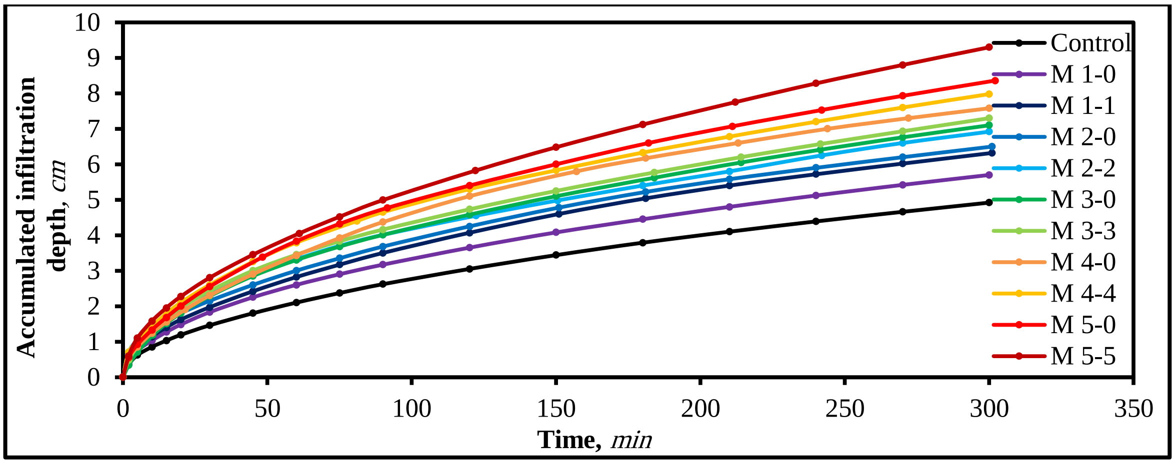

Figure 8. Variation of accumulated infiltration depth with time for clayey soil, *v*=0.69*cm/s*.

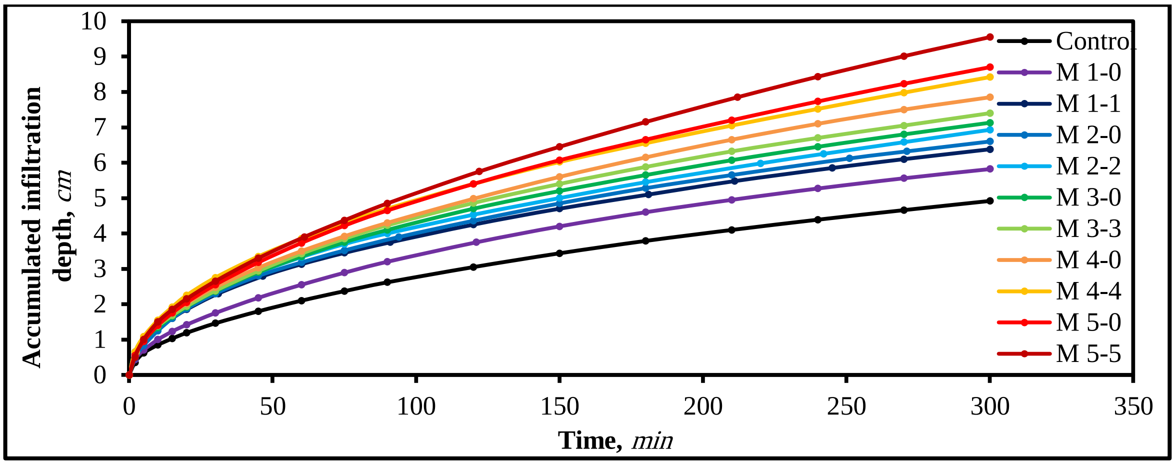

Figure 9. Variation of accumulated infiltration depth with time for clayey soil, *v*=0.59*cm/s*.

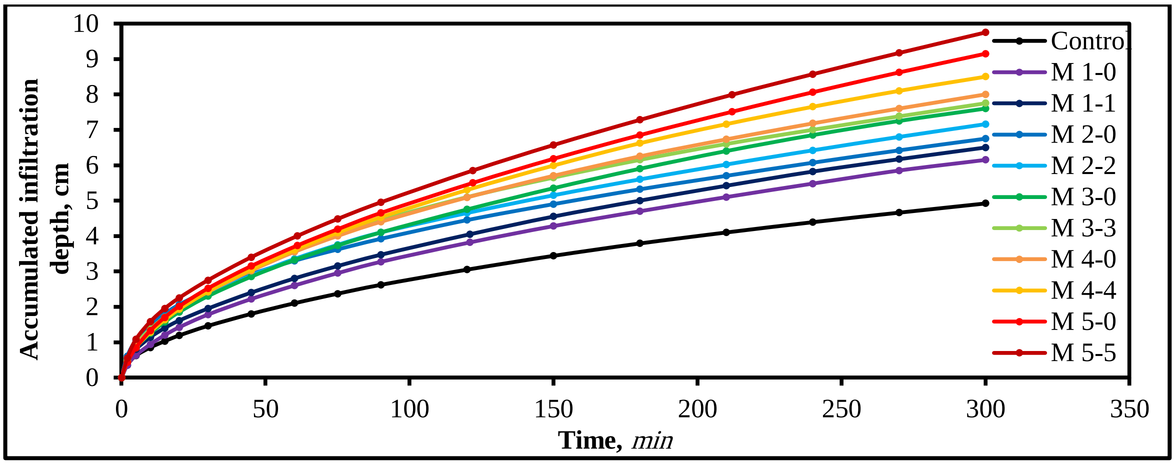

Figure 10. Variation of accumulated infiltration depth with time for clayey soil, *v*=0.29*cm/s*.

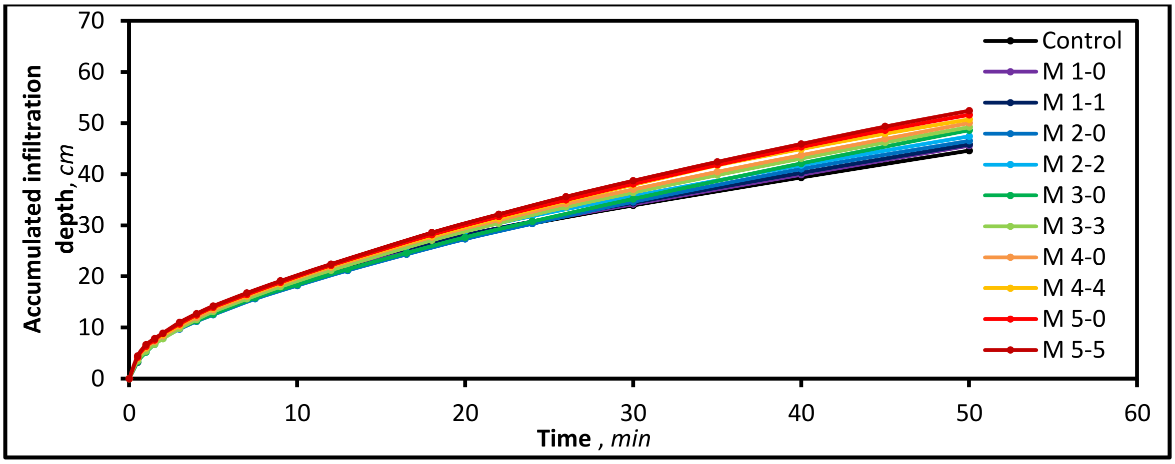

Figure 11. Variation of accumulated infiltration depth with time for sandy soil, *v*=1.19*cm/s*.

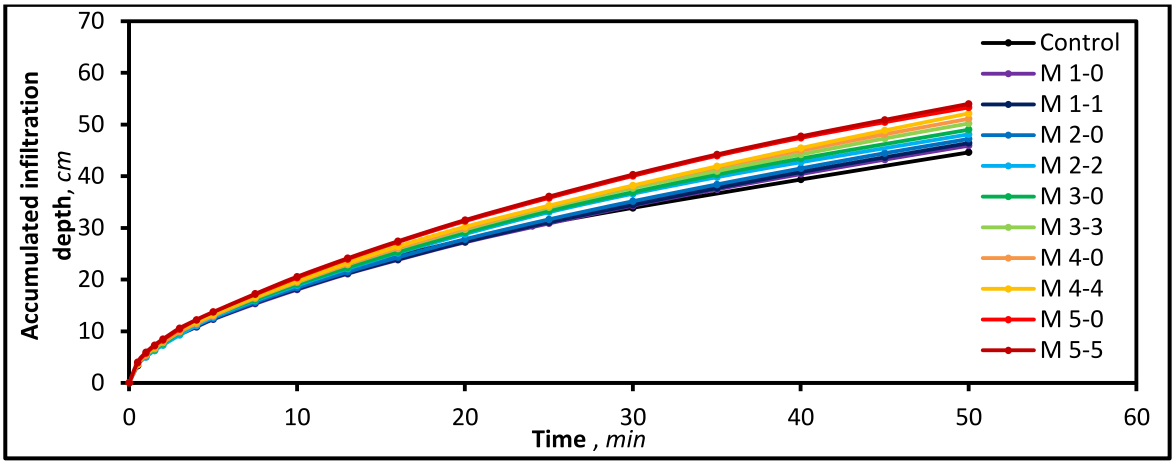

Figure 12. Variation of accumulated infiltration depth with time for sandy soil, *v*=0.99*cm/s*.

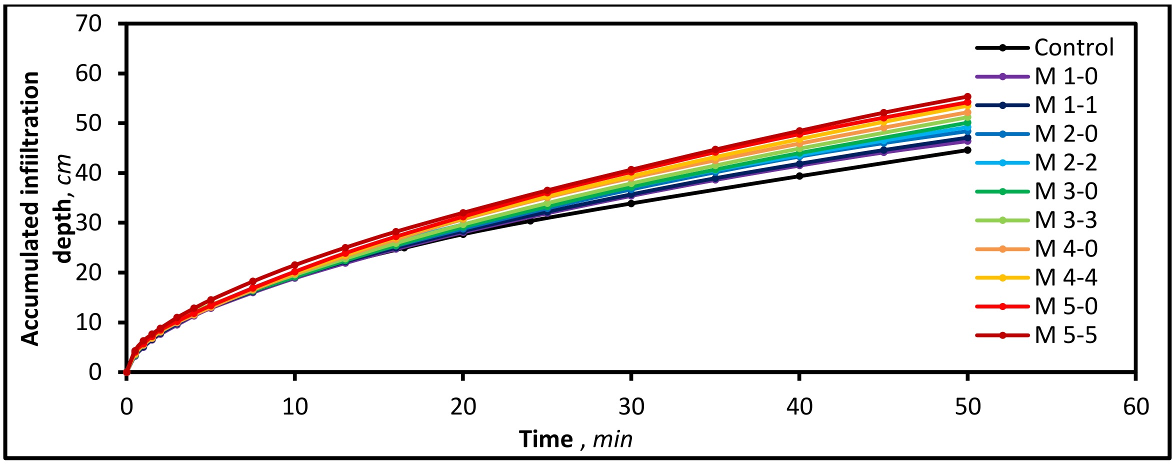

Figure 13. Variation of accumulated infiltration depth with time for sandy soil, *v*=0.79*cm/s*.

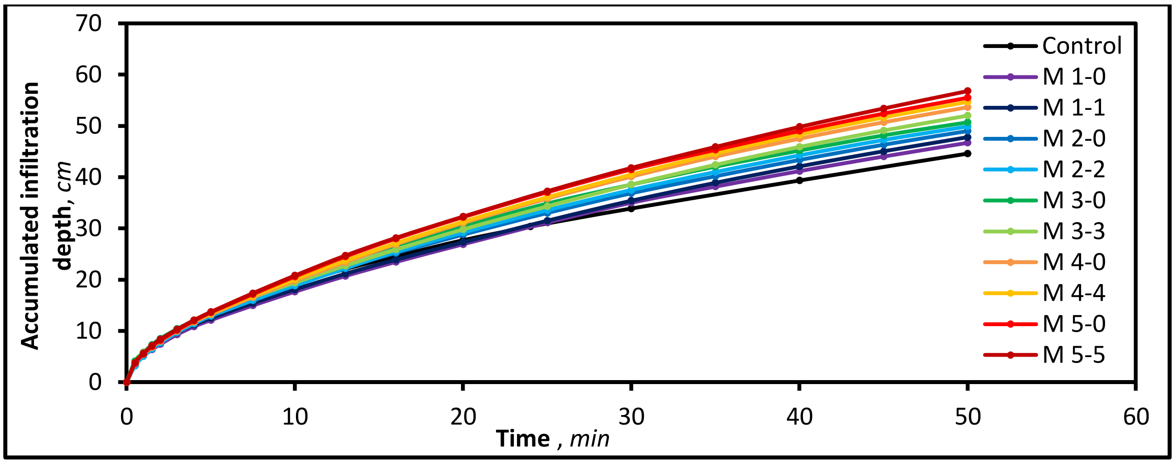

Figure 14. Variation of accumulated infiltration depth with time for sandy soil, *v*=0.69*cm/s*.

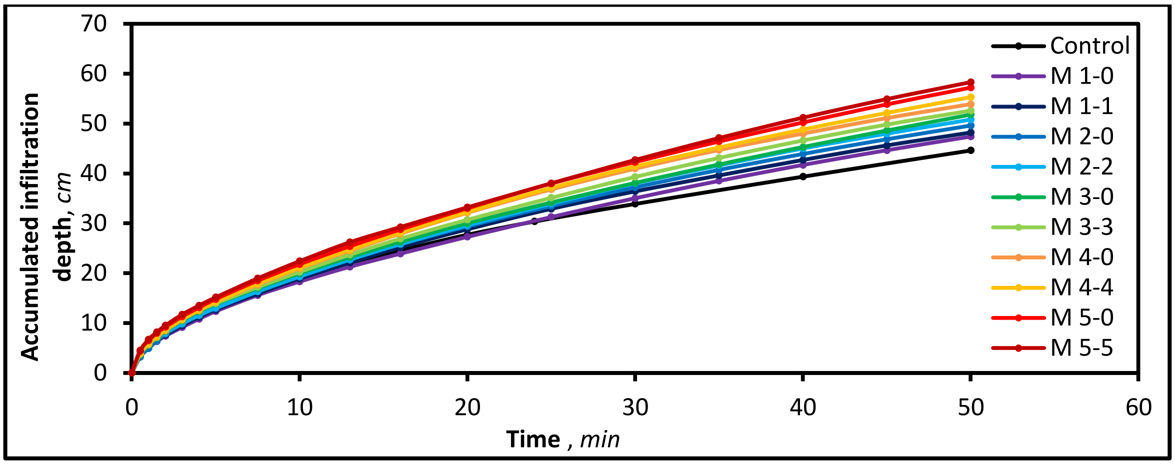

Figure 15. Variation of accumulated infiltration depth with time for sandy soil, *v*=0.59*cm/s*.

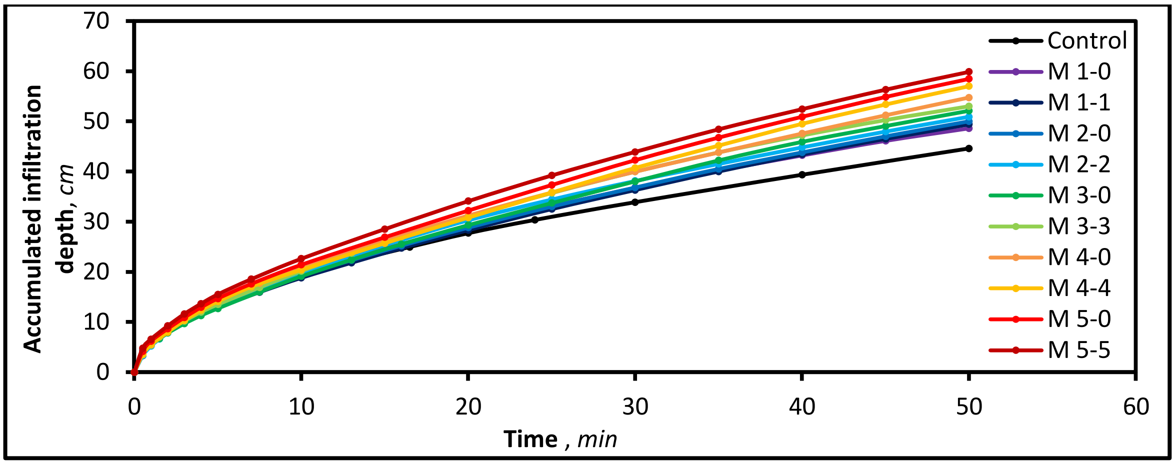

Figure 16. Variation of accumulated infiltration depth with time for sandy soil, *v*=0.29*cm/s*.

Table 1. Results of the tests carried out on the two soils used in the study.

Parameter	Soil from site1	Soil from site2
Moisture content, %	2.60	0.45
Particle size distribution:		
- % Sand	8.60	96.8
- % Silt	31.50	3.00
- % Clay	59.90	0.20
Texture class	Clay	Sand

Table 2. Results of the tests carried out on the diluted water used in the study.

Parameter	
PH	8.01
Electrical conductivity EC, *dS/m*	1.07
TDS, *mg/l*	697
TSS, *mg/l*	0.054
Alk. as $CaCO_3$, *mg/l*	90
T.H. as $CaCO_3$, *mg/l*	70
Calcium Ca^{+2}, *mg/l*	138
Magnesium Mg^{+2}, *mg/l*	60
Sodium Na^{+}, *mg/l*	152
Potassium K, *mg/l*	5.3
Chloride, Cl^{-}, *mg/l*	132
Sulfate, SO_4^{-2}, *mg/l*	145
Carbonate CO_3^{-}, *mg/l*	Nil
Bicarbonate HCO_3^{-}, *mg/l*	71
Nitrate, NO_3, *mg/l*	2.561
Phosphate, PO_4, *mg/l*	0.352
Aluminum, Al, *mg/l*	0.152
Iron, Fe, *mg/l*	0.316
Manganese, Mn, *mg/l*	0.265
Zinc, Zn, *mg/l*	0.202
Copper, Cu, *mg/l*	0.0813
Lead, Pb, *mg/l*	0.097
Cadmium, Cd, *mg/l*	0.042
Nickel, Ni, *mg/l*	0.117
Mercury, Hg, *mg/l*	0.079
Chrome, Cr, *mg/l*	0.095

Table 3. Increase in accumulated infiltration depth for clayey soil.

Magnets Configuration	Increase in accumulated infiltration depth, *%*					
	Velocities, *cm/sec.*					
	1.19	**0.99**	**0.79**	**0.69**	**0.59**	**0.29**
M_{1-0}	6.3	8.1	9.4	15.9	18.3	25
M_{1-1}	17.5	17.9	20.9	28.5	29.7	32.1
M_{2-0}	26.6	28.1	30.3	32.1	34.2	37.2
M_{2-2}	31.7	33.1	35.6	40.7	40.9	45.5
M_{3-0}	34.2	36.2	42.7	44.3	44.9	54.5
M_{3-3}	41.3	43.5	45.3	48.4	50.4	57.5
M_{4-0}	45.7	47	48.4	54.1	60	62.6
M_{4-4}	48.8	50.8	56.1	62.2	71.1	72.76
M_{5-0}	53.5	57.9	60.8	69.9	76.8	86
M_{5-5}	66.7	68.7	79.9	89	94.1	98.2

Table 4. Increase in accumulated infiltration depth for sandy soil.

Magnets configuration	**Increase in accumulated infiltration depth**, %					
	Velocities, *cm/sec.*					
	1.19	**0.99**	**0.79**	**0.69**	**0.59**	**0.29**
$\mathbf{M}_{\mathbf{1-0}}$	2.2	2.9	4	4.7	6.3	9
$\mathbf{M}_{\mathbf{1-1}}$	2.7	4	5.6	7.2	8.1	10.8
$\mathbf{M}_{\mathbf{2-0}}$	4.3	5.8	8.5	9.9	11.2	12.1
$\mathbf{M}_{\mathbf{2-2}}$	6.3	7.9	10.3	11.9	13.9	14.1
$\mathbf{M}_{\mathbf{3-0}}$	9	9.9	12.3	13.7	16.1	16.8
$\mathbf{M}_{\mathbf{3-3}}$	10.3	12.6	14.8	16.6	17.9	18.8
$\mathbf{M}_{\mathbf{4-0}}$	12.1	14.6	17	20.3	20.9	22.7
$\mathbf{M}_{\mathbf{4-4}}$	13.7	16.9	20	22.6	24	27.8
$\mathbf{M}_{\mathbf{5-0}}$	15.7	19.5	21.5	24.4	28.3	31.1
$\mathbf{M}_{\mathbf{5-5}}$	17.5	21.1	24.1	27.4	30.7	34.2

Estimation of Lifting Capacity for Selected Wells in Rumaila Field

Dr. Rafid Kadhim Abbas
Lecturer
Faculty of Engineering,Chemical Engineering dept.,University of Al- Qadisiyah, Al-Diwaniya city, 58002, Iraq,
Rafid.1972@gmail.com
Rafid.Abbas@qu.edu.iq

ABSTRACT

This paper deals with studying the effect of hole inclination angle on computing slip velocity and consequently its effect on lifting capacity. The study concentrates on selected vertical wells in Rumaila field, Southern Iraq. Different methods were used to calculate lifting capacity. Lifting capacity is the most important factor for successful drilling and which reflex on preventing hole problems and reduces drilling costs. Many factors affect computing lifting capacity, so hence the effect of hole inclination angle on lifting capacity will be shown in this study. A statistical approach was used to study the lifting capacity values which deal with the effect of hole inclination angle and those values that do not put the effect of hole inclination angle under consideration. Results illustrated that low hole inclination angles had a slight effect on lifting capacity values , but this study could be used on high inclination angles like directional wells or horizontal wells , hence high hole inclinations angle will yields high effect on lifting capacity values.

Key words: hole cleaning; cuttings transport; lifting capacity; hole inclination angle; slip velocity.

تخمين قابلية الرفع لابار مختارة في حقل الرميلة

د. رافد كاظم عباس
مدرس
كلية الهندسة جامعة القادسية

الخلاصة

هذا البحث يتناول دراسة تاثير زاوية انحراف البئر على حساب سرعة الانزلاق و بالتالي على قابلية رفع الصخور.
الدراسة تركّزت على ابار عمودية مختارة في حقل الرميلة جنوبي العراق.
طرق مختلفة تم استخدامها لحساب قابلية رفع الصخور . قابلية رفع الصخور هي العامل الاكثر أهمية لعملية حفر ناجحة و التي تنعكس على تجنب مشاكل الحفر و تخّفض كلفة الحفر. عوامل كثيرة تؤثر على حساب قابلية رفع الصخور ، لذا هنا تاثير زاوية انحراف البئر على قابلية رفع الصخور سيتم توضيحها في هذه الدراسة. دراسة احصائية تم استخدامها لدراسة قيم قابلية رفع الصخور بوجود زاوية لانحراف البئر مع القيم التي لا تأخذ زاوية انحراف البئر بنظر الاعتبار . النتائج وضحّت بأن زوايا انحراف قليلة لها تأثير ضعيف على قيم قابلية رفع الصخور ، لكن هذه الدراسة يمكن استخدامها على زوايا انحراف عالية مثل الابار المنحرفة و الابار الافقية ، حيث هنا زوايا احراف عالية ستؤدي الى تأثير عالي على قيم قابلية رفع الصخور .

الكلمات الرئيسية: تنظيف البئر، نقل قطع الصخور، قابلية رفع الصخور، زاوية انحراف البئر، سرعة السقوط.

1. INTRODUCTION

Sifferman and Becker ,1992 conducted after 4 – years multifactor experimental study on hole cleaning in inclined wellbores, ten variables were used. They concluded that the variables with significance influence on cuttings transport are mud annular velocity, mud density, inclination angle and drill pipe rotation as well as pipe eccentricity.

The annular velocity of an oil well drilling operation is chosen to transport drill cuttings from the bottom of the well to the surface , meanwhile it must maintain the concentration of cuttings in the annulus within certain limits dictated by the drilling and formation conditions. Using available experimental data, empirical equations describing the setting velocity of the drill cuttings were first determined. Increasing the mud density, creating laminar annular mud flow or rotating the drill pipe may also improve the carrying capacity of mud, **Hopkin, 1967** and **Chain, 1969**.

A simple rig-site graphical technique was presented for determining hole cleaning requirements for a range of hole sizes. This method used a set of charts which had been derived from a computer model based on both laboratory and field measurements. Mud rheologywais shown to be a key variable for optimizing hole cleaning in deviated wells, **Luo, 1994**.

It has been shown that in vertical annuluses, the fluid annular velocity has a major effect on the carrying capacity of muds, while other parameters have an effect only at low to medium fluid annular velocities, **Hussaini** and **Azar, 1983**.

Using the concept of minimum transport velocity, which presumes that a hole can be efficiently cleaned by either maintaining cuttings rolling or in suspension if the annular velocity is equal to or greater than the minimum transport velocity for that operational condition, **Paden** and **Ford, 1990**.

Several experimental studies have been performed to determine the minimum annular velocity required to lift the cuttings, and the results showed that a minimum annular velocity of 50 ft/min is required to provide effective cutting transport for a typical drilling fluid. However the slip velocity of the cuttings determines how effective the cutting transport will be, **Mojisola, 2005**.

Rabia, 2001 showed that for optimum lifting capacity the following factors must be considered:

1- Turbulent flow is most favorable for efficient removal of cuttings.
2- Low viscosity and low gel strength of mud are desirable properties for cuttings removal.
3- High mud density efficiently helps to remove cuttings away from the wellbore.
4- Pipe rotation aids the removal of cuttings.

Jerzy et al., 2013 studied the behavior of the slip velocities in a two-phase (solid and liquid) mixture flow in a vertical pipe. It was noted that the measured slip velocities in the two-phase flow were influenced by the fluctuations in the concentration of the flowing mixture during the measurement. Furthermore, the shape of the cuttings could affect the precision of the measured slip velocities.

Onuoha et al., 2015 illustrated the effect of hole inclination angle on the Cutting Transport Ratio (*CTR*). It was concluded that when using water-base mud as a drilling fluid, the *CTR* found to be decreased when the inclination angle is between 0º and 60º. On the other hand, when using polypropylene beads with water base mud would improve the *CTR*, especially at high inclination angle (i.e. 75º – 90º).

Mohammadsalehi and **Malekzadeh**, **2011** developed a computer program that combines Larson's and Moore models to predict the minimum flow rate of the transported cuttings for the hole inclination angles range from 0º to 90º. For inclination angles between 55º – 90º, the rheological properties of the drilling mud goes higher causing the flow rate to be decreased, while for higher inclination angles, lower rheological properties of the drilling mud is more favorable to obtain better hole cleaning efficiency.

2. THEORETICAL BACKGROUND

Efficient removal of cuttings from the wellbore is one of the major considerations during both design and operational stages of a drilling process. Inadequate hole cleaning may give rise to serious drilling problems, like increase in torque and drag, stuck pipe, loose control on density, difficultly when running and cementing casing, etc. To avoid such problems, generated cuttings have to be removed from the wellbore by the help of the drilling fluid. The ability of the fluid to lift such cuttings is generally referred to as carrying capacity of the drilling fluid.
Factors affecting the ability of drilling mud to lift cuttings are (1) fluid rheological properties, (2) particle setting velocity, (3) particle size and size distribution, geometry and concentration, (4) penetration rate of drill bits, (5) rotary speed of drill string, (6) fluid density, (7) hole inclination, (8) mud type, (9) drill pipe position and (10) drill pipe size. Simultaneously, the determination of carrying capacity of a mud becomes a complicated problem.

2.1 Cuttings transport parameters:

1- Slip velocity (V_{sl}). Slip velocity is the falling cuttings velocity in the annulus, according to the law of gravity.
2- Cutting velocity (V_{cut}). Cutting velocity is the velocity that must be fulfill by cutting to the surface.
3- Minimum velocity (V_{min}). Minimum velocity is a required velocity of the annular fluid so than the cutting can be transported to the surface.
The mathematical relation is defined as follows, **Indra** and **Rudi, 2002**:

$$V_{cut} = V_{\min} - V_{sl} \tag{1}$$

4- The Cutting Transport Ratio (*CTR*), which is defined as the ratio of the cutting transport velocity over the minimum mean annular velocity as follows:

$$CTR = \frac{V_{cut}}{V_{\min}} = 1 - \frac{V_{sl}}{V_{\min}} \tag{2}$$

A (*CTR*) of 1.0 or 100% implies perfect hole cleaning.
- If *CTR* > 0 cuttings are moving upward.
- *CTR* should be > 0.5 for optimum hole cleaning.

Obviously total removal of drill solids would correspond to a transport ratio of 100 percent, however this degree of efficiency can be difficult to achieve because of practical constraints.

2.1.1 Moore correlation:
Several equations were presented by **Moore, 1974** for the calculations. Reynold's number is calculated from:

$$N_{\text{Re}} = \frac{928\,\rho_f\,V_{sl}\,d_s}{\mu} \tag{3}$$

For Reynold's number greater than 300, the slip velocity can be calculated as follows:

$$V_{sl}(ft/\sec) = 1.54\sqrt{d_s\,.\frac{\rho_s-\rho_f}{\rho_f}} \tag{4}$$

For Reynold's number less than 3, when flow is considered to be laminar, the slip velocity equation becomes:

$$V_{sl}(ft/\sec) = 82.87\,\frac{{d_s}^2}{\mu}\,(\rho_s-\rho_f) \tag{5}$$

For intermediate Reynold's numbers corresponding to the transitional flow regime, slip velocity can be calculated as:

$$V_{sl}(ft/\min) = \frac{174.7\,d_s\,(\rho_s-\rho_f)^{0.667}}{{\rho_f}^{0.333}.\ {\mu_e}^{0.333}} \tag{6}$$

2.1.2 Chien correlation:
Chien correlation assumed a general empirical equation for calculating slip velocity as follows, **Chien, 1972**:

$$V_{sl}(ft/\min) = 86.5\,\left(\frac{d_s(\rho_s-\rho_f)}{\rho_f}\right)^{0.5} \tag{7}$$

Moore correlation is used in normal vertical well to determine these parameters. But in deviated or even horizontal wells Moore correlation cannot be applied. **Indra** and **Rudi , 2002** developed a new correlation for this problem that is used to determine the parameters. The correlations are as follows:

For the case of $\theta < 45^\circ$:
where θ represents the hole inclination angle.

$$V_{\min}(ft/\min) = V_{cut}(ft/\min) + \left[\frac{(45+2\theta)(600-N)(3+\rho_f)}{405000}\right] V_{sl}(ft/\min) \tag{8}$$

For $\theta > 45^\circ$:

$$V_{\min}(ft/\min) = V_{cut}(ft/\min) + \left[\frac{(600-N)(3+\rho_f)}{3000}\right] V_{sl}(ft/\min) \tag{9}$$

While, V_{cut} is solved as following:

$$V_{cut}\,(ft/\sec) = \frac{ROP}{36\left[1-\left(\frac{d_{pipe}}{d_{hole}}\right)^2\right] C_{conc}} \tag{10}$$

V_{cut} should convert to (ft/min) units. Another method to predict the value of cuttings transport ratio assumed by **Darely and Gray, 1988** as follows:

1- Calculating annular velocity (V_{min}) based on flow rate (Q), hole and pipe diameter:

$$V_{\min} = \frac{24.5\,Q}{d_{hole}^{\;2} - d_{pipe}^{\;2}} \tag{11}$$

2- After calculating V_{min} the next step is to use Sifferman's graph by plotting the velocity (V_{min}) to intersect with the type of drilling fluid used where this approach four types of drilling fluids (water, thin mud, intermediate mud and thick mud), and from this intersection , cuttings transport ratio will be determined as shown in **Fig. 1**.

Guo *et al*. (1993) presented an equation to determine the expected cutting size as follows:

$$d_s = \frac{12}{60}\,\frac{ROP}{N} \tag{12}$$

Wolfgang, 2001 submitted another approach to know the cutting size as:

$$d_s = \frac{\tau_g}{10.4\,(\rho_s - \rho_f)} \tag{13}$$

$$\rho_s = \rho_f + \frac{\tau_g}{10.4\,d_s} \tag{13a}$$

where τ_g represents the gel strength required to suspend particle of the cutting diameter.

3. COLLECTION OF DATA

Data was collected from Iraqi South Oil Company. Drill bit records, mud control, and drilling tubular data for five drilled wells in Rumaila field, Southern Iraq were used for the calculations in this study.

4. RESULTS AND DISCUSSION

4.1 Regular calculations (when angle of inclination was not taken under consideration):

4.1.1 Annular velocity calculations:

First of all, the unknown parameters must be determined such as cutting size diameter and cutting density. Taking into consideration that all used parameters must be in homogenous units by using conversion factors. Guo equation, i.e. eq. (12) is used to compute cutting size diameter (d_s). To calculate cutting density (ρ_s) equation (13a) is used, where τ_g in eq.(13) represents the highest reading of zero gel or 10 min. gel, **Lee *et al.* 2004**.
Both computed cutting size diameter and cutting density are tabulated in Tables (1), (2) , (3) , (4) and (5) for wells Ru-273 , Ru-301 , Ru-285 , Ru-283 and Ru-281 respectively. Surprisingly, some of the calculated cutting density exhibits high values. This might be attributed to the inexact estimation of the cuttings size as there is no perfect approach for the cutting size estimation.
The next step of calculations is annular velocity computation using equation (11) and its results were tabulated in Tables (6), (7), (8), (9) and (10). The computed annular velocity is used to determine cutting transport ratio (*CTR*) by Sifferman's graph, **Fig.1**. This approach is considered the quickest, but not the most accurate method of *CTR* determination. The determined values of cutting transport ratio (*CTR*) by Sifferman's graph are tabulated in Tables (6), (7), (8), (9) and (10). It is noticed from Sifferman's graph that this method Is extremely limited to fixed types of drilling fluid properties such as μ_p , Y_p , zero min. gel and 10 min. gel for four types of fluids. Furthermore, it is noted that for high values of flow rate (Q), there is considerable corresponding values for *CTR*, whereas low Q values produced unknown *CTR* values as shown in Tables 6-10.
The computed values of annular velocities by eq. (11) are used later beside the slip velocity to compute cutting transport ratio (*CTR*) by using eq. (2).
According to **Rabia, 2001**, hole cleaning will be efficient if annular velocity V_a or $V_{min.}$ must be greater than slip velocity V_s and it is observed that at annular velocities of less than 100 ft/min. , particle slip velocity in both Newtonian and non-Newtonian fluids is independent of the fluid annular velocity. Above an annular velocity of 100 ft/min., there appears to be a dependence of slip velocity on annular velocity.

4.1.2 Slip velocity calculations:

According to **Rabia, 2001**, the type of flow considered for slip velocity calculations will be chosen to be transitional (between laminar and turbulent), because the type of flowing is unknown. Using power-law model equations:

$$n = 3.32 \log\left(\frac{\phi_{600}}{\phi_{300}}\right) \quad \textbf{(14)}$$

The following equations are so useful for k, μ_p and Y_p calculations:

$$\mu_p = \phi_{600} - \phi_{300} \quad (15), \qquad \phi_{600} = \mu_p + \phi_{300} \quad (15a)$$

$$Y_p = \phi_{300} - \mu_p \quad (16), \qquad \phi_{300} = Y_p + \mu_p \quad (16a)$$

$$K = \frac{\phi_{300}}{(511)^{n}} \tag{17}$$

$$\mu_e = \left[\frac{2.4 * V_a * (2n+1)}{(D_h - OD_p * 3n} \right]^n * \frac{200K(D_h - OD_p)}{V_a} \tag{18}$$

$$V_{sl} \ (ft/\min) = 174.7 \ \frac{d_{pipe} * (\rho_s - \rho_f)^{0.667}}{\rho_f^{\ 0.333} * \mu_e^{\ 0.333}} \tag{19}$$

$$C_{conc.} \ (\%) \ = \ \frac{1}{60} \ \frac{ROP * D_h^{\ 2}}{(V_a - V_{sl})(D_h^{\ 2} - OD_p^{\ 2})} \tag{20}$$

From the given data the parameters φ_{300}, φ_{600} , n, K, μ_e and V_{sl} are computed using Equations (16a),(15a),(14),(17),(18) and (19) respectively. Later, *CTR* and $C_{conc.}$ will be computed using equations (2) and (20) respectively.
The results of the used equations above were tabulated in Tables (11), (12), (13), (14) and (15) for wells Ru-273 , Ru-301 , Ru-285 , Ru-283 and Ru-281 respectively .
All the previous calculations were done when the angle of inclination was not considered.

4.2 Calculations when small angles of inclination were considered (semi vertical well):
4.2.1 Cutting velocity calculation:
By getting the benefit of C_{conc} values computed from above equations, cutting velocity will be computed using equation (10). The resulted cutting velocity will be in units of ft/sec. and should be converted to units of ft/min.

4.2.2 Annular velocity calculations:
For the case of inclination, annular velocity will be calculated using equation (8), because the data given were exclusive for the case of angle of inclination ($\theta < 45^{\circ}$).
Slip velocity values computed above when angle of inclination was not under consideration will be used altogether with the computed values of V_{mim} and $V_{cut(inc.)}$ for case of inclination to calculate *CTR* values for case of inclination. The resulted values were tabulated in Tables (16), (17), (18), (19) and (20) for wells Rumaila-273, Rumaila -301, Rumaila -285, Rumaila -283 and Rumaila -281 respectively. It is noted that, some values of slip velocities were obtained due to the uncertain method of cutting size determination. Cutting size (d_s) affect the slip velocity (V_{sl}) and consequently Cutting Transport Ratio (*CTR*).

4.3 Figures interpretation:

From the obtained results, plotting depth vs. Cuttings Transport Ratio (*CTR*) for three cases (Normal, Sifferman's and inclined).
Figures 2-6 represent the plot of *CTR* vs. depth for wells Rumaila -273, Rumaila -301, Rumaila -285, Rumaila -283 and Rumaila -281 respectively.

From these figures, it has been realized that Sifferman's method gave an approximate values of *CTR* i.e. not accurate as the other methods mentioned above. Furthermore, the methods applied in this study when small angles of inclination are considered also gave some abnormal values which confirm that there is no ideal method of the *CTR* determination when the case of inclination angle is considered.
In addition, Figures 2-6 plotted showed that the inclination angles hence were so low and near to 1° or less (vertical wells) subsequently it had a slight effect on *CTR* calculated values that took angle of inclination into consideration, but when the angle of inclination increases, it is supposed that it gives higher effect on calculated *CTR* values and that point is extremely clear for inclined wells (deviated wells) and horizontal wells where the effect of gravity is obvious.

4.4 Statistical study of normal and inclined values of CTR:

The Paired-Samples T- test procedure compares the means of two variables for a single group. It computes the differences between values of the two variables for each case and tests whether the average differs from 0.

Statistics: For each variable: mean, sample size, standard deviation, and standard error of the mean. For each pair of variables: correlation, average difference in means, t test, and confidence interval for mean difference standard deviation and standard error of the mean difference will be determined as shown below by using SPSS program :

T-test for well Rumaila-273

Paired Samples Statistics

		Mean	N	Std. Deviation	Std. Error Mean
Pair 1	CTR_NOR	94.964125	4	5.062440	2.531220
	CTR_INC	96.184533	4	3.660406	1.830203

Paired Samples Correlations

		N	Correlation	Sig.
Pair 1	CTR_NOR & CTR_INC	4	.998	.002

Paired Samples Test

		Paired Differences					t	df	Sig. (2-tailed)
					95% Confidence Interval of the Difference				
		Mean	Std. Deviation	Std. Error Mean	Lower	Upper			
Pair 1	CTR_NOR - CTR_INC	-1.220408	1.430310	.715155	-3.496350	1.055535	-1.706	3	.186

T-test for well Rumaila -301

Paired Samples Statistics

		Mean	N	Std. Deviation	Std. Error Mean
Pair 1	CTR_NOR	93.228835	4	4.095601	2.047801
	CTR_INC	94.927175	4	2.840964	1.420482

Paired Samples Correlations

		N	Correlation	Sig.
Pair 1	CTR_NOR & CTR_INC	4	.998	.002

Paired Samples Test

		Paired Differences					t	df	Sig. (2-tailed)
					95% Confidence Interval of the Difference				
		Mean	Std. Deviation	Std. Error Mean	Lower	Upper			
Pair 1	CTR_NOR - CTR_INC	-1.698340	1.276486	.638243	-3.729515	.332835	-2.661	3	.076

T-test for well Rumaila -285

Paired Samples Statistics

		Mean	N	Std. Deviation	Std. Error Mean
Pair 1	CTR_NOR	91.375008	4	7.571113	3.785557
	CTR_INC	93.521985	4	5.441166	2.720583

Paired Samples Correlations

		N	Correlation	Sig.
Pair 1	CTR_NOR & CTR_INC	4	.999	.001

Paired Samples Test

		Paired Differences					t	df	Sig. (2-tailed)
					95% Confidence Interval of the Difference				
		Mean	Std. Deviation	Std. Error Mean	Lower	Upper			
Pair 1	CTR_NOR - CTR_INC	-2.146978	2.145157	1.072579	-5.560401	1.266446	-2.002	3	.139

T-test for well Rumaila -283

Paired Samples Statistics

		Mean	N	Std. Deviation	Std. Error Mean
Pair 1	CTR_NOR	89.538175	4	7.126445	3.563223
	CTR_INC	91.980903	4	5.338956	2.669478

Paired Samples Correlations

		N	Correlation	Sig.
Pair 1	CTR_NOR & CTR_INC	4	.999	.001

Paired Samples Test

		Paired Differences					t	df	Sig. (2-tailed)
					95% Confidence Interval of the Difference				
		Mean	Std. Deviation	Std. Error Mean	Lower	Upper			
Pair 1	CTR_NOR - CTR_INC	-2.442728	1.800726	.900363	-5.308084	.422629	-2.713	3	.073

T-test for well Rumaila -281

Paired Samples Statistics

		Mean	N	Std. Deviation	Std. Error Mean
Pair 1	CTR_NOR	92.565325	4	5.744746	2.872373
	CTR_INC	94.328388	4	4.264596	2.132298

Paired Samples Correlations

		N	Correlation	Sig.
Pair 1	CTR_NOR & CTR_INC	4	1.000	.000

Paired Samples Test

		Paired Differences					t	df	Sig. (2-tailed)
					95% Confidence Interval of the Difference				
		Mean	Std. Deviation	Std. Error Mean	Lower	Upper			
Pair 1	CTR_NOR - CTR_INC	-1.763063	1.484251	.742125	-4.124837	.598711	-2.376	3	.098

As shown above from the statistical correlation between normal *CTR* and inclined *CTR* the difference between standard deviation for both normal and inclined *CTR* are relatively low also , the same thing applied on the difference between standard error mean and that means that the values of *CTR* are approximate and subsequently it means that the effect of angle of inclination on inclined *CT*R values had slightly effect, because the angle of inclination does not exceed 1.75° but it is reasonable that when the angle of inclination is high and that reflects on the values of *CTR* for inclination and subsequently the difference between normal *CT*R and inclined *CTR* will be high and the analysis for that case will be absolutely different especially for deviated and horizontal wells.

5 CONCLUSIONS

1- From the obtained results of *CTR* during the case of inclination, the hole inclination angle has slight effect on *CTR* values, especially for angles less than 1°, whereas for inclination angles greater than 1°, the *CTR* values seemed to be slightly decreased.
2- For shallow depths, high rate of penetration values are used to achieve maximum drilling efficiency leading to high cuttings concentration and consequently low *CTR*, i.e. *CTR* values are inversely proportional with cuttings concentration.
3- In general, low inclination angles taken in the present study did not show clearly an effective influence on the *CTR* values. Further investigation for high inclination angles i.e. (derived or horizontal wells) is required for future studies.
4- The calculations obtained in this study when small values of inclination angles are considered showed abnormal values of cutting density, slip velocity, minimum annular velocity and cutting transport ratio due to the inexact determination of cutting size. Accurate determination of the cutting size is required to give more precise results.

NOMENCLATURE

$C_{conc.}$: cutting concentration, percentage.
CTR : cutting transport ratio ,percentage or fraction.
d_{hole} or D_h : hole diameter ,in..
d_{pipe} or OD_p : pipe outside diameter ,in.
d_s : cutting diameter ,in.
N : rotary speed ,RPM.
$N_{Re:}$ reynold's number, dimensionless.
Q : flow rate ,gal./min.
ROP : rate of penetration ,ft/hr.
V_{cut} : cutting transport velocity ,ft/sec.
$V_{min.}$: minimum annular velocity ,ft/min.
V_{sl} : slip velocity ,ft/min
Y_p : yield point (lb/100ft^2).
θ : angle of inclination ,degree.
μ_a : apparent viscosity c.p.
μ_e : effective viscosity ,c.p.
μ_p : plastic viscosity c.p.
ρ_f *or* ρ_m : fluid mud density ,lb/gal..
ρ_s : cutting density ,lb/gal.
τ_g : gel strength ,lb/100ft^2.
Φ_{300} : dial reading @ 300 rpm.
Φ_{600} : dial reading @ 600 rpm.

ACKNOWLEDGMENTS

The author is grateful for the assistance provided by Dr. Ali Hussain Abbar, Faculty of Engineering,Chemical Engineering department, *University of Al- Qadisiyah.*

REFERENCES

- Chein , S. 1972. *Annular Velocity for Rotary Drilling Operations*. International Journal of Rock Mechanics, **9**(3), PP. 403-416.

- Darley , H. ,and Gray , G. 1988. *Composition and Properties of Drilling and Completion Fluids*. Gulf professional publishing, Houston, Texas. USA.

- Guo , B. , Herland , G., and Rajitar , J. 1993. *Computer Simulation Predicts Unfavorable Mud Rate for Aerated Mud Drilling*. In: *The SPE Eastern regional conference*, 2-4 Nov. 1993, *Pittslourgh*, Panama.

- Hopkin , E. 1967. Factors Affecting *Cuttings Removal During Rotary Drilling*. Journal of Petroleum Technology . **19**(6), PP. 807-814.

- Hussani , S. and Azar , J. 1983. *Experimental Study of Drilled Cuttings Transport Using Common Drilling Muds.* SPE Journal. **23**(1), PP. 11-20.

- Indra , G. , and Rudi , R. . 2002. *Determining Cutting Transport Parameter in a Horizontal Coiled Tubing Underbalanced Drilling Operation*. In: *The SPE Asia pacific oil and gas conference and exhibition, 8-10 October 2002, Melbourne*, Australia.

- Jerzy, S., Pvel, V., Leszek, P. and Marcin, Z. 2013. *Slip Velocities in Mixture Vertical Pipe Flow***.** *In: The Tenth ISOPE Ocean Mining and Gas Hydrates Symposium, 22-26 September, 2013, Szczecin,* Poland**.**

- Lee, J., Friedhelm , J. , Toups , B. , and Vanort , E. 2004. *A New Approach to Deep Water Drilling Using SBM with Fluid Rheology* . In: *The AADE drilling fluids technical conference, 6-7 April 2004, Houston*, Texas. USA.

- Luo , Y. 1994. *Simple Charts to Determine Hole Cleaning Requirements in Deviated Wells.* In: *The SPE /IADOC drilling conference, 15-18 Feb.1994, Dallas,* Texas. USA.

- Mohammadsalehi, M. and Malekzadeh, N. 2011. *Optimization of Hole Cleaning and Cutting Removal in Vertical, Deviated and Horizontal Wells*. In: *The SPE Asia Pacific Oil and Gas Conference and Exhibition, 20-22 September 2011, Jakarta,* Indonesia.

- Mojisola , G. , 2005. *Development and Evaluation of Various Drilling Fluids for Slim Hole Wells.* Msc. thesis, University of Oklahoma.

- Moore, P.L., 1974. *Drilling Practices Manual*. Petroleum Publishing Company, Tulsa.

- Onuoha, M., Ismail, I., Piroozian, A., Mamat, N., and Ismail, A. 2015. *Improving the Cuttings Transport Performance of Water-based Mud Through the Use of Polypropylene Beads.* Sains Malaysiana **44**(4), PP. 629–634.

- Paden, J.M., Ford, J.T. and Obyeneyin, M.B. 1990. *Comprehensive Experimental Investigation of Drilled Cuttings Transport in Inclined Wells Including the Effects of Rotation and Eccentricity*. In: *The European petroleum conference, 21-24 Oct.1990*, *The Hague*, Netherlands.

- Rabia , H. , 2001. *Well Engineering and Construction*. Entrac Consulting, London, UK.

- Sifferman , T. R. , and Becker , T.E. 1992. *Hole Cleaning in Full Scale Inclined Wellbores.* SPE Drilling Engineering Journal. **7**(2), PP. 115-120.

- Wolfgang, F.P., 2007. *Drilling Engineering*. DEPARTMENT 313086, March, 2007, Curtin University of Technology, Australia.

Table 1. Parameters of well Rumaila -273.

Depth (m)	**Specific gravity**	**ρ_f (lb/gal)**	**τ_g (lb/100ft^2)**	**ROP (m/hr)**	**ROP (ft/hr)**	**N (rpm)**	**d_s (in.)**	**ρ_s (lb/gal)**
525	1.08	8.9964	10	9.495	31.153	100	0.0623	24.43
1917	1.17	9.7461	17	1.7662	5.795	80	0.0144	123.15 **(abnormal value)**
2332	1.22	10.162	5	1.454	4.77	70	0.0136	45.5
2395	1.19	9.9127	5	4.666	15.31	60	0.051	10.61

Table 2. Parameters of well Rumaila -301.

Depth (m)	**Specific gravity**	**ρ_f (lb/gal)**	**τ_g (lb/100ft^2)**	**ROP (m/hr)**	**ROP (ft/hr)**	**N (rpm)**	**d_s (in.)**	**ρ_s (lb/gal)**
460	1.06	8.8298	8	12.74	41.914	100	0.0838	18.004
1850	1.14	9.4962	8	2.61	8.5869	70	0.0245	40.875
2296	1.17	9.7461	15	2.28	7.501	80	0.0187	86.831 **(abnormal value)**
2346	1.18	9.8294	14	2.3	7.567	50	0.0302	54.379

Table 3. Parameters of well Rumaila -285.

Depth (m)	Specific gravity	ρ_f lb/gal)	τ_g (lb/100ft^2)	ROP (m/hr)	ROP (ft/hr)	N (rpm)	d_s (in.)	ρ_s (lb/gal)
461	1.07	8.9131	16	15.36	50.534	90	0.112	22.641
1850	1.12	9.3296	12	3.48	11.449	60	0.038	39.676
2288	1.17	9.7461	10	2.89	9.508	80	0.023	51.528
2358	1.15	9.5795	10	6	19.74	50	0.0789	21.759

Table 4. Parameters of well Rumaila -283.

Depth (m)	Specific gravity	ρ_f (lb/gal)	τ_g (lb/100ft^2)	ROP (m/hr)	ROP (ft/hr)	N (rpm)	d_s (in.)	ρ_s (lb/gal)
503	1.08	8.996	15	10.93	35.959	80	0.0898	25.048
1918	1.14	9.496	14	3.29	10.824	80	0.027	59.325
2325	1.17	9.7461	14	2.89	9.508	80	0.0237	66.513 **(abnormal value)**
2378	1.15	9.579	12	4.9	16.121	50	0.0645	27.458

Table 5. Parameters of well Rumaila -281.

Depth (m)	Specific gravity	ρ_f (lb/gal)	τ_g (lb/100ft^2)	ROP (m/hr)	ROP (ft/hr)	N (rpm)	d_s (in.)	ρ_s (lb/gal)
500	1.08	8.996	16	10.17	33.459	80	0.0836	27.388
1955	1.15	9.579	14	3.6	11.844	60	0.0395	36.355
2377	1.18	9.829	11	3.28	10.791	80	0.0269	49.126
2421	1.15	9.579	14	2.8	9.212	50	0.0367	46.1

Table 6. Annular velocity calculations of well Rumaila -273.

Depth (m)	Q (L/min.)	Q (gal/min.)	d_{hole} (in.)	OD_{pipe} (in.)	V_{min} (ft/min)	CTR by Siff. graph (%)
525	2000	528.36	17.5	5	46.026	near 78%
1917	1400	369.81	12.25	5	72.446	near 91%
2332	1500	396.225	8.5	5	205.45	unknown
2395	760	200.754	6	3.5	207.093	unknown

Table 7. Annular velocity calculations of well Rumaila -301.

Depth (m)	Q (L/min.)	Q (gal/min.)	d_{hole} (in.)	OD_{pipe} (in.)	V_{min} (ft/min)	CTR by Siff. graph (%)
460	2250	594.337	17.5	5	51.773	near 79.5%
1850	1200	316.98	12.25	5	62.097	near 84%
2296	1500	396.225	8.5	5	205.45	unknown
2346	825	217.923	5.875	3.5	239.798	unknown

Table 8. Annular velocity calculations of well Rumaila -285.

Depth (m)	Q (L/min.)	Q (gal/min.)	d_{hole} (in.)	OD_{pipe} (in.)	V_{min} (ft/min)	CTR by Siff. graph (%)
461	2287	604.111	17.5	5	52.624	near 79%
1850	1220	322.263	12.25	5	63.1319	near 83.5%
2288	1525	402.828	6	3.5	415.548	unknown
2358	838	221.357	6	3.5	228.347	unknown

Table 9. Annular velocity calculations of well Rumaila -283.

Depth (m)	Q (L/min.)	Q (gal/min.)	d_{hole} (in.)	OD_{pipe} (in.)	V_{min} (ft/min)	CTR by Siff. graph (%)
503	2135	563.96	17.5	5	49.127	near 79.5%
1918	1830	483.394	12.25	5	94.6978	near 93%
2325	1448	382.489	8.5	5	198.327	unknown
2378	750	198.112	6	3.5	204.368	unknown

Table 10. Annular velocity calculations of well Rumaila -281.

Depth (m)	Q (L/min.)	Q (gal/min.)	d_{hole} (in.)	OD_{pipe} (in.)	V_{min} (ft/min)	CTR by Siff. graph (%)
500	2240	591.696	17.5	5	51.543	near 81%
1955	1982	523.545	12.25	5	102.5635	near 97%
2377	1525	402.828	8.5	5	208.873	Unknown
2421	780	206.037	6	3.5	212.543	Unknown

Table 11. Slip velocity and cuttings transport ratio calculations of well Rumaila -273.

Depth (m)	d_{hole} (in.)	OD_{pipe} (in.)	Φ_{300}	Φ_{600}	n	K	μ_e (c.p)	V_{sl} (ft/min)	CTR (%)	$C_{conc.}$ (%)
525	17.5	5	22	30	0.447	1.353	227.172	5.335	88.409	1.389
1917	12.25	5	24	30	0.322	3.227	213.053	4.639	93.597	0.171
2332	8.5	5	22	32	0.540	0.757	42.766	3.389	98.351	0.060
2395	6	3.5	20	30	0.585	0.522	31.486	1.035	99.500	0.188

Table 12. Slip velocity and cuttings transport ratio calculations of well Rumaila -301.

Depth (m)	d_{hole} (in.)	OD_{pipe} (in.)	Φ_{300}	Φ_{600}	n	K	μ_e (c.p)	V_{sl} (ft/min)	CTR (%)	$C_{conc.}$ (%)
460	17.5	5	44	30	0.6517	0.481	115.433	6.395	87.649	1.676
1850	12.25	5	50	30	0.689	0.421	87.041	4.553	92.667	0.298
2296	8.5	5	58	32	0.728	0.373	50.8178	7.505	96.347	0.0966
2346	5.875	3.5	52	30	0.7	0.407	41.282	8.985	96.253	0.085

Table 13. Slip velocity and cuttings transport ratio calculations of well Rumaila -285.

Depth (m)	d_{hole} (in.)	OD_{pipe} (in.)	Φ_{300}	Φ_{600}	n	K	μ_e (c.p)	V_{sl} (ft/min)	CTR (%)	$C_{conc.}$ (%)
461	17.5	5	26	38	0.547	0.857	164.922	9.899	81.190	2.147
1850	12.25	5	27	39	0.530	0.989	130.613	6.068	90.388	0.401
2288	6	3.5	40	65	0.700	0.508	44.435	6.416	98.456	0.059
2358	6	3.5	26	40	0.621	0.540	37.755	10.270	95.503	0.229

Table 14. Slip velocity and cuttings transport ratio calculations of well Rumaila -283.

Depth (m)	d_{hole} (in.)	OD_{pipe} (in.)	Φ_{300}	Φ_{600}	n	K	μ_e (c.p)	V_{sl} (ft/min)	CTR (%)	$C_{conc.}$ (%)
503	17.5	5	40	65	0.700	0.508	136.632	9.350	80.967	1.641
1918	12.25	5	25	36	0.526	0.942	101.311	6.493	93.143	0.245
2325	8.5	5	28	42	0.585	0.731	51.611	7.716	96.109	0.127
2378	6	3.5	22	32	0.540	0.757	36.725	10.946	94.644	0.211

Table 15. Slip velocity and cuttings transport ratio calculations of well Rumaila -281.

Depth (m)	d_{hole} (in.)	OD_{pipe} (in.)	Φ_{300}	Φ_{600}	n	K	μ_e (c.p)	V_{sl} (ft/min)	CTR (%)	$C_{conc.}$ (%)
500	17.5	5	40	60	0.585	1.044	218.962	8.146	84.195	1.399
1955	12.25	5	30	46	0.616	0.643	89.583	6.518	93.645	0.247
2377	8.5	5	38	58	0.610	0.848	65.981	6.297	96.985	0.136
2421	6	3.5	29	46	0.665	0.458	41.069	9.699	95.436	0.115

Table 16. Cutting velocity, annular velocity and cuttings transport ratio calculations for case of inclination for well Rumaila -273.

Depth (m)	V_{cut} (ft/sec)	V_{cut} (ft/min)	Angle of inc.(θ), Degree	V_{min} (ft/min)	CTR for inclination , (%)
525	0.678	40.691	1	44.405	91.637
1917	1.130	67.807	1.75	71.489	94.849
2332	3.368	202.061	1	204.805	98.661
2395	3.434	206.058	1.25	206.905	99.591

Table 17. Cutting velocity, annular velocity and cuttings transport ratio calculations for case of inclination for well Rumaila -301.

Depth (m)	V_{cut} (ft/sec)	V_{cut} (ft/min)	Angle of inc.(θ), Degree	V_{min} (ft/min)	CTR for inclination , (%)
460	0.7563	45.379	1	49.768	91.1803
1850	0.9591	57.544	1	61.043	94.268
2296	3.299	197.945	0.25	203.533	97.254
2346	3.847	230.813	0.25	237.936	97.006

Table 18. Cutting velocity, annular velocity and cuttings transport ratio calculations for case of inclination for well Rumaila -285.

Depth (m)	V_{cut} (ft/sec)	V_{cut} (ft/min)	Angle of inc.(θ), Degree	V_{min} (ft/min)	CTR for inclination , (%)
461	0.712	42.726	0.25	49.482	86.345
1850	0.951	57.064	0.5	61.653	92.557
2288	6.819	409.132	0.75	414.015	98.821
2358	3.637	218.077	0.75	226.235	96.394

Table 19. Cutting velocity, annular velocity and cuttings transport ratio calculations for case of inclination for well Rumaila -283.

Depth (m)	V_{cut} (ft/sec)	V_{cut} (ft/min)	Angle of inc.(θ), Degree	V_{min} (ft/min)	CTR for inclination , (%)
503	0.663	39.777	0.5	46.4015	85.723
1918	1.47	88.204	1	93.101	94.741
2325	3.177	190.611	0.5	196.42	97.043
2378	3.224	193.422	0.5	202.023	95.742

Table 20. Cutting velocity, annular velocity and cuttings transport ratio calculations for case of inclination for well Rumaila -281.

Depth (m)	V_{cut} (ft/sec)	V_{cut} (ft/min)	Angle of inc.(θ), Degree	V_{min} (ft/min)	CTR for inclination , (%)
500	0.723	43.397	0.75	49.231	88.149
1955	1.601	96.046	0.5	101.074	95.0249
2377	3.376	202.577	0.25	207.296	97.723
2421	3.381	202.844	0.25	210.383	96.417

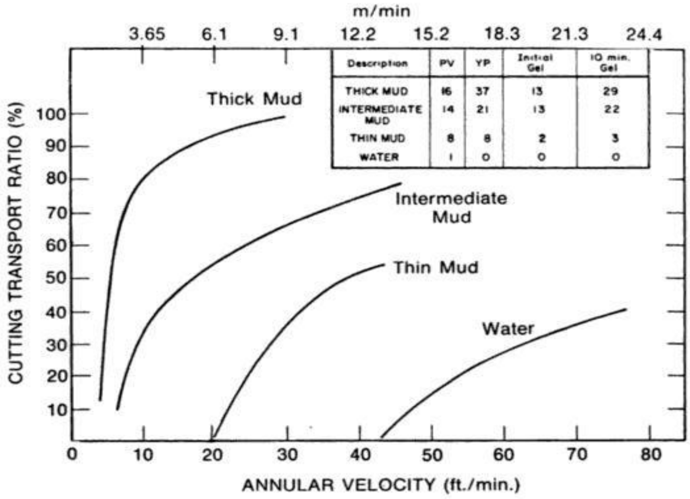

Figure 1. Sifferman's graph for cutting transport ratio determination

(**Sifferma**n and **Becker, 1992**).

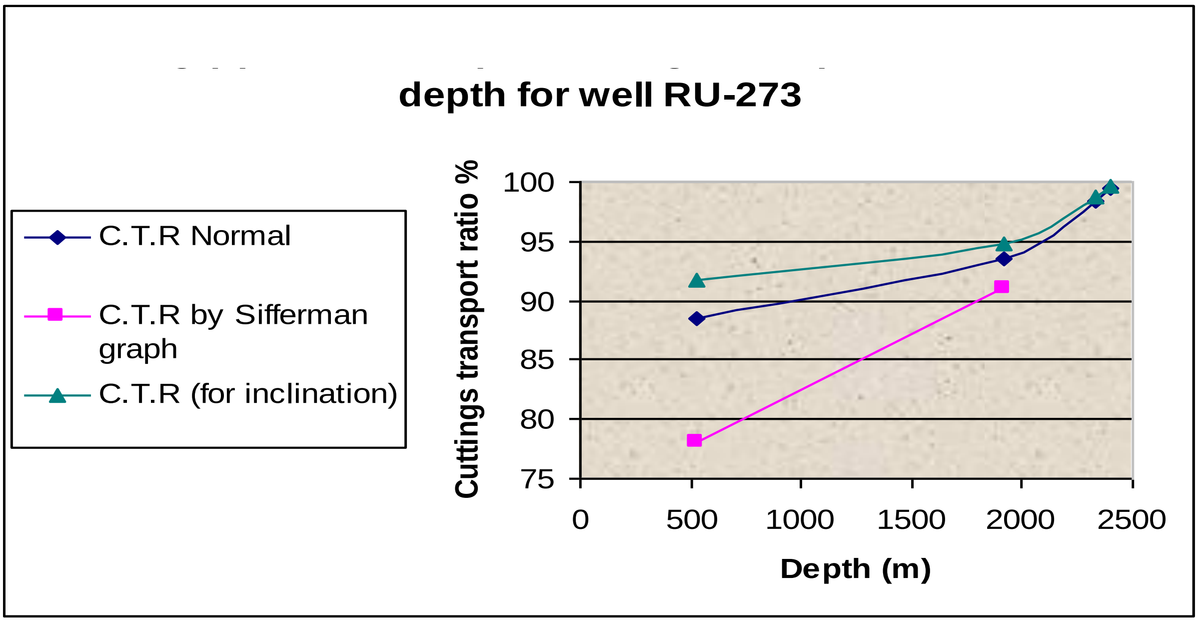

Figure 2. Relationship of cuttings transport ratio vs. depth for well Rumaila -273.

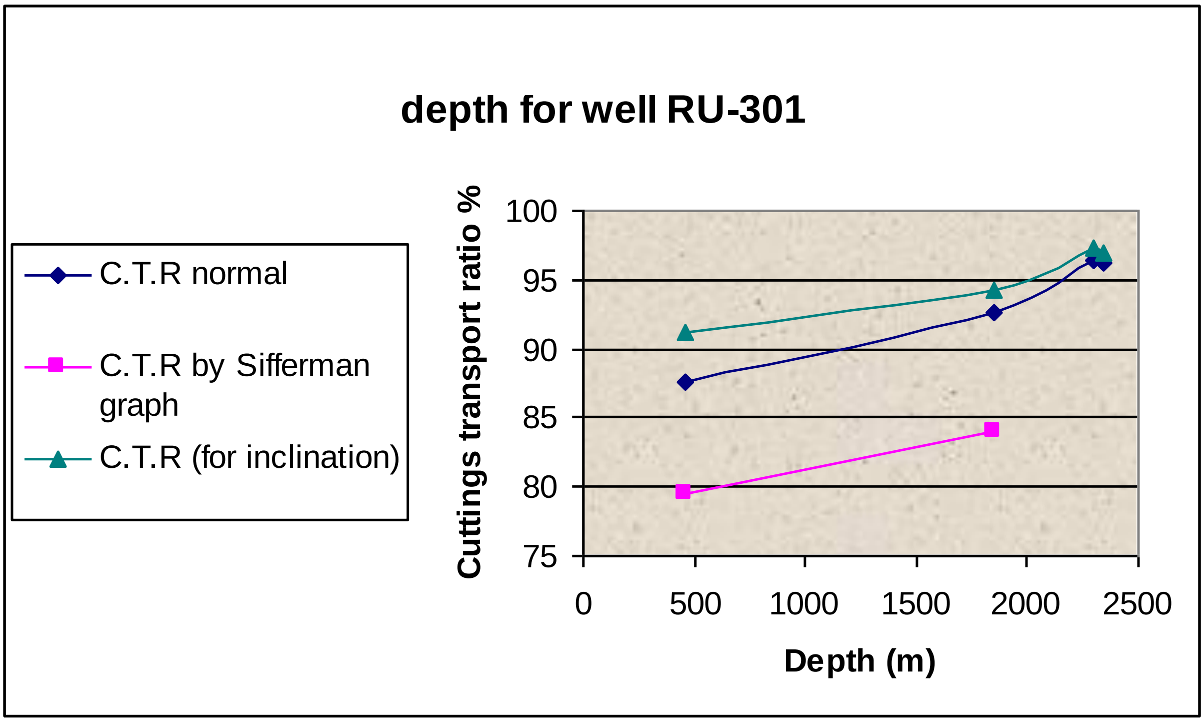

Figure 3. Cuttings Transport Ratio (*CTR*) vs. depth for well Rumaila -301.

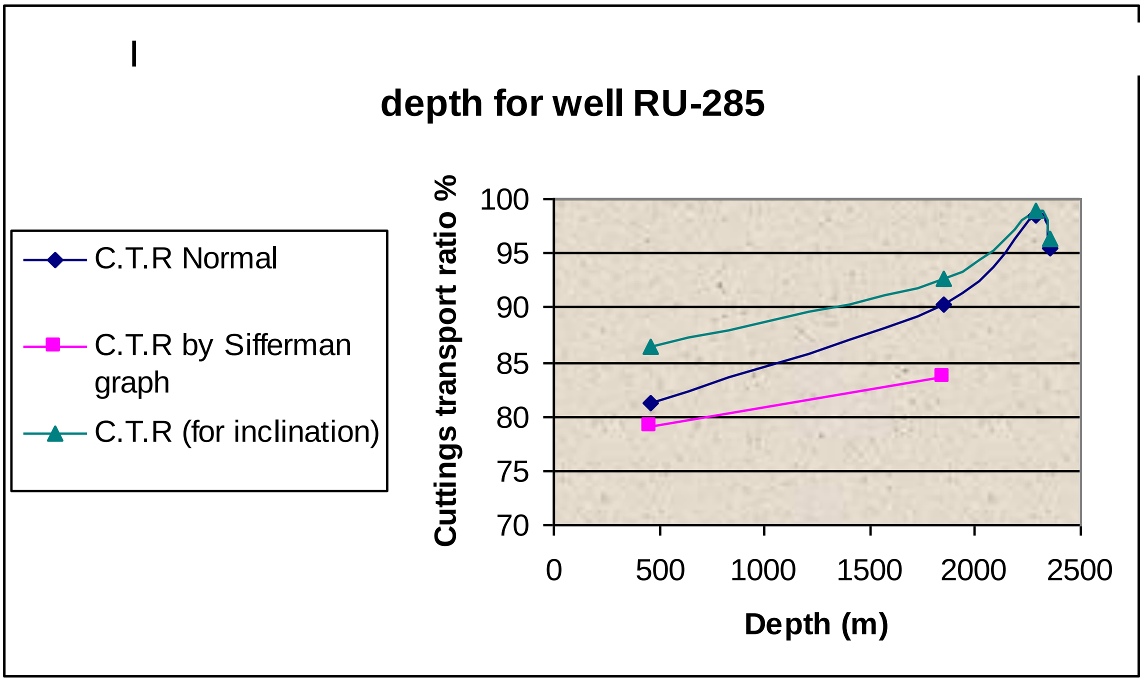

Figure 4. Cuttings Transport Ratio (*CTR*) vs. depth for well Rumaila -285.

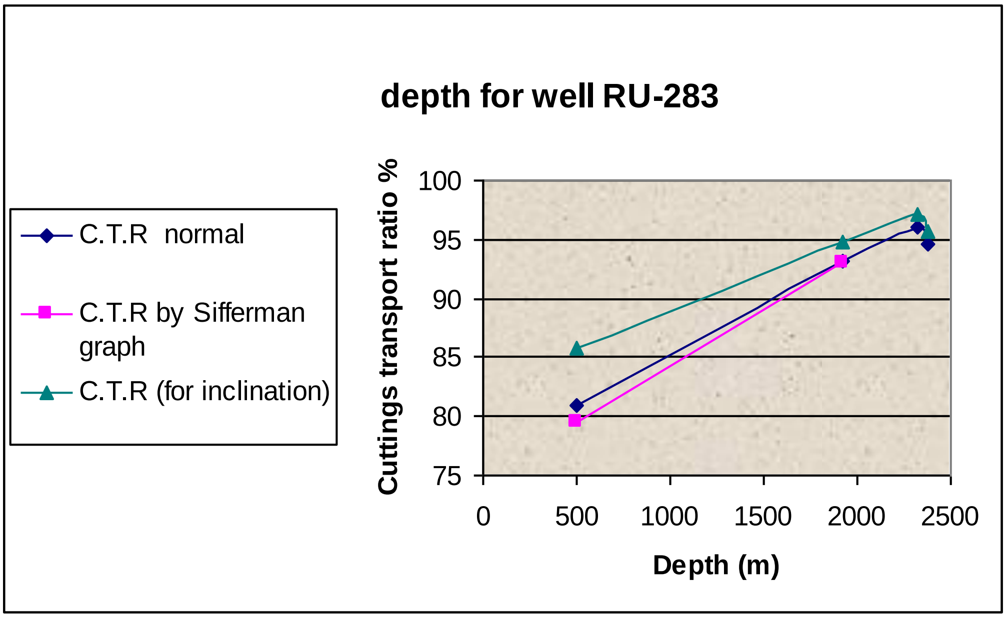

Figure 5. Relationship of cuttings transport ratio vs. depth for well Rumaila -283.

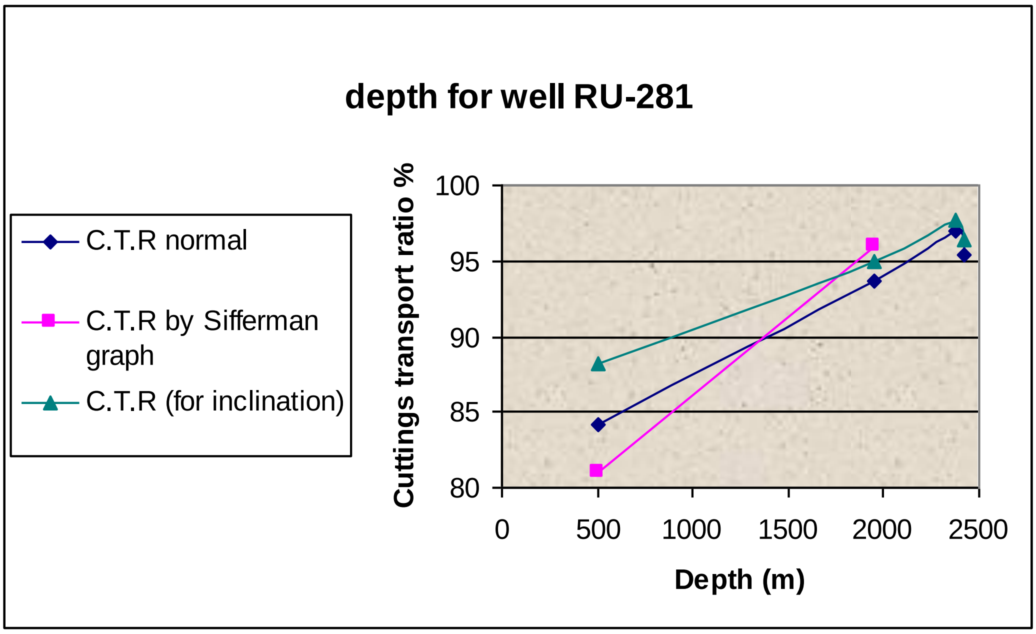

Figure 6. Relationship of cuttings transport ratio vs. depth for well Rumaila -281.

أثر معالجة النفايات الحضرية الصلبة على البيئة الحضرية

الباحث: المدرس د. خالد عبد الوهاب
قسم هندسة العمارة
جامعــة النهريــن
almudares99@yahoo.com

الباحث: المدرس د. نوفـل جوزيـف رزقـو
قسم هندسة العمارة
جامعــة النهريــن
Mahabanawfal@yahoo.com

الخلاصة

ان ازدياد عدد السكان وارتفاع مستوى المعيشة في المدن فضلاً عن زيادة النشاطات التجارية والصناعية والزراعية حول العالم ادت الى انتاج الكثير من المخلفات التي لايحتاج لها الانسان بما تحويه من مواد قابلة للتحلل والتفسخ او مواد غير قابلة للتحلل ،تتباين اشكال هذه المواد ما بين المواد الصلبة والسائلة والغازية الا ان المواد الصلبة تعتبر الاكثر ضرراً على البيئة ، لذلك تعتبر عملية جمع النفايات ونقلها ومن ثم التخلص منها مشكلة كبيرة تعاني منها مدن العالم. أذ ان تكدس النفايات سواءً في الازقة أوالساحات أوالمناطق السكنية يؤثر بشكل كبير على التصاميم الحضرية المستدامة لتلك المناطق وصحة سكانها كما ان هذه الحالة ستكون مؤشراً خطيراً على تردي مستوى الحياة في تلك الاماكن ومن ثم على المشهد الحضري للمدينة .

وبأعتبار أن النظافة معيار اساسي لجمال المدينة ومؤشراً على مدى الحماية التي توفرها المدينة لبيئتها ومستوى المحافظة على صحة سكانها، فان تكدس النفايات وتركها بدون معالجة يؤثر بشكل كبير على سلوكيات افراد تلك المناطق العملية والنفسية تجاه مجتمعهم وبيئتهم ويؤثر بشكل اساس وكبير على صحتهم الجسمية والنفسية ومن ثم تصرفاتهم تجاه مناطقهم ومدنهم. من هنا ظهرت **المشكلة البحثية العامة** وهي ان الحضارة والمدنية ادت الى نمط حياة ينتج الكثير من الملوثات ومنها (النفايات البلدية الصلبة) التي اصبحت مشكلة كبيرة تواجه المدن ابتداءً من عمليات جمعها و نقلها ومن ثم التخلص او الاستفادة منها من خلال عمليات التحويل أوالتدوير او استخدامها كمصدر لانتاج الطاقة بالشكل الذي يخدم النمو المستدام للمدن ، وعليه فقد تم صياغة **المشكلة البحثية الخاصة** المتعلقة بـعدم وجود وضوح كافي لتاثير اساليب جمع النفايات و نقلها و التخلص منها او ساليب معالجتها للاستفادة منها على المدينة وبيئتها الحضرية. **فرضية البحث** : ان عملية جمع ونقل النفايات واساليب التخلص أو الاستفادة منها تؤثر بشكل كبير على البيئة الحضرية للمدينة وبطريقة تفرض وجودها على مشهدها الحضري .

الكلمات الرئيسية:النفايات الحضرية الصلبة، ،مكبات النفايات،المتنزهات الايكولوجية.

The Impact of Urban Solid Waste Management on Urban Environment

ABSTRACT

The growing population and the rising standard of living in cities as well as the increased commercial, industrial and agricultural activities around the world led to massive production of waste containing different materials and one of them is the municipal solid waste (MSW), so there is a major problem facing the cities around the

world about the waste, how to collect, transfer it and how to discard it. Because the accumulation of wastes, whether in the city alleys or in its squares and especially in its residential areas affect the health of their populations besides this situation will be a major indication of the deteriorating quality of life in the city, as hygiene considered a fundamental criterion for the city beauty as well as an indication of the protection provided by the city to their environment and the level of protection provided to the health of city residence. The accumulated waste which is left in the city without treatment significantly affects the psychological behavior of the residence of these areas towards their community and environment and therefore their behavior towards their regions and their cities. From here emerged **the general research problem** concerning the modern civilization and its lifestyle that produced great amounts of (municipal solid waste), which became a big problem facing the modern cities concerning their collection, transportation and finally their disposal, how can these great amounts of waste be used whether by recycling, energy recovery or transferring to plant fertilizers ... etc. To serve the sustainable growth of these modern cities, this lead to **the specific research problem** concerning the lack of clarity concerning the impact of waste collection, transporting and treating and city urban environment and its townscape. **Research Hypothesis**: The process of collecting, transporting and treating city solid waste or using it has a great impact on city urban environment and its townscape.

Key words: Urban solid waste, landfills, Ecological urban park.

1-المقدمة:

تعتبر النفايات الحضرية الصلبة من أهم القضايا البيئية التي تستحوذ على اهتمام المجالس البلدية والحكومات والرأي العام الوطني والعالمي نظراً لارتباطها بشكل مباشر بحياة الناس.اذ تزداد كمية النفايات الصلبة مع مرور الزمن بزيادة عدد السكان وتحسن دخل الفرد وتحوله إلى إنسان مستهلك وسعيه إلى انتهاج أسلوب ونمط الحياة العصرية التي تعتمد بشكل كبير على الاستهلاك المفرط للمنتجات ، مما أدى إلى زيادة الطلب على المواد الخام الأولية لتلبية احتياجات الناس و إلى استنزاف العديد من الموارد الطبيعية للبيئة .ولم يقتصر خطر استنزاف الموارد الطبيعية على التعدي على مخزون الأجيال القادمة فحسب، بل تسبب في حدوث اختلال للتوازن البيئي نتيجة لفقدان البيئة لبعض أهم مكوناتها .وقد استرعى ذلك انتباه علماء البيئة، مما حذا بالمنظمات الإقليمية والدولية إلى عقد الاتفاقيات ووضع البرامج والأنشطة اللازمة للحد من استنزاف الموارد؛ وذلك بتقليل إنتاج النفايات و بتشجيع الاستفادة منها وتقليل كمياتها المنتجة او اعادة تدويرها.وعلى الرغم من أن مشكلة النفايات الصلبة الحضرية تشكل هاجساً اجتماعياً واقتصادياً وبيئياً إلا أن معظمها يمكن أن يكون ذو فائدة كبيرة، إذا ما أُحسن استغلاله وفق الحاجات والإمكانيات المتاحة الذي يندرج ضمن مبدأ تحقيق التنمية المستدامة مع الحفاظ على البيئة الطبيعية أكثر نقاءاً و جمالاً. لذلك يعتبر موضوع جمع و نقل النفايات ومن ثم التخلص منها واحدة من المشاكل الرئيسية التي تواجهها جميع دول العالم . و كنتيجة للتقدم التقني تم ايجاد عدة تقنيات و منظومات جديدة لجمع ونقل النفايات وعدة تقنيات للاستفادة منها ومن ثم التخلص منها التي اثرت بمجموعها بشكل بسيط على تخطيط المدينة وتصميمها الحضري وستؤثر مستقبلاً بشكل كبير.

2- تعريف المخلفات الصلبة:

المخلفات الصلبة هى المواد الصلبة أو شبه الصلبة التى تتولد نتيجة للأنشطة المختلفة .وهى مواد غير مرغوب فيها يراد التخلص منها ولكن يمكن الاستفادة من بعض مكوناتها وفى هذا السياق تستخدم كلمة " مخلفات " وليس نفايات لأن الأخيرة تعني المواد المتخلفة من الأنشطة البشرية التي لا يمكن الإفادة منها. .(Ranjith,2012,p.28)

لذلك يعتبر عدم اتباع الطرق المناسبة في عملية جمع ونقل وتخزين ومعالجة هذه النفايات واحدة من المشاكل التي تعاني منها دول العالم النامي والمتقدم على السواء. الا ان ان حجم هذه المشكلة في دول العالم النامي كبيرة

جداً على العكس لما موجود في دول العالم المتقدم التي اولت هذا الموضوع اهتماماً كبيراً وذلك لاهميته وما يمكن ان يسببه من مشاكل بيئية وصحية وجمالية سلبية على المدن و سكانها في حالة عدم معالجة هذه المشكلة بشكل دقيق ومدروس.مما تقدم فاننا نواجه عدة مشاكل تتعلق بالمواضيع الاتية:

- نقل النفايات.
- الاستفادة من النفايات.
- التخلص من النفايات.

3 - نظرة تاريخية على معالجة مشكلة النفايات:

ان تاريخ النفايات مرتبط بتاريخ الحضارة أذ تم خلال الاف السنين الماضية انتاج كميات كبيرة من النفايات و نجد من خلال نظرة الى التاريخ أن اليونانيين من الاوائل الذين تعاملوا مع النفايات ، أذ أصدورا في عام 500 قبل الميلاد فى أثينا أمر بعدم إلقاء القمامة فى الشوارع، وتم تخصيص موقع خارج المدينة لإلقاء المخلفات فيه، و بذلك يكون من اقدم مكبات النفايات البلدية الصلبة في العالم. كما صدرت عدة قوانين تتعلق بجمع ونقل النفايات إلى أماكن خارج النطاق العمراني وتم اعداد مواقع خاصة لردمها بمسافة لا تقل عن ميل واحد عن حدود المناطق السكنية، ومعاقبة كل من يرمي المخلفات في الشوارع أو يخالف تلك القوانين.

أما الرومان فقد أنشأوا إدارة خاصة للصحة العامة وجمع النفايات والتخلص منها وذلك في فترة حكم القيصر أغسطوس في العام الرابع عشر بعد الميلاد. في حين تم في عام 200 قبل الميلاد انشاء أول فرق للنظافة فى المدن تتكون من فردين يعملان على جمع المخلفات الصلبة من الشوارع ونقلها بعربات تجرها الخيول إلى مقالب مخصصة خارج المدن .ويعد هذا أول نظام لما يعرف الآن بإدارة المخلفات الصلبة.

(Chandrappa and Bhusan das,2012,p.10-11)

وفى عام (1388م) اصدر البرلمان البريطاني قراراً يمنع القاء المخلفات البلدية الصلبة في المسطحات المائية . وفى القرن الرابع عشر ومع زيادة تراكم المخلفات فى شوارع المدن الأوربية، بدأت البلديات فى تولى مسؤولية جمع المخلفات ونقلها إلى المقالب التي بدأ حجمها يزداد وبدأت مشاكلها فى التفاقم، وبعد أن أصبحت مصدراً للروائح الكريهة ومرتعاً لتوالد الحشرات والقوارض والحيوانات السائبة، بدأت بعض البلديات في إقامة حفر في الأرض واستخدامها في دفن المخلفات وكان ذلك بداية لما يعرف الآن بالمدافن الصحية .وفى عام (1875م) تم تشغيل أول محرقة لحرق المخلفات البلدية الصلبة فى انجلترا ومع الزيادة السكانية الكبيرة فى العالم ونمو المناطق الحضرية وزيادة دخل الفرد وتغير أنماط الاستهلاك،ارتفع حجم المخلفات البلدية الصلبة بشكل كبير وحدثت تغييرات جذرية فى مكوناتها .وأمام هذه التغييرات المتسارعة تراجعت قدرة البلديات فى معظم دول العالم على إدارة المخلفات بكفاءة. (deq.louisiana.gov/portal/Portals/0/.../DYK- Landfills. pdf).

4- مصادر المخلفات الصلبة:

لاتعد "المخلفات الصلبة " هي " القمامة " أو المخلفات البلدية المتولدة فى المنازل والمتاجر والمؤسسات فى المدن والقرى .وهذا اعتقاد خاطئ، حيث أن المخلفات الصلبة تتضمن المخلفات المتولدة من جميع الأنشطة البشرية وهى بذلك تتضمن:

3-1- المخلفات الزراعية والحيوانية.

3-2- المخلفات الحضرية الصلبة.

3-3- المخلفات الصناعية.(Ryidh A. Y. and Zaidun N. A., 2009, p.137)

5- كميات النفايات التي تنتج في مدن العالم:

تشكل النفايات تحدياً بيئياً واجتماعياً واقتصادياً أذ ينتج العالم اليوم كميات نفايات تصل الى (1.3) بليون طن سنوياً ومن المتوقع ان تتضاعف الى (2.2) بليون طن سنوياً في عام (2025)، مما يعني زيادة في انتاج النفايات للفرد الواحد على مستوى العالم من (1.2) كغم يومياً الى (1.42) كغم يومياً وهذه زيادة كبيرة وتعتبر هذه التخمينات اولية لكونها تختلف من قارة الى اخرى ومن بلد لاخر و من مدينة لاخرى بل ومن فصل الى اخر.

(Daniel H. and Perinaz T., 2012, p.8)

فعلى سبيل المثال ينتج الفرد الامريكي نفايات بمعدل (2) كغم يومياً حسب احصائيات عام (2011) مقارنةً بـ (1.7) كغم يومياً لما كان ينتجه عام (1980) (World Bank Report,2014,p15) وعما كان ينتجه من نفايات عام (1960) والتي كانت بمعدل (1.2) كغم. بينما ينتج الفرد الواحد في دول الاتحاد الاوربي ما معدله (1.4) كغم من النفايات يومياً وهنا نرى التباين في انتاج النفايات من دولة الى اخرى تبعاً لنمط الحياة والمستوى الاقتصادي.(Waste Management Services policy round table, 2013, p.10)

وفي العراق يبلغ تعداد السكان (32) مليون نسمة تقريباً وبسبب النمو الاقتصادي المتسارع ومستوى الدخل المرتفع ازدادت مشكلة النفايات في البلد.أذ تشير التقديرات الى ان العراق ينتج (31000) طن من النفايات يومياً و تنتج مدينة بغداد وحدها (1.5) مليون طن من النفايات سنوياً. ان الطرح المتسارع للنفايات مع فقدان الادارة الملائمة لمعالجتها مقترناً بتدهور البنى التحتية اللازمة لهذا الغرض ادى الى انتشار مواقع خزن النفايات وطمرها في مواقع عشوائية ومتعددة وبدون رقابة مما ادى الى تلوث الهوء فضلاً عن الحرق العشوائي وتلوث التربة والمياه الجوفية اضافة الى تعرض النفايات للعبث من قبل اشخاص يسعون للاستفادة من المخلفات الموجودة فيها (http://www.ecomena.org/swm-iraq).

وقد جرت دراسة في العراق عام (2007) لمعرفة كمية النفايات التي يتم جمعها من المحافظات التالية: (الانبار،السليمانية و ذي قار) .وقد اشارت النتائج الى ان نسبة النفايات التي يتم جمعها كانت (34%) لمحافظة الانبار ، (67%) للسليمانية و (45%) لمحافظة ذي قار وهذا سيوفر لنا المعلومة المتعلقة بكمية النفايات المنتشرة عشوائياً في الشوارع ومناطق الطمر العشوائية فضلاً عما يتم حرقه (United nation development group report,2009,p.6).

لذلك تم وضع الخطة الوطنية لادارة النفايات في العراق بالتنسيق مع الاختصاصين الدولين منذ عام (2007) والتي ارتكزت على عدة محاور احدها محور التنمية المستدامة حيث شملت الخطة انشاء (33) منطقة لطمر النفايات مصممة بشكل هندسي متكامل لطمر ما مقداره (600) مليون متر مكعب من النفايات في كافة محافظات العراق بحلول عام (2027).كما شملت الخطة موضوع اعادة تدوير النفايات وطريقة جمعها ونقلها ومنظومات اعادة الاستخدام.وكانت محافظة كركوك اول المحافظات التي وضعت مخططاً لانشاء مناطق طمر للنفايات مصممة هندسياً وبمساحة (20) هكتار شمال المحافظة وتبعد عنها بـ (10) كيلومترات.

ان الخطة الوطنية لمعالجة النفايات في العراق التي وضعت عام (2007) تم تصميمها لخدمة الاهداف الاتية :

- تحديد الخطة الخاصة بمعالجة النفايات للسنوات القادمة.

- توفير التقنيات اللازمة لمعالجة النفايات وضمن تدرج خاص بنوعها والمعالجات الملائمة لها.

الا ان العديد من الاستراتيجيات لم يتم تطبيقها ومنها :

- التنمية المستدامة .

- الاجراءات الاحترازية .(http://www.ecomena.org/swm-iraq)

6- النفايات على المستوى الحضري وتصميم المدينة:

تعتبر المعلومات الخاصة بكميات و مصادر وطبيعة مخلفات المدينة الاساس لتخطيط وتصميم خطة التخلص من النفايات فضلاً عن كونها تسهل السيطرة عليها والتخلص منها بسلاسة بما تشمله من (طريقة جمع النفايات، مناطق تجميعها و نقلها ومن ثم طريقة التخلص منها) ،الا ان النوعية والكمية الناتجة من النفايات تتاثر بشكل كبير بعدد من الظروف مثل (المناخ، الفصل من السنة ، الحالة الاقتصادية ، ومستوى الدخل وغيرها) ، فضلا عن نمط الفعالية التي تنتج النفايات، لذلك جرت دراسة على مدينة الناصرية عام (2008) بينت ان معدل النفايات المتولدة من الوحدات السكنية في المدينة قد بلغ ما معدله (0.68) (كغم /شخص/يوم) ما عدا النفايات الناتجة من الفعاليات التجارية والصناعية و المستشفيات ، وهذه النسبة مقاربة لما يتم توليده من النفايات في المدن العراقية الاخرى، وتشير الدراسات التي تمت في بغداد الى ان معدل النفايات التي يتم انتاجها تصل الى (0.7) (كغم/شخص/يوميا) من النفايات وان معدل انتاجها يزداد في فصل الصيف عن الشتاء بسبب زيادة أستهلاك الاغذية وخاصة الفاكهة والخضراوات .الا انه لا توجد معلومات محددة حول طبيعة المخلفات المنتجة في العراق وذلك لعدم اجراء تحاليل دورية على النفايات ، الا ان بعض الدراسات اشارت الى ان نسبة (63%) من النفايات هي مواد عضوية[1]. (Riydh A. y., 2009, p.140-141)

و لغرض تطبيق أفضل الخيارات لما يتعلق بالتنمية المستدامة فمن اللازم جمع معلومات عن النفايات المنتجة وعلى اعتبار ان لا يوجد الا القليل من المعلومات المتعلقة بانتاج النفايات من العراق واغلب هذه المعلومات غير

[1] اشارت دراسة الى ان ما نسبته (69.03%) من النفايات هو مواد عضوية كما هو موجود في النجف كما أشار اليه (Hamoud) أما (الجميلي) فان أشار الى أن ما معدله (70.6%) من النفايات في الفلوجة هي مواد عضوية أغلبها مواد غذائية.(Riydh A. y.,2009,p.140)

موثق و غير محدد ومن الصعب التاكد من تلك المعلومات. لذلك كانت هناك حاجة لوضع قاعدة بيانات تتعلق بالنفايات والكميات المنتجة التي أفترضت انتاج ما مقداره (1.4) (كغم/شخص/يوم) والتي على ضوئها وحسب سكان كل محافظة تم تحديد عدد وحجم مناطق ردم النفايات اللازمة في (بغداد) ، تبعاً لتوقعات النمو السكاني في بغداد و حتى عام (2027).حيث ترى الجهات الاستشارية أن مكبات النفايات هي الحل الافضل لمعالجة مشكلة النفايات لكون النفايات غير مصنفة وغير مفروزة. وان هذا الحل سيستمر لفترة ليست بالقصيرة على ان تكون نوع محطات ردم النفايات مسيطر عليها فيما يتعلق بأنتشار الغازات والملوثات البيئية وتكون عملية معالجة النفايات مشتركة ما بين الحكومة والافراد مما يتطلب وضع خطط لهذا الجهد تتمثل بالتالي:

اولاً: خطة قصيرة الامد لخمس سنوات يكون فيها دور الحكومة توعوي واعلامي لتوعية الناس بمضار النفايات وطرق معالجتها على المستوى الوطني او المحلي وهي جزء رئيس من تطوير البلد. وسيكون التعليم في كافة المراحل و المستويات المدخل لهذا الموضوع والوسيلة الافضل لنشر هذه الثقافة في المجتمع .

ثانياً: خطة متوسطة المدى تمتد من (5-10) سنوات تعتمد على زرع الثقافة والمعلومات الخاصة بخفض انتاج النفايات واهمية تدوير النفايات الذي سيمكن من الدخول في مواضيع بيئية أخرى مثل التنمية المستدامة والتغير المناخي. (Knowles, 2008,p.5-6)

توجد علاقة ما بين انتاج النفايات وطرق جمعها واساليب معالجتها وتقنيات الاستفادة او التخلص منها وبين المدينة وبيئتها ومشهدها الحضري التي تعرف كالاتي:

1-6- مفهوم البيئة الحضرية:

البيئة الحضرية هي كل ما يحيط بالإنسان من فراغات و شوارع و أماكن انتظار السيارات و ممرات المشاة و فراغات مفتوحة ومناطق خضراء و غيرها، و كتل المباني الخدمية و الإدارية، المباني السكنية و التجارية،مباني صناعية ومرافق عامة و غيرها، بالإضافة إلى تنسيق المواقع و الوظائف و الأنشطة التي يقوم بها الإنسان المختلفة باختلاف طبيعة و نوعية الموقع و الموضع و السكان و ظروفهم المختلفة.كما يراها أخرون بأنها تمثل كل عناصر و مكونات المنطقة الحضرية سواءاً كانت فيزيائية أو ثقافية،عملت الطبيعة على تكوينها او عمل الإنسان مع الطبيعة في إنشاؤها.

2-6- المشهد الحضري:

يعرف الحيدري (2010) المشهد الحضري بانه عبارة عن مجموعة الأشكال والتفاصيل المعمارية و الواجهات و منظومات الخدمات العامة كإنارة الطرق و مسالك الحركة،الجلوس و المساحات الخضراء و غيرها، و التي تمتزج مع الشكل التكويني للفضاء.يعتمد تنظيم المشهد الحضري على المبادئ الأساسية المتمثلة بكل من الكثافة البصرية، حيث التماسك الهيكلي و التنظيم الانسيابي للمباني، و الاستمرارية و التجانس، من حيث الاستمرارية و التجانس ضمن تكوينات المشهد الحضري و تناغم العلاقات بين مكوناته البصرية كالمقياس و الارتفاع و غيرها.(بن مشيرح،2015 ،ص31-35)

7- منظومات جمع ونقل النفايات:

واحدة من اكثر التحديات التي تواجه التخطيط الحضري المعاصر وواحدة من الاهداف التي يجب حلها في تخطيط وتصميم المدن هي عملية جمع و نقل النفايات ومعالجتها و الاستفادة ثم التخلص منها، لتكون المشكلة التي اصبحت هاجساً للحكومات المحلية في معظم دول العالم الامر الذي دفع لابتكار تقنيات حديثة لجمع ونقل النفايات يتم تبنيها بصورة تدريجية في عدد من المشاريع والمناطق الحضرية حول العالم وهي تقنية جمع النفايات الالي باستعمال اسلوب الشفط (Automated Vacuum Waste Collection) والتي تعتمد على شبكة من الانابيب المدفونة تحت الارض لشفط النفايات بعد رميها من نقاط معينة فوق سطح الارض (تكون مخصصة للانواع المختلفة من النفايات التي تتراوح ما بين العلب المعدنية والزجاجيات والاوراق والفضلات العامة) وتمتد الى عدة كيلومترات الى ان تصل محطات المعالجة والكبس التي منها يتم استخراج النفايات لمعالجتها بالطريقة الامثل سواءاً كانت التدوير او استخراج الطاقة او الطمر (Ramon B. and Cesar F. and Felip M.,2012,p.264)

واحدة من المشاريع التي طبقت هذه المنظومة هو مشروع (لؤلؤة قطر) وهي جزيرة صناعية استخدامت منظومة شفط النفايات المكونة من شبكة انابيب مدفونة تحت الارض لنقل النفايات بطول (55) كم و القادرة على شفط

(135) طن من النفايات يومياً (شكل-1) متصلة بـ (415) منفذ لرمي النفايات (شكل -2) موزعة في عدة مواقع من الجزيرة و داخل ابنيتها المختلفة. (www.envacgroup.com/MediaBinaryLoader.axd).

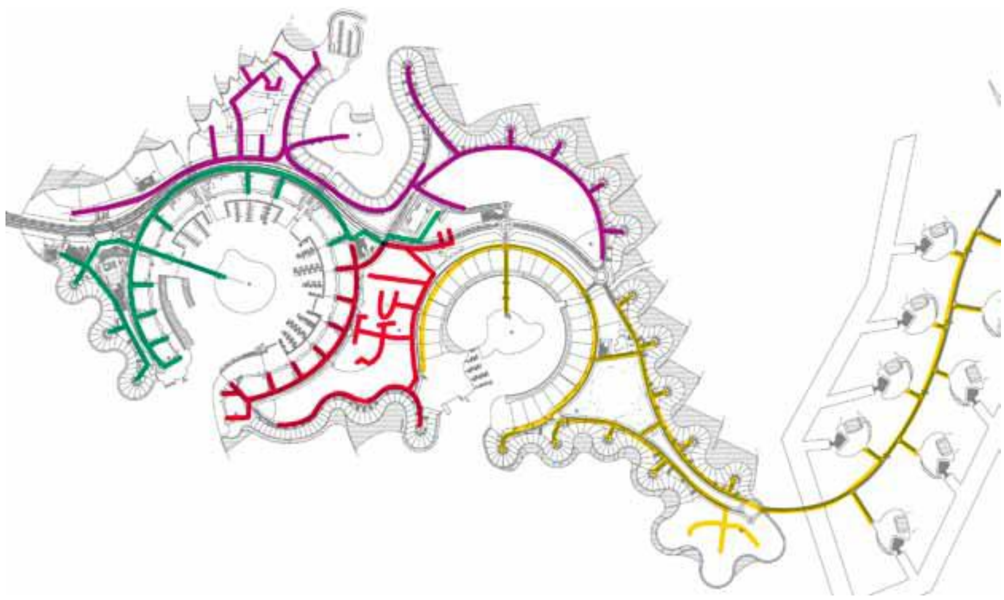

(شكل− 1) منظومة انابيب شفط النفايات في مشروع لؤلؤة قطر وتظهر شبكات الانابيب المدفونة تحت الارض بالوان مختافة تبعاً لنوع الابنية المخدومة سواءاً كانت شقق او فلل او مناطق تجارية وغيرها من انواع الابنية
www.en**vac**group.com/MediaBinaryLoader.axd?MediaArchive_FileID

(شكل−2) منافذ رمى النفايات الموزعة فى مشروع لؤلؤة قطر
www.envacgroup.com/MediaBinaryLoader.axd?.

مشروع اخر سيتم تنفيذه في مدينة (Vantaa Kivistö) في فنلندا والذي سيخدم (13000) نسمة وسيضم (110) موقع لرمي النفايات و(440) منفذ لرميها أي بواقع أربعة منافذ لكل موقع تصنف تبعاً لنوع النفايات التي يراد لاستغناء عنها.تمتد شبكة الأنابيب تحت الأرض بطول (9) كيلومتر(شكل-3) . كما سيتم تنفيذ اكبر منظومة في العالم لشفط النفايات في مكة المكرمة لخدمة الحجاج حيث ستمتد شبكة الأنابيب لمسافة (30) كيلومتر تحت الأرض ومن خلال (400) نقطة لرمي النفايات وستكون قادرة على نقل نفايات تقدر بـ (000 900) كيلوغرام / يومياً . (https://www.iswa.org/index.php?eID=tx_iswaknowledgebase_download...).

(شكل-3) مخطط مدينة (Vantaa Kivistö) وتظهر فيها مواقع رمي وجمع النفايات في المدينة
www.famad.fr/sites/make-ai/-upload-/3432_12745_20140417183153.pdf)

ان نقاط شفط النفايات التي سيتم توزيعها في المدينة بأحيائها وشوارعها ستكون احد المفردات المستحدثة إلى (أثاث الشارع) و ستكون باشكال و أحجام تتلاءم مع طبيعة موقعها سواءاً كانت في الحدائق او في المحلات السكنية مما سيؤثر على طبيعة وشكل تلك المنطقة من ناحية ومن ناحية ثانية سيجبر المصمم الحضري على تحديد مناطق معينة ومخصصة لمثل هذه المنظومات الخدمية بشكل يتلاءم مع منظومة شفط النفايات المستخدمة في تلك المنطقة باعتبارها جزءاً أساسيا من البنى التحتية الخاصة بالمدينة مما سيؤدي الى انتشار هذه المنظومات في عموم المدينة لتكون جزء اساسي من تكوينها (شكل-4). وفي حالة عدم امكانية استخدام هذه المنظومة فانه من اللازم التحول نحو منظومات شفط النفايات المتنقلة التي تعمل على شفط النفايات من حاويات خاصة لحفظ النفايات بطريقة لا تؤثر على جمالية المدينة و لاتؤدي الى تطاير النفايات او انسكابها في الشوارع مما سيؤدي الى انتشار الروائح الكريهة في المنطقة (شكل-5) .

(شكل –4) مناطق رمي النفايات تصمم حسب موقعها وتحدد اعدادها تبعاً لانواع النفايات التي ترمى من خلالها

www.envacgroup.com/BinaryLoader.axd?...Movac.

8- تقليل إنتاج النفايات:

تبدأ الإدارة الجيدة للنفايات بتقليل كميات النفايات منذ المراحل الأولى وبالتالي تحتلّ هذه المعالجة الأولوية في أي خطة لإدارة النفايات وتعني اي عملية قادرة على عدم انتاج نفايات سواءاً كان من خلال تصاميم افضل او تحسين طريقة الانتاج او التوجه نحو طريقة استهلاك جديدة وصولاً الى مستوى الصفر من النفايات ورغم ان هذه فكرة مثالية الا انها تمثل هدفاً للوصول اليه من خلال تغيير المواقف و الاتجاهات لدى المجتمع او من خلال التصاميم المقتصدة بالمواد الاولية. (Waste reduction,2007,p.12,p.19)

9- آليات معالجة النفايات:

9-1- إعادة التدوير:

تحولت عملية تدوير النفايات في الولايات المتحدة الامريكية خلال العقود الثلاثة الاخيرة من شئ صعب الى واقع حال مفروض ليكون جزءاً من المعالجة الحديثة لمشكلة النفايات. ففي عام (1960) كان معدل تدوير النفايات يعادل (6%) من مجمل النفايات التي تنتجها الولايات المتحدة انذاك.و بقت هذه النسبة تقريباً ثابتة حتى عام (1985) الا انها ارتفعت بشكل حاد ما بين عامي (1985-1995) لتصل الى نسبة (25%) من مجمل النفايات المنتجة ولتصل نسبة تدوير النفايات حسب احصائيات عام (2014) الى (83%) من مجمل النفايات المنتجة.لقد جاءت هذه التطورات استجابة لحملة الحفاظ واستعادة المواد الاولية التي بدأت الصناعة باستهلاكها بشكل متسارع وادت الى تقليل خزين المواد الاولية في الوقت ذاته بدأت المؤسسة الصناعية بطرح نفاياتها الى الارض بشكل مفتوح مما ادى الى تلوث البيئة بمياهها و هوائها وتربتها مما دفع الجهات الحكومية للتشجيع على استرداد جزء من المواد الاولية الملقاة في النفايات لتكون بذلك طريقة لتقليل استخدام المواد الاولية البكر و لتكون الخطوة الاولى نحو تحقيق التنمية المستدامة. (Jared S., 2014, p.5)

(شكل –5) منظومة شفط النفايات المتنقلة

www.**envac**group.com/storage/cms/.../pdf/.../**Movac**%20brochure_ENG.pdf

وبذلك أثرت طريقة نقل النفايات الجديدة على المدينة و بيئتها ومشهدها الحضري و اضافت عناصر معمارية جديدة لتؤثر بشكل واضح عليها و في ذات الوقت تم التخلص من الطريقة التقليدية لنقل النفايات التي كانت تؤثر سلباً على بيئة المدينة وجمالها.

9-1-1-انتاج الطاقة من النفايات بالحرق:

يعتبر استخراج الطاقة من النفايات بالحرق واحدة من الطرق لتحويل النفايات الى طاقة . تتم هذه العملية في محطات خاصة لإنتاج الطاقة قادرة على تقليل انبعاث الغازات و المواد الملوثة الناتجة عن عملية الحرق الى الجو وتمنع تسربها الى الأرض (كما كان يحصل سابقاً عندما كانت النفايات يتم ردمها في مكبات عامة مفتوحة ويتم حرقها في ظروف غير مسيطر عليها) (شكل-6).من الممكن الحصول على أشكال مختلفة من الطاقة من خلال هذه العملية مما سيقلل الطلب على الطاقة المنتجة من الوقود الاحفوري بشكل كبير كما ان هذه العملية ستعمل على تقليص حجم النفايات المطلوب التخلص منها.(Alexander K. and Nickolas J., 2003, p.1)
إذ أن حرق النفايات سيؤدي إلى تقليص حجمها بنسبة (75%) ويقلل من وزنها بنسبة تتراوح ما بين (60-40%) ورغم كفاءة هذه الطريقة الا انه ما زالت الطريقة الأكثر شيوعاً للتخلص من النفايات (خاصة في دول العالم الثالث) هي ردمها في المكبات.(Adrie V. et al,2005,p.3)

(شكل–6) مكبات النفايات المفتوحة فى العراق و عملية الحرق العشوائية الملوثة للجو والتربة
Johann F. www.iswa.org/.../5b%20**Landfilling**%20in%20**Iraq**%20-%20From%,

تمتلك دول العالم المتقدم تاريخاً طويلاً في الاستفادة من النفايات كمصدرلانتاج الطاقة ففي السويد انشأت اول محطة لانتاج الطاقة عن طريق حرق النفايات عام (1904)، وبعد انتهاء الحرب العالمية الثانية وسعت السويد استخدام النفايات كمصدر لانتاج الطاقة الحرارية للتدفئة. حيث ارتفعت نسبة الطاقة المنتجة من المصادر المتجددة بما فيها النفايات من (10%) عام (1985) الى نسبة (22%) عام (1996) من مجمل الطاقة المستخدمة في السويد و هي تسعى لايصال هذه النسبة الى (50%) بحلول عام (2020).اشارت التقارير الى ان النفايات جهزت السويد بطاقة تشكل (32%) من مجمل الطاقة المستهلكة فيها عام (2010) حيث تم حرق ما يقارب خمسة ملايين طن من النفايات خلال ذلك العام.

وكذلك الحال في الولايات المتحدة الامريكية التي انشأت اول محطة لانتاج الطاقة من النفايات بداية القرن العشرين الا ان هذا الاتجاه لانتاج الطاقة تذبذب صعوداً و هبوطاً حتى عام (1999) حيث تم استخدام (15%) من كمية النفايات المنتجة في منازل الولايات المتحدة كمصدر لانتاج الطاقة في ذلك العام تشير الدراسات التي تم اجرائها عام (2010) الى وجود (87) محطة لانتاج الطاقة من النفايات في الولايات المتحدة وتنتج ما نسبته (0.4%) من مجمل الطاقة التي تستخدمها الولايات المتحدة.(Matt W.,2011,p3-6). تتم عملية حرق النفايات في درجة حرارة تصل الى (850) درجة مئوية ومن ثم يتم الاستفادة من الطاقة الناتجة لتوليد الكهرباء او استخدامها للتدفئة ، تستهلك محطات انتاج الطاقة كميات نفايات تتراوح ما بين (50-300) الف طن سنوياً كما يمكن الاستفادة من مخلفات النفايات بعد الحرق و المسماة (الرماد السفلي) كحصى أو كبديل لطبقة الـ (Sub base) المستخدمة في تبليط الشوارع ، في عام (2010) انتجت المملكة المتحدة نفايات منزلية تقدر بـ (32) مليون طن تم تدوير ما نسبته (39%) و تم ردم (48%) منها في المكبات المنتشرة في المملكة و تم استخراج طاقة من (13%) من هذه الكمية من النفايات فقط. يقدر الخبراء بانه من الممكن انتاج (17%) من الطاقة التي تحتاجها المملكة المتحدة من النفايات بحلول عام (2020) كما ان المملكة المتحدة تنتج سنوياً ما مقداره مئة مليون طن من النفايات العضوية الرطبة التي يمكن ان تكون مصدراً متجدداً لانتاج الغاز البايولوجي (Biogas) الذي يمكن ان يغطي (4%-8) من نسبة الطاقة المتجددة التي تسعى المملكة المتحدة لانتاجها عام (2020)(شكل-7) .(Renewable Energy Assossiation,2011,p.3-5)

محطة Staffordshire المملكة المتحدة التي تم افتتاحها عام (2014) وتستهلك (300) الف طن من النفايات سنوياً المتحدة

(Renewable Energy Assossiation, 2011, p.6)

محطة stafforshire لانتاج الطاقة من النفايات في المملكة المتحدة
ee.ricardo.com/.../**Lakeside**-Visitors-Presentation-abrdgd-dc-112-EP.

محطة (Marchwood) في المملكة المتحدة تم افتتاحها عام (2004) وتستهلك (165) الف طن من النفايات سنويا
www.google.iq/search?q=marcwood+waste+power+plant&sa

(شكل–7) نماذج مختلفة لمحطات انتاج الطاقة من النفايات التي اثرت على البيئة الحضرية للمدينة و مشهدها الحضري

كما سعت الإمارات العربية المتحدة لإنشاء محطة لإنتاج الطاقة من النفايات و التي ستستهلك مليون طن من النفايات سنوياً و تمنع انبعاث ما مقداره (1.5) مليون طن من غاز ثاني اوكسيد الكربون إلى الجو و ستزود (20) ألف عائلة بالكهرباء عبر إنتاجها (100) ميجا واط من الطاقة الكهربائية (شكل-8).
(www.ramboll.com/projects/re/waste-to-energy-facility-in-abu-dhabi)

(شكل -8) محطة ابو ظبي لانتاج الطاقة من النفايات
http://www.gsda.co.uk

وتخطط الصين لبناء محطة (Schenzhen) التي ستستهلك (5000) طن من النفايات يومياً وستكون واحدة من (300) محطة سيتم بنائها في المستقبل. ما يميز المشروع فضلاً عن ضخامته هو وجود ممر للزوار يمر حول مكونات المحطة لشرح كل مرحلة من مراحل العمل في المحطة و بذلك لتكون نموذجاً تعليمياً للاشخاص. كما ان المحطة ستزود بسقف مغطى بخلايا شمسية بمساحة (44) الف متر مربع لتوفير الطاقة الكهربائية فضلاً عن وجود سقوف خضراء و مناطق لمعالجة مياه الأمطار على السقف (شكل-9).
www.fastcoexist.com/.../this-massive-**waste**-to-energy-**plant**-will-be-t.

(شكل–9) محطة (Schenzhen) لانتاج الطاقة من النفايات–الصين اكبر محطة فى العالم
www.fastcoexist.com/.../this-massive-**waste**-to-energy-**plant**-will-be-t.

9-2- ردم النفايات التحلل اللاهوائى(Bio-Mass):

يعرف التحليل اللاهوائي بانها عملية تقوم فيها الكائنات الدقيقة بتكسير المواد العضوية (بما فيها فضلات الطعام بدون وجود غاز الأوكسجين) لإنتاج الغاز العضوي الغني بالميثان الذي يمكن استخدامه كوقود لإنتاج الطاقة الكهربائية في الموقع والاستفادة من المتبقي من النفايات كأسمدة ويعتبر التحلل اللاهوائي أعلى مرتبة من التحليل الهوائي. إلا إن العمليتين لا يمكن الاعتماد عليهما أو استخدامهما بدون عزل الفضلات الغذائية وباقي المواد الملائمة لمثل هذا النوع من المعالجة عن باقي أنواع النفايات غير العضوية لان وجود المواد الغريبة في النفايات مثل المعادن أو المواد الضارة تؤثر على هذه العملية و تمنع استخدام النفايات المتبقية كأسمدة. (Ranjith, 2012, p.43)

9-2-1- امكانيات مساهمة منظومات توليد الطاقة من النفايات في تحقيق الاهداف المستقبلية التنموية:

اوضحت الدراسات في المملكة المتحدة عن امكانية انتاج طاقة كهربائية باستخدام تقنيات التحلل اللاهوائي تقدر بـ (6 Mtoe[2]) من الوقود الحيوي نظرياً و التي يمكن ان تساهم في معالجة مشكلة النقل وما ينتج عنها من ملوثات بيئية. ان التقنيات الحرارية لانتاج الطاقة من الفضلات في (المملكة المتحدة) يمكن استخدامها لمعالجة ما نسبته (25%) من النفايات الكلية المنتجة في المملكة بحلول عام (2020) لتنتج ما مقداره (21 Mtoe) من الطاقة المتجددة كما سيساهم غاز المكبات بتوفير ما مقداره (2 Mtoe) من الطاقة المستخدمة عام (2020) مع امكانية تحويل النفايات والجيل الثاني من الوقود الحيوي بما مقداره (1.3 Mtoe) من الطاقة لنفس الفترة. وكمجموع عام فان الطاقة المستخدمة من النفايات يمكن ان تساهم بما مجموعه (11 Mtoe) التي تعادل (50%) من كمية الطاقة المتجددة اللازم انتاجها عام (2020) لذا يمكن ملاحظة ان الطاقة المستخرجة من النفايات ستعوّض ما نسبته (13%) من الطاقة المستمدة من الوقود اليوم.(Goyanfi, 2007, P: 10) وفي السويد يتم طمر ما نسبته (4%) من النفايات فقط في المكبات، ونظراً لنجاح و كفاءة انتاج الطاقة من النفايات بداءت السويد باسترداد ما يقدر بــ (800 000) طن من النفايات من الدول المجاورة لتنتج طاقة لـ (250 000) عائلة وهي بذلك تعطي مثالاً لامكانية تحويل النفايات الى مصدر للحصول على الاموال بدلاً من طمرها او القائها في البحار (http://florence20.typepad.com/renaissance/2012/12/sweden-wants-your-trash.html).(شكل-10)

(شكل –10) محطة لانتاج الطاقة من النفايات في السويد تحرق ما مقداره (20) طن من النفايات في الساعة

http://florence20.typepad.com/renaissance/2012/12/sweden-wants-your-trash.html

اما في الدانمارك فقد تم وضع تصميم لاكبر محطة لانتاج الطاقة من النفايات وهي محطة (Amagerforbraending) بتصميم معماري جميل ومفيد ومستدام حيث تم استغلال سطح المبنى كمنصة للتزلج على الجليد أذ يتم الوصول الى السطح من خلال مصاعد ترتفع مع مدخنة المبنى وتؤمن النظر الى داخل

[2] (Mote) وحدة طاقة والتي تعادل الطاقة الناتجة عن حرق طن واحد من النفط الخام.

المبنى للتعريف بفعالياته الداخلية، تعمل مداخن المشروع على اطلاق حلقات من الدخان بقطر (30) متر كاشارة تحذير كلما تم انتاج طن واحد من غاز ثاني اوكسيد الكاربون لتذكير سكان مدينة (كوبنهاجن) بظرورة ترشيد استهلاك الطاقة واثر انتاجها على البيئة والمناخ (شكل-11).

(شكل -11) محطة (Amagerforbraending) لانتاج الطاقة من النفايات في الدانمارك
http://www.bustler.net/index.php/article/big_puts_a_ski_slope_on_copenhagens_new_waste-to-energy_plant

وقد وضع الاتحاد الاوربي هدفاً لتقليل انبعاث الغازات الدفيئة الى الجو وتقليل الاعتماد على الوقود الاحفوري ملزماً دول الاتحاد الاوربي بانتاج (20%) من الطاقة اللازمة لدوله من المصادر المتجددة بما فيها النفايات بحلول عام (2020) لذلك بدأت بعض الدول الاوربية بالتعامل مع نوع مميز من التجارة يتعلق بمسمى جديد هو (النفايات الخضراء) التي تحوي على مواد قابلة للتدوير و الحرق يتم تصديرها من بلد الى اخر كما هو الحال في السويد و الدانمارك. (Mette C.,2012 p.52-49)

وبذلك اثر استخدام النفايات لانتاج الطاقة على المدينة وبيئتها ومشهدها الحضري من خلال اضافة منشات معمارية خاصة لهذا الغرض ضمن مكونات المدينة كما استوجب وضع مواقع خاصة لهذه المنشات ضمن المخطط العام للمدينة.

9-3- طمر النفايات:

يتم طمر النفايات في حفر او فجوات على سفوح التلال او في الفجوات الموجودة على سطح الارض بعدها يتم كبسها بواسطة معدات ثقيلة وتغطيتها بطبقة من البلاستك التي يوضع فوقها كميات كبيرة من الاتربة.تمثل هذه الطريقة الاسلوب الاكثر استخداماً لطمر النفايات في العالم كما تم ذكره.الا ان هذه العملية تشكل خطراً كبيراً على البيئة وتؤدي لتلوث الهواء و المياه و خاصة المياه الجوفية، لذلك تتم احاطة مناطق الطمر باسيجة مرتفعة لاخفاء هذه المناطق عن المشاهدين كما يتم في بعض البلدان المتقدمة نشر كميات كبيرة من المعطرات لاخفاء الرائحة النتنة المنبعثة من هذه المناطق (Wikipedia Municipal solid waste)

لذلك انتهت معظم النفايات التي تنتج في دول العالم الثالث في مناطق الطمر غير المسيطر عليها، بما فيها دول الاتحاد الاوربي رغم تشريعه لقوانين صارمة تحث على عدم طمر النفايات الا ان نصف دول الاتحاد تطمر (75%) من نفاياتها في مكبات عامة.(R. Taylor and A. Allen,2003,p.1)

و رغم السياسات الدولية لخفض انتاج النفايات او اعادة تدويرها لتقليل الكميات اللازم طمرها ستبقى مكبات النفايات و مناطق الطمر مستخدمة لعقود قادمة مع امكانية تقليل كميات النفايات التي ستطمر فيها وهذه الظاهرة يمكن ملاحظتها في الدول العربية ومنها الاردن أذ كان الموقع المعتمد لطمر النفايات في مكبات مفتوحة يتم فيها حرق النفايات بدون سيطرة لتنتشر روائحها ومخلفاتها الى الجو و التربة. مما دعى الى ضرورة انشاء مكبات نفايات صحية مسيطر عليها ، كما ظهرت دعوات متزايدة لاعادة تدوير النفايات في مراحل مختلفة للاستفادة منها قبل طمرها.(Mohammed A. and Kenneth M., 2012)

ورغم ان عملية طمر النفايات غير محبذة الا انها افضل من ترك النفايات مفتوحة الى الهواء بدون تغطية لان ذلك سيؤدي الى:

1-اشتعال الحرائق الذاتية في النفايات مع انبعاث الابخرة الملوثة الى الجو.

2-انتشار الحشرات والقوارض الناقلة للأمراض والطفيليات.

3–انبعاث الروائح الكريهة خاصة بعد تخمر المواد العضوية وعفن الحيوانات النافقة.

4-تشويه منظر المدينة بسبب منظر المقالب المكشوفة.

5-تلويث المقالب المكشوفة للمياه الجوفية.

6-تطاير ألاتربة والرماد الناتج من الحرائق الى الجو بفعل الرياح مما يسبب العديد من الامراض مثل التهاب العين وحساسيةالجهاز التنفسي. (فريد،2015 ،ص35).

4-9-مناطق الطمر من حزام نفايات الى حزام اخضر:

لقد سعت الدول المتقدمة لتقليل كميات النفايات التي يتم طمرها. فالدانمارك تطمر (10%) من كمية النفايات التي تنتجها وتستخرج طاقة من (25%) منها، في حين تطمر المملكة المتحدة (50%) من نفاياتها و تستخرج جزءاً قليلاً من الطاقة منها. (Mette C., 2012 p. 52)، ومع الزمن شكلت مناطق الطمر حزام نفايات احاط بالمدن وأثر بشكل كبير على شكلها و قلل من جماليتها و جعلها مناطق منفرة للسياحة و غير صالحة لاي استخدام ،كما انه اثر على البيئة في تلك المنطقة بل اصبحت هذه المناطق بؤرة لانتشار الروائح الكريهه و الامراض المعدية ومصدراً لانتشار الذباب والحشرات الضارة، الامر الذي دفع عدداً من دول العالم الى تحويل هذه المناطق الى متنزهات او ملاعب خضراء لتكون جزءاً مكملاً للحزام الاخضر الذي يحيط بالمدن و يتحول حزام النفايات الى حزام اخضر مستدام يساعد على تحسين مناخ و بيئة المدينة و يضفي عليها الجمال مما يساعد على زيادة التصاق السكان بمدنهم ومناطقهم و يشجع على استخدام تلك المناطق لاغراض مختلفة (الباحث).

ففي الولايات المتحدة تم اعتبار المناطق المهملة والمتروكة المسماة (Brownfield) مثالاً للإهمال ولإثارة المشاعر السلبية وعدم العدالة البيئية و نموذجاً لفشل المجتمع في معالجة البيئة أذ شكلت هذه المناطق المهجورة والمهملة معضلة كبيرة للمخططين الحضريين، و يعاظم حجم المشكلة عندما تمتد هذه المناطق على مساحات واسعة و ضمن مواقع مهمة حول المدينة و قرب المناطق المأهولة لكون هذه المواقع ذات قيمة كبيرةمما حذا لمعالجتها واعادة تاهيلها و تطويرها ، ودفع الجهات الحكومية بهذا الاتجاه بالتعاون مع سكان تلك المناطق. لذلك كانت فكرة تحويل مناطق ردم النفايات إلى متنزهات من أفضل الحلول كمعالجة مقترحة و لتتحول مكبات النفايات الى متنزهات تكون جزءاً من مشروع التشجير الحضري للمدينة من جهة. كما إنه يعمل على الحد من توسع المدن أفقياً وبالتالي يمنع الزحف على الاراضي الزراعية المحيطة بالمدن من جهة اخرى، وبذلك وفر هذا الحل العدالة البيئية و حقق أهداف التنمية المستدامة لذلك يرى بعض الاختصاصين ان هذا يمثل افضل حل لمشكلة مناطق الطمر المتروكة والمهملة في المدينة او كالمناطق الصناعية أو العسكرية المتروكة ومناطق طمر النفايات ومكبات المخلفات الزراعية والصناعية وبالتالي فان اكثر من نصف هذه المناطق من الممكن أن يتحول إلى متنزهات تنشط السكان وتزيد من مساحة المناطق الخضراء داخل أو خارج المدن وهذا يتطابق مع افكار و توجهات صانعي القرارات السياسية الرامية الى انشاء المتنزهات و زيادة مساحة المناطق الخضراء داخل المدن وحولها لنشر الفعاليات الترفيهية كإستراتيجيات لإعادة تطوير المدن و المناطق الحضرية لتعمل المتنزهات على تمتين العلاقة ما بين السكان من ناحية ومن ناحية اخرى تقلل من التوتر العصبي لمرتاديها وتقوي الشعور بالجيرة و الشعور بالأمان و تقلل من الجرائم. (Amanda J., 2009, P: 85)

10-امثلة على تحويل مناطق ردم النفايات الى متنزهات

يعتبر مشروع (Rainier Dump) في مدينة (سياتل)/ الولايات المتحدة الامريكية أول مكب للنفايات تحول إلى ملعب) (Rainier play Field)عام (1916) و منذ ذلك الحين تم تحويل (1000) موقع في العالم من مكب نفايات إلى متنزهات او ملاعب.

اما في هونج كونج فان اول مكب نفايات تم تحويله الى متنزه متعدد الاغراض هو متنزه (Sai Tso Wan) حيث تم عزل النفايات عن التربة الجديدة الخاصة بالمتنزه بشكل محكم وفي الموقع الجديد تم انشاء متنزة يضم ملاعب و ساحات رياضية و معسكرات للتخييم مما اعطى اهمية اكبر للمنطقة التي انشأ فيها و ضاعف اقبال الناس على السكن في تلك المنطقة بعدما كانت منطقة متروكة و غير مرغوب فيها بل اصبح المتنزه الشعار الرسمي للحركة الخضراء في هونج كوج (شكل-12) A. P. Rijs. ,2007,p.20

(شكل–12) متنزه (Sai Tso Wan) اول متنزه في هونج كونج يتحول من مكب تفايات الى متنزه

A. P. Rijs. ,2007,p.20

كما يعتبر متنزه (Fresh Kills Park) الموجود في جزيرة (Western Staten) /مدينة (نيويورك)/ الولايات المتحدة الامريكية أكبر موقع لردم النفايات في العالم تم تحويله إلى متنزه. حيث أستمر طمر نفايات المدينة في هذا الموقع لمدة مئة عام وتم رمي ما يقدر بـ (150) مليون طن من النفايات في هذا الموقع أذ تمت دراسة جميع مخاوف السكان التي أثيرت وتم وضع المعايير البيئية اللازمة لمعالجتها للوصول الى السلامة البيئية اللازمة للمتنزه و لزواره (شكل-13) . اوصت الدراسات الى تحويل هذا المكب الى متنزه كبير تزيد بثلاث اضعاف عن مساحة متنزه (سنترال بارك) الموجود في وسط مدينة (نيويورك) ، تم استخدام الوسائل الهندسية والتقنيات الايكولوجية لجعل هذا الموقع آمناً. (Jenni C. et-al,2012,p.23)

متنزه (Nanjido) في مدينة (سيئول – كوريا الجنوبية) مساحة المتنزه (3,46) كيلومتر مربع ، أفتتح جزئيا عام (2002) ومن المتوقع انجاز العمل فيه بالكامل عام (2020) بعد أن كان مكب نفايات غير مسيطر عليه مما أدى إلى تلوث تربة و مياه المنطقة وخاصة نهر (Han) المجاور.، تصاميمه تركزت على المعالجات البيئية و الايكولوجية أذ تم استغلال النفايات الموجودة في الموقع كمصدر لإنتاج غاز الميثان الذي مكن من انتاج طاقة كهربائية تكفي لخدمة (000 180) منزلا/يوميا ، وبذلك تم منع انبعاث الغازات إلى الجو و تم تقليل الروائح

الكريهة المنتشرة والسيطرة على امكانية انفجارها في حالة عدم السيطرة عليها. تزامن افتتاحه مع كاس العالم لعام (2002) (شكل-14) .

أما مكب (Mount Trash) للنفايات فانه تحول إلى متنزه (Mount Trash Park) والذي تبلغ مساحته (0.66) كيلومتر مربع ، الذي تم افتتاحه عام (1974) بعد أن كان مكباً للنفايات للمدة الممتدة ما بين عامي (1967-1972) وهو الآن من أكثر المتنزهات شعبية في ساحل (فرجينيا)/ الولايات المتحدة الأمريكية، ويزوره مليون زائر سنوياً، ويضم حديقة تعليمية للنباتات الصحراوية وملعب تزلج، وبحيرتان صناعيتان مستدامتان تعملان كحوضان لجمع مياه الأمطار للاستفادة منها (شكل-15)(Jenni C., et al., 2012, p.23, p, 72).

مكب النفايات (Fresh kills) في الولايات المتحدة

Benjamin A. L. , 2015, p.43

(شكل-13) متنزة (Fresh kills) في الولايات المتحدة

Jenni C., 2012

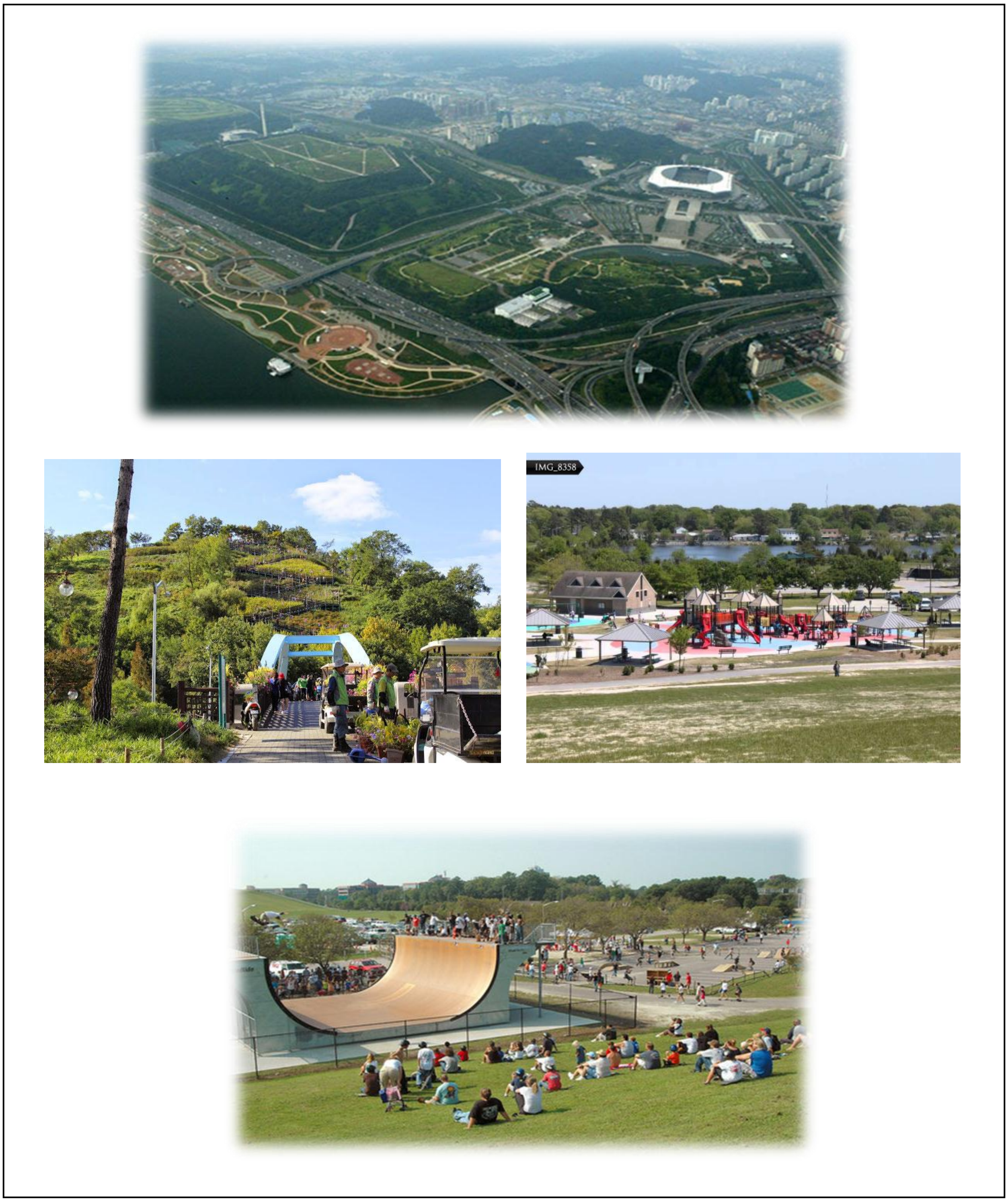

(شكل-14) منتزه (Nanjido) سيؤل- كوريا الجنوبية تحول من مكب نفايات الى منتزه ايكولوجي يضم ملاعب اطفال و مناطق تزلج

www.facenfacts.com/.../seouls-**landfill**-turnaround:-**nanjido**-**park**-where-flowers-

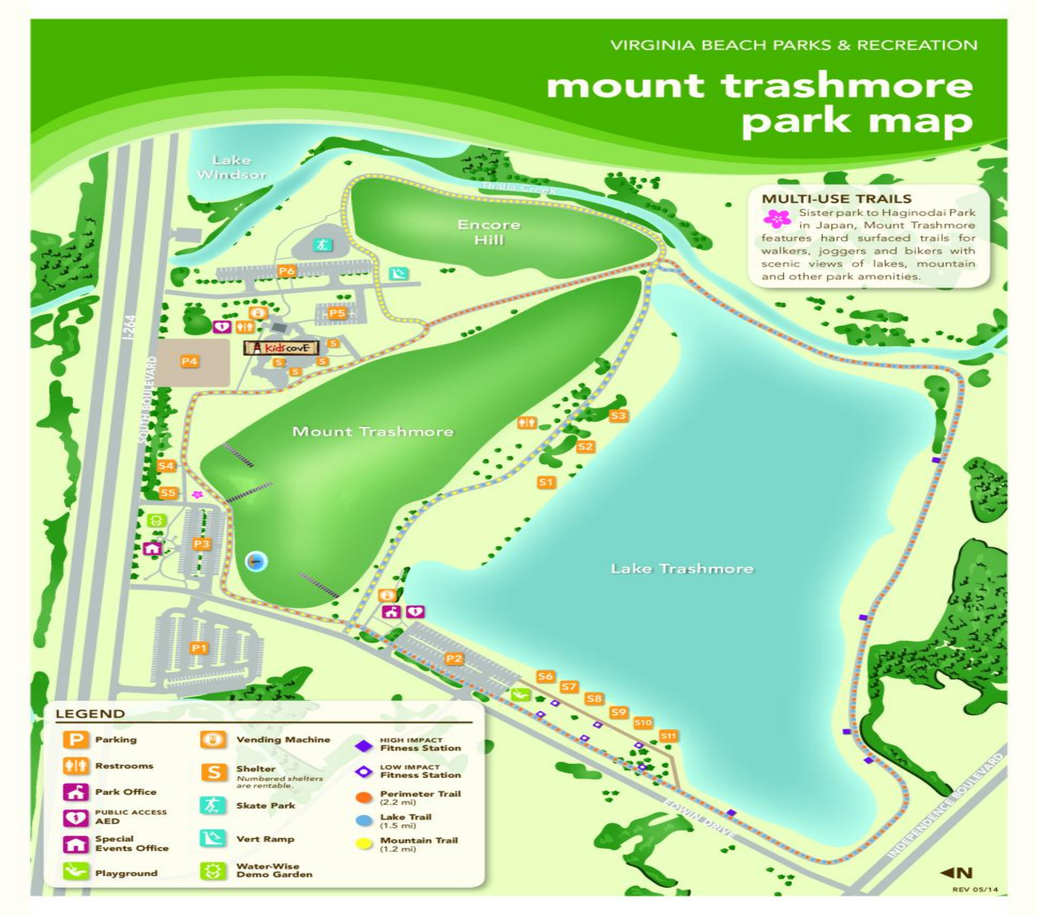

مخطط متنزه (Mount trash) فيرجينيا/الولايات المتحدة

https://www.vbgov.com/government/.../**parks**.../**parks**.../**mount-trashmore-park**-map

(شكل –15) متنزه (Mount trash) فيرجينيا – الولايات المتحدة الذي تحول من مكب نفايات الى متنزه

https://en.wikipedia.org/wiki/Mount_Trashmore_Park

الاستنتاجات و التوصيات

- انتجت الحضارة المعاصرة نوعاً جديداً من المشاكل البيئية و التخطيطية و التصميمية التي تتعلق بمعالجة النفايات الحضرية الصلبة التي انتجتها مفردات الحياة المعاصرة بكافة مرافقها السكنية والصناعية و التجارية واصبحت جزءاً لا يتجزأ من حياتنا مما استوجب ضرورة معالجة جميع المشاكل المتعلقة بانتاج النفايات وعلى كافة المراحل ابتداءاً من جمعها الى نقلها و الاستفادة منها ومن ثم التخلص منها.أذ ان كل مرحلة من هذه المراحل تحتاج الى معالجات خاصة و محددة ستفرض معالجاتها تاثيرات على البيئة الحضرية للمدينة ومشهدها الحضري تبعاً لنوع المعالجة وحدودها.
- ان معالجة مشكلة جمع و نقل النفايات و التحول من الطريقة التقليدية المتبعة لجمع النفايات الى المنظومات الحديثة لشفط النفايات ستفرض نوعاً جديداً من اثاث الشارع متمثلة بمناطق رمي النفايات التي تحدد مواقعها تبعاً لمنظومة الشفط، كما ان تصميمها و شكلها سيتحدد تبعاً لموقعها المقترح و طبيعته ،سيقلل هذا التحول الحاجة لاستخدام مركبات نقل النفايات الكبيرة الملوثة للبيئة التي تعيق حركة المرور في الشوارع عامة والضيقة خاصة . كما ان استخدام هذه سيحسن من بيئية المدينة وجمالها من خلال عدم رمي وتجميع النفايات في شوارعها. فضلاً عن ان هذه الطريقة ستقلل الضوضاء الناتجة عن عملية جمع النفايات بما فيها قلب الحاويات وستعيد الهدوء الى الاحياء السكنية والمناطق التجارية خاصة اوقات جمع النفايات.لذلك ستؤثر الطريقة المقترحة لجمع ونقل النفايات على شكل المدينة و بيئتها ومشهدها الحضري.
- ان معالجة مشكلة النفايات والاستفادة منها لانتاج الطاقة الكهربائية أو الحرارية سيؤدي الى التاثير على تخطيط المدينة و ذلك للحاجة الى محطات خاصة لتحويل النفايات الى طاقة والتي ستكون جزءاً من المدينة و بناها التحتية مما سيؤثر على شكل المدينة و بيئتها ومشهدها الحضري.
- ان معالجة مناطق طمر النفايات للتخلص من مشاكلها البيئية وتحويلها الى متنزهات و مناطق لعب خضراء سيؤثر على تخطيط المدينة و جمالها وبيئتها لان تحويل مكبات النفايات المفتوحة و حتى المغطاة الى متنزهات سيمنع من انتشار الروائح الكريهة الى الجو ويقلل من تسرب المواد الملوثة السائلة الى الارض او الى المياه الجوفية ،كما انه سيحول تلك المناطق المنفرة والطاردة للافراد و للسكن و للاستثمار الى مناطق جاذبة لهذه الفعاليات و يرفع من قيمتها (خاصة اذا ما كانت هذه المناطق قريبة من المدينة أومن احيائها السكنية)، اما اذا كانت هذه المناطق خارج المدن ومحيطة او قريبة منها فان تحولها الى متنزهات سيجعلها جزءاً من الحزام الاخضر الذي يحيط بالمدن، العامل الذي سيحسن بيئة تلك المنطقة ليؤثر ايجابياً على تخطيط المدينة و تصميمها الحضري.كما توجد امكانية للاستفادة من الغازات الناتجة عن مناطق الطمر واستغلالها لانتاج الطاقة ومنع انبعاثها الى الجو مما يقلل من تاثير هذه الغازات على البيئة و المناخ مما سيؤثر ايجابياً على شكل المدينة و بيئتها ومشهدها الحضري.

المصادر العربية

بن مشيرح ،جمعة،2015، *دور التكنلوجيا الخضراء في تحسين المشهد الحضري* ،رسالة ماجستير في هندسة العمارة جامعة الحاج لخضر –جمهورية الجزائر ، ص31-35)

يوسف ، فريد ،2012 ، *واقع الأوضاع البيئية في مصر لامركزية اتخاذ القرار من خلال التخطيط بالمشاركة لتحسين الأوضاع البيئية (بعد 25 يناير)* ،ماعت للتنمية والسلام وحقوق الانسان.

المصادر الاجنبية

Adrie Veeken, Pim Hamminga, and Zhang Mingshu, *Improving Sustainability of Municipal Solid Waste Management in China*, Source Separated Collection and Biological Treatment of the Organic Fraction,2005, Urban Environment Group, Department of Environmental Technology, Wageningen University and Research).

Amanda J. Johnson,2009, *One person trash is another person treasure the public place making of mount trash*, Journal of Park and recreation admin., Vol.27,No.1,pp:85-103/ 2009.p,85

Alexander Klein and Nickolas J. Themelis,2003, *Energy Recovery from Municipal Solid Wastes by Gasification*, North American Waste to Energy Conference (NAWTEC 11)11 Proceedings, ASME International,Tampa FL (April 2003),p.1.

A.P. Rijs, 2007, *Planning for: the Redevelopment of Former Landfill Sites and the Establishment of Alternative Waste Facilities*, 2007, MUNICIPAL ENGINEERING FOUNDATION 2007 STUDY TOUR

Benjamin A. Lawson,2015, *Garbage mountains: the use, redevelopment, and Artistic representation of New York City's Fresh Kills*, Greater Toronto's Keele Valley, A thesis submitted in partial fulfillment of the requirements for the Doctor of Philosophy degree in History in the Graduate College of the University of Iowa.

Chandrappa ,R.,Bhusan .d..Diganta.S.2012. *Solid Waste Management Principles and Practice* ,Springer, ISBN-13: 000-3642286801.

Daniel H. and Perinaz T.,2012, *What a waste a Global Review of solid Waste Management*, Urban Development & Local Government Unit,p.8
World Bank**.**

Goyanfi, K.A., 2007, *Renewable energy Land Fill gas and EFW, next and future* , p.10.

Jared, S, *Patterns in Trash: Factors that Drive Municipal Solid Waste Recycling* , 2014.

Jenni C., et al, 2012, *Freshkills Park A Communications Strategy to Address Public Health Concerns*,, Columbia university.

Klein**,** A.& Nickolas J. Themelis, *Energy Recovery from Municipal Solid Wastes by Gasification* ,North American Waste to Energy Conference (NAWTEC 11)11 Proceedings, ASME International, Tampa FL (April 2003),

Knowles, J.A.,*National solid waste in Iraq*, proceedings waste 2008,Golder associates(UK) managing organization for waste.

Mackwood,2004, *Energy from Waste a Guide for Decision Makers* ,renewable energy assossiation ,p.3-5

Matt W, *Waste to energy success factors in Sweden and the united states*,2011,p3-6.

Mette , C.,2012, *Waste, a resource* , Cand. Merc.International Business ", Master Thesis CopenhagenBusiness School, 2012, p.52.

Mohammad Aljaradin1, Kenneth M. Persson,2012, *Comparison of Different Waste Management Technologies and Climate Change Effect*, Jordan , ,Department of Water Resources Engineering, Lund University, Lund, Sweden Sydvatten AB, Malmö, Sweden .

Ram´on B´ejar1, C`esar Fern´andez1, Carles Mateu1, Felip Many`a, and Francina, *Solving The Automated VacuumWaste Collection Optimization Problem*, 2012, Sole-Mauri, Dpt. Of Computer Science, Universitat de Lleida, Spain,p.264.

Ranjith, K. N., 2012, *Sustainable Solid Waste Management in India***,** Submitted in partial fulfillment of the requirements for the degree of Master of Science in Earth Resources Engineering Department of Earth and Environmental Engineering Fu Foundation School of Engineering and Applied Science Columbia University.

Renewable Energy Association, 2011,p.3-5.

Riydh A. yasir, *Characteristics and compositions of solid waste in Nassiriya city*,2009, Al Qadisiya journal for engineering science , Vol.2 , Mo. 2,pp.137-140.

R. Taylor and A. Allen,2007, *Waste Disposal and Landfill: Information Needs* Accessed on 26 March 2007, pp. 1-8. http://www.google.Taylor,p.1p:1.

Ryidh A. Y. and Zaidun N. A., 2009, *Characteristics and Compositions of Solid Waste in Nassirya City*, Al- Qadisiya Journal for Engineering Sciences Vol. 2.

Waste Management Services policy round table Report, 2013, OECD, p.10.

Waste Reduction, vol.1 report, 2007, house of lords,p.12, p.19.11.

مصادر الانترنيت

http://www.ecomena.org/swm-iraq.

http://www.bustler.net/index.php/article/big_puts_a_ski_slope_on_copenhagens_new_waste-to-energy_plant

www.ramboll.com/projects/re/**waste-to-energy**-facility-in-abu-dhabi

www.fastcoexist.com/…/this-massive-**waste**-to-energy-**plant**-will-be-t.

http://florence20.typepad.com/renaissance/2012/12/sweden-wants-your-trash.html.

www.iswa.org/.../5b%20**Landfilling**%20in%20**Iraq**%20-%20From%

www.ee.ricardo.com/…/**Lakeside-Visitors-Presentation**-abrdgd-dc-112-EP.

www.google.iq/search?q=marcwood+waste+power+plant&sa

www.envacgroup.com/BinaryLoader.axd.

www.google.iq/search?q=marcwood+waste+power+plant&sa

http://www.gsda.co.uk

Wikipedia Municipal solid waste

www.deq.louisiana.gov/portal/Portals/0/.../DYK- Landfills. Pdf

www.famad.fr/sites/make-ai/-upload-/3432_12745_20140417183153.pdf

ISSN 1726 - 4073

Journal of Engineering

A Scientific Refereed Journal
Published by
College of Engineering
University of Baghdad

March
2017

Number 3
Volume 23

ENGINEERING

College of Engineering University of Baghdad No.3 Vol. 23 March 2017

List of Contents

English Section: Page

ISSN 1726 - 4073

مجلة الهندسة

مجلة علمية محكمة تصدرها
كلية الهندسة ـ جامعة بغداد

أذار
2017

العدد 3
المجلد 23

قائمة المحتويات

القسم العربي: